

Aus dem CharitéCentrum 12 für Innere Medizin und Dermatologie
Medizinische Klinik mit Schwerpunkt Rheumatologie und Klinische Immunologie
Fachvertreter: Prof. Dr. med. Frank Buttgereit

Habilitationsschrift

Implementation of the 3R principle in musculoskeletal research – Refinement measures and *in vitro* replacement methods

Zur Erlangung der Lehrbefähigung
für das Fach Experimentelle Rheumatologie

vorgelegt dem Fakultätsrat der Medizinischen Fakultät
Charité-Universitätsmedizin Berlin

von

Dr. med. vet. Annemarie Lang, PhD

Eingereicht: Dezember/2021
Dekan: Prof. Dr. med. Axel R. Pries Elizabeth Balmayor
1. Gutachterin: Prof. Dr. Anita Ignatius, Ulm
2. Gutachterin: Prof. Dr. Elizabeth Balmayor, Aachen

*“In [The Principles of Humane Experimental Technique] we have sought only to
limn the barest of outlines; it will remain for others to fill in the interior.
We hope the book may stimulate some experimentalists
to devote special attention to the subject, and many others to work in full
awareness of its existence and possibilities.”*

Russell and Burch 1959 *The Principles of Humane Experimental Technique* [1] Chapter 8 - Conclusion

Table of Contents

ABBREVIATIONS	IV
1. INTRODUCTION	5
1.1 Overview on musculoskeletal disorders and preclinical research	5
1.2 The definition of the 3R principle by Russell and Burch	7
1.3 Refinement measures in musculoskeletal research with a specific focus on murine fracture models	8
1.4 Replacement approaches to recapitulate musculoskeletal disorders – <i>In vitro</i> methods for fracture healing and joint diseases	10
1.4.1 <i>Fracture healing and overview on in vitro models</i>	11
1.4.2 <i>Osteoarthritis and overview on in vitro methods</i>	13
1.4.3 <i>Rheumatoid arthritis and overview on in vitro methods</i>	14
1.5 Aims and Objectives	15
2. OWN PUBLICATIONS	16
2.1 Evaluation of pain management protocols in a mouse-osteotomy model	16
2.2 Characterization of an <i>in vitro</i> equine fracture hematoma model	33
2.3 Development of a human <i>in vitro</i> fracture gap model	54
2.4 <i>In vitro</i> and <i>in silico</i> modelling to study the pathogenesis of osteoarthritis	68
2.5 Recapitulating arthritis-related effects on the osteochondral unit <i>in vitro</i>	90
3. DISCUSSION	116
3.1 Pain management and assessment in mice – Fundamental challenges in the implementation of refinement measures	116
3.2 Recapitulating the initial phase of fracture healing <i>in vitro</i> – Modelling the crosstalk between immune cells and bone	119
3.3 Mimicking key features of joint disorders <i>in vitro</i> – Technical considerations on complexity and its limitations	122
3.4 The active implementation of the 3R principle in biomedical research – Closing thoughts on challenges and opportunities	126
SUMMARY	128
ZUSAMMENFASSUNG	129
REFERENCES	130
DANKSAGUNG	139
ERKLÄRUNG	140

Abbreviations

3D	three-dimensional
COL	collagen
COX2	cyclooxygenase 2
CXCL	C-X-C motif ligand
DFO	deferoxamine
ETPLAS	Education and Training Platform for Laboratory Animal Science
FH	fracture hematoma
IL	interleukin
JRC	Joint Research Centre
LDHA	lactate dehydrogenase A
MCP-1	monocyte chemotactic protein 1
MIF	macrophage migration inhibitory factor
MMP	matrix metalloproteinase
MSC	mesenchymal stromal cells
NSAID	non-steroidal anti-inflammatory drugs
OA	osteoarthritis
OTM	osteocondral tissue model
PLGA	poly-lactic-co-glycolic acid
RA	rheumatoid arthritis
ROS	reactive oxygen species
RUNX2	Runt-related transcription factor 2
SFBC	scaffold-free bone-like construct
SFCC	scaffold-free cartilage-like construct
SPP1	secreted phosphoprotein 1 (osteopontin)
TCP	tricalcium phosphate
TGF β	transforming growth factor beta
TNF α	tumour necrosis factor alpha
VEGFA	vascular endothelial growth factor A

1. INTRODUCTION

1.1 Overview on musculoskeletal disorders and preclinical research

The musculoskeletal system determines the bodies' shape and enables unrestricted locomotion [2]. Bone ensures stability and force distribution, while e.g. muscles, cartilage, ligaments, and tendons connect the skeleton and allow flexibility during movements. Musculoskeletal disorders are a major cause of morbidity and the main reason for the existence of rehabilitation programs. Limitations in everyday activity, physical disability or even immobility together with chronic pain result in a loss of life quality and enormous costs for the health care economy. The musculoskeletal conditions of most interest and impact include osteoarthritis, rheumatoid arthritis, osteoporosis, low back pain, traumas and injuries including fractures.

Bone has the unique ability to completely regenerate without any scar formation. However, fracture repair is a challenging clinical problem. Each year, millions of patients worldwide experience bone fracture: one every two-to-three seconds. Over 10–15% of these fractures suffer from impaired healing, resulting in estimated costs of over \$10,000 per treatment and an average disablement duration of 50 days for limb fractures [3]. Bone is therefore the second-most grafted tissue behind blood transfusion. Especially the elderly population is disproportionately affected, being associated with permanent impairment and increased mortality [4]. These adverse outcomes and slow repair cause significant burdens to the patient's life and the socio-economic and health care systems.

Osteoarthritis (OA) is a complex and serious chronic degenerative joint disease with an increasingly high global prevalence and burden. According to the World Health Organization, 18% of women and 10% of men aged 60 or older show forms of symptomatic OA, with 25% being unable to perform daily life activities [5]. Over the last decades, the prevalence has been growing due to an increased life expectancy and a rise in associated risk factors such as physical inactivity and obesity. These risk factors influence the complex interplay between reduced load or overload, mechanical stress, inflammation, molecular and cellular catabolic mechanisms, and matrix-degrading factors, that lead to OA initiation and progression [6, 7]. Despite its prevalence, the molecular mechanisms triggering OA are poorly characterized and there are currently no disease-modifying therapies that can halt or revert OA.

Rheumatoid arthritis (RA) is a common autoimmune disease and typically presents with pain, stiffness, and symmetrical swelling of the joints in the hands or feet. RA is a progressive disease that advances from painful joint inflammation to irreversible bony erosions and joint deformation. The overall prevalence is higher in women than men and individuals af-

ected by RA are often between 35 and 45 years at onset. Globally, 0.1–2.0% of the population suffer from RA and in the US about 1 in 4 adults (23.7%) has been diagnosed with arthritis between 2013 and 2015 [8]. According to current recommendations, today's treatment goal is to achieve remission or at least low disease activity [9]. However, despite major progress in the treatment of RA, a strong unmet medical need remains, as only a minor proportion of patients reaches sustained clinical remission, and about 25% of patients still suffer from moderate or even high disease activity [10].

Further fundamental and translational preclinical research is imperative to address the unmet medical needs, ensuring health throughout the life course and reducing hospitalization time and mortality in the (elderly) population. The current standard of preclinical research to develop new sophisticated therapeutic strategies and to identify potential targets and drug compounds is the use of animal models, i.e. mainly rodents (mouse, rat). In general, animal models serve to i) examine pathophysiological processes of musculoskeletal disorders in a complete physiological system and ii) to evaluate and determine new therapeutics such as anti-inflammatory biologics, tissue regenerating compounds and biomaterials for regenerative tissue reconstruction [11]. The possibility for genetic modification, high reproductive rates, minimal housing requirements, the existence of varying analysis tools, including diverse antibodies, and their known genome sequence led to the fact that rodents are preferably used. In fact, they account for more than half of all animals used in musculoskeletal research. However, for translational purposes, a two-step approach is most often employed, using a rodent model (e.g. mouse or rat) for proof-of-concept studies and a large animal model (e.g. sheep or pig) as follow-up evaluation. Since musculoskeletal disorders are the major contributor to disability worldwide, preclinical research is steadily increasing and contributes a non-negligible number of animals to the total use of animals in science. According to the report of the European Commission published in 2017 (2015–2017; Directive 2010/63/EU), the research category on the musculoskeletal system accounts for approx. 100,000 animals in basic research and approx. 40,000 animals in translational and applied research out of the total of 9 million animals [12, 13]. Since mice and rats are not covered by the Animal Welfare Act in the US, the number of animals used in science is estimated at 11–23 million (2018; [14]). Considering the NIH funding shares for musculoskeletal disease research are less than 2%, an approximate number of 220,000 – 460,000 animals can be assumed to be used in this scientific field [13, 15].

Although animal models have allowed the scientific community to uncover numerous fundamental pathways and to study the complexity of a whole organism, inter-species differences may be the reason for the high failure rates of potential new therapeutic compounds

in clinical testing scenarios. Exemplary, main challenges in the translation with a specific focus on rodents include [16]:

- structural differences on the micro- and macro-scale of bones in rodents (e.g. no Haversian canals) as well as the lifelong skeletal remodelling due to a late closing of the growth plates;
- altered posture and walking behaviour based on tetrapod motion, resulting in different mechanical strains when compared to the upright walk;
- restricted lifespan, which opposes the development of age-induced chronic disorders (e.g. OA) requiring the induction of disease complexes in young healthy individuals in species where the specific disease might not occur naturally (e.g. osteoporosis in rodents);
- restricted heterogeneity between individuals due to controlled housing conditions and inbred strains.

Hence, traditional research approaches in biomedicine should be rethought towards a human patient-driven translation. Thereby, the active implementation of the 3R principle and therefore, the humane use of animals in research can accelerate and does definitively not oppose the translational process.

1.2 The definition of the 3R principle by Russell and Burch

In 1959, Russell and Burch published their book *The Principles of Humane Experimental Technique*. They proposed a new framework to ameliorate the treatment of laboratory animals which is known as the 3R principle [1]. Their scientific philosophical treatise does not only contain the humane treatment of laboratory animals but also important arguments about how this approach enhances and ensures scientific quality in studies using animals [1]. The ultimate destination of the 3Rs is to achieve humanity by reducing or even eliminating inhumanity. Inhumanity is therefore synonymously discussed as distress with concerning the mental state of the animal used. Thus, the 3Rs intend to minimize distressful experiences of laboratory animals and are introduced as following: “*We turn now to consideration of the ways in which inhumanity can be and is being diminished or removed. These ways can be discussed under the 3 broad headings of Replacement, Reduction, and Refinement....(T)he 3 modes now considered have conveniently been referred to as the 3Rs of humane technique. Replacement means the substitution for conscious living higher animals of insentient material. Reduction means reduction in the numbers of animals used to obtain information of a given amount and precision. Refinement means any decrease in the incidence or severity of inhumane procedures applied to those animals which still have to be used.*” ([1]; Chapter 4 – *The Removal of Inhumanity: The Three R's*)

During the past decades, the 3R principle has been moved into focus of the scientific community and has been subject to numerous discussions and further interpretations [17-19]. The currently used definition of *replacement* exclusively comprises so-called “alternative” methods, ideally without the use of any animal material (e.g. non-animal technologies – NAMs) which, according to the definition of Russell and Burch, is equivalent to *absolute replacement* and the absolute ideal to completely eliminate distress from the animal’s experience [1, 19]. However, they precisely point out that the reduction of distress is the primary goal of the 3Rs rather than eliminating the use of animal experiments by using insentient material, whether animal or non-animal. Thus, the term *relative replacement* is additionally introduced to describe situations in which animals are still required but do not experience any distress, e.g. collecting organs and tissue for cell culture preparation after euthanasia or performing experiments under deep anaesthesia [1]. This does partly overlap with today’s interpretation of *reduction*. However, Russell and Burch discuss the term *reduction* solely in the specific context of using statistical methods, including knowledge and experience of potential variances, to use the minimum number of animals that is required to provide a sufficient answer to the scientific question [1]. *Refinement* does specifically focus on the absolute minimization of any distress of these animals that still need to be used. Interestingly, today’s definition most often equates the definition with enhancing animal wellbeing which was later on also included and confirmed by Russell and Burch during presentations and follow-up publications [1, 19]. Hence, there are differences in the today’s generally used interpretations of the 3Rs compared to the original definitions by Russell and Burch which need to be considered carefully, especially when evaluating potential 3R measures and their impact in a scientific context.

The integration of the 3R principles into European legislation with the Directive 2010/63/EU, including the request to address and facilitate the 3Rs, represents a milestone for the potential implementation of the 3R principle into research [17].

1.3 Refinement measures in musculoskeletal research with a specific focus on murine fracture models

Fracture healing is a spatiotemporally tightly regulated regeneration process leading to a complete restoration of the broken bone without fibrous scar formation. Naturally, this regeneration process resembles endochondral bone formation due to the occurrence of interfragmentary movement within the fracture gap. Several risk factors are known to potentially disturb the natural healing process, such as medications (e.g. non-steroidal anti-inflammatory drugs – NSAIDs or glucocorticoids), comorbidities (e.g. Diabetes mellitus, osteoporosis) or lifestyle (e.g. obesity, smoking, alcohol abuse). Impaired fracture healing can occur

with different manifestations. Normal bone regeneration takes 3–4 months, whereas extensions are determined as delayed healing and a non-union describes no healing after 6–9 months. Preclinical orthopaedic research aims at recapitulating the different scenarios and risk factors by using adequate animal models. In fracture research, mice and rats are most prominently used to study underlying mechanisms of pathophysiological processes and define potential new therapeutic strategies [20]. To stabilize a (femoral or tibial) fracture in mice, three established methods are known: the intramedullary pin, the external fixator, and plates [21, 22]. The fracture gap can be created by either osteotomy (cutting the bone with e.g. a Gigli wire saw) or fracturing using e.g., a 3-point bending system. Fracture models with stable fixation are ranked as moderately painful according to the severity catalogue of the EU-Directive 2010/63/EU, which makes a sufficient pain management protocol indispensable [23].

Insufficiently treated pain impacts animal wellbeing and induces discomfort and stress. Moreover, pain is known to have unpredictable effects on the physiology of the whole organism, e.g. by impairing wound healing or immune response [24–26]. Thus, adequate pain management is not only an obligation based on ethical standards but is also based on scientific merits to ensure the integrity and quality of the gained research data. Human patients with trauma and fracture most often experience pain from the injury and soft tissue damage itself rather than the plain bone trauma [27]. Patients with acute long bone fractures normally report moderate to severe pain [28]. Even though soft tissue injuries are avoided in experimental procedures, the pain usually peaks on day 2 post-operatively in stable fixed rodent fracture models and might be similar to what human patients experience [29, 30].

The selection of analgesics for rodent fracture models is limited due to potential interfering properties of anti-inflammatory drugs. Prostaglandins play a crucial role during the initial, inflammatory phase of fracture healing [31, 32]. NSAIDs and Coxibs reduce prostaglandin synthesis by inhibition of cyclooxygenase 2 (COX-2) and are therefore described to negatively interfere with fracture repair [25, 33, 34]. However, clinical studies in humans and preclinical studies in animal models exhibited inconclusive results, especially on the inhibitory effect of NSAIDs [35–38]. Nevertheless, COX2 inhibitors are often replaced with opioids in laboratory animal care to avoid the potential risk for interfering with the physiological healing process [39]. Buprenorphine and tramadol, an opioid analogue, are commonly applied in preclinical research. Due to insufficient empirical data on effectiveness and dosage, application recommendations vary substantially in the literature. Buprenorphine is fast-acting, highly potent and mainly administered s.c. or i.p. (0.05–0.75 mg/kg). The most common injection interval is 12 h, although recent studies reported a short half-life and recommend administration every 6 h to avoid periods of insufficient pain treatment [40]. Tramadol can

be administered in high dosages (> 50–100 mg/kg s.c.) to ameliorate severe pain, e.g. in bone cancer models [41], but also acts to relieve more acute and moderate pain conditions in reduced concentrations [42]. However, the 1-2 h half-life of tramadol is rather short, resulting in the fact that tramadol is most often applied via drinking water rather than injection [43, 44]. Recommendations for oral administration of tramadol vary from 0.025 mg/ml up to 1 mg/ml [45-49]. Table 1 summarizes the different reported analgesic protocols used in stable fixated mouse femoral fracture models based on a systematic literature review [22]. However, data on the effectiveness of commonly used analgesic treatment regimens, especially in orthopaedic mouse models, is scarce to date [25, 50].

Table 1: Overview of commonly used pain management protocols in mouse femoral fracture models. Adapted and reproduced from [22].

Intra-operative				Post-operative			
Substance	Application method	Dose	Application point	Application method	Dose	Application point	Duration (in days)
Buprenorphine	s.c., i.p.	0.03 – 0.1 mg/kg	pre- or intraoperative	s.c., i.p.	0.03 – 0.1 mg/kg	every 6–12 h, daily (every 24h)	single dose, 1, 5, 2, 3, 5, 7 d
				drinking water	0.009 mg/ml	<i>ad libitum</i>	3 d
				jelly	0.15 mg/kg	<i>ad libitum</i>	2–3 d
SR Buprenorphine	s.c.	1 mg/kg	intraoperative	-	-	-	-
Tramadol	s.c.	15 – 20 mg/kg	pre- or intraoperative	s.c.	20 mg/kg	every 12 h	1.5 d
	DW	25 mg/l – 100 mg/l	0–2 d pre-operative	DW	25 mg/l – 100mg/l	<i>ad libitum</i>	1–3 d
Carprofen	s.c., i.m.	4 – 5 mg/kg	pre- or intraoperative	s.c., i.m.	4 – 5 mg/kg	every 24h	1–3 d/ as needed

SR – sustained-release; DW – drinking water; s.c. – subcutaneous; i.p. – intraperitoneal; i.m. – intramuscular

1.4 Replacement approaches to recapitulate musculoskeletal disorders – *In vitro* methods for fracture healing and joint diseases

During recent years, there has been a turnaround in traditional cell culture technology to provide more physiological and human-relevant features. This development was also driven by methodological innovations in tissue engineering for regenerative therapies, e.g. to produce huge batches of primary cells, three-dimensional (3D) nature-like artificial tissues or biocompatible biomaterials. A positive side effect is the rapid technical evolution towards more innovative biomaterials, microfluidic systems, organ-on-a-chip technologies and adaptable modular bioreactor platforms [2]. *In vitro* methods for musculoskeletal research bring forth the need to consider several key aspects. Cell-cell and cell-tissue interaction are essential in a three-dimensional environment to recapitulate nano-/micro-mechanical conditions. In detail, most musculoskeletal tissues, especially bone and cartilage, consist of far more extracellular matrix than cells. Thus, the interaction of these cells with the surrounding matrix is fundamental for cell fate, shape, and functionality. Based on this, milli- or macroscale approaches are indispensable to generate enough material for further analysis. In

addition, tissues such as cartilage are not vascularized and therefore, require precise considerations of nutrient supply and oxygenation. Finally, the musculoskeletal system is maintained by a highly dynamic and active biomechanical environment, which needs to be included if relevant to corresponding modelling approaches.

1.4.1 Fracture healing and overview on *in vitro* models

Endochondral bone healing consists of four phases: i) initial inflammatory phase; ii) fibrocartilaginous or soft callus; iii) mineralized or hard callus; and iv) the remodelling phase [51]. Pro- and anti-inflammatory processes in the immediately formed fracture hematoma control the initial phase of fracture healing, which is crucial activating the subsequent regeneration cascade [31, 52] (Fig. 1). The accumulation of immune cells in the fracture hematoma combined with a restricted microenvironment (hypoxia, low pH, and high lactate concentrations) results in complex pro-inflammatory processes, which are essential for the subsequent reconstruction. Thus, monocytes and macrophages, as well as mesenchymal stromal cells (MSCs), periosteal cells and endothelial cells, are recruited to the fracture area to rebuild the bone matrix and the vascular system, leading to an anti-inflammatory and pro-angiogenic phase [53, 54]. The consecutive process of endochondral ossification is characterized by proliferation and differentiation of progenitor cells towards the chondrogenic and/or osteogenic lineage forming cartilage (soft callus) and initiation of mineralization (hard callus). Parts of this phase reflect key elements of the embryological bone development including cell proliferation and maturation as well as the formation of extracellular matrix [55]. The remodelling phase comprises the resorption of the formed woven bone by osteoclasts and the formation of lamellar bone structures with a medullary cavity by osteoblasts leading to the complete restoration of the biomechanical properties of the bone. Taken together, the first phase of endochondral ossification is characterized by i) bio-mechanical insults due to loss of bone integrity; ii) a hypoxic microenvironment; iii) invasion of progenitor cells; and iv) neovascularization.

Current related *in vitro* systems can be divided into different groups based on purpose and methodological approach [13]. The focus currently relies on mimicking bone development, endochondral ossification itself and bone homeostasis, whereby *ex vivo* and *in vitro* approaches can be distinguished. *Ex vivo* organ cultures are suggested to be close to the *in vivo* situation since primary whole tissue material is collected and further cultivated *in vitro* [16]. Bone growth is studied using limb organ cultures, while bone healing can be partly mimicked by calvarial cultures, mandible/molar slice cultures or trabecular core cultures. Plain *in vitro* models rely on the development of artificial systems to simulate key features of the tissue or disease of interest. Therefore, spheroid cultures, scaffold-based and scaffold-free model systems, such as spheroids, are to be distinguished.

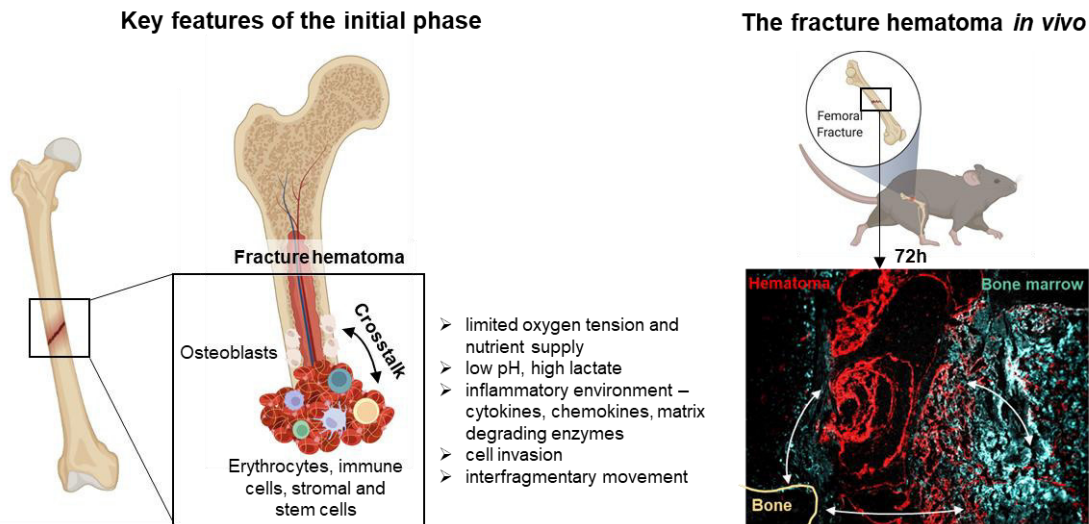


Figure 1: Overview of key features of the initial phase of fracture healing including characteristics of the fracture hematoma highlighting the crosstalk between blood, immune, bone marrow and bone cells. Immunofluorescence image on the right side exemplifies the *in vivo* situation in a fracture gap 72h after osteotomy in a mouse model – reproduced and modified from [56]. Figure contains graphics which were created with BioRender.com.

Commonly used cells include osteoblasts, osteocytes, osteoclasts and MSCs as progenitor cells in single cell approaches or co-cultures [2, 57]. The combination of a scaffold and bone-related cells represents the most described form of artificial bone development. The following cultivation can be either static or dynamic and current approaches report the successful integration of endothelial cells. The scaffold mainly consists of either inorganic bone material (hydroxyapatite; calcium phosphate) or organic matrix (e.g. collagen type I) to primarily support cell colonization, invasion and differentiation [58]. Therefore, adequate imitation of the native bone matrix is achieved by improving material properties and quality towards i) biocompatibility for cell attachment and maintained viability [59], ii) adapted surface properties triggering cell proliferation, maturation and potentially differentiation [60], iii) naturally-inspired mechanical properties by the tissue of interest [61], iv) porous structures to permit cell reorganization and nutrient and oxygen supply [60], and v) biodegradability to initiate remodelling. In contrast to the more modular principle of scaffold-based approaches, scaffold-free approaches are based on the cell's own ability to produce, form and remodel matrix. To create e.g. spheroids, mesenchymal condensation and endochondral ossification are recapitulated to allow cellular self-organization and follow the natural process of osteogenic tissue formation. Models focused on the initial phase of fracture healing have not been described in the literature and require additional modelling capacities as immune cells must be included in a complex *in vitro* setting.

1.4.2 Osteoarthritis and overview on *in vitro* methods

Articular cartilage is an avascular and non-innervated tissue that mainly consists of extracellular matrix composed of 60–80% water, 20% proteoglycans/aggrecans, 5% collagen type II and only contains low numbers of cells – 1–5% chondrocytes [62]. Nutrient supply is maintained by diffusion from the subchondral bone and synovium lining the joint capsule [63]. Thus, chondrocytes are adapted to hypoxia and restricted nutrients. Moreover, they are highly dependent on biomechanical forces and shear stress to maintain cartilage integrity and their metabolism. The general pathogenesis of OA is dominated by cartilage degradation driven by inflammatory processes on the molecular level. Hyaline cartilage has a limited regenerative capacity, resulting in a complete cartilage loss over time and reasoning joint-related remodelling processes such as synovial membrane hypertrophy and thickening of the subchondral bone area (Fig. 2).

Current *ex vivo* and *in vitro* approaches specifically aim to mimic the cartilage degradation, inflammation, and changes in cellular homeostasis. As model systems, monolayer cultures (cell lines vs. primary cells), 3D cultures and cartilage explants are widely used [64–69] (Fig. 2). A major challenge for the use of primary chondrocytes or explants is the tissue origin and availability, as sample collection is performed during knee or hip replacement surgeries (patients with end-stage OA). Samples collected from large animals (e.g. slaughterhouses) represent an alternative option, although species differences and availability of antibodies can be challenging. The cultivation of primary chondrocytes in a 3D microenvironment recapitulates the naturally surrounding structures *in vivo* more closely. However, to create 3D cultures, scaffolds are most often used to provide a predefined structure, which might have beneficial but also disturbing effects on the cells (e.g. non-tissue-derived proteins). To avoid the used of scaffold, scaffold-free tissue-engineered approaches have been developed and tested as alternatives and for successful cartilage repair *in vivo*. These approaches can easily be transferred as *in vitro* technology to study matrix homeostasis and degradation in a human-relevant setting [70–72]. Current cartilage-on-a-chip approaches also include the application of biomechanical forces on a microscale. However, the sample size (miniaturization), type and direction of loading (only compression) and usage of different hydrogels as artificial extracellular matrix lead to an oversimplification impeding the utility potential of such systems for biomedical basic and translational research [73, 74]. Interleukin (IL)-1 β plays a crucial role as key mediator in OA pathophysiology and joint inflammation and thus, is commonly used to induce OA-related changes in *in vitro* models [75–78]. Other inflammatory stimuli used in three-dimensional *in vitro* OA models include tumour necrosis factor (TNF) α , with and without IL-1 β or transforming growth factor (TGF)- β , macrophages in co-culture, synovial fluid or joint capsule, as well as exosomes from IL-1 β stimulated fibroblast-like synoviocytes [79].

1.4.3 Rheumatoid arthritis and overview on *in vitro* methods

RA is a disabling disease characterized by persistent synovitis and systemic inflammation. With the production of autoantibodies and via the involvement of cells such as neutrophils, lymphocytes, macrophages and fibroblastic-like synoviocytes, the immune system attacks endogenous tissues such as cartilage, bone, and connective tissues. The persistent inflammation of the joint is one of the key features of this systemic, chronic inflammatory disease accounting for progressive cartilage destruction. The complex pathogenesis includes inflammation-induced expansion of the synoviocyte layer (hypertrophy and pannus formation) and infiltration of pannus tissue, especially by neutrophils and other immune cells later on, as well as increased angiogenesis [80] (Fig. 2). The infiltration of neutrophils, B-cells, T-cells and macrophages in the normally cell-poor synovial membrane and the increased number of macrophage- and mesenchymal/fibroblastic-like synoviocytes in the pannus tissue lead to increased metabolic demand and, therefore, to an undersupply of the synovial tissue with both nutrients and oxygen [81, 82]. As a consequence of the subsequent local hypoxia, new vessels are formed (angiogenesis) further facilitating the inflammatory process [83]. The high concentrations of pro-inflammatory cytokines produced by invading immune cells, as well as the increasing levels of matrix-degrading enzymes – matrix metalloproteinases (MMP) and the tumour-like invasion of pannus tissue destroy the cartilage and negatively affect the subchondral bone (Fig. 2). Without treatment, the chronic-progressive joint destruction may result in deformities, considerable disabilities, and invalidity.

To define the underlying mechanism and to design new therapeutic strategies, animal models are crucial in the context of autoimmune diseases, especially genetically-modified mice models [84]. However, the existing mouse models only display key features of the disease; they are not able to reflect the human disease in all aspects [85]. Therefore, different *in vitro* models have been developed and evaluated during the last years [86]. The variety of *in vitro* models ranges from simple monolayer culture of synoviocytes to co-culture systems with chondrocytes or the *in vitro* cultivation of pannus tissue explants from RA patients [68, 87, 88] (Fig. 2). Despite current progress in joint-on-a-chip technologies aiming to implement the immune component, e.g. via macrophages [74, 89] (Fig. 2), no appropriate *in vitro* model exists to mimic either a healthy or an arthritic joint including most of the relevant tissue types, cells and humoral factors (e.g. cytokines, prostaglandins etc.) involved and thereby allowing the testing of multispecific approaches. Additionally, for biologics, such as antibodies, that are highly specific for the human target proteins, non-humanized rodent animal models are not suitable.

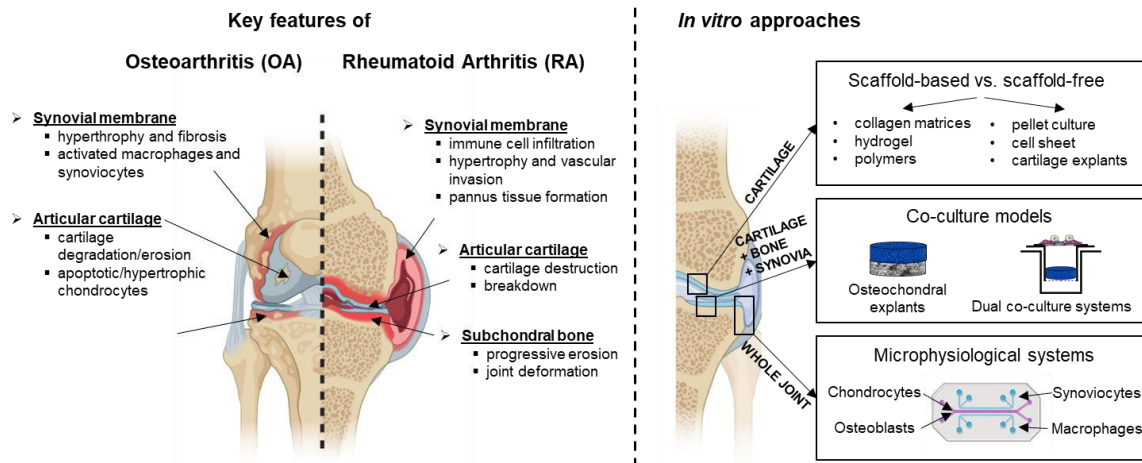


Figure 2: Overview of key features of OA and RA and exemplary representation of commonly used approaches. Figure contains graphics that were created with BioRender.com.

1.5 Aims and Objectives

Preclinical fundamental and translational research, target screening and compound development relies on animal models. However, insufficient knowledge on laboratory animal physiology and trans-species differences may be responsible for the limited transferability of findings to the human patient.

My recent work and this thesis aim to

1. evaluate the pain regimens in mouse-osteotomy models to avoid unnecessary pain and discomfort for the animals and increase the transferability of results to the human patient;
2. recapitulate the in-patient situation by developing *in vitro* approaches to evade cross-species differences and to *replace* lab animal usage with a specific focus on fracture healing and joint pathologies (OA and RA).

Thus, I specifically show the diversity of implementing the 3R principle in musculoskeletal research and highlight that the humane treatment of laboratory animals is not opposed to performing ground-breaking research, but rather strengthens its innovative capacity, forward-thinking sustainability, and rapid translation to the clinic.

2. OWN PUBLICATIONS

2.1 Evaluation of pain management protocols in a mouse-osteotomy model

To enhance the current knowledge on *refinement* measures in fundamental research studies and to provide evidence-based data on pain management protocols, we evaluated two analgesics, tramadol and buprenorphine in the drinking water, for their efficiency and side effects on experimental readout in a mouse-osteotomy model. The study was efficiently embedded in a fundamental research study [56, 90, 91] and therefore, shows the possibility to combine such studies and effectively *reduce* animals.

The following text corresponds to the abstract of the work:

Jirkof, P.*, Durst, M.*, Klopfleisch, R., Palme, R., Thöne-Reineke, C., Buttgerit, F., Schmidt-Bleek, K., **Lang, A.** (2019) Administration of Tramadol or Buprenorphine via the drinking water for post-operative analgesia in a mouse-osteotomy model. *Scientific Reports*. Jul 24; 9(1):10749. [doi: 10.1038/s41598-019-47186-5]

“Adequate analgesia is essential whenever pain might occur in animal experiments. Unfortunately, the selection of suitable analgesics for mice in bone-linked models is limited. Here, we evaluated two analgesics – Tramadol [0.1 mg/ml (Tlow) vs. 1 mg/ml (Thigh)] and Buprenorphine (Bup; 0.009 mg/ml) – after a pre-surgical injection of Buprenorphine, in a mouse-osteotomy model. The aim of this study was to verify the efficacy of these opioids in alleviating pain-related behaviors, to provide evidence for adequate dosages and to examine potential side effects. High concentrations of Tramadol affected water intake, drinking frequency, food intake and body weight negatively in the first 2–3 days post-osteotomy, while home cage activity was comparable between all groups. General wellbeing parameters were strongly influenced by anesthesia and analgesics. Model-specific pain parameters did not indicate more effective pain relief at high concentrations of Tramadol. In addition, ex vivo high-resolution micro computed tomography (μ CT) analysis and histology analyzing bone healing outcomes showed no differences between analgesic groups with respect to newly formed mineralized bone, cartilage and vessels. Our results show that high concentrations of Tramadol do not improve pain relief compared to low dosage Tramadol and Buprenorphine, but rather negatively affect animal wellbeing.”

SCIENTIFIC REPORTS

OPEN

Administration of Tramadol or Buprenorphine via the drinking water for post-operative analgesia in a mouse-osteotomy model

Paulin Jirkof¹, Mattea Durst^{1,2}, Robert Klopffleisch³, Rupert Palme⁴, Christa Thöne-Reineke⁵, Frank Buttgereit^{2,6}, Katharina Schmidt-Bleek^{7,8} & Annemarie Lang^{2,6,8}

Adequate analgesia is essential whenever pain might occur in animal experiments. Unfortunately, the selection of suitable analgesics for mice in bone-linked models is limited. Here, we evaluated two analgesics – Tramadol [0.1 mg/ml (T_{low}) vs. 1 mg/ml (T_{high})] and Buprenorphine (Bup; 0.009 mg/ml) – after a pre-surgical injection of Buprenorphine, in a mouse-osteotomy model. The aim of this study was to verify the efficacy of these opioids in alleviating pain-related behaviors, to provide evidence for adequate dosages and to examine potential side effects. High concentrations of Tramadol affected water intake, drinking frequency, food intake and body weight negatively in the first 2–3 days post-osteotomy, while home cage activity was comparable between all groups. General wellbeing parameters were strongly influenced by anesthesia and analgesics. Model-specific pain parameters did not indicate more effective pain relief at high concentrations of Tramadol. In addition, *ex vivo* high-resolution micro computed tomography (μ CT) analysis and histology analyzing bone healing outcomes showed no differences between analgesic groups with respect to newly formed mineralized bone, cartilage and vessels. Our results show that high concentrations of Tramadol do not improve pain relief compared to low dosage Tramadol and Buprenorphine, but rather negatively affect animal wellbeing.

Untreated or insufficiently treated pain hampers animal welfare and may have diverse and uncontrollable effects on an organism, such as impaired wound healing, blood flow disorders, or immunosuppression^{1–3}. Therefore, adequate pain management is essential for ethical and scientific reasons whenever pain might occur in animal experiments. Unfortunately, data on the efficacy of specific analgesic treatments in commonly used surgical mouse models is still scarce^{2,4}.

Human patients with fractures are exposed to experiences such as injury and pain⁵. Acute pain ranging from moderate to severe is observed in emergency departments when patients arrive with e.g. long bone fractures⁶. In rodent models of closed femur fractures with a stable pin fixation, the pain peak is expected at day 2 post-operatively and might be comparable to the pain experienced by human patients⁷. Even though the acute pain in a fracture is reduced by manual fixation in the animal model, the impact catalogue of the EU-Directive

¹Division of Surgical Research, University Hospital Zurich, University of Zurich, Zurich, Switzerland. ²Charité – Universitätsmedizin Berlin, corporate member of Freie Universität Berlin, Humboldt-Universität zu Berlin, and Berlin Institute of Health, Department of Rheumatology and Clinical Immunology, Berlin, Germany. ³Institute of Veterinary Pathology, Department of Veterinary Medicine, Freie Universität Berlin, Berlin, Germany. ⁴Unit of Physiology, Pathophysiology and Experimental Endocrinology, Department of Biomedical Sciences, University of Veterinary Medicine, Vienna, Austria. ⁵Institute of Animal Welfare, Animal Behavior and Laboratory Animal Science, Department of Veterinary Medicine, Freie Universität Berlin, Berlin, Germany. ⁶German Rheumatism Research Centre (DRFZ) Berlin, a Leibniz Institute, Berlin, Germany. ⁷Charité – Universitätsmedizin Berlin, corporate member of Freie Universität Berlin, Humboldt-Universität zu Berlin, and Berlin Institute of Health, Julius Wolff Institute and Center for Musculoskeletal Surgery, Berlin, Germany. ⁸Charité – Universitätsmedizin Berlin, corporate member of Freie Universität Berlin, Humboldt-Universität zu Berlin, and Berlin Institute of Health Berlin Brandenburg Center for Regenerative Therapies, Berlin, Germany. Paulin Jirkof and Mattea Durst contributed equally. Correspondence and requests for materials should be addressed to A.L. (email: annemarie.lang@charite.de)

Groups	Food intake (g) Median (Min – Max)					Water intake (ml) Median (Min – Max)				
	0h	24h	48h	72h	96h	0h	24h	48h	72h	96h
T _{low} OT	7.69 (7.5–8.8)	5.09 (4.4–5.8)	7.92 (6.4–9.7)	7.63 (5.4–10.1)	10.25 (3.0–14.5)	9.26 (7.4–9.9)	7.26 (3.8–11.7)	9.88 (6.2–11.3)	10.67 (10.5–13.2)	7.90 (7.4–10.0)
T _{high} OT	9.05 (8.5–9.2)	4.56 (2.8–14.2)	3.75 (2.9–4.0)	8.05 (5.0–9.0)	11.76 (10.2–16.8)	9.38 (8.5–11.0)	10.19 (8.7–12.5)	5.35 (3.1–11.1)	5.69 (5.0–6.3)	9.52 (9.1–9.9)
Bup OT	8.54 (8.3–9.7)	6.84 (5.2–9.8)	4.77 (4.0–6.1)	11.92 (10.1–17.1)	8.97 (5.8–12.5)	9.15 (8.2–10.2)	8.65 (4.5–11.7)	7.38 (4.5–11.6)	11.34 (10.0–12.7)	9.80 (9.4–10.9)

Table 1. Food and water intake per cage for the osteotomy groups. N = 4 cages (with 2 mice per cage). See Supplementary Table S1 for values of control groups (AN, DW).

2010/63/EU classifies stable osteotomies as moderately painful procedures; therefore, reliable analgesic treatment is essential in these models.

Unfortunately, the selection of suitable analgesics for mice in bone healing research is limited, since concerns have been raised about potential adverse effects of non-steroidal anti-inflammatory drugs (NSAIDs) on the initial, inflammatory phase of bone healing^{8,9}.

The opioid Buprenorphine and the opioid analogue Tramadol are applied widely in many fields of research, although empirical data on effective doses for rats and mice are rare, and thus dosage recommendations vary substantially in the literature. Buprenorphine is a commonly used fast acting and potent opioid that is mainly administered s.c. or i.p. in dosages of 0.05–0.75 mg/kg every 12 h although recent studies indicate the short half-life and recommend the administration at every 4–6 h¹⁰. Tramadol, for example, is used in high dosages for bone cancer models (>50–100 mg/kg s.c.)¹¹, but appears also effective in lower concentrations to treat acute pain¹². The application of Tramadol via injections is questionable due to its short half-life of 1–2 h^{13,14}, which should be taken into account when designing studies on the efficacy of Tramadol in order to avoid drawing misleading conclusions¹⁵. Concentrations recommended for oral administration of Tramadol range from 0.025 mg/ml up to 1 mg/ml^{16–20}. Nevertheless, to our knowledge, no evidence-based recommendations exist for the treatment of osteotomy pain with Tramadol or Buprenorphine. Therefore, the need for evidence-based and empirical data on the dosage and effectiveness of analgesics in bone research is apparent and further studies must be enrolled.

Here, we performed a refinement study embedded in a basic research study of a mouse-osteotomy model²¹. We evaluated two commonly used pain management protocols, Tramadol (0.1 mg/ml = T_{low} vs. 1 mg/ml = T_{high}) and Buprenorphine (0.009 mg/ml = Bup) administered via drinking water, after an initial pre-operative injection of Buprenorphine (0.03 mg/kg, s.c.), for their efficacy and side effects on experimental readouts in a mouse-osteotomy model. We asked the research question whether the application of Tramadol or Buprenorphine in commonly used dosages via drinking water represents a continuous, stress-free method of administering effective analgesia in the mouse-osteotomy model with no adverse impact on fracture healing in the model used.

Results

Drinking frequency and water intake are affected by type and concentration of opioid. Overall water intake was reduced compared to baseline in the T_{high} osteotomy (OT) group at 48 h and 72 h after surgery (Table 1, for other groups see Supplementary Table S1). Prior to surgery or start of treatment, the baseline of the drinking frequency over 48 h was assessed for n = 8 mice, which resulted in a median of 182 events in 48 h (interquartile range: 170.5, 207). Video analysis for 48 h starting 9 h after osteotomy enabled the examination of the drinking frequency and therefore the monitoring of continuous analgesia up-take (Fig. 1b,c). After start of the experiment, the number of drinking events decreased significantly in the T_{high} OT group compared to the T_{low} OT groups (Kruskal-Wallis test and Dunn's multiple comparison test; H = 7.42; exact p = 0.01; adjusted p = 0.04 – T_{low} vs. T_{high}) and showed a non-significant tendency for reduction compared to the Bup OT (adjusted p > 0.99 T_{low} vs. Bup, p = 0.07 Bup vs. T_{high}) (Fig. 1b). To evaluate the impact of the anesthesia and the treated drinking water alone on the outcome parameters, two control groups were used in the study. In the anesthesia (AN) group, animals underwent isoflurane anesthesia and were treated with either high or low dose Tramadol or Buprenorphine via drinking water for 3 days. In the drinking water (DW) group, animals received either high or low dose Tramadol or Buprenorphine via drinking water over 3 days. In the AN and DW groups, the drinking frequency was slightly higher in the Bup groups compared to the T groups (Supplementary Fig. S1). The depiction of individual drinking events indicates a decline in the drinking frequency in the T_{high} OT group between 36 h and 48 h post-osteotomy (Fig. 1c).

T_{low} Tramadol and M1 serum concentrations appear sufficient. To verify sufficient intake of Tramadol, sera from T_{low} OT mice euthanized 3 days after osteotomy were analyzed for Tramadol and O-Desmethyl-Tramadol – the analgesic active/effective metabolite (M1) – concentrations. The mean serum concentration of Tramadol was 27.1 ng/ml (±12.9 ng/ml) and the mean M1 concentration was 119.6 ng/ml (±81.1 ng/ml; Fig. 1d).

High concentrations of Tramadol in the drinking water impact body weight and food intake. As a parameter of general wellbeing, body weight was measured every 24 h and normalized to the initial body weight directly before osteotomy (baseline). Animals of all treatment groups lost weight compared to baseline values, regardless of whether they underwent surgery or not. The body weights of all groups undergoing OT were significantly reduced at 24 h after surgery compared to the initial body weight before surgery and recovered on the

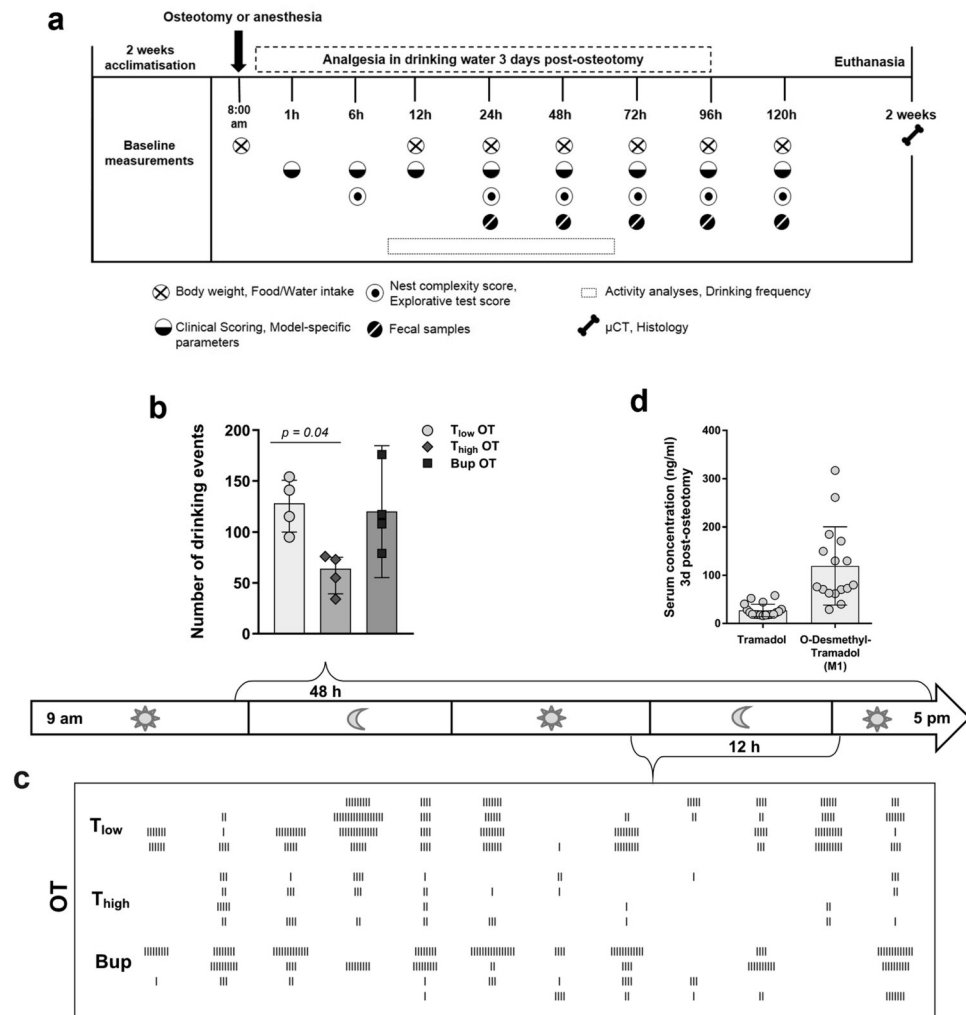


Figure 1. Drinking frequency is reduced concentration-dependent by Tramadol. (a) Study design. Overview on time points and measurements of the different parameters. (b) Total number of drinking events for 48 h was assessed via video recording. Data are shown for OT groups as scatter dot plot and bar with median \pm interquartile ranges ($n = 4$). For group differences Kruskal-Wallis test and Dunn's multiple comparison test were applied; adjusted p -values are indicated. Results of AN and DW groups are provided as Supplementary Fig. S1. (c) Depiction of the drinking events over 12 h between 36 h and 48 h post-osteotomy. Each line indicates one drinking event ($n = 4$). (d) Concentrations of Tramadol and M1 3 days post-osteotomy were analyzed in sera from mice treated with the same regime as the T_{low} OT group. Data are shown as scatter dot plot and bar with mean \pm SD ($n = 18$).

following days depending on the analgesia protocol (one sample t test; exact p -values are listed in Supplementary Table S2) (Fig. 2a). Bup OT and T_{low} OT mice reached initial body weight levels ($\geq 100\%$) at 72 h post-osteotomy. In contrast, T_{high} OT mice showed significant decreased body weight until 120 h after osteotomy. Significant group differences were found at 24, 48, 72 and 96 h post-osteotomy, $F(14, 100) = 26.21$ ($p < 0.001$) (One-way ANOVA with Bonferroni's multiple comparisons test; selected pairs comparison; adjusted p -values are indicated in Fig. 2a). In detail, mice of the Bup OT group revealed significant lower fold changes compared to the T_{high} OT group at 24 h, 48 h, 72 h and 96 h, respectively and the T_{low} OT at 24 h. Additionally, at 72 h and 96 h after surgery, differences were observed between the T_{low} OT and T_{high} OT groups. At 24 h after anesthesia and/or start of the analgesic treatments, the AN and DW groups showed significant lower body weights compared to the initial body weight, which paralleled the observations from the OT groups (Fig. 2b,c). Overall positive body weight development was more pronounced in the DW groups (reaching 100% – T_{low} 72 h, T_{high} 96 h, Bup 48 h) (Fig. 2b) than in the AN groups (reaching 100% – T_{low} 96 h, T_{high} 120 h, Bup 72 h) (Fig. 2c) or OT groups (reaching 100% – T_{low} 96 h, T_{high} 120 h, Bup 96 h) (Fig. 2a). There was a significant difference between the AN groups ($F(14, 45) = 12.16$; $p < 0.001$) and DW groups ($F(14, 45) = 23.39$; $p < 0.001$) at different time points (One-way ANOVA; adjusted p -values are indicated in Fig. 2b). In the AN groups, Bup-treated animals showed significant higher body weights than T_{low} (24 h and 48 h) and T_{high} (48 h and 72 h) treated animals. This was also observed in the DW groups (Bup vs. T_{low} or T at 24 h and 48 h; Bup vs. T_{high} at 24 h, 48 h and 72 h). Additionally, T_{low} DW groups showed significant differences towards the T_{high} DW groups at 72 h and 96 h. Intra-group differences over time were

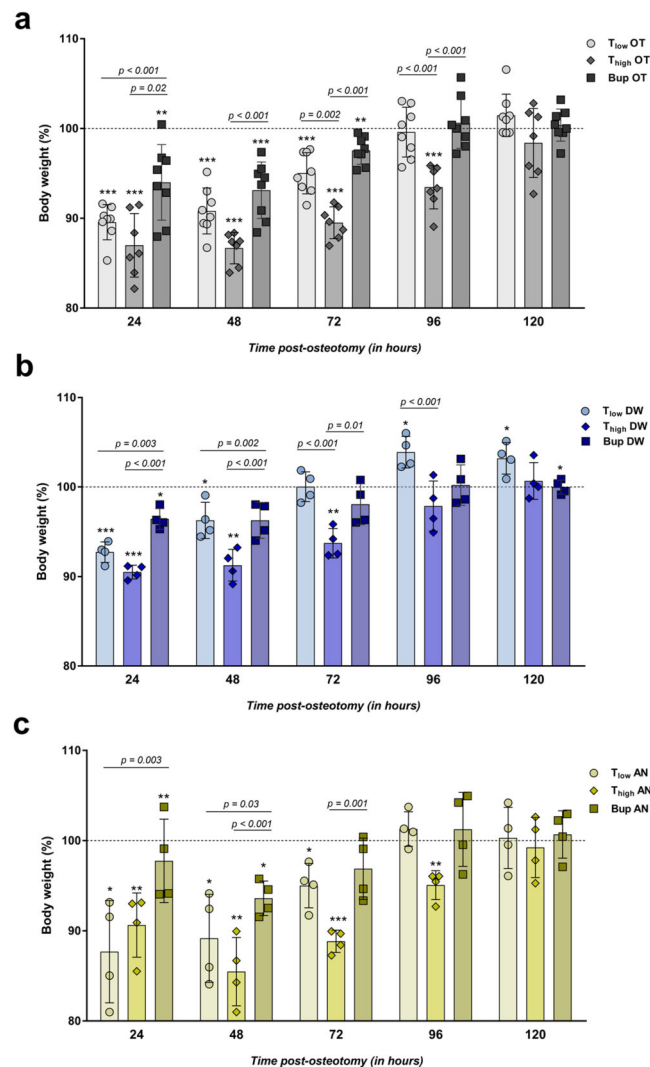


Figure 2. Body weight development is affected by type and concentration of opioid. **(a–c)** Body weight was measured every 24 h and normalized to the initial weight before surgery (=100%). Graphs depict the osteotomy groups **(a, OT)** and the control groups including anesthesia and analgesics via the drinking water **(b, AN)** and only analgesics via the drinking water **(c, DW)**. Data are shown as scatter dot plot and bar with mean \pm SD for $n = 8$ (OT) and $n = 4$ (AN, DW). One sample t test was used to determine statistical significance towards the initial body weight (hypothetical mean = 100; exact p -values are listed in Supplementary Table S2); p -values are indicated with * $p < 0.05$, ** $p < 0.01$ and *** $p < 0.001$. For group differences One-way ANOVA with Bonferroni's multiple comparisons test was performed; adjusted p -values are indicated.

mostly significant for all OT groups and the T_{low}/T_{high} AN and DW groups when applying a repeated measures two-way ANOVA with a Tukey's multiple comparisons test (Interaction: $F(40, 192) = 5.59$; $p < 0.001$; Time: $F(4, 192) = 130.8$; $p < 0.001$; Fold change body weight – column factor: $F(10, 48) = 25.84$; $p < 0.001$; adjusted p -values for each comparison per group are listed in Supplementary Table S3).

Food intake was measured daily before and after osteotomy. All OT groups showed a reduced food intake 24 h post-osteotomy that remained low for the Bup OT and T_{high} OT groups for 48 h or 72 h, respectively (Table 1). Similar trends were observed in the AN and DW groups (Supplementary Table S1).

Composite pain score (facial expression + appearance) decreases constantly over time in all OT groups and is strongly influenced by anesthesia and analgesia protocol.

A composite score consisting of parameters of facial expression and overall appearance was determined by transferring the mice individually to an observation box at 1, 6, 12, 24, 48 and 72 h post-osteotomy. In order to familiarize the mice with the procedure, scoring was performed at three time points (9 a.m., 3 p.m. and 8 p.m.) on the day before surgery or treatment (baseline). The baseline score was 0 for all mice. After surgery/treatment, OT groups showed a significant increase of the score at 1 and 6 h independent of the treatment and compared to the baseline score of 0 (Wilcoxon signed rank test; hypothetical median = 0; exact p -values are listed in Supplementary Table S4) (Fig. 3a). AN groups showed higher scores than baseline at several time points in the immediate

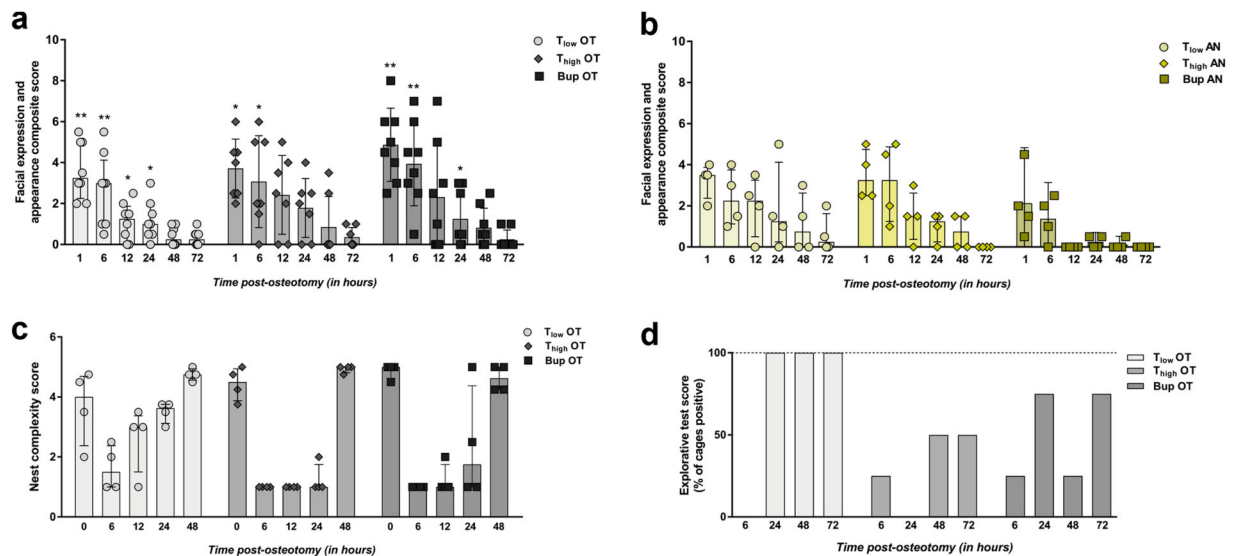


Figure 3. General wellbeing parameters are reduced in osteotomy groups and influenced by anesthesia and analgesia. **(a,b)** Mice were transferred individually to observation boxes, allowed to acclimate for 1 min and were observed for 3 min. Facial expression and appearance composite score was assessed in the OT **(a)** and AN **(b)** groups at 1, 6, 12, 24, 48 and 72 h post-osteotomy/post-anesthesia. DW groups were continuously scored with 0. Measured scores are shown as scatter dot plot and bar with median \pm interquartile range for $n = 8$ (OT) and $n = 4$ (AN). Wilcoxon signed rank test was used to determine statistical significance towards the initial score (hypothetical median = 0; exact p -values are listed in Supplementary Table S4); p -values are indicated with * $p < 0.05$, ** $p < 0.01$ and *** $p < 0.001$. **(c)** Nest complexity score of the OT groups are depicted for 0, 6, 12, 24 and 48 h post-osteotomy. Data are shown as scatter dot plot and bar with median \pm interquartile range for $n = 4$ (cages). **(d)** The explorative test score is depicted for the OT groups as mean – percentage of cages that were determined positive for $n = 4$ (cages). Nest complexity and explorative test scores are provided in Supplementary Fig. S2.

post-anesthesia phase that were not statistically significant (Fig. 3b). DW groups scored continuously low as baseline (=0). Treatment group comparison (T_{low} , T_{high} vs. Bup) at every time point (selected pairs comparison) using Kruskal-Wallis test (non-parametric) revealed significant differences in medians within the OT groups ($H = 68.66$; app. $p < 0.001$) and AN groups ($H = 41.92$; app. $p < 0.001$). The following Dunn's multiple comparison test showed no significance. As shown in the graphs, the median scores reached nearly baseline values at 48 h for the T_{low} OT group and 72 h for the T_{high} OT and Bup group. This was comparable to the T_{high} AN group (72 h) while median scores of T_{low} AN reached baseline values at 72 h and Bup AN at 12 h.

Nest building and explorative behavior are influenced by type and concentration of opioid.

The nest complexity score was used to detect changes in general behavior that might indicate changes in wellbeing as described previously²². At 7 a.m., 1 h before surgery or treatment, the baseline nest complexity score, determined for all groups, reached almost the maximum score of 5. Normalization of the scores towards the baseline score was not performed to show the variance of the scores between the groups in absolute numbers per cage. Therefore, the baseline scores (time point = 0) are depicted within the graph (Fig. 3c). Post-osteotomy all OT groups showed a decline in the nest complexity score towards 1 (Fig. 3c). T_{low} OT groups recovered faster between 12 h and 48 h than the T_{high} OT and Bup groups comparing the medians. A statistically significant difference in group medians was found (Kruskal-Wallis test; non-parametric; $H = 48.51$; app. $p < 0.001$) while the Dunn's multiple comparison test revealed no significance between the selected pairs ($p > 0.99$). However, strong differences can be seen between the T_{low} OT and T_{high} OT group at 12 h and 24 h. Animals from AN and DW groups showed a comparable decline at 6 h, but achieved the initial state more continuously and faster over the following 42 h (Supplementary Fig. S2).

Explorative behavior scores are presented in the percentage of cages that were scored positive (100% = four cages scored positive). In general, the scores were more variable in the OT groups than in the other treatment groups (Fig. 3d). While all animals showed explorative behavior in the baseline measures prior to surgery, explorative behavior declined towards zero at 6 h after surgery. T_{low} OT recovered to stable values at 24 h (=100%). Animals from T_{high} OT showed reduced explorative behavior over time compared to T_{low} OT mice. Bup OT groups demonstrated varying behavior between a mean of 25% (one cage out of four positive) and 75% (three cages out of four positive). AN groups showed comparable results to the OT groups while DW groups were highly explorative with a mean score of 100% (Supplementary Fig. S2).

Additionally, the time spent in the nest (resting time) was assessed for each individual and normalized to the total recorded time. As shown in Supplementary Fig. S2, there was no significant difference between the OT groups (Kruskal-Wallis test; $H = 2.67$; exact $p = 0.28$). There was a slight decrease of the relative time spent in nest with the AN and DW groups compared to the OT groups. In order to track the normal time in the nest over 48 h,

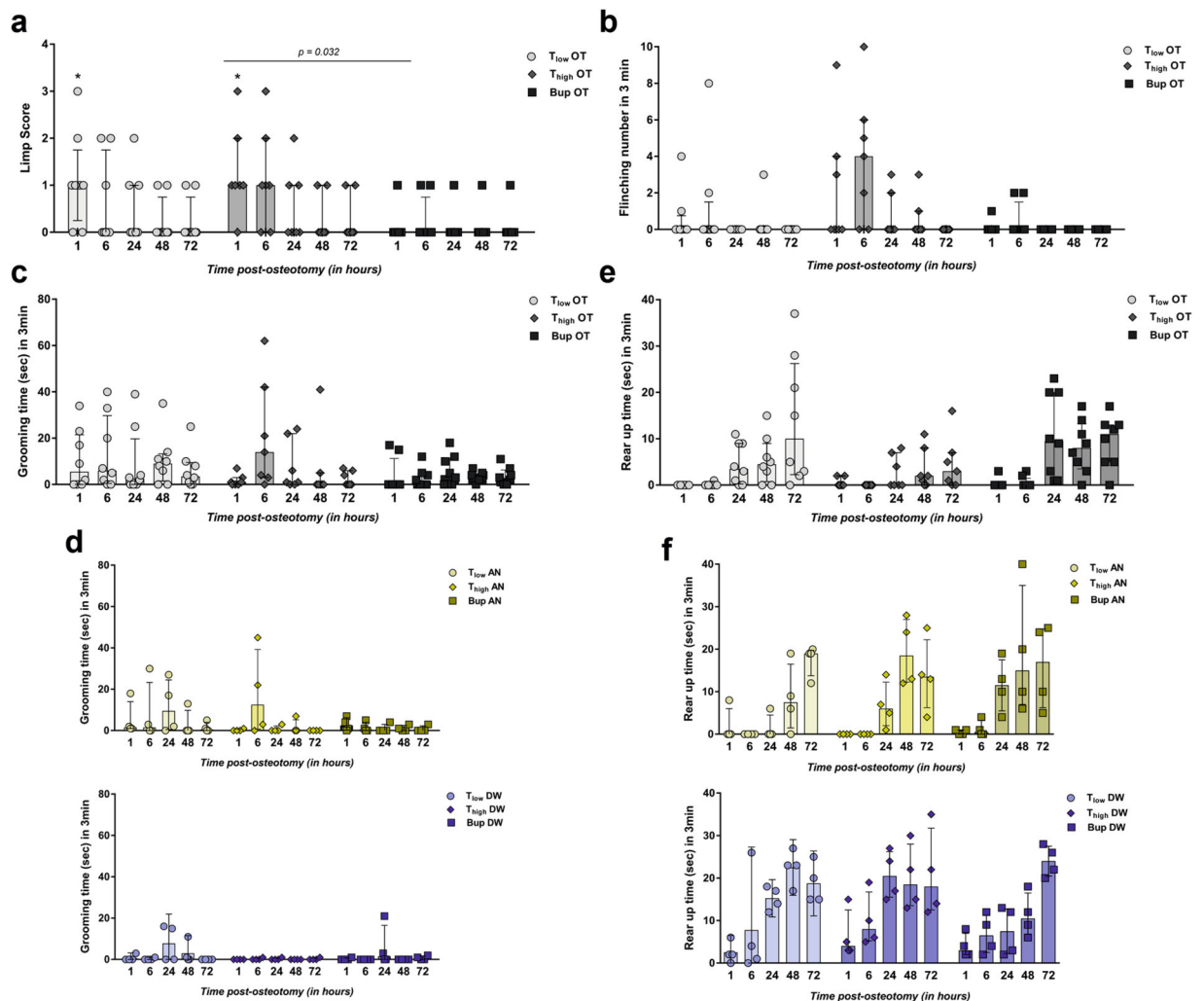


Figure 4. Higher concentrations of Tramadol do not further ameliorate model-specific pain-related parameters. **(a)** The limp score included limping and dragging. Only the scores for the OT groups are shown in the graph as AN and DW groups showed no positive score. Measured scores are shown as scatter dot plot and bar with median \pm interquartile range for $n = 8$. Wilcoxon signed rank test was used to determine statistical significance towards the initial score (hypothetical median = 0; exact p -values are listed in Supplementary Table S5); p -values are indicated with * $p < 0.05$, ** $p < 0.01$ and *** $p < 0.001$. For group differences, Kruskal-Wallis test with Dunn's multiple comparison test for selected pairs (time point) was performed; adjusted p -values are indicated. **(b)** Number of flinching per 3 min observation are depicted for OT groups (no flinching was observed in AN and DW groups). **(c,d)** Graphs show grooming time during 3 min for OT **(c)** and AN and DW **(d)** groups. **(e,f)** Rear up time during 3 min is shown for OT **(e)** and AN and DW **(f)** groups. **(b–f)** Data are shown as scatter dot plot and bar with median \pm interquartile range for $n = 8$ (OT) and $n = 4$ (AN, DW).

baseline measurements were performed prior to surgery or treatments for $n = 8$ mice. The median of the relative time in nest was 47.05% (interquartile range: 43.13%, 48.18%), indicating an increase in resting time for all groups after surgery or treatments compared to normal conditions.

Model-specific pain behavior are reduced by Buprenorphine and low concentrations of Tramadol.

To assess model-specific pain behaviors, a limp score (limping and dragging), the frequency of flinching, the duration of grooming the operated leg as well as the rear up duration, i.e., time standing on both hind limbs in 3 min, were determined. Limp score and flinching are described only for OT animals as AN and DW groups showed no positive limp scores or flinching. Baseline limp score and flinching were assessed prior to osteotomy, revealing no positive limping or dragging (score = 0) and no flinching. Mice of the T_{low} OT and T_{high} OT group showed significant higher limp scores at 1 h post-osteotomy compared to the baseline scores (=0) (Wilcoxon signed rank test; hypothetical median = 0; exact p -values are listed in Supplementary Table S5) (Fig. 4a). Group medians were statistically significant (Kruskal-Wallis test; non-parametric; $H = 29.45$; app. $p < 0.009$) between the Bup OT and T_{high} OT groups (Dunn's multiple comparison test; selected pairs comparison; $p = 0.032$). In general, the Bup OT and T_{low} OT groups showed a median score of 0 at 6 h post-osteotomy compared to the T_{high} OT group with a median of 1 that was reduced towards the baseline at 12 h post-osteotomy.

Flinching was not statistically significantly increased in the OT groups compared to the baseline (=0) (Wilcoxon signed rank test; hypothetical median = 0; $p > 0.25$ except T_{high} OT at 6 h $p = 0.063$) (Fig. 4b). The Kruskal-Wallis test showed a significant difference in the group medians ($H = 32.28$; app. $p < 0.004$) while the Dunn's multiple comparison test revealed no significance between the selected pairs ($p > 0.99$; except Bup OT vs. T_{high} OT $p = 0.1$ and T_{low} OT vs. Bup OT $p = 0.15$). Nevertheless, flinching was observed more often in the T_{high} OT group (median = 4) compared to the T_{low} OT and Bup OT groups (median both = 0) at 6 h (Fig. 4b).

Baseline measurements of leg grooming duration showed durations between 0 and 4 sec ($n = 8$); no statistical test was performed for group comparisons. However, grooming time was prolonged in OT groups for up to 3 days after osteotomy, with no difference between the three groups (Kruskal-Wallis test; non-parametric; $H = 15.28$; app. $p = 0.36$) (Fig. 4c). Interestingly, increased grooming was also seen in T_{high} AN, T_{low} AN and T_{low} DW mice (Fig. 4d).

Normal rear up time was determined during baseline measurements ($n = 8$) with a median = 14.2 sec and a range from 8 to 27 sec. No statistical test was performed for comparison with baseline. Rear up was shown only rarely by OT groups at 1 h and 6 h post-osteotomy (Fig. 4e), which is in line with the results of the AN groups (Fig. 4f). Between 24 h and 96 h, rear up time increased in the OT as well as in the AN and DW groups (Fig. 4f). Statistical differences in the OT group medians were found (Kruskal-Wallis test; non-parametric; $H = 60.03$; app. $p < 0.001$) while Dunn's multiple comparison test revealed no significance between the selected pairs ($p > 0.99$; except Bup OT vs. T_{high} OT $p = 0.36$). In general, rear up was more apparent in the Bup OT and T_{low} OT compared to the T_{high} OT group.

Physiological stress response varies in regard to osteotomy surgery and analgesic treatment. To evaluate stress non-invasively, FCMs were determined. Samples were collected during the animals' stay in the observation boxes after spontaneous and voluntary defecation (no samples at 1 h, 6 h and 12 h post-osteotomy/post-anesthesia). Consequently, different numbers of fecal samples were collected per time point and group. FCM concentration peaked at 24 h post-osteotomy in the OT groups, with no significant differences between groups (Kruskal-Wallis test; $H = 3.82$; $p = 0.15$; Fig. 5a) and declined immediately at 48 h to values lower than DW mice (Fig. 5c). Nevertheless, FCM concentrations in AN and DW groups were also slightly elevated at 24 h and declined over time (Fig. 5b,c).

Opioid analgesia does not significantly affect fracture healing outcome. In order to evaluate the potential side effects of opioid pain management on fracture healing outcomes, we performed *ex vivo* μ CT, histomorphometric analysis and vessel staining via immunofluorescence. Within the protocol, animals from each OT group were assigned randomly to one of two groups receiving different treatment of the osteotomy gap. While in group 1, the osteotomy gap was empty, a scaffold was applied in group 2 that inhibits fracture healing, as we have shown previously²¹. In the present study, we focused on potential differences within group 1 or 2 to evaluate the potential influence of the pain management regime. The total volume (TV), bone volume (BV) and bone volume fraction (BV/TV) were determined during *ex vivo* μ CT analyses. The BV revealed no significant differences between the analgesics groups within the treatment groups (Kruskal-Wallis test; selected pairs; $H = 10.01$; $p = 0.75$) while the medians of TV and BV/TV were significant (Kruskal-Wallis test; selected pairs; TV: $H = 11.18$; $p = 0.05$; BV/TV: $H = 13.05$; $p = 0.02$), but not in the Dunn's multiple comparison test ($p > 0.99$) (Fig. 6a). Moreover, we detected a significant difference in the Bup OT group between group 1 and 2 (Mann-Whitney U test; p -values indicated in graphs) (Fig. 6a). Histomorphometric results analyzing the total mineralized bone (Tt.Md.B.Ar) and cartilage area (Tt.Cg.Ar) as well as the callus width were significantly different in group medians within one fracture gap treatment group and between the analgesic protocols (Kruskal-Wallis test; selected pairs; Tt.Md.B.Ar: $H = 16$; $p = 0.007$; Tt.Cg.Ar: $H = 11.05$; $p = 0.05$; Callus width: $H = 17.89$; $p = 0.003$). Dunn's multiple comparison test showed no significance ($p > 0.99$) (Fig. 6b–d). Within group 1, Bup OT revealed a higher Tt.Md.B.Ar compared to the T OT groups, but conversely, T_{high} OT exhibits slightly more cartilage within the fracture gap. Between the treatment groups, significant differences were found for T_{low} OT and Bup OT, showing significant higher amounts of mineralized bone and cartilage in group 1 compared to group 2 (Mann-Whitney U test; p -values indicated in graphs) (Fig. 6c). This was also observed for the callus width, which was also significant higher in the T_{high} OT group 2 compared to group 1 (Fig. 6d).

To evaluate vessel formation within the fracture gap, staining was performed for CD31 and endomucin (Emcn), two common endothelial markers. In a first step, the relative cell count was determined within the fracture gap (Fig. 7a). No significant differences were identified between analgesic protocols or treatment groups (Kruskal-Wallis test; $H = 4.65$; $p = 0.46$). This was also observed for CD31 and Emcn alone (Kruskal-Wallis test; CD31: $H = 6$; $p = 0.31$; Emcn: $H = 10.85$; $p = 0.054$) (Fig. 7c). Therefore, the obvious higher amount of Emcn^{hi} cells in the T_{high} OT group 2 seems to be an effect of random sampling. Additionally, there were no differences between treatment groups for CD31^{hi} Emcn^{hi} (Kruskal-Wallis test; $H = 9.54$; $p = 0.089$) although the Dunn's multiple comparison test showed a significance in group 1 between the T groups ($p = 0.04$) (Fig. 7b).

Unexpected observations of the study. One animal from the T_{high} OT group was euthanized 2 days after osteotomy due to reaching a humane endpoint. Autopsy revealed a hepatomegaly. In order to exclude the influence of the pain medication, this liver as well as the livers of all other animals from the OT group were assessed via histology; the results revealed a high-grade fatty liver in the respective animal (Fig. 8b) and no changes in the others (beside mild hepatitis due to *Helicobacter* infection) (Fig. 8a).

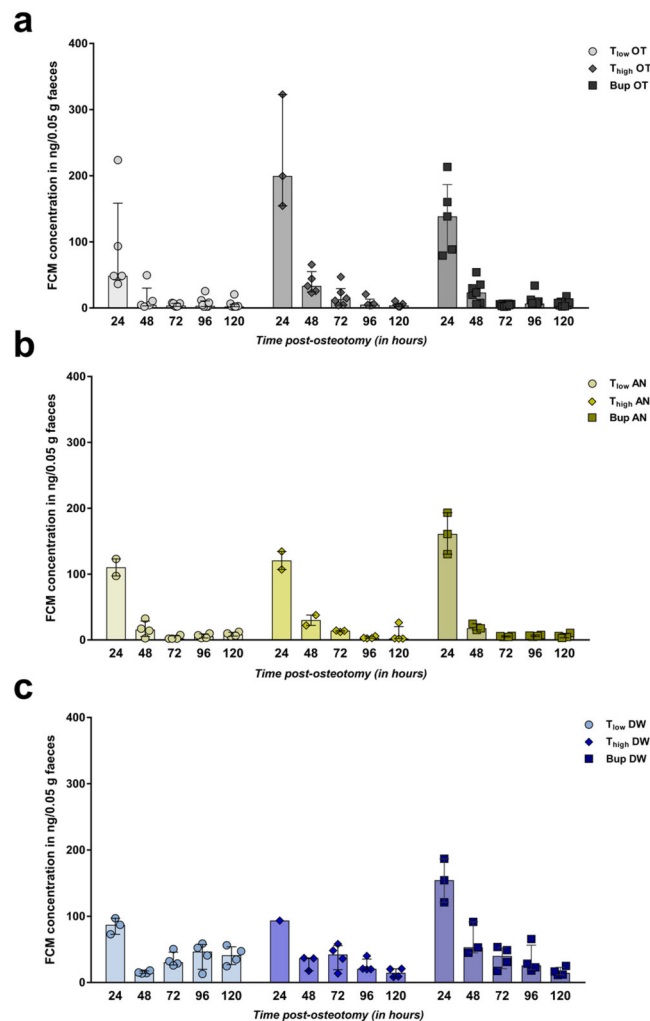


Figure 5. Assessment of adrenocortical activity indicate varying physiological stress responses. (a–c) Fecal corticosterone metabolite (FCM) concentrations were analyzed in all groups: OT (a), AN (b) and DW (c) group. Data are shown as scatter dot plot and bar with median \pm interquartile range for $n = 8$ (OT) and $n = 4$ (AN, DW).

Discussion

This study evaluated three used analgesia protocols, Tramadol (0.1 mg/ml = T_{low} vs. 1 mg/ml = T_{high}) and Buprenorphine (0.009 mg/ml) administered via drinking water, in a mouse osteotomy model after a pre-operative injection of Buprenorphine. Analgesia, anesthesia, surgery and testing had clear effects on the measured parameters assessed. All protocols tested reduced pain without side effects on fracture healing outcome. Nevertheless, mice that were treated with T_{high} showed more signs of reduced wellbeing and pain compared to mice treated with T_{low} or Buprenorphine.

Daily water intake in female B6 mice is about 3–6 ml²³, which resembles our baseline values. After osteotomy water intake was reduced but remained sufficient for adequate analgesia in groups receiving Buprenorphine or T_{low} . In contrast, water intake and drinking frequency were reduced significantly in animals that received T_{high} after surgery. While overall, water intake was not distinctly reduced in controls without surgery receiving T_{high} compared to other analgesia protocols, drinking frequency during the first 2 days was low compared to animals that received a lower dose or Buprenorphine. Comparable effects were observed in a previous study: in contrast to sufficient overall 24 h intake of Tramadol-treated water after laparotomy in female B6 mice, drinking frequency was distinctly reduced in the acute post-surgical phase (<4 h)²⁴. Reduced water intake might result in insufficient concentrations of Tramadol or M1, the analgesic metabolite of Tramadol, and, therefore, in insufficient pain relief. However, based on the amount of water intake, the total amount of Tramadol intake can be calculated and compared between the T_{low} and T_{high} groups. Considering a total water up-take at 48 h for two mice with a median of 9.88 ml (T_{low}) and 5.35 ml (T_{high}), the calculated up-take of Tramadol per mouse would be 0.49 mg (T_{low}) compared to 2.68 mg (T_{high}) which is a 5-fold difference and indicates a sufficient up-take of Tramadol in T_{high} although the water intake amount was reduced. Nevertheless, this calculation does not include the timing of the water intake over 24 h and the short half-life of Tramadol¹⁴. It can be assumed that the bitter taste or aversive side effects of T_{high} result in reduced willingness to ingest. As effective drinking water administration relies on frequent and sufficient

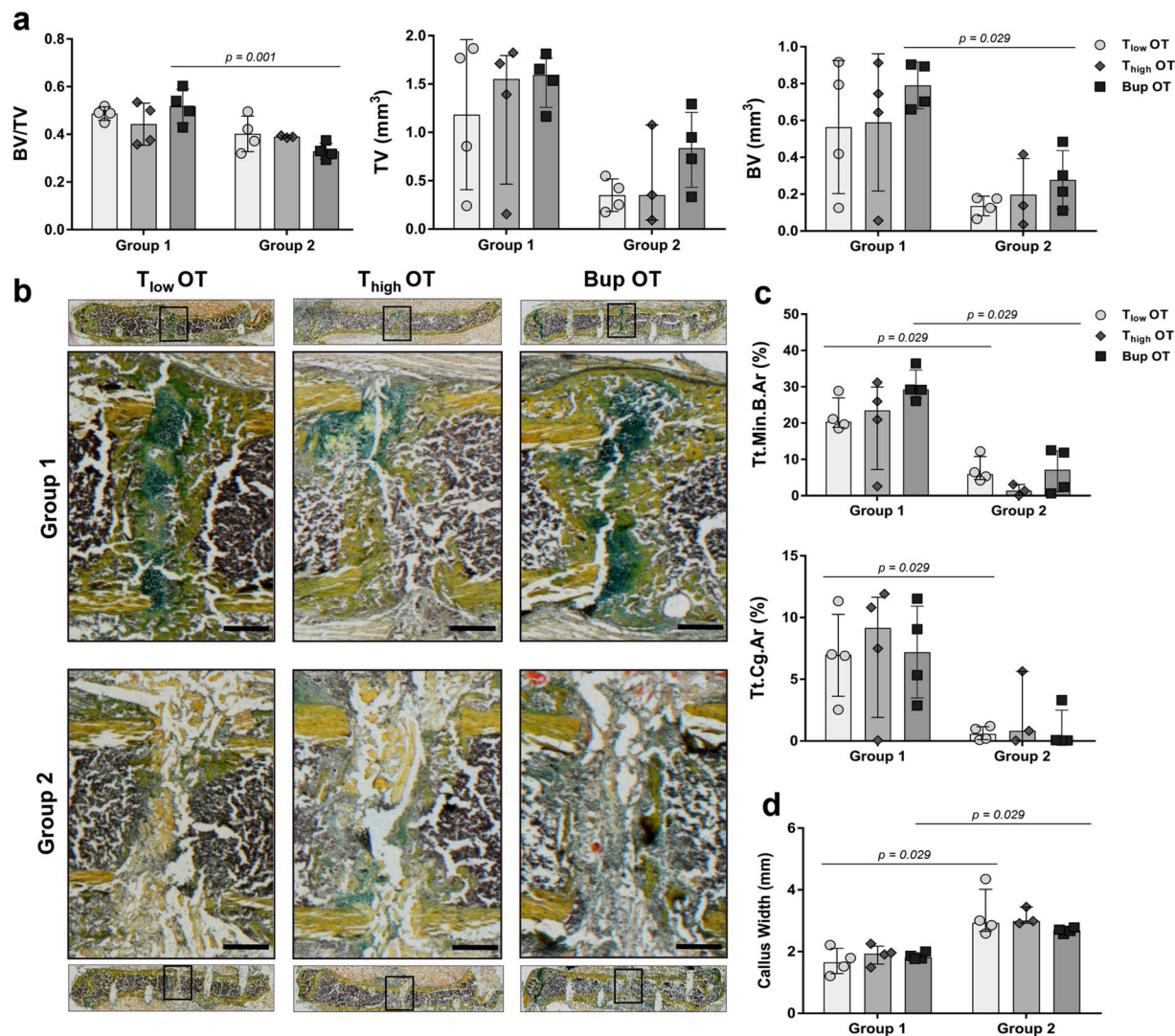


Figure 6. Fracture healing outcomes are not affected by type and concentration of opioid. **(a)** Using *ex vivo* μ CT, the bone volume (BV), the total volume (TV) and the bone volume fraction (BV/TV) were determined. **(b)** Exemplary images for Movat's pentachrome staining allowing for the differentiation between tissues: yellow/orange = mineralized bone; light yellow = scaffold; green = cartilage; purple/brown = bone marrow and cells. Scale bars = 500 μ m. **(c)** Histomorphometry was performed for quantitative assessment of different tissue components - mineralized bone (Tt.Min.B.Ar), cartilage (Tt.Cg.Ar) and **(d)** callus width. **(a–d)** Data are shown as scatter dot plot and bar with median \pm interquartile range for $n = 3-4$. Differences between group 1 and 2 within one analgesic group were determined using the Mann-Whitney U test. Exact p -values are indicated in the graphs.

water intake, sweetened drinking water as well as application of pain medications via the drinking water prior to surgery might be used to avoid the observed effect and to ensure sufficient intake^{16,25}. In addition, the voluntary ingestion via nut paste, jelly²⁶ or by syringe feeding can be an alternative in order to ensure the adequate intake, although animals should be used to the food or technique beforehand²⁷.

We determined the serum levels of Tramadol and M1 following administration of T_{low} . The M1 value was found to be nearly three times as high than the human minimal effective serum level of M1²⁸. Nevertheless, analgesic serum concentrations of Tramadol or M1 in mice are not known; we can therefore only assume that mice received sufficient doses.

Weight reduction, and reduced food intake, might be indicators of pain^{10,29} but are also known side effects of analgesics¹⁰. All animals lost weight after the start of experiments, suggesting an effect of treatment but also of the testing procedure. This tendency was stronger after osteotomy and anesthesia – a result that can possibly be explained by a loss of fluid during anesthesia and the observed drop in food and water intake after anesthesia. The impact of surgery on these parameters was minor compared to the effect of analgesia and anesthesia only. Interestingly, animals treated with T_{high} lost more body weight and recovered weight more slowly compared to the other groups. This effect was seen in surgery and controls, and can therefore be more likely attributed to the side effects, of T_{high} and less likely to pain due to osteotomy.

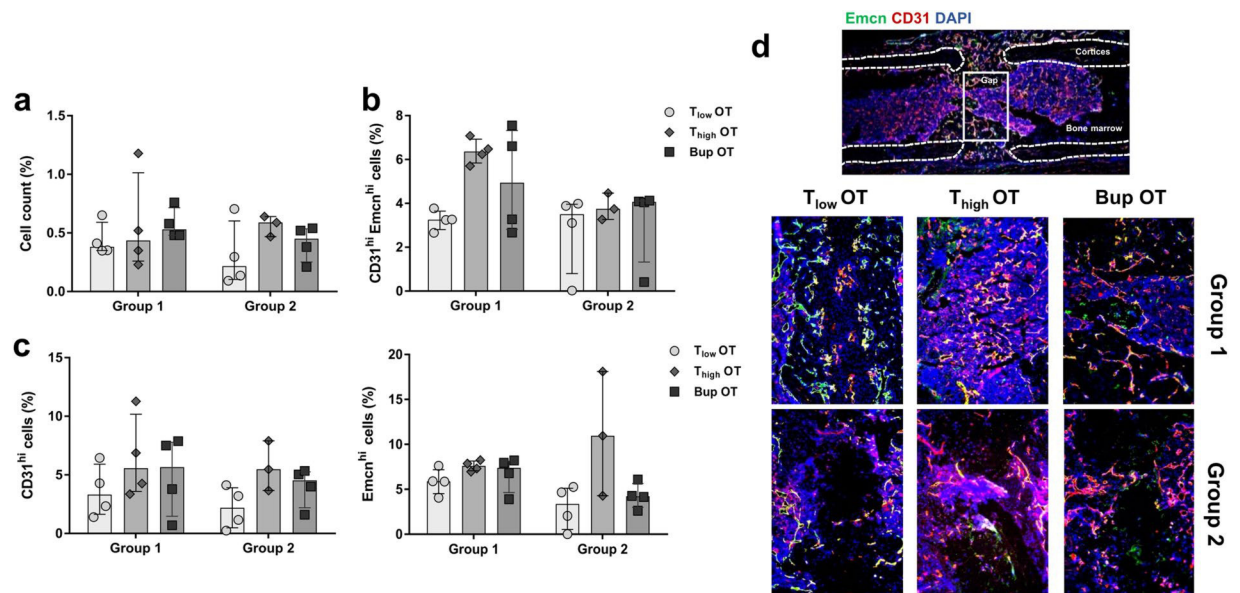


Figure 7. Vessel formation is comparable between treatment groups. Immunofluorescence staining was performed to measure (a) the cell count, (b) the number of double-positive cells (CD31^{hi} Emcn^{hi}) and (c) the number of CD31^{hi} and Emcn^{hi} cells alone in the osteotomy gap. Data was normalized to the total analyzed area and are shown as scatter dot plot and bar with median \pm interquartile range $n = 3-4$. (d) Exemplary immunofluorescence vessel staining (CD31 = red, Emcn = green, DAPI = blue). Scale bars = 200 μm .

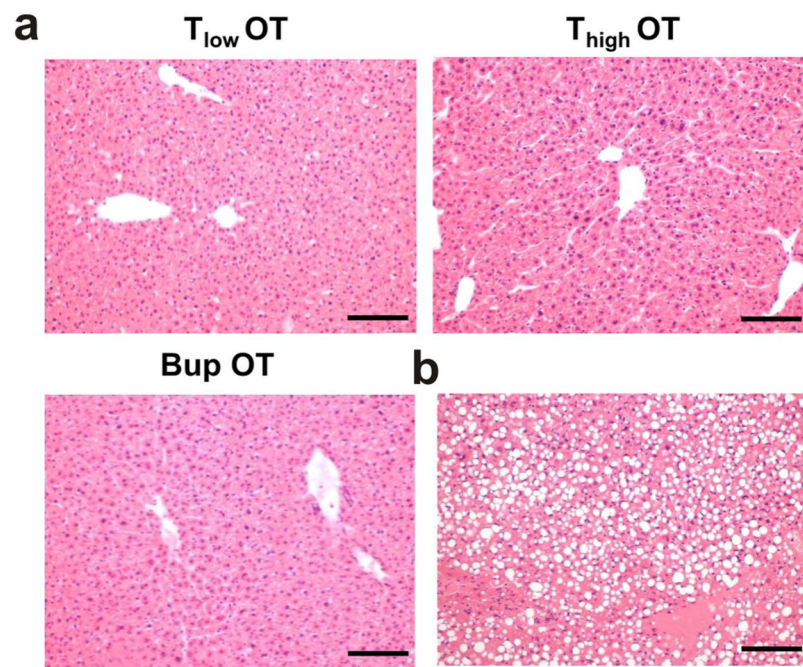


Figure 8. Liver histology reveal no differences between groups. (a) Histology of the livers from all OT animals ($n = 4$) was performed as one animal needed to be euthanized 48 h after osteotomy; this animal showed a high-grade fatty liver (b). Scale bars = 200 μm .

Composite scores comparable to the scoring system used, have been applied successfully for pain evaluation in other mouse models (e.g.^{10,30}). In our study, scores increased during the acute post-anesthesia and post-osteotomy phase. Nevertheless, the increase in scores towards mean scores of 3–6 was significant compared to baseline in the surgery groups only and scores of osteotomized animals recovered slower towards baseline levels compared with anesthesia groups. In a previous study, we showed that, after ovariectomy, B6 mice that did not receive pain treatment reached mean composite scores of 4.5, while animals that received effective pain treatment after surgery

reached mean scores of 1.5–2.5¹⁰. Compared to the increase in scores after anesthesia and analgesia without surgery, osteotomized animals showed only slightly higher scores, hinting at very mild residual post-surgical pain.

The influence of anesthesia is in line with findings that subunits of the score are not pain-specific. An increase in the MGS, part of the pain scoring used in our study, after anesthesia is also described by Miller *et al.*³¹.

High nest scores – an indicator of good general wellbeing^{30,32,33} – were observed during baseline. Nest scores were reduced in all groups after the start of experiments. This reduction in nest building is a known side effect of anesthesia and opioid analgesia^{32,34}. Nevertheless, the impact on nest building was less severe in animals that received T_{low} compared to T_{high} or Buprenorphine, hinting at fewer side effects on wellbeing. Changes in activity might have been the underlying cause of reduced nest building. Groups that scored higher in nest scores in general also spent less time inactive in their nest.

The explorative test used in our study is a modification of the time-to-integrate-to-nest test (TINT)³⁵. Mice observed in pilot studies rarely started to integrate provided nest building material into their existing nest within 10 min as described by Rock *et al.*, therefore we assessed exploration of new nest material rather than nest building behavior. Exploration might be a useful measure of activity and anxiety³⁶ and therefore an interesting parameter to assess overall wellbeing in mice. In the explorative test, all mice scored positive in baseline, animals that received analgesia only showed a comparable high level of explorative behavior during the observation time. After anesthesia, exploration was reduced in all OT groups. This reduction seemed to be stronger in animals that received T_{high}, suggesting a negative effect of the higher dose on wellbeing.

Assessment of limp scores and rearing behavior to quantify altered gait and weight bearing are commonly used in bone fracture, neuropathy or cancer pain studies^{37–40}. Additionally, grooming in terms of an increased tending to the painful limb and flinching as a pain-specific symptom is applied^{41–43}. No limping, flinching or guarding was observed during baseline or in the AN and DW groups. Limping and flinching occurred rarely after osteotomy. Rear up time was shorter in surgery groups compared to AN and DW groups. These changes are therefore clearly connected to the surgery and do not represent a side effect of analgesia or anesthesia.

We cannot discriminate if these changes are due to functional impairment, due to the fixator, or residual osteotomy pain. Minville *et al.* reported that mice with a fractured tibia have a significantly higher “subjective pain” score, defined as reduced use of fractured limb with regards to limping and weight bearing, than sham-operated animals⁴⁰. This score was reduced with an opioid + NSAID combination, which proves the pain specificity of the parameters. In other studies using fractured femurs, flinching occurs more frequently than in our model when animals are not treated with analgesia^{42,43}. In contrast to our model, these studies used an internal pin to fixate the closed fracture.

Regardless of dose, animals that received Tramadol showed higher limp scores and more flinching than animals that received Buprenorphine. T_{high} animals showed a tendency towards more limping and flinching and less rearing and a slower recovery of behaviors. Buprenorphine treatment seemed to be slightly superior to Tramadol.

Guarding behavior, even though observed typically in rodent bone fracture pain models^{41–44}, was not observed in our mice. Again, the lack of could therefore be a sign of sufficient or acceptable pain relief. Grooming of the wounded leg, which might be a sign of pain⁴⁵, occurred in all animals, but was increased mainly in the operated and anesthetized animals. As both groups received a dressing spray to close the wound, it is assumed that grooming is not due to pain but rather induced by the sticking spray on the animal’s skin.

Measuring FCM is a non-invasive technique to monitor adrenocortical activity^{46–49}. At 24 h after start of the experiments, elevated FCM levels were observed with no significant differences between groups. The increase in FCM concentrations in AN and DW groups on day one could be explained by frequent handling, which has been shown to potentially induce an acute stress response in mice^{50,51}.

Finally, we evaluated the influence of Tramadol and Buprenorphine on fracture healing outcomes. No differences were found between analgesic groups in formation of mineralized bone, cartilage and vessels. In addition, we reproduce our previous finding on applying a scaffold to inhibit fracture healing²¹. Negative effects of opioids on bone homeostasis in humans have been described only in case of long-term administration, and include a high incidence of spontaneous fractures related to, e.g., loss of bone mineral density due to direct effects on osteoclasts and osteoblasts or indirect effects via the endocrine system^{52–54}. However, results from animal experiments do not clearly indicate any influence of either Tramadol or Buprenorphine on bone homeostasis and/or regeneration^{55,56}.

Within the study only female B6 mice were used without determination of the estrous cycle status. Therefore, we are not able to exclude potential hormonal influences, which have been also shown to be strain-dependent⁵⁷. In addition, conclusion towards male mice should be carefully taken. Moreover, the presented analgesia protocols could be further refined by sweetening the medicated drinking water for better water intake as well as the use of local anesthesia during surgery.

Although we cannot rule out minor, short-lasting pain in the post-surgery phase, this study provides evidence for pain relief after osteotomy in female B6 mice when administering analgesics stress-free and continuously via the drinking water. Additionally, potential overdosing of Tramadol can lead to changes in wellbeing without further pain relief. Nevertheless, as we have not compared oral with injection protocols, we cannot evaluate if the injection of analgesics or the combination of injection and oral administration for several post-surgical days might have been superior, i.e. reduces remaining signs of pain further, compared to the oral protocols. Therefore, further model-specific studies on pain management should be performed to provide evidence-based refinement of analgesia protocols, to enhance animal wellbeing, reproducibility and translation.

Methods

Animals, housing and study design. The study was performed in accordance with the German Animal Welfare Act and was approved by the local Berlin state authority – “Landesamt für Gesundheit und Soziales” (LaGeSo; permit numbers: G0039/16 and G0111/13). A total of 48 female C57BL/6N mice aged 10 weeks was purchased from Charles River Laboratories (Sulzfeld, Germany). Only female mice are used routinely in

our osteotomy model as bone healing is slower in female mice than in males, allowing for a stepwise, complete bone healing within a time period of 21 days^{27,58,59}. The mean body weight was 21.3 ± 1.3 g. Mice were housed in a conventional (non-SPF) facility, habituated to the housing room in groups of 8–10 animals for 1 week in Eurostandard Type III clear-transparent plastic cages and afterwards randomly split into groups of two for another week before experiments started. Mice were housed in Eurostandard Type II clear-transparent plastic cages (two animals per cage) covered with a wire lid and built-in u-shaped feed hopper and closed with a filter top. As bedding material, fine wood chips (Lignocel FS 14, J. Rettenmaier & Söhne GmbH + Co. KG, Germany) and nesting material (Envirodri[®], Shepherd Specialty Papers, USA) was provided. Due to the external fixator, houses and pipes are contraindicated in order to avoid injuries. Food (Standard mouse diet, Ssniff Spezialdiäten, Germany) and tap water was available *ad libitum*, and room temperature was constant, at between 20 and 22 °C with a humidity of 45–50%. The light/dark cycle was a 12/12-h cycle with lights on at 0600 hours and off at 1800 hours. Cage changing was performed weekly during the acclimatisation phase (two weeks prior to start) by the experimenter; animals were tail handled. Nesting material was transferred to new cages when dry and clean. All experimenters were female (see⁶⁰).

The study design (Fig. 1a) began with baseline measurements during the week prior to the osteotomy. Cages were allocated randomly to three post-operative treatment groups: Tramadol (Drops, Grünenthal GmbH) was applied in two different concentrations: $T_{\text{low}} = 0.1$ mg/ml and $T_{\text{high}} = 1$ mg/ml, Buprenorphine (Temgesic, RB Pharmaceuticals Limited) was applied with Bup = 0.009 mg/ml. Analgesics were administered via drinking water (tap water) for three consecutive days directly after osteotomy or anesthesia. The medicated water was not changed during treatment time¹³. Eight animals of each analgesic regime were osteotomized (OT), four animals of each regime underwent anesthesia only for 15 min and received analgesics post-anesthesia (AN) and four animals of each regime received only analgesics (DW; Supplementary Table S6). Two weeks after surgery, osteotomized animals were anesthetized with ketamine and xylazine (i.p. ketamine 120 mg/kg, xylazine 16 mg/kg). Once depth of anesthesia was achieved, blood was withdrawn from the heart and euthanasia was conducted by cervical dislocation.

Osteotomy. All animals received Buprenorphine (0.03 mg/kg) s.c. as analgesic 1 h prior to surgery. Anesthesia was induced at 2.5% isoflurane (CP-Pharma, Germany) in a transparent Plexiglas box where anesthetic gas was provided using a rodent inhalation anesthesia system (Ohmeda Isotec 4, DRE, USA). Once the animal was asleep and breathing independently deeply and continuously, it was moved to a heating mat (37 °C) and anesthesia was maintained via a nose mask at 1.5% isoflurane. Eye ointment and clindamycin (0.02 ml) were applied s.c. After shaving and disinfecting the left femur area with an alcoholic iodine solution (Braunoderm, B. Braun, Germany), osteotomy was performed as described earlier²⁰. In short, a lateral longitudinal incision of the skin (2 mm) along an imaginary line from knee to hip followed by a blunt preparation of the femur between the *Musculus vastus lateralis* and *Musculus biceps femoris* while protecting the subjacent nerve. Pin placement (0.45 mm diameter) was performed through the connector bar of the external fixator (MouseExFix, RISystem, Davos, Switzerland) by serially drilling to place the fixator laterally parallel to the femur. A 0.70-mm osteotomy gap was created between the middle pins using a Gigli wire saw (RISystem, Davos, Switzerland). According to the protocol of the basic research study, the osteotomy gap was either flushed with NaCl and left empty for group 1 or filled with a PBS-soaked bovine collagen-I scaffold, Lyostypt[®] for group 2 (B. Braun Vet Care GmbH, Tuttlingen, Germany). After skin closure, the wound was covered with a permeable spray dressing, the mice were given pre-warmed NaCl (0.2 ml) s.c. and then returned to their cages. Recovery from anesthesia was conducted under an infrared radiator and was monitored closely. Surgery was performed by two trained veterinarians. Approximately 45 min after surgery, cages were transferred back to the housing room for further analgesic treatment and behavioral assessment. General scoring and humane endpoints were applied as recommended and summarized in Lang *et al.*²⁷.

Body weight, behavioral home cage analyses and food/water intake. Animals were weighed daily starting 1 day prior to surgery and continuing until the day of euthanasia. Food and water intake were determined for each cage every 12 h. For each analgesic treatment group, 8 animals (4 OT, 2 AN, 2 DW) were filmed in their home cages starting for 48 h at 6 p.m. (9 h after osteotomy). This time point was chosen as we expected the pre-emptive Buprenorphine treatment to deliver a pain relief for up to 8 h. Cages were filmed from above (at a distance of ~ 1.5 m) with an infrared sensitive USB 3.0 Monochrome-Camera (The Imaging Source Europe GmbH, Germany). Cage grids were removed for better visibility and plastic walls elevated to prevent escape. Mice were kept with their familiar partner, provided with nesting material, food and water. One mouse in every cage was marked with black stripes (Edding permanent marker 3000) on the tail. An infrared light was turned on during dark cycles. Videos were analyzed manually by one blinded observer with event-logging software (BORIS - Behavioral Observation Research Interactive Software). The drinking frequency of each mouse was assessed manually, where the contact of a mouse's snout with the bottle tip was counted as one drinking event and continuous drinking for a longer time was also counted as one drinking event. Time spent active was measured (defined as animal moving outside of the nest) and used to calculate resting time in the nest.

Tramadol/M1 analysis in serum. There is no available data on the minimum effective serum concentration of Tramadol in mice; Evangelista *et al.* only recently published data on the pharmacokinetics of Tramadol with different application routes¹³. Due to this lack of knowledge, sera were additionally collected and analyzed during an unrelated parallel study in our lab. Serum from mice (n = 18) euthanized 3 days after osteotomy and treated with Tramadol via drinking water at a concentration of 0.1 mg/ml (comparable to analgesic regime of the T_{low} group) were analyzed by TOXILAB Ludwigsburg for Tramadol and O-Desmethyl-Tramadol (M1)

concentrations. The analysis was conducted based on an established method to determine the concentration of Tramadol and M1 in urine. Inter- and intra-assay controls and QM were applied.

Clinical, behavioral and model-specific pain scoring. Animal scoring was performed by two researchers blinded to the groups' analgesic treatment. To assess the facial expression and appearance composite score, mice were transferred individually to a transparent plastic observation box, allowed to acclimate for 1 min and were observed for 3 min. Scoring was performed according to Jirkof *et al.*⁶¹ but slightly adapted (Supplementary Table S7). A maximum score of 11 could be reached. The nest complexity score was assessed in the home cage using the naturalistic system developed by Hess *et al.*²². To assess motivation to interact with an object in the home cage, we performed an explorative test. A ball of four Envirodri[®] stripes was put in the home cage and the animals were observed for 1 min by a blinded observer. The outcome was either negative (score = 0) with no interaction or positive (score = 1) if there was an interaction with the provided material. Interaction was defined as gnawing, fraying, carrying, holding with forelimbs, rolling and intensive sniffing of the material. As model-specific pain or severity parameters, several established behaviors related to gait and weight bearing were observed^{40,43,62}. Mice were transferred individually in standard cages covered with a filter top and given an acclimation time of 15 min before taking a video for 3 min. Offline video analysis was performed by one blinded observer. The frequency of limping and dragging with the operated leg (=limp score) as well as total time an animal spent with grooming the operated leg was measured in seconds (see Supplementary Table S8). Additionally, the frequency of flinching with the left hind limb was recorded. Flinching is characterized as a rapid, repetitive lifting of the affected limb⁴⁰. The total time of remaining in a rear up position with weight bearing apparently on both legs was determined in seconds.

Measurement of fecal corticosterone metabolites (FCMs). Following observation, fecal samples were collected from the observation box, and urine was carefully absorbed with a facial tissue. Fecal samples were stored at -20°C immediately after collecting. FCM analysis was carried out as described and validated previously^{46,63}. In short, the material was dried at 70°C , homogenized with a mortar and weighed. A portion of 0.05 mg of each sample was vortexed for 2 min in 1 ml 80% methanol followed by a centrifugation step ($2,500 \times g$ for 15 min). Supernatants were stored at -80°C and analyzed using a 5α -pregnane- $3\beta,11\beta,21$ -triol-20-one enzyme immunoassay⁶³.

Ex vivo μCT of osteotomized femora. Three-dimensional (3D) bone formation was analyzed after euthanasia using high-resolution μCT . Osteotomized femora were fixed in 4% PFA and ascending glucose solutions. After removal of the pins and external fixator, femora were scanned with an isotropic voxel size of $10.5 \mu\text{m}$ (Viva40 micro-CT, Scanco Medical AG[®], Switzerland, 70 KVp, $114 \mu\text{A}$). The scan axis coincided with the diaphyseal axis of the femora while 191 slides were scanned between the middle pins to include the complete osteotomy gap. The provided software package (Scanco[®], Switzerland) was used for 3D reconstruction, post-processing and analyses. The osteotomy gap was defined per sample from half broken up cortical bone to the other before the volume of interest (VOI) was defined manually excluding the cortical bone. A fixed global threshold of 240 mg HA/cm^3 was applied for the automatic 3D callus tissue analysis. The total volume (TV, mm^3), the total bone volume (BV, mm^3) and the bone volume fraction (BV/TV) were included for evaluation. Analysis was performed blinded to treatment.

Histology and immunofluorescence of osteotomized femora. In order to investigate undecalcified bones, embedding and slice preparation was conducted as described previously²¹. In detail, femora were fixed for 6 h in 4% PFA followed by an ascending sugar solution treatment (10%, 20%, 30%) for 24 h, respectively, and cryo-embedding with SCEM medium (Sectionlab, Japan) and subsequent storing at -80°C . A specific cryofilm (Sectionlab, Japan) was used to provide slices (7 mm) with a cryotom and storage at -80°C . Slices were air-dried for 20 min and fixed with 4% PFA prior to every histological staining. Movat's Pentachrome staining was conducted using an already published protocol²⁰. Pictures were taken with a LSM 710 confocal microscope (Carl Zeiss, Jena, Germany) and analysed using ImageJ. For immunofluorescence staining, the slides were air dried for 20 min, rehydrated with PBS and blocked with PBS/5% FCS for 30 min. Primary PECAM-1 antibody (goat anti-mouse; R&D Systems; AF3628) was diluted 1:50 in PBS/5% FCS/0.1% Tween 20 and incubated for 2 h. After washing with PBS/0.1% Tween 20, secondary antibody (donkey anti-goat A568; Life Technologies/ThermoScientific; A-11057) was diluted 1:500 in PBS/5% FCS/0.1% Tween 20 and applied for 1 h. A subsequent washing step was followed by a blocking step with PBS/10% normal goat serum. Primary Endomucin antibody (rat anti-mouse Endomucin; Santa Cruz; V.7C7) diluted 1:500 in PBS/5% FCS/0.1% Tween 20 was applied for 2 h. After washing secondary antibody (goat anti-rat A647; Life Technologies/ThermoScientific; A-21247) was used for 1 h. A washing step and DAPI (1:500; 1 mg/ml in PBS) completed the staining. Pictures were taken with a Keyence fluorescence microscope BZ 9000 using the DAPI, TexasRed and Cy5 channels. Image analysis was performed using ImageJ by a treatment-blinded researcher.

Liver histology. The liver of each osteotomized mouse was collected after euthanasia, frozen, and stored at -80°C . Before embedding in paraffin, the livers were fixed in 4% PFA for 24 h and then transferred to the Institute of Veterinary Pathology at the Department of Veterinary Medicine FU Berlin. The livers were paraffin embedded and HE stained. The samples were assessed histologically blinded to the analgesic treatment to assess any possible influence of the analgesia on the liver.

Statistical analysis. Samples size calculation for primary endpoints (composite score, model-specific pain score) was based on the resource equation approach with focus in the 3 groups with osteotomy and different analgesia (min. number per group = 4; max. number per group = 8). For secondary endpoints such as water intake

(ml) and BV/TV (bone volume fraction), power analysis was possible, calculated via G*Power 3.1 program and compared to the group sizes calculated via the resource equation approach. For more detailed information please see Animal Study Registry (Bf3R, Germany, <https://doi.org/10.17590/asr.0000113>).

The number of animals is either stated in the text, figure legend or indicated as a scatter dot plot in the graphs. Statistical analysis was carried out with GraphPad Prism V.7 software. As a first step, data sets were tested for Gaussian distribution using Shapiro-Wilk normality test ($n < 8$) or Kolmogorov-Smirnov normality test ($n > 4$). Data with $n \leq 4$ were assumed as non-parametric. Only the body weight showed a Gaussian distribution compared to all other data sets. Therefore, the body weight is presented as mean \pm SD and normalized to the initial body weight. To statistically compare the measured body weight to the initial body weight, one sample *t* test was performed (hypothetical mean = 100). One-way ANOVA with Bonferroni's multiple comparisons test (selected pairs) was used to determine group differences. Changes over time were assessed with a repeated-measure two-way ANOVA with a Tukey's multiple comparisons test. Normalization to baseline measurements was not useful in the other datasets. Where reasonable, baseline measurements are stated in the text or depicted in the graphs (time point = 0). Data with no Gaussian distribution are shown as median \pm interquartile range. To determine statistical differences towards the baseline measurements, Wilcoxon signed rank test was used. As non-parametric statistical test for group differences, the Kruskal-Wallis test with Dunn's multiple comparison test was applied for selected pairs. All important numbers and adjusted *p*-values are either stated in the text, the graphs or are listed in the Supplement.

Data Availability

The authors declare that all data supporting the findings of this study are available within the paper and its supplementary information file. Further information on the study design and the protocols are available in the Animal Study Registry (Bf3R, Germany; <https://doi.org/10.17590/asr.0000113>). Further information are made available by the authors upon request.

References

- Carbone, L. & Austin, J. Pain and Laboratory Animals: Publication Practices for Better Data Reproducibility and Better Animal Welfare. *PLoS one* **11**, e0155001, <https://doi.org/10.1371/journal.pone.0155001> (2016).
- Jirkof, P. Side effects of pain and analgesia in animal experimentation. *Lab animal* **46**, 123–128, <https://doi.org/10.1038/labana.1216> (2017).
- Peterson, N. C., Nunamaker, E. A. & Turner, P. V. To Treat or Not to Treat: The Effects of Pain on Experimental Parameters. *Comparative medicine* **67**, 469–482 (2017).
- Flecknell, P. Rodent analgesia: Assessment and therapeutics. *Veterinary journal (London, England: 1997)* **232**, 70–77, <https://doi.org/10.1016/j.tvjl.2017.12.017> (2018).
- Santy, J. & Mackintosh, C. A phenomenological study of pain following fractured shaft of femur. *Journal of Clinical Nursing* **10**, 521–527, <https://doi.org/10.1046/j.1365-2702.2001.00506.x> (2001).
- Minick, P. *et al.* Long-bone fracture pain management in the emergency department. *Journal of emergency nursing: JEN: official publication of the Emergency Department Nurses Association* **38**, 211–217, <https://doi.org/10.1016/j.jen.2010.11.001> (2012).
- Bove, S. E., Flatters, S. J., Inglis, J. J. & Mantyh, P. W. New advances in musculoskeletal pain. *Brain research reviews* **60**, 187–201, <https://doi.org/10.1016/j.brainresrev.2008.12.012> (2009).
- Bhattacharyya, T., Levin, R., Vrahas, M. S. & Solomon, D. H. Nonsteroidal antiinflammatory drugs and nonunion of humeral shaft fractures. *Arthritis and rheumatism* **53**, 364–367, <https://doi.org/10.1002/art.21170> (2005).
- Cottrell, J. & O'Connor, J. P. Effect of Non-Steroidal Anti-Inflammatory Drugs on Bone Healing. *Pharmaceuticals* **3**, 1668 (2010).
- Jirkof, P., Tourvielle, A., Cinelli, P. & Arras, M. Buprenorphine for pain relief in mice: repeated injections vs sustained-release depot formulation. *Laboratory animals* **49**, 177–187, <https://doi.org/10.1177/0023677214562849> (2015).
- Mouedden, M. E. & Meert, T. F. Pharmacological evaluation of opioid and non-opioid analgesics in a murine bone cancer model of pain. *Pharmacology, biochemistry, and behavior* **86**, 458–467, <https://doi.org/10.1016/j.pbb.2007.01.003> (2007).
- Aydin, O. N. *et al.* The antinociceptive effects of systemic administration of tramadol, gabapentin and their combination on mice model of acute pain. *Agri: Agri* **24**, 49–55, <https://doi.org/10.5505/agri.2012.31032> (2012).
- Evangelista Vaz, R. *et al.* Preliminary pharmacokinetics of tramadol hydrochloride after administration via different routes in male and female B6 mice. *Veterinary anaesthesia and analgesia* **45**, 111–122, <https://doi.org/10.1016/j.vaa.2016.09.007> (2018).
- Matthiesen, T., Wohrman, T., Coogan, T. P. & Uragg, H. The experimental toxicology of tramadol: an overview. *Toxicology letters* **95**, 63–71 (1998).
- Wolfe, A. M., Kennedy, L. H., Na, J. J. & Nemzek-Hamlin, J. A. Efficacy of Tramadol as a Sole Analgesic for Postoperative Pain in Male and Female Mice. *Journal of the American Association for Laboratory Animal Science: JAALAS* **54**, 411–419 (2015).
- Ehrnthaller, C. *et al.* Complement C3 and C5 deficiency affects fracture healing. *PLoS one* **8**, e81341, <https://doi.org/10.1371/journal.pone.0081341> (2013).
- GV-SOLAS. Fachinformation Schmerztherapie bei Versuchstieren aus dem Ausschuss für Anästhesie der GV-SOLAS. (2015).
- Haffner-Luntzer, M. *et al.* Midkine-deficiency delays chondrogenesis during the early phase of fracture healing in mice. *PLoS one* **9**, e116282, <https://doi.org/10.1371/journal.pone.0116282> (2014).
- Heilmann, A. *et al.* Systemic treatment with the sphingosine-1-phosphate analog FTY720 does not improve fracture healing in mice. *Journal of orthopaedic research: official publication of the Orthopaedic Research Society* **31**, 1845–1850, <https://doi.org/10.1002/jor.22426> (2013).
- Schlundt, C. *et al.* Macrophages in bone fracture healing: Their essential role in endochondral ossification. *Bone* **106**, 78–89, <https://doi.org/10.1016/j.bone.2015.10.019> (2018).
- Lang, A. *et al.* Collagen I-based scaffolds negatively impact fracture healing in a mouse-osteotomy-model although used routinely in research and clinical application. *Acta Biomaterialia*. <https://doi.org/10.1016/j.actbio.2018.12.043> (2019).
- Hess, S. E. *et al.* Home Improvement: C57BL/6J Mice Given More Naturalistic Nesting Materials Build Better Nests. *Journal of the American Association for Laboratory Animal Science: JAALAS* **47**, 25–31 (2008).
- Bachmanov, A. A., Reed, D. R., Beauchamp, G. K. & Tordoff, M. G. Food intake, water intake, and drinking spout side preference of 28 mouse strains. *Behav Genet* **32**, 435–443 (2002).
- Evangelista Vaz, R. E. A. Evaluation of the analgesic efficacy of a 25 mg/kg Tramadol s.c. injection-oral combination in a surgical model in C57BL/6J mice. *Journal of the American Association for Laboratory Animal Science: JAALAS*, Unpublished (2017).
- Rapp, A. E. *et al.* Analgesia via blockade of NGF/TrkA signaling does not influence fracture healing in mice. *Journal of orthopaedic research: official publication of the Orthopaedic Research Society* **33**, 1235–1241, <https://doi.org/10.1002/jor.22892> (2015).
- Khan, S. N. *et al.* The temporal role of leptin within fracture healing and the effect of local application of recombinant leptin on fracture healing. *Journal of orthopaedic trauma* **27**, 656–662, <https://doi.org/10.1097/BOT.0b013e3182847968> (2013).

27. Lang, A., Schulz, A., Ellinghaus, A. & Schmidt-Bleek, K. Osteotomy models - the current status on pain scoring and management in small rodents. *Laboratory animals* **50**, 433–441, <https://doi.org/10.1177/0023677216675007> (2016).
28. Lehmann, K. A., Kratzberg, U., Schroeder-Bark, B. & Horrichs-Haermeyer, G. Postoperative patient-controlled analgesia with tramadol: analgesic efficacy and minimum effective concentrations. *Clin J Pain* **6**, 212–220 (1990).
29. Morton, D. B. & Griffiths, P. H. Guidelines on the recognition of pain, distress and discomfort in experimental animals and an hypothesis for assessment. *Vet Rec* **116**, 431–436 (1985).
30. Arras, M., Rettich, A., Cinelli, P., Kasermann, H. P. & Burki, K. Assessment of post-laparotomy pain in laboratory mice by telemetric recording of heart rate and heart rate variability. *BMC Vet Res* **3**, 16, <https://doi.org/10.1186/1746-6148-3-16> (2007).
31. Miller, A., Kitson, G., Skalkoyannis, B. & Leach, M. The effect of isoflurane anaesthesia and buprenorphine on the mouse grimace scale and behaviour in CBA and DBA/2 mice. *Applied animal behaviour science* **172**, 58–62, <https://doi.org/10.1016/j.applanim.2015.08.038> (2015).
32. Jirkof, P. *et al.* Assessment of postsurgical distress and pain in laboratory mice by nest complexity scoring. *Laboratory animals* **47**, 153–161, <https://doi.org/10.1177/0023677213475603> (2013).
33. Gaskill, B. N., Karas, A. Z., Garner, J. P. & Pritchett-Corning, K. R. Nest building as an indicator of health and welfare in laboratory mice. *J Vis Exp*, 51012, <https://doi.org/10.3791/51012> (2013).
34. Darbyshire, A. An Assessment of the Safety of Recuvyra following Topical Administration in Mice - Abstracts of Scientific Presentations: 2015 AALAS National Meeting Phoenix, Arizona. *Journal of the American Association for Laboratory Animal Science: JAALAS* **54**, 568–668 (2015).
35. Rock, M. L. *et al.* The time-to-integrate-to-nest test as an indicator of wellbeing in laboratory mice. *J Am Assoc Lab Anim Sci* **53**, 24–28 (2014).
36. Crawley, J. N. Behavioral phenotyping strategies for mutant mice. *Neuron* **57**, 809–818, <https://doi.org/10.1016/j.neuron.2008.03.001> (2008).
37. Attal, N., Jazat, F., Kayser, V. & Guilbaud, G. Further evidence for 'pain-related' behaviours in a model of unilateral peripheral mononeuropathy. *Pain* **41**, 235–251 (1990).
38. Luger, N. M. *et al.* Osteoprotegerin diminishes advanced bone cancer pain. *Cancer Res* **61**, 4038–4047 (2001).
39. Minville, V., Fourcade, O., Mazoit, J. X., Girolami, J. P. & Tack, I. Ondansetron does not block paracetamol-induced analgesia in a mouse model of fracture pain. *British journal of anaesthesia* **106**, 112–118, <https://doi.org/10.1093/bja/aeq277> (2011).
40. Minville, V., Laffosse, J. M., Fourcade, O., Girolami, J. P. & Tack, I. Mouse model of fracture pain. *Anesthesiology* **108**, 467–472 (2008).
41. Majuta, L. A., Longo, G., Fealk, M. N., McCaffrey, G. & Mantyh, P. W. Orthopedic surgery and bone fracture pain are both significantly attenuated by sustained blockade of nerve growth factor. *Pain* **156**, 157–165, <https://doi.org/10.1016/j.pain.000000000000017> (2015).
42. Jimenez-Andrade, J. M. *et al.* Nerve growth factor sequestering therapy attenuates non-malignant skeletal pain following fracture. *Pain* **133**, 183–196, <https://doi.org/10.1016/j.pain.2007.06.016> (2007).
43. Koewler, N. J. *et al.* Effects of a monoclonal antibody raised against nerve growth factor on skeletal pain and bone healing after fracture of the C57BL/6J mouse femur. *J Bone Miner Res* **22**, 1732–1742, <https://doi.org/10.1359/jbmr.070711> (2007).
44. Freeman, K. T. *et al.* A fracture pain model in the rat: adaptation of a closed femur fracture model to study skeletal pain. *Anesthesiology* **108**, 473–483, <https://doi.org/10.1097/ALN.0b013e3181649351> (2008).
45. Leach, M. C. *et al.* The assessment of post-vasectomy pain in mice using behaviour and the Mouse Grimace Scale. *PLoS one* **7**, e35656, <https://doi.org/10.1371/journal.pone.0035656> (2012).
46. Touma, C., Palme, R. & Sachser, N. Analyzing corticosterone metabolites in fecal samples of mice: a noninvasive technique to monitor stress hormones. *Hormones and behavior* **45**, 10–22 (2004).
47. Goldschlager, G. B., Gillespie, V. L., Palme, R. & Baxter, M. G. Effects of multimodal analgesia with LowDose buprenorphine and meloxicam on fecal glucocorticoid metabolites after surgery in New Zealand white rabbits (*Oryctolagus cuniculus*). *J Am Assoc Lab Anim Sci* **52**, 571–576 (2013).
48. Hohlbaum, K. *et al.* Impact of repeated anesthesia with ketamine and xylazine on the well-being of C57BL/6J mice. *PLoS one* **13**, e0203559, <https://doi.org/10.1371/journal.pone.0203559> (2018).
49. Resch, M., Neels, T., Tichy, A., Palme, R. & Rulicke, T. Impact assessment of tail-vein injection in mice using a modified anaesthesia induction chamber versus a common restrainer without anaesthesia. *Laboratory animals*, 23677218786982, <https://doi.org/10.1177/0023677218786982> (2018).
50. Balcombe, J. P., Barnard, N. D. & Sandusky, C. Laboratory routines cause animal stress. *Contemporary topics in laboratory animal science/American Association for Laboratory Animal Science* **43**, 42–51 (2004).
51. Bowers, S. L., Bilbo, S. D., Dhabhar, F. S. & Nelson, R. J. Stressor-specific alterations in corticosterone and immune responses in mice. *Brain Behav Immun* **22**, 105–113, <https://doi.org/10.1016/j.bbi.2007.07.012> (2008).
52. Coluzzi, F., Pergolizzi, J., Raffa, R. B. & Mattia, C. The unsolved case of "bone-impairing analgesics": the endocrine effects of opioids on bone metabolism. *Therapeutics and Clinical Risk Management* **11**, 515–523, <https://doi.org/10.2147/tcrm.S79409> (2015).
53. Gotthardt, F. *et al.* Bone mineral density and its determinants in men with opioid dependence. *Journal of Bone and Mineral Metabolism* **35**, 99–107, <https://doi.org/10.1007/s00774-015-0732-9> (2017).
54. Hirst, A., Knight, C., Hirst, M., Dunlop, W. & Akehurst, R. Tramadol and the risk of fracture in an elderly female population: a cost utility assessment with comparison to transdermal buprenorphine. *The European Journal of Health Economics* **17**, 217–227, <https://doi.org/10.1007/s10198-015-0673-1> (2016).
55. Hedenqvist, P. *et al.* Carprofen neither reduces postoperative facial expression scores in rabbits treated with buprenorphine nor alters long term bone formation after maxillary sinus grafting. *Research in Veterinary Science* **107**, 123–131, <https://doi.org/10.1016/j.rvsc.2016.05.010> (2016).
56. Vivian, B. Evaluation of Osteoporosis Risk Associated with Chronic Use of Morphine, Fentanyl and Tramadol in Adult Female Rats. *Current Drug Safety* **6**, 159–163, <https://doi.org/10.2174/157488611797579267> (2011).
57. Mezziane, H., Ouagazzal, A. M., Aubert, L., Wietrzyk, M. & Krezel, W. Estrous cycle effects on behavior of C57BL/6J and BALB/cByJ female mice: implications for phenotyping strategies. *Genes, brain, and behavior* **6**, 192–200, <https://doi.org/10.1111/j.1601-183X.2006.00249.x> (2007).
58. Haffner-Luntzer, M., Kovtun, A., Rapp, A. E. & Ignatius, A. Mouse Models in Bone Fracture Healing Research. *Current Molecular Biology Reports* **2**, 101–111, <https://doi.org/10.1007/s40610-016-0037-3> (2016).
59. Mehta, M. *et al.* A 5-mm femoral defect in female but not in male rats leads to a reproducible atrophic non-union. *Archives of orthopaedic and trauma surgery* **131**, 121–129, <https://doi.org/10.1007/s00402-010-1155-7> (2011).
60. Sorge, R. E. *et al.* Olfactory exposure to males, including men, causes stress and related analgesia in rodents. *Nature Methods* **11**, 629, <https://doi.org/10.1038/nmeth.2935>, <https://www.nature.com/articles/nmeth.2935#supplementary-information> (2014).
61. Jirkof, P., Pourvielle, A., Cinelli, P. & Arras, M. Buprenorphine for pain relief in mice: repeated injections vs sustained-release depot formulation. *Laboratory animals*, <https://doi.org/10.1177/0023677214562849> (2014).
62. Luger, N. M. *et al.* Efficacy of systemic morphine suggests a fundamental difference in the mechanisms that generate bone cancer vs inflammatory pain. *Pain* **99**, 397–406 (2002).
63. Touma, C., Sachser, N., Mostl, E. & Palme, R. Effects of sex and time of day on metabolism and excretion of corticosterone in urine and feces of mice. *General and comparative endocrinology* **130**, 267–278 (2003).

Acknowledgements

The authors would like to thank Manuela Jakstadt and Theresia Reding Graf for excellent technical assistance and Juliane Unger and Margarete Arras for their support. This study was funded by the German Federal Institute for Risk Assessment (BfR) and the German Centre for the Protection of Laboratory Animals (Bf3R), Berlin, Germany (project no.: 1328-542; RefineMOMo) and the Deutsche Forschungsgemeinschaft (DFG) as part of the research group “Severity Assessment for animal based research FOR 2591”. We acknowledge support with regard to the publication fee from the German Research Foundation (DFG) and the Open Access Publication Fund of Charité – Universitätsmedizin Berlin. These funding bodies did not have any role in designing the study, in collecting, analysing and interpreting the data, in writing this manuscript, and in deciding to submit it for publication. A.L., F.B. and C.T.R. are members of Berlin-Brandenburg research platform BB3R. A.L., F.B. and K.S.B. are active members of Charité3R.

Author Contributions

Study design: A.L., P.J., K.S.B. and F.B. Data collection, analysis and interpretation: all authors; Drafting manuscript: A.L., P.J. and M.D. Revising manuscript: K.S.B., F.B., C.T.R., R.P. and R.K. Approved final version of manuscript: all authors. A.L. and P.J. are responsible for the integrity of the manuscript.

Additional Information

Supplementary information accompanies this paper at <https://doi.org/10.1038/s41598-019-47186-5>.

Competing Interests: The authors declare no competing interests.

Publisher’s note: Springer Nature remains neutral with regard to jurisdictional claims in published maps and institutional affiliations.



Open Access This article is licensed under a Creative Commons Attribution 4.0 International License, which permits use, sharing, adaptation, distribution and reproduction in any medium or format, as long as you give appropriate credit to the original author(s) and the source, provide a link to the Creative Commons license, and indicate if changes were made. The images or other third party material in this article are included in the article’s Creative Commons license, unless indicated otherwise in a credit line to the material. If material is not included in the article’s Creative Commons license and your intended use is not permitted by statutory regulation or exceeds the permitted use, you will need to obtain permission directly from the copyright holder. To view a copy of this license, visit <http://creativecommons.org/licenses/by/4.0/>.

© The Author(s) 2019

2.2 Characterization of an *in vitro* equine fracture hematoma model

To go a step further, we developed in parallel sophisticated *in vitro* models to specifically study the initial phase of fracture healing integrating the interaction between immune cells and mesenchymal stromal cells/bone-related cells. Comparative medicine in the “One health” context aims to closer link animal and human health for mutual benefit. The horse is an important orthopaedic patient and due to its size, comparable anatomical features and similar bone micro- and macrostructure suggested as an ideal experimental model for human orthopaedic conditions. However, there is a lack of scientific knowledge on the mechanistic and temporal course of fracture healing in horses. In this study we wanted to i) define the influence of hypoxia and mesenchymal stromal cells during the initial phase of fracture healing in an equine *in vitro* fracture hematoma model and ii) use the gained knowledge for translation to a human fracture hematoma model.

The following text corresponds to the abstract of the work:

Pfeiffenberger, M.*, Bartsch, J.*, Hoff, P., Ponomarev, I., Barnewitz, D., Thöne-Reineke, C., Buttgerit, F., Gaber, T.*, **Lang, A.*** (2019) Hypoxia and mesenchymal stromal cells as key drivers of initial fracture healing in an equine *in vitro* fracture hematoma model. *PlosONE*. Apr 4; 14(4):e0214276. [doi: 10.1371/journal.pone.0214276] (*shared last authorship)


“Fractures in horses – whether simple fractures with just one clean break, or incomplete greenstick with stress fractures, or complications such as shattered bones can all be either minimal or even catastrophic. Thus, improvement in fracture healing is a hallmark in equine orthopedics. The fracture healing process implements a complex sequence of events including the initial inflammatory phase removing damaged tissue, re-establishment of vessels and mesenchymal stromal cells, a soft and hard callus phase closing the fracture gap as well as the remodeling phase shaping the bone to a scar-free tissue. Detailed knowledge on processes in equine fracture healing in general and on the initial phase in particular is apparently very limited. Therefore, we generated equine in vitro fracture hematoma models (FH models) to study time-dependent changes in cell composition and RNA-expression for the most prominent cells in the FH model (immune cells, mesenchymal stromal cells) under conditions most closely adapted to the in vivo situation (hypoxia) by using flow cytometry and qPCR. In order to analyze the impact of mesenchymal stromal cells in greater detail, we also incubated blood clots without the addition of mesenchymal stromal cells under the same conditions as a control. We observed a superior survival capacity of mesenchymal stromal cells over immune cells within our FH model maintained under hypoxia. Furthermore, we demonstrate an upregulation of relevant angiogenic, osteogenic and hypoxia-induced markers within 48 h, a time well-known to be crucial for proper fracture healing.”

RESEARCH ARTICLE

Hypoxia and mesenchymal stromal cells as key drivers of initial fracture healing in an equine *in vitro* fracture hematoma model

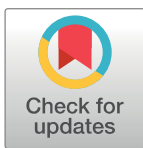
Moritz Pfeiffenberger^{1,2}, Janika Bartsch¹, Paula Hoff^{1,2}, Igor Ponomarev³, Dirk Barnewitz³, Christa Thöne-Reineke⁴, Frank Buttgereit^{1,2}, Timo Gaber^{1,2}, Annemarie Lang^{1,2}*

1 Department of Rheumatology and Clinical Immunology, Charité-Universitätsmedizin Berlin, corporate member of Freie Universität Berlin, Humboldt-Universität zu Berlin, and Berlin Institute of Health, Berlin, Germany, **2** German Rheumatism Research Centre (DRFZ) Berlin, a Leibniz Institute, Berlin, Germany, **3** Research Center of Medical Technology and Biotechnology, Bad Langensalza, Germany, **4** Institute of Animal Welfare, Animal Behavior and Laboratory Animal Science, Department of Veterinary Medicine, Freie Universität Berlin, Berlin, Germany

 These authors contributed equally to this work.

‡ These authors also contributed equally to this work.

* annemarie.lang@charite.de



 OPEN ACCESS

Citation: Pfeiffenberger M, Bartsch J, Hoff P, Ponomarev I, Barnewitz D, Thöne-Reineke C, et al. (2019) Hypoxia and mesenchymal stromal cells as key drivers of initial fracture healing in an equine *in vitro* fracture hematoma model. PLoS ONE 14(4): e0214276. <https://doi.org/10.1371/journal.pone.0214276>

Editor: Francesc Xavier Donadeu, University of Edinburgh, UNITED KINGDOM

Received: July 25, 2018

Accepted: March 11, 2019

Published: April 4, 2019

Copyright: © 2019 Pfeiffenberger et al. This is an open access article distributed under the terms of the [Creative Commons Attribution License](https://creativecommons.org/licenses/by/4.0/), which permits unrestricted use, distribution, and reproduction in any medium, provided the original author and source are credited.

Data Availability Statement: All relevant data are within the paper and its Supporting Information files.

Funding: This study was funded by the Bundesministerium für Bildung und Forschung (BMBF) (031A334 to FB). Author TG is funded by the Deutsche Forschungsgemeinschaft (DFG) (353142848). The funders had no role in study design, data collection and analysis, decision to publish, or preparation of the manuscript.

Abstract

Fractures in horses—whether simple fractures with just one clean break, or incomplete greenstick with stress fractures, or complications such as shattered bones can all be either minimal or even catastrophic. Thus, improvement in fracture healing is a hallmark in equine orthopedics. The fracture healing process implements a complex sequence of events including the initial inflammatory phase removing damaged tissue, re-establishment of vessels and mesenchymal stromal cells, a soft and hard callus phase closing the fracture gap as well as the remodeling phase shaping the bone to a scar-free tissue. Detailed knowledge on processes in equine fracture healing in general and on the initial phase in particular is apparently very limited. Therefore, we generated equine *in vitro* fracture hematoma models (FH models) to study time-dependent changes in cell composition and RNA-expression for the most prominent cells in the FH model (immune cells, mesenchymal stromal cells) under conditions most closely adapted to the *in vivo* situation (hypoxia) by using flow cytometry and qPCR. In order to analyze the impact of mesenchymal stromal cells in greater detail, we also incubated blood clots without the addition of mesenchymal stromal cells under the same conditions as a control. We observed a superior survival capacity of mesenchymal stromal cells over immune cells within our FH model maintained under hypoxia. Furthermore, we demonstrate an upregulation of relevant angiogenic, osteogenic and hypoxia-induced markers within 48 h, a time well-known to be crucial for proper fracture healing.

Competing interests: The authors have declared that no competing interests exist.

Introduction

Fractures in horses are often fatal, extremely expensive to treat, and in certain cases an injury leading to euthanasia [1, 2]. Additionally, equine fractures and their subsequent treatment are of great economic interest [3], especially for horses deployed in racing. Various studies indicated an incidence of fractures in races between 1–2% per race start [2, 4, 5], with pelvic and tibial stress fractures identified as the most common cases of fracture [5]. Furthermore, the number of horses used in leisure sports is still increasing and includes a trend towards free-range husbandries in groups leading potentially to injuries and contortions especially in the fetlock area [6, 7]. Similar to treatment in humans, current strategies towards long bone fractures in horses focus on stabilization of the fracture site by means of screws or nails [8, 9]. Nowadays more elicit methods of treatment utilizing internal fixators [1], locking compression plates [10], external fixators [11] or hydrogels [12] are being applied in clinics. Moreover, cell therapy with either mesenchymal stromal cells [13, 14] or osteoprogenitor cells [15] is of upcoming interest especially for fractures that cannot be stabilized due to the location (fetlock, coffin bone). Nevertheless, the biggest challenge still remains the appropriate stabilization that remains perpetuated during the recovery time after surgery when approximately 400–600 kg of body weight are loaded onto the bones. As to the processes of fracture healing and particularly those during the initial phase of fracture healing, only little is known. In horses, bone healing is generally considered to be delayed [16] and contradictory to phylogenetically lower developed animals, the bone quality is diminished after trauma [17].

Generally, fracture healing can be divided into four different phases: (i) initial/inflammatory phase, (ii) soft callus formation, (iii) hard callus formation, and (iv) remodelling phase. During fracture, the bone marrow channel is shattered and evading cells such as mesenchymal stromal cells (MSCs), hematopoietic stem cells (HSC), immune cells and their precursor cells are mixed with cells from ruptured blood vessels (immune cells) within the fracture gap. These cells coagulate and form the so-called fracture hematoma (FH), which initiates the ongoing inflammatory phase within a hypoxic milieu [18]. Main research progress focusing on the initial phase has been conducted in sheep or rodents [19, 20], facing the problem of translation towards the human situation and/or the horse as a patient. Mice for instance lack the Haversian canal system [21], which is typical for human and equine bone physiology and remain in general an arguable model for disease patterns with ongoing inflammation processes [22]. In contrast, large animal models show considerably more similarity to human bone physiology concomitant processes when it comes to the pathophysiology of fracture healing [23]. In a human *ex vivo* study in 2011, Hoff et al. could show that besides myeloid cells of the innate immune system (monocytes, granulocytes) and cells of the adaptive immune system (T and B cells), also hematopoietic stem cells and MSCs are prominent cells in the FH [18].

Based on the general assumption that within the initial phase of bone healing immediately following the trauma, a hematoma is generated which accumulates cells from both peripheral and intramedullary blood, as well as bone marrow cells including mesenchymal stromal cells (MSCs) [24]. The initial phase is known to involve an acute inflammatory response including the production and the release of several important molecules, such as IL6, IL8 and MIF [25], and the recruitment of MSCs in order to generate a primary cartilaginous callus [24]. Thus, we generated a blood clot with MSCs to simulate the shift from the initial hematoma to the soft callus phase and to determine the importance of MSCs in the equine fracture healing process. In brief, the rationale of our study was to study the influence of MSCs, which are considered to be the main driver of tissue regeneration during the initial phase of fracture healing, since MSCs are the progenitor cells both for cartilage (endochondral ossification) and bone cells (intramembranous ossification). We also implemented microenvironmental conditions found

at the fracture site *in vivo* (hypoxia). For simulating the hypoxic conditions, we incubated our FH models under hypoxia (1% O₂), with normoxia serving as a control. To underline the impact of MSCs, we also incubated in parallel blood clots without the supplementation of MSCs as a second control. This way we had the opportunity to (i) contextualize our data to existing *in vivo* and *ex vivo* data and (ii) to use this system to eventually analyze the impact of fracture healing-relevant drugs or therapies in subsequent studies. To this end, we used our *in vitro* FH model in order to study the influence of hypoxia and mesenchymal stromal cells on the initial phase of fracture healing.

Materials and methods

Blood samples

EDTA blood samples (residual material from diagnostic blood drawings) were obtained from the equine clinic at the Department of Veterinary Medicine, Freie Universität Berlin (clinic's own horses). The horses showed no indication of illness, systemic inflammation or infection. For the *in vitro* FH models we used the blood of three different horses and mixed them with 2.2×10^5 MSCs. Correspondingly, we used the blood of three different horses for the coagulation of the blood clots. Age and gender of the respective donors can be found in Table B in [S1 Appendix](#). Blood collection was approved by the local legal representative animal rights protection authorities (Landesamt für Gesundheit und Soziales Berlin: O 344/13)

Bone marrow-derived MSC isolation and incubation

Bone marrow was obtained from the sternum shortly after euthanasia from horses which were euthanized for other ethical justifiable reasons (cadavers) at the equine clinic Seeburg (Dallgow-Döberitz, Germany). Horses showed no indices of illness, systemic inflammation or infection. Bone marrow was transported aseptically in phosphate-buffered saline (PBS) and at RT. Collected bone marrow was transferred into 175 cm² cell culture flasks (Greiner Bio-one, Kremsmünster, Austria) and flushed with 25 ml of DMEM plus GlutaMAX (Thermo Fisher Scientific, Waltham, USA) supplemented with 20% (v/v) StemMACS MSC Expansion Media Kit XF (Miltenyi Biotech, Bergisch Gladbach, Germany), 10% (v/v) FCS (Thermo Fisher, Waltham, USA), 100 units/ml penicillin and 100 mg/ml streptomycin (Thermo Fisher, Waltham, USA), further referred to here as MSC culture medium. Incubation was carried out at 37° C in humidified atmosphere containing 5% CO₂. The MSC culture medium was completely replaced after two days of incubation in order to remove remaining bone marrow, blood and non-adherent cells. Hereafter the medium was replaced weekly.

Differentiation and characterization of bone marrow-derived MSCs

To ascertain the differentiation capability, cells were plated at 1×10^4 cells/well in 96-well plates (Greiner Bio-one, Kremsmünster, Austria) and incubated in the appropriate differentiation medium for 3 weeks.

Osteogenesis: MSCs were differentiated in StemMACS OsteoDiff (Miltenyi Biotech, Bergisch Gladbach, Germany). Cells were fixated with a 4% (w/v) paraformaldehyde solution (Carl Roth, Karlsruhe, Germany) for 10 min at RT and stained with 2% (w/v) Alizarin Red (in H₂O_{dd}, pH 4.1; Sigma Aldrich, St. Louis, USA) for 10 min at RT.

Adipogenesis: MSCs were incubated in α -MEM (Sigma Aldrich, St. Louis, USA) supplemented with 10% (v/v) human serum AB (EUROCLONE, Via Figino, Italian), 100 units/ml penicillin, 100 mg/ml streptomycin, 12 mM L-glutamine (GE Healthcare, Little Chalfont, England), 5 μ g/ml insulin (Lilly, Bad Homburg, Germany), 50 μ M indomethacin (Sigma

Aldrich), 1 μM dexamethasone (Sigma Aldrich) and 0.5 μM isobutylmethylxanthine (Sigma Aldrich, St. Louis, USA). Cells were fixed with 4% (w/v) paraformaldehyde for 10 min at RT and stained with 0.3% (v/v) Oil Red O (Sigma Aldrich, St. Louis, USA) in 60% (v/v) isopropanol (Merck, Darmstadt, Germany) for 15 min.

Further phenotypic characterization was carried out by the expression analysis of three surface MSC markers. Antibodies against equine CD29 and CD105 were used as positive markers and an antibody against equine CD14 as negative marker. Further procedure is described below ("Flow cytometric analysis").

Establishment of 3D fracture hematoma model and control hematomas

For the production of one hematoma model, 100 μl of blood (collected in vacutainer tubes with EDTA) were mixed with 2.2×10^5 MSCs and 100 μl of a 10 mM CaCl_2 solution in a 96-well-plate (round bottom, Greiner Bio-one, Kremsmünster, Austria). Control hematomas (blood clots) were produced analogously without any supply of MSCs. After 30 min incubation at 37°C the blood clots ($n = 4$) and the FH models ($n = 4$) were transferred into DMEM + GlutaMAX supplemented with 10% (v/v) FCS, 100 units/ml penicillin, 100 mg/ml streptomycin, 0.2% (w/v) β -glycerophosphate (Sigma Aldrich, St. Louis, USA), 10 nM dexamethasone (Sigma Aldrich, St. Louis, USA) and 0.002% (w/v) l-ascorbic acid (Sigma Aldrich, St. Louis, USA), further referred as osteogenic differentiation medium. Hematomas/blood clots were incubated for 6, 12, 24, 48, and 72 h under hypoxia at 5% CO_2 and 1% O_2 , balanced with N_2 . Normoxic controls were incubated at 37°C under 5% CO_2 balanced with room-air in a humidified atmosphere (resulting in 18% O_2) for 6, 12, 24, 48, and 72 h as well.

RNA isolation

After incubation, coagulated hematoma models were washed with PBS and cells were separated via a cell strainer (70 μm , Corning, New York, USA). Erythrocyte lysis was performed (erythrocyte lysis buffer: 0.01 M KHCO_3 , 0.155 M NH_4Cl , 0.1 mM EDTA, pH 7.5) for 6 min at 4°C three times, and cells were washed with 0.5% (w/v) BSA in PBS (PBS/BSA). Total RNA was extracted using Arcturus PicoPure RNA Isolation Kit (Applied Biosystems, Foster City, USA), according to the manufacturer's instructions and the RNA concentration was determined using Nanodrop ND-1000 (Peqlab Biotechnologie, Erlangen, Germany). RNA was stored at -80°C until further processing.

Quantitative PCR (qPCR)

The cDNA was synthesized by reverse transcription using TaqMan Reverse Transcription Reagents (Applied Biosystems) for RNA concentrations >10 ng/ μl or Sensiscript Reverse Transcription Kit (QIAGEN GmbH, Hilden, Germany) for RNA concentrations ≤ 10 ng/ μl . cDNA was stored at -20°C until further processing. qPCR was performed using the DyNAmo Flash SYBR Green qPCR Kit (Thermo Fisher, Waltham, USA) and the Stratagene Mx3000P (Agilent Technologies, California, USA). Initial denaturation was for 7 min at 98°C followed by 45 cycles with 5 s at 98°C, 7 s at 58°C and 9 s at 72°C. Finally, the melting curve was analyzed by a stepwise increase of the temperature from 50 to 98°C every 30 s.

All primers were purchased from TIB Molbiol (Berlin, Germany; gene symbol: forward primer, reverse primer):

B2M: CCCCTGATAGTTAAGTGGGATCG, AGTACAGCTTCCTGATTTATGTGC;

MIF: GCAAGCCAGCCCAGTACATC, GCTGTAGGAGCGGTTCTGTG;

VEGFA: TTGCTGCTCTACCTCCACCAT, ATCAGGGGCACACAGGAT;

RUNX2: TGTCATGGCGGGTAACGAT, TCCGGCCACAAATCTCA;

SLC2A1: GAAACCTCACCCACATCCT, TTCGCCTTCCGTAGTTCTCA;
LDHA: GCCGTCTTAATTTGGTCCAG, TGGATTGGAAACAACAAGCA;
PFKFB3: GATTTAGCACAAAGCACGTTT, CTCCAAGGGCATCTTCACAG;
PGKI: GAACACGGAGGATAAAGTCAGC, AGGAACCAAAAAGGCAGGAAA;
SPPI: CCAGTGAGCATTCCGATGTG, TCTCCCACCCCGCTATTATTT;
PPARG: GGGTGTGAGTTTCGCTCAGT, GGGCTCCATAAAGTCACCAA.

Data were normalized to the expression of *Beta-2-Microglobulin* (B2M) and to the time point 0 h, using the $\Delta\Delta C_t$ -method. Focusing on the influence of hypoxia and the effect of MSCs on a model of a fracture hematoma using equine samples under a sterile inflammatory situation, we had to exclude commonly used housekeeping genes that are known to be regulated by hypoxia or inflammation such as *GAPDH* or *ACTB*. We have ultimately chosen *B2M* as a housekeeping gene which has been reported to be a stable housekeeping gene in horse and under hypoxic conditions at least in human MSCs [26, 27]. Furthermore, using qPCR based on the same template concentrations we observed neglectable deviations of the C_t -values of *B2M* with regard to incubation duration for different time points (0 h, 12 h, 48 h) data not shown.

Flow cytometric analysis

After erythrocyte lysis, the isolated cells were washed with PBS/BSA. After Fc-receptor blocking with Flebogamma the cells were washed with PBS/BSA and antibody staining was performed for 15 min on ice. Table A in [S1 Appendix](#) shows all antibodies with their specificity, dilution used and the corresponding isotype controls. All isotype controls were obtained from Miltenyi Biotech GmbH (Bergisch Gladbach, Germany). The cells were washed with PBS/BSA and incubated with 1:25-diluted 7-AAD (BioLegend, San Diego, USA) for 15 min at RT. After a further washing step with PBS/BSA, the cells were resuspended in 0.05% (w/v) NaN₃ in PBS/BSA (PBS/BSA/Azide). The cells were recorded using flow cytometry with a MACS Quant Analyzer (Miltenyi Biotech, Bergisch Gladbach, Germany) and analyzed with FlowJo software (Tree Star, USA). The antibodies and gating strategy utilized are given in the supplementary files (Table A and Fig A in [S1 Appendix](#)).

Embedding, cryosections and DAPI stain

For immunofluorescence, FH models (0 h, 24 h and 48 h) were embedded as follows: FH models were transferred into 4% paraformaldehyde, then into a 10%, 20% and finally 30% glucose solution, each for 24 h. Storage was at 4°C. Cryo-embedding was followed by cryosections as described previously [28]. Slides were air dried and subsequently stained with DAPI. The DAPI staining solution was 0.1% (v/v) DAPI (Sigma Aldrich, St. Louis, USA); 0.1% (v/v) Tween 20 (Carl Roth, Karlsruhe, Germany); 5% (v/v) FCS (Thermo Fisher, Waltham, USA) in PBS. The whole procedure was performed at RT. Sections were first incubated in PBS with 0.1% (v/v) Tween 20 for 10 min. After 10 min incubation in DAPI staining solution, the sections were washed three times in PBS with 0.1% (v/v) Tween 20. Stained sections were put on a slide and then mounted (Fluoromount™ Aqueous Mounting Medium, Sigma Aldrich, St. Louis, USA) under a cover slip. Examination of the sections was performed and photos were taken, using a KEYENCE BZ-X700 fluorescence microscope and depicted in pseudo-colors.

Statistical analysis

Statistical tests were performed using Graph Pad Prism Software (La Jolla, USA). Differences were compared using the Mann–Whitney U-test. Probability values of $p < 0.05$ were

considered to be statistically significant, and values of $p < 0.1$ were considered to have a statistical trend (* $p < 0.05$; + $p < 0.1$).

Results

MSCs play a fundamental role in the initial phase of fracture healing. Therefore, MSCs represent an important cell fraction within our hematoma models. For the use of MSCs, we established well-defined minimal criteria based on their potential to adhere to plastics, to differentiate into osteoblasts and adipocytes, and to express typical surface markers. Only MSCs that fulfill these criteria were utilized to establish the equine *in vitro* FH model, consisting of peripheral blood and MSCs. After cultivation for three passages, the MSCs adhered to the plastic surface and showed their typical fibroblastoid morphology (Fig 1A). They also could be differentiated into the osteogenic lineage as the Alizarin Red S staining showed

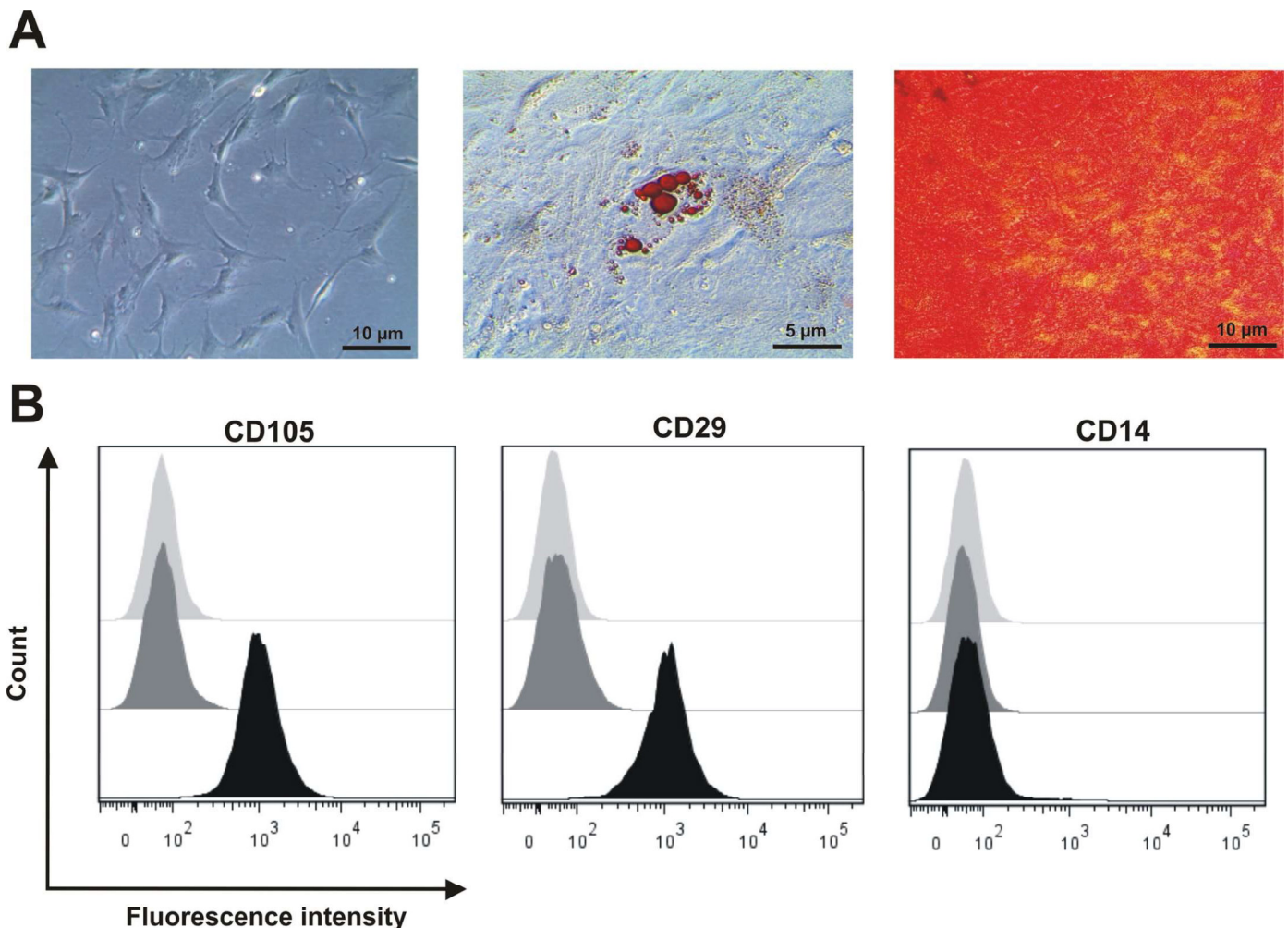


Fig 1. Bone marrow-derived cells obtained from sternum-biopsies are characterized as MSCs. Characterization of equine bone marrow-derived MSCs obtained from sternum-biopsies with regard to their potential to (A) adhere to plastic surfaces and typical morphology, their differentiation potential towards adipogenic and osteogenic lineage and (B) express surface markers CD29, CD105, and CD14 (unstained fractions, isotype control stainings and antigen-specific stainings are depicted in light grey, dark grey and black, respectively).

<https://doi.org/10.1371/journal.pone.0214276.g001>

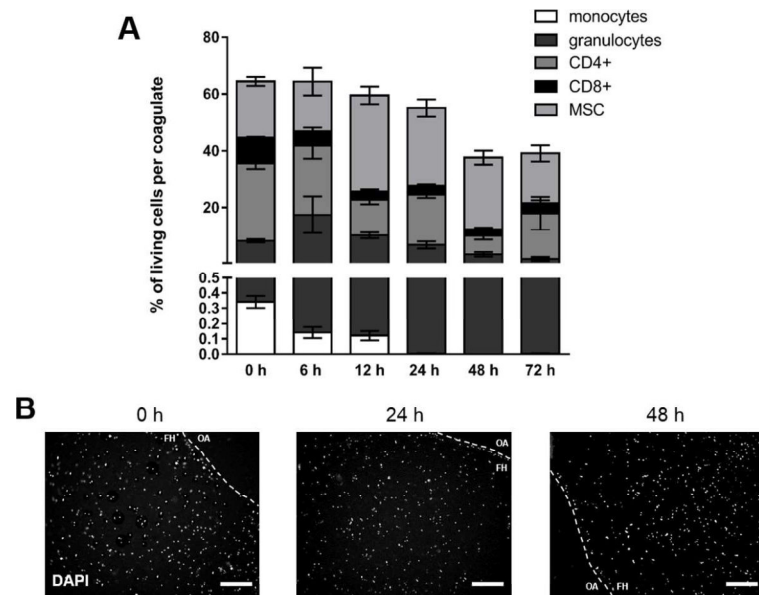


Fig 2. Immune cell vitality in the FH model decreases over time irrespective of subpopulation and spatial distribution after incubation under normoxic conditions. (A) Frequency of immune cell populations (granulocytes, CD14+ monocytes, CD4+ T cells, CD8+ T cells) and MSCs (CD29+, CD 105+, CD14-) negative for 7-AAD present in the *in vitro* FH model as incubated in osteogenic differentiation medium under normoxic conditions (37°C, 5% CO₂, 18% O₂) for 6, 12, 24, 48, and 72 h (mean ± SEM, n = 3). Depicted is the frequency of total cells and the corresponding frequencies of the cell populations. (B) Spatial distribution of cells within the *in vitro* FH model as determined by DAPI-staining and depicted as representative staining for incubation periods of 0, 24, and 48 h (The dotted line indicates the border of the *in vitro* hematoma; FH = area of the fracture hematoma model and OA = outer area).

<https://doi.org/10.1371/journal.pone.0214276.g002>

calcium-complexes stained in red colour and the adipogenic lineage as the cells secrete lipid droplets which are stained red via Red oil staining (Fig 1B). Additionally, the typical surface markers CD29 and CD105 were expressed with no expression of the exclusion marker CD14 (Fig 1C; Table A in S1 Appendix).

Cell composition of *in vitro* FH models under normoxic conditions

To mimic the initial phase of fracture healing *in vitro*, we generated *in vitro* FH models by mixing and coagulating MSCs and blood cells. After incubation of the *in vitro* FH models for 6, 12, 24, 48, and 72 h under normoxic conditions (37°C, 5% CO₂, 18% O₂), we observed a continuous decline in the frequency of cells alive which resulted in 45 ± 3% of cells alive after an incubation period of 72 h (Fig 2A). Within the FH model, the frequency of immune cells decreased over time, while the frequency of MSCs increased within the first 12 h. As a result, the MSC population became the major cell population in the *in vitro* FH model, although it decreased between 12 and 72 h (Fig 2A). With regard to the proportion of immune cells, we observed a continuous decrease in the frequency of granulocytes over time. The frequency of monocytes was negligible, with almost no cells detectable after 6 h of cultivation, while the frequency of CD8+ cells also decreased perpetually. Interestingly, the most prominent population at 0 h—namely CD4+ T cells—remains the most stable cell population within the incubation period analyzed (Fig 2A). In contrast, with regard to the blood clots (Fig B in S1 Appendix) the frequency of granulocytes as well as T cells was very stable. As to the spatial distribution, we observed no clustering of cells but an even distribution within the FH model using DAPI-staining (Fig 2B).

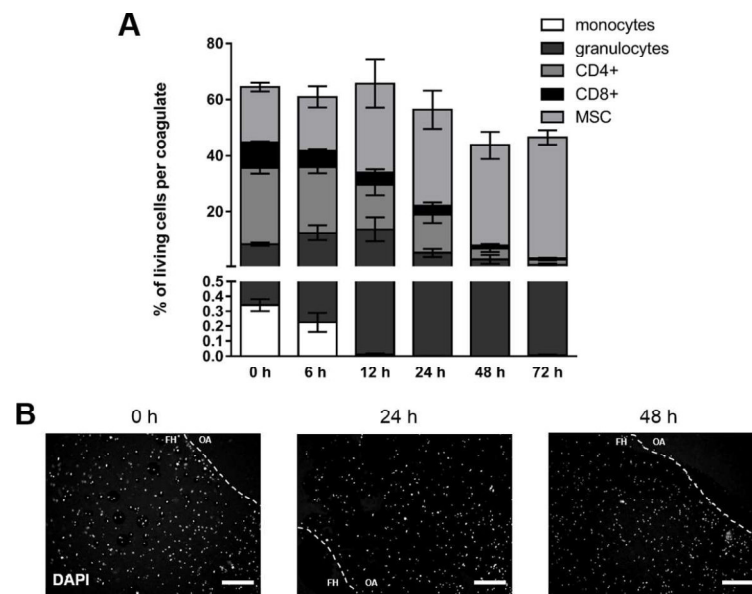


Fig 3. Hypoxia favors survival of MSCs while decreasing immune cell fractions. (A) Frequency of immune cell populations (granulocytes, CD14+ monocytes, CD4+ T cells, CD8+ T cells) and MSCs (CD29+, CD 105+, CD14-) negative for 7-AAD in the FH models cultured in osteogenic differentiation medium under hypoxic conditions (37°C, 5% CO₂, 1% O₂) for 6, 12, 24, 48, and 72 h (mean ± SEM, n = 3). Depicted is the frequency of total cells and the corresponding frequencies of the cell populations. (B) Spatial distribution of cells within the FH model as determined by DAPI-staining and depicted as representative staining for 0, 24, and 48 h of incubation (The dotted line indicates the border of the *in vitro* hematoma; FH = area of the fracture hematoma model and OA = outer area).

<https://doi.org/10.1371/journal.pone.0214276.g003>

Cell composition of *in vitro* FH models under hypoxic conditions

To mimic the restricted microenvironment in the initial phase of fracture healing more adequately, we generated *in vitro* FH models and incubated them under hypoxic conditions (37°C, 5% CO₂, 1% O₂) for 6, 12, 24, 48, and 72 h. We observed a perpetual decline of the cells alive with a final frequency of $43 \pm 2\%$ after 72 h of incubation (Fig 3A). With regard to the immune cell populations, the frequency of CD4+ T cells and CD8+ T cells again constantly decreased over time, whereas the frequency of granulocytes increased from zero to 12 h before massively decreasing. The frequency of monocytes alive was barely detectable at any time point analyzed. Finally, none of the analyzed immune cell populations survived the FH model after 72 h of cultivation under hypoxic conditions. In contrast, the proportion of MSCs within the FH model permanently increased from a ratio of $20\% \pm 1\%$ at 0 h to $42 \pm 2\%$ at 72 h after cultivation (Fig 3A). With regard to the blood clots (Fig B in S1 Appendix), we observed a stable frequency of granulocytes and T cells. Regarding the spatial distribution, we again observed no clustering of cells but an even distribution within the FH model using DAPI-staining (Fig 3B).

Impact of oxygen availability on cellular vitality and composition in the *in vitro* FH models

When comparing cellular vitality and composition of the FH models incubated under normoxia with those incubated under hypoxia, we observed no differences in respect to overall cell survival, either after 72 h, or throughout the whole decline in time. However, as far as the cellular composition is concerned, the frequencies of all immune cell populations in the FH model declined under hypoxia, whereas under normoxia, survival of CD4+ and CD8+ T cells

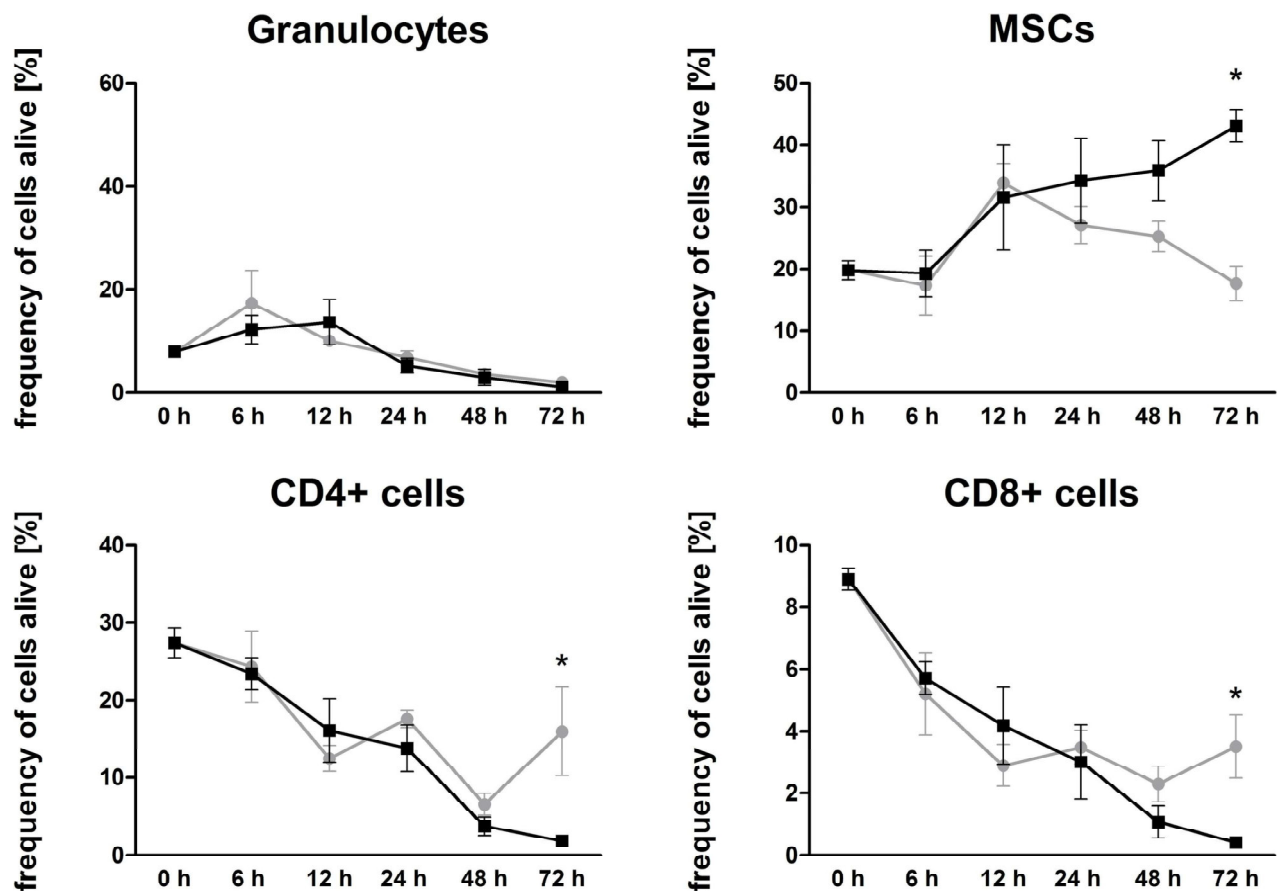


Fig 4. Hypoxia favors survival of MSCs while decreasing granulocytes, CD4+ and CD8+ immune cells. Frequency of granulocytes, CD4+ and CD8+ immune cells negative for 7-AAD in the FH model cultured in osteogenic differentiation medium under either normoxic (grey) or hypoxic (black) conditions (n = 3). Statistical analysis was conducted using the Mann-Whitney U-test, *p < 0.05.

<https://doi.org/10.1371/journal.pone.0214276.g004>

after 72 h of incubation was significantly higher than that under hypoxic incubation (Fig 4). In contrast, the frequency of granulocytes remains unaffected by the incubation conditions, and for monocytes the case was likewise negligible. Hence, the frequency of MSCs was significantly higher under hypoxic conditions after 72 h of cultivation when compared to that of the corresponding control (Fig 4).

MSCs along with their time-dependent increase were by far the most abundant cells, a most striking situation seen from 12 to 72 h. Compared to normoxic conditions, MSCs survived better under hypoxic conditions, whereas immune cells seem to have a diminished survival rate (Fig 4).

Time-dependent RNA-expression of fracture-healing-relevant markers in the *in vitro* FH models

To analyze the impact of hypoxia on all cells in the FH model, we focused on markers for osteogenesis, glycolytic adaptation towards hypoxia and angiogenesis on the transcriptional level (Fig 5). Therefore we analyzed the RNA-expression of fracture-relevant markers. We cultivated the *in vitro* hematomas for 6, 12 and 48 h. Within the hematomas, osteogenic (*RUNX2*, *SPP1*), angiogenic (*VEGFA*, *MIF*) as well as hypoxia-induced (*LDHA*, *PGK1*, *PFKFB3*,

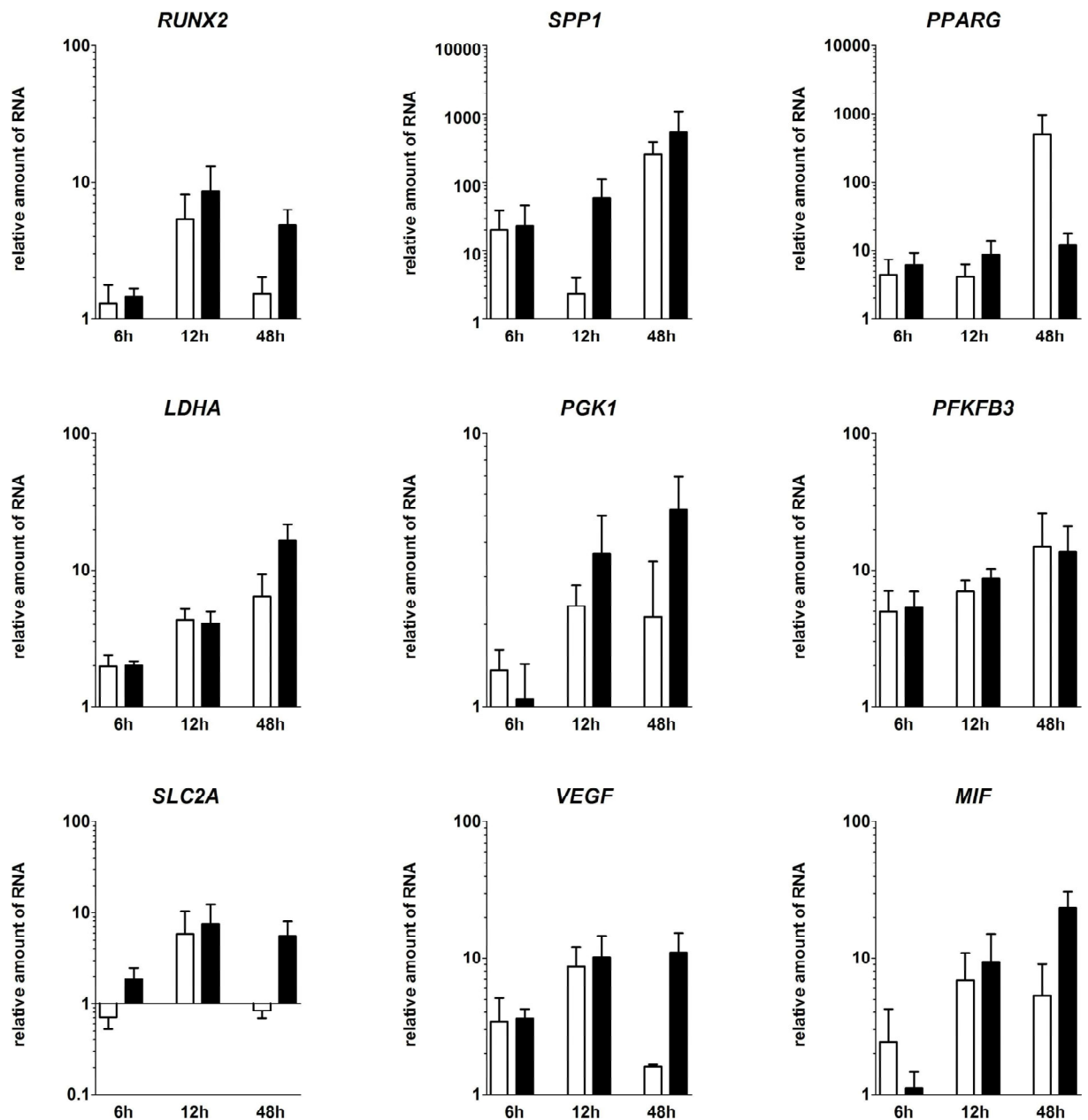


Fig 5. Within the FH models, osteogenic, hypoxia-induced and angiogenic markers were upregulated over time until 48 h of incubation. Depicted is the relative RNA-expression of the osteogenic markers *RUNX2*, *SPP1*, the adipogenic marker *PPARG*, the hypoxia induced genes *LDHA*, *PGK1*, *PFKFB3*, *SLC2A1*, and the angiogenic genes *VEGFA*, and *MIF* within the *in vitro* FH models after cultivation in osteogenic differentiation medium for 6, 12, and 48 h under either normoxia (white bars) or hypoxia (black bars). All values are normalized to the "housekeeping gene" *B2M* and 0 h (Mean \pm SEM, n = 3). Statistical analysis was conducted using Mann-Whitney U-test.

<https://doi.org/10.1371/journal.pone.0214276.g005>

SLC2A1) markers were higher expressed after 48 h. Concerning the osteogenic markers, we demonstrated a time-dependent upregulation of *RUNX2* and *SPP1*. While *RUNX2* was upregulated after 12 h of cultivation, the highest upregulation of *SPP1* was observed at 48 h. Additionally, this effect was even stronger under hypoxic conditions, where *RUNX2* was upregulated to a higher extent. In contrast, the adipogenic transcription factor *PPARG* was less

strongly induced in FH models incubated under hypoxic conditions. Drawing the focus towards angiogenic markers, we could show the upregulation of typical markers (peaks: *VEGFA* after 12 and *MIF* after 48 h). Interestingly, both *VEGFA* and *MIF* showed higher levels of expression in FH models incubated under hypoxic conditions. *LDHA*, *PGK1*, *PFKFB3* and *SLC2A1* were also upregulated at least after 12 h. After 48 h, the majority of genes analyzed were expressed to a higher extent under hypoxic conditions except for *PFKFB3* and *PPARG* (Fig 5).

Differences of the mRNA-expression of *in vitro* hematomas versus blood coagulates after 48 h of cultivation under normoxic or hypoxic conditions

To analyze if the observed changes in gene expression patterns are due to the different survival rates of the analyzed immune cell populations and MSCs, we compared the data gained from *in vitro* hematomas to blood coagulates without MSCs. Focusing on the differences between the mRNA-expression of blood coagulates and *in vitro* hematomas, we could show that except for *SPP1* the expression of relevant genes was higher in the *in vitro* hematomas (significant for *PFKFB3* and *VEGFA*). In the *in vitro* FH model, osteogenic-relevant genes (*RUNX2*, *SPP1*) were upregulated, even more pronounced under hypoxic conditions, whereas the adipogenic marker *PPARG* was upregulated, but about 100 times less under hypoxic conditions. Hypoxia-induced genes (*PGK1*, *PFKFB3* and *SLC2A1*) were also upregulated under both cultivation methods, except for *SLC2A1* which was only upregulated under hypoxic conditions. *PGK1* and *SLC2A1* showed a higher expression under hypoxic conditions. For the angiogenic markers *VEGFA* and *MIF* as well as for the pH-regulating marker *LDHA*, we could show an upregulated expression which was even more evident under the influence of hypoxia (Fig 6).

Discussion

To study the underlying cellular mechanisms of the initial inflammatory phase of fracture healing in horses, we aimed to establish an equine *in vitro* FH model. To this end, we first created protocols for the isolation and characterization of major cell types involved in the generation of the FH model, namely immune cells—released from the ruptured vessels and from the bone marrow—and mesenchymal stromal cells (MSCs) from bone and bone marrow. The limited availability of suitable antibodies for immunological characterization but also the limited knowledge of lineage markers for equine cells especially for equine MSCs belong to the challenging issues we wanted to address in the study presented here.

To characterize MSCs, standardized criteria for human material have already been established and defined more than ten years ago [29]. In brief, human MSCs have to fulfill minimal requirements including attachment to plastic surfaces, the capacity to differentiate into multiple lineage [30], as verified by differentiation towards osteogenic, chondrogenic and adipogenic lineage, and finally the presence or absence of typical surface markers (CD73+, CD90+, CD105+; CD45-, CD34-, CD14-, CD19- and HLA-DR-) [29]. Focusing on equine MSCs, it is disparately more difficult to characterize these cells in a similar way. Although a variety of characterization procedures have already been described [31–34], only few surface markers are available for immunophenotyping due to the limited availability of suitable antibodies. Here, we characterized MSCs by demonstrating (i) plastic adherence, (ii) differentiation towards osteogenic (demonstrated by Alizarin Red staining) and adipogenic (demonstrated by Red Oil staining) lineage, and (iii) immunological characterization using CD105 and CD29, previously described as stable equine MSCs markers and widely used to characterize equine MSCs [35–38] and CD14 as a negative marker (Fig A and Table A in S1 Appendix). These have also been previously demonstrated to characterize equine monocytes (2013) [39]. We defined this characterization procedure as a minimum criterion for the use of equine MSCs within our study.

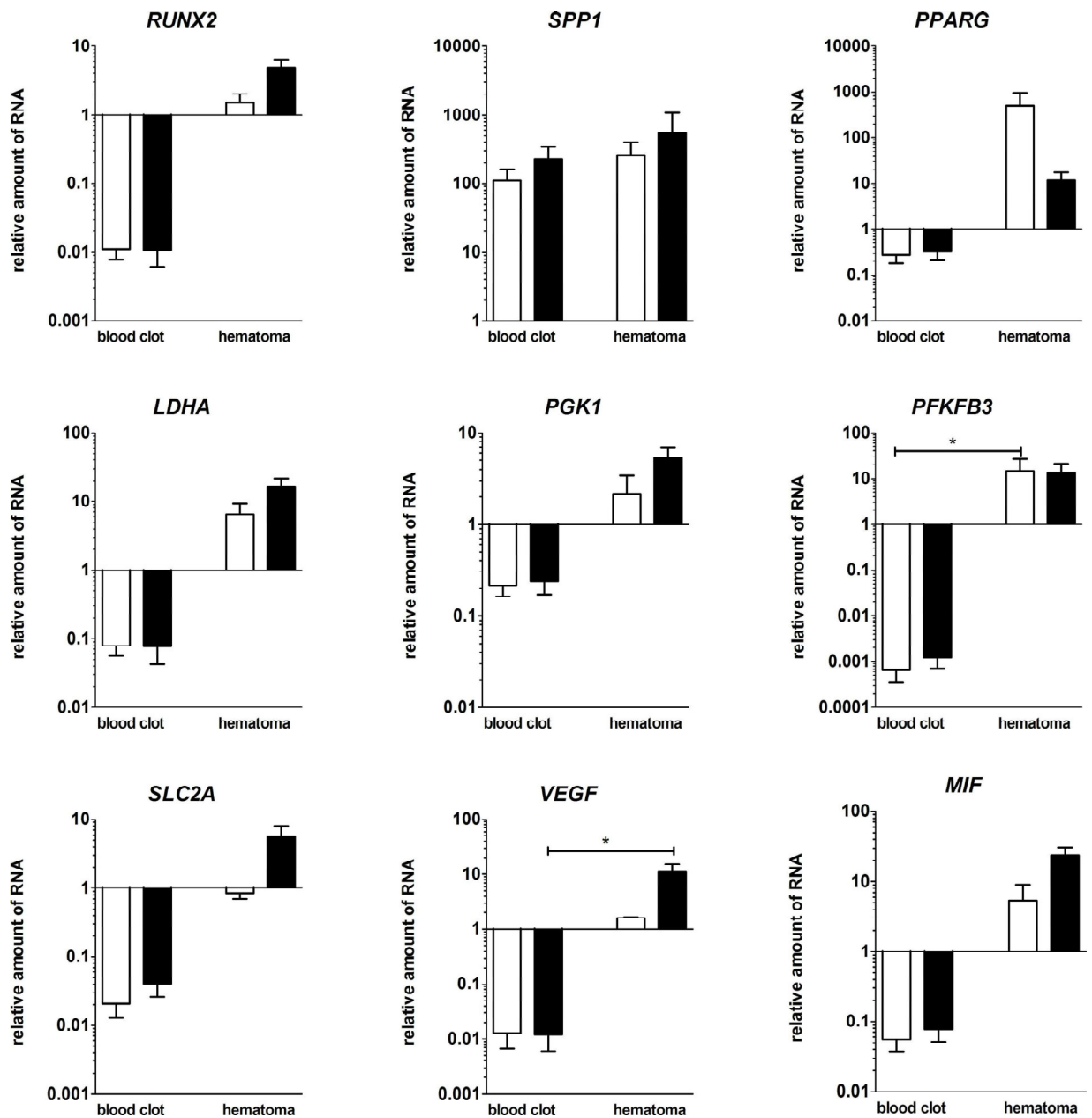


Fig 6. Osteogenic, hypoxia-induced and angiogenic markers were upregulated in the *in vitro* FH models compared to blood coagulates. Depicted is the relative RNA-expression of the osteogenic markers *RUNX2*, *SPP1*, the adipogenic marker *PPARG*, the hypoxia induced genes *LDHA*, *PGK1*, *PFKFB3*, *SLC2A1* and the angiogenic genes *VEGFA* and *MIF* within the FH models and the blood-only coagulates after cultivation in osteogenic differentiation medium for 48 h under either normoxic (white bars) or hypoxic conditions (black bars). All values are normalized to the “housekeeping gene” *B2M* and to 0 h (mean ± SEM, blood clots: n = 4, FH models: n = 3). Statistical analysis was conducted using Mann-Whitney U-test, *p<0.05.

<https://doi.org/10.1371/journal.pone.0214276.g006>

For the characterization of equine immune cells, we used antibodies against CD4, CD8, and CD14, while granulocytes were determined by granularity and size using flow cytometry (Table A in Appendix 1). Separation of MSCs from the immune cell populations in the FH model was achieved by flow cytometry (Fig A in [S1 Appendix](#)).

Although *in vitro* FH models were generated in a standardized manner with regard to cell numbers and incubation times, we had to face limitations in terms of low cell recovery from coagulates after incubation, variations in hematoma size after coagulation and a massive impact on cell survival after incubation (Figs 2 and 3).

Analyzing the impact of a restricted microenvironment by focusing on hypoxia in our *in vitro* model, we did not observe any difference between normoxia and hypoxia concerning overall cell survival (Figs 2 and 3). However, we did observe a shift in the distribution of cell population towards an increase in the proportion of MSCs after incubation under hypoxic conditions (Fig 3). We assume that MSCs, well-known key players in the process of fracture healing [40–42], may promote the termination of the inflammatory phase especially in a hypoxic microenvironment, and this may resemble the *in vivo* situation at the fracture site [18]. Thus, MSCs can be assumed to be likely suitable candidates in cell-based therapeutic strategies to overcome fracture healing disorders in horses and humans [13, 14]. Additionally, we had observed previously that the osteogenic differentiation of human MSCs is enhanced in a hypoxic microenvironment but also that it does not influence cell survival or proliferation [43]. Conversely, Ranera et al. (2012) demonstrated that hypoxia limits the proliferation of equine MSCs in 2D cultures [34]. Whether or not these differences are species-specific needs to be clarified.

Focusing on myeloid cells such as monocytes and polymorph nuclear cells (PMNC), we observed a time-dependent decline of their frequencies within the *in vitro* FH model without any significant impact of hypoxia on cell survival (Figs 2–4). In general, the role of neutrophils with regard to fracture healing has to our knowledge been poorly investigated or is discussed controversially, although granulocytes are the most abundant cells in the early FH [44]. Grogaard et al. (1990) reported that neutropenia in mice did not have any significant effect on fracture healing [45]. In addition, Chung et al. (2006) observed a slight increase of bony trabeculae when treating young rats with neutrophil-neutralizing antiserum in a growth plate injury model [46]. In the human *in vitro* FH model, which was performed recently from our group neutrophils seem to only marginally influence fracture healing, while being time-dependently depleted in the FH model, and even more strongly so under hypoxic conditions [47]. In contrast, a study of Kovtun et al. (2016) reveals a crucial role of neutrophils in bone healing [44]. They drastically reduced the number of neutrophils using a Ly-6G antibody in fractured mice and observed impaired bone healing after 21 d, with diminished bone content as well as impaired mechanical properties, implicating the important role of neutrophils in the very early phase of fracture healing [44]. With regard to PMNCs in our model, we could not determine any impact of hypoxia on the frequency of granulocytes (Figs 2–4). Neutrophils are primarily responsible for the removal of debris and spoil cells in accordance with attracting monocytes to the fracture site [48] in the very early inflammatory phase, while their importance seems to be diminished in the ongoing process of fracture healing. In our study here, we could show the presence and survival of granulocytes within the first hours as well as their time-dependent decline of their frequencies within the *in vitro* FH models, which may resemble the *in vivo* situation (Figs 2–4). Although the frequency of granulocytes is time-dependently diminished, we cannot exclude, that granulocytes in apoptosis or netosis or degranulation processes have an influence on the ongoing process of fracture healing.

Among the adaptive immune cell populations, we observed a significantly enhanced hypoxia-mediated reduction in the frequencies of CD4+ and CD8+ cells after incubation of FH models for 72 h (Figs 2–4). In the line of our observation, reduction of an adaptive immune response has been reported to accelerate during bone healing [49, 50]. In more detail, Toben et al. demonstrated an accelerated fracture healing in recombination activating gene 1 knock-out (RAG1(-/-)) mice lacking the adaptive immune system [49]. Although it has been

demonstrated that proliferation of CD8+ cells is diminished under hypoxic conditions [51], depletion of CD8+ T-cells in a mouse osteotomy model further has been reported to enhance fracture healing [50]. These findings and our findings presented here indicate that the continuous depletion of CD8+ T cells within the fracture site seems to be a feature beneficial for the fracture healing process. However, in an *ex vivo* human FH model, we demonstrated a decrease in lymphocyte survival after 24 h—independently of oxygen availability—although the frequencies of lymphocytes after hypoxic incubation increase. The latter can be explained by the relatively decreased granulocyte proportions after 24 h of incubation under hypoxia. Interestingly, we could detect a relevant expression of active caspases indicating apoptosis in granulocytes only after 24 h of incubation under hypoxia. However, human lymphocytes from *ex vivo* human FH models did express active caspases under all incubation conditions but with the highest expression after 24 h under hypoxia which is in the line with the findings in the equine FH model after 48 h [47].

Moreover, it has been well demonstrated that MSCs exhibit immunosuppressive functions [52], and that they are immunotolerant [53] and known to inhibit the proliferation of T-lymphocytes [42, 52, 54–56]. Here, we demonstrate that the increase in the frequency of MSCs over time is associated with a decrease of T-lymphocytes when investigating the incubation of these cells under hypoxia. This anti-correlative development may indicate that MSCs are limiting the initial inflammatory hypoxic phase of fracture healing in a human *ex vivo* FH model and also in an equine *in vitro* FH model.

In view of the impact of hypoxia on the expression of selected genes in our equine *in vitro* FH model, we observed that upregulation of osteogenic (*RUNX2*, *SPP1*), hypoxia-induced (*PGK1*, *LDHA*, *PFKFB3*, *SLC2A1*) and angiogenic (*VEGFA*, *MIF*) genes/factors essential for fracture healing after incubation for 48 h takes place at a higher extent under hypoxic than under normoxic conditions (Fig 5). In this line of observation, we could previously demonstrate a time-dependent increase in the expression of the osteogenic *RUNX2* and *SPP1* in a human *ex vivo* FHs [18]. Although we demonstrate an increase in the expression of *PPARG* (a key marker for the adipogenic differentiation of MSCs under normoxia), its upregulation is abolished under hypoxia. Thus, hypoxia seems to shift MSCs into the osteogenic lineage, as demonstrated previously [43].

To analyze the impact of MSCs, we compared the *in vitro* generated FH models (blood coagulates with MSCs) with blood coagulates without MSCs, focusing on the expression of selected genes (Fig 6). In general, MSCs contribute either directly or indirectly to the induction of gene expression from osteogenic (*RUNX2*, *SPP1*), hypoxia-induced (*PGK1*, *LDHA*, *PFKFB3*, *SLC2A1*) and angiogenic (*VEGFA*, *MIF*) factors essential for fracture healing. The contribution of MSCs in the equine *in vitro* FH models demonstrate a similar pattern of expression with regard to the hypoxia-induced genes *LDHA*, *PGK1* and *SLC2A1* after 48 h when compared to in human *ex vivo* as well as *in vitro* studies [18, 47]. The induction of these genes especially under hypoxia may reflect the adaptation towards a hypoxic environment and the shift towards anaerobic glycolysis [57–60]. All hypoxia-related genes were to a great extent more highly expressed in the *in vitro* hematomas when compared to blood coagulates, indicating the huge influence of MSCs on the expression of hypoxia-induced genes/factors in the FH models, which also involves the gene expression of *VEGFA* and *MIF* coding for angiogenic factors. *VEGFA* is known to be expressed locally by pre-osteoblasts [61] and MSCs, and also plays an important role in the fate of MSCs towards either adipocyte or osteoblast lineage [61, 62]. Several studies identified *VEGFA* as a key factor in osteogenesis as well as in angiogenesis [63–65]. Upregulation of *VEGFA* in our model may indicate the initiation of fracture healing-relevant processes involving angiogenesis and vascularization. *MIF* is also an essential molecule for fracture healing [25, 66] and several knock-out rat models have underlined the importance

of *MIF*, demonstrating a delayed fracture healing in the absence of *MIF* [67, 68]. *MIF* is secreted by MSCs [69] and is known to promote their survival [70].

Taken together, we observed in our present equine *in vitro* FH model profound similarities to our previously published results derived from a human *in vitro* FH model. These concern the expression of genes analyzed for the upregulation of angiogenic and hypoxia-induced markers, and the indication that they are more pronounced under hypoxic conditions [47].

Conclusion

In our study presented here, we characterized equine immune cells as well as MSCs and used these cells to establish an equine *in vitro* FH model. We demonstrate that hypoxia favors the survival of MSCs over that of immune cells and that the expression of fracture healing-relevant genes, most often enhanced by hypoxia, is widely induced. Compared to human *in vitro* and *ex vivo* data and *in vivo* data based on animal models, we could highlight significant similarities. However, further investigations of *ex vivo* equine fracture hematoma are needed to validate our approach and to clarify the cellular and molecular process of the initial phase of fracture healing in the “patient” horse more in detail.

Supporting information

S1 Appendix. File name: Supporting information.
(PDF)

Acknowledgments

The authors would like to thank Manuela Jakstadt for excellent technical assistance. FACS analysis were performed together with the Core Facility at the German Rheumatism Research Centre. Equine blood and bone-marrow were kindly provided by the equine clinic at the Department of Veterinary Medicine, Freie Universität Berlin and the equine clinic Seeburg (Dallgow-Däberitz, Germany). MP and AL are members of the Dahlem Research School Biomedical Sciences (DRS). AL is a member of the Berlin-Brandenburg School for Regenerative Therapies (BSRT). MP, AL, FB, CTR and TG are members of Berlin-Brandenburg research platform BB3R.

Author Contributions

Conceptualization: Moritz Pfeiffenberger, Timo Gaber, Annemarie Lang.

Data curation: Moritz Pfeiffenberger, Janika Bartsch.

Formal analysis: Moritz Pfeiffenberger, Paula Hoff, Christa Thöne-Reineke, Frank Buttgerit, Timo Gaber, Annemarie Lang.

Funding acquisition: Frank Buttgerit, Timo Gaber, Annemarie Lang.

Investigation: Moritz Pfeiffenberger, Janika Bartsch, Annemarie Lang.

Methodology: Moritz Pfeiffenberger, Janika Bartsch, Igor Ponomarev.

Project administration: Timo Gaber, Annemarie Lang.

Resources: Igor Ponomarev, Dirk Barnewitz, Frank Buttgerit, Timo Gaber.

Supervision: Paula Hoff, Christa Thöne-Reineke, Frank Buttgerit, Timo Gaber, Annemarie Lang.

Writing – original draft: Moritz Pfeiffenberger, Janika Bartsch, Timo Gaber, Annemarie Lang.

Writing – review & editing: Paula Hoff, Igor Ponomarev, Dirk Barnewitz, Christa Thöne-Reineke, Frank Buttgerit.

References

1. Auer JA, Grainger DW. Fracture management in horses: Where have we been and where are we going? *Veterinary journal* (London, England: 1997). 2015; 206(1):5–14. Epub 2015/06/23. <https://doi.org/10.1016/j.tvjl.2015.06.002> PMID: 26095036.
2. Rosanowski SM, Chang Y-M, Stirk AJ, Verheyen KLP. Risk factors for race-day fatality in flat racing Thoroughbreds in Great Britain (2000 to 2013). *PLOS ONE*. 2018; 13(3):e0194299. <https://doi.org/10.1371/journal.pone.0194299> PMID: 29561898
3. Peloso JG, Mundy GD, Cohen ND. Prevalence of, and factors associated with, musculoskeletal racing injuries of thoroughbreds. *Journal of the American Veterinary Medical Association*. 1994; 204(4):620–6. Epub 1994/02/15. PMID: 8163419.
4. Maeda Y, Hanada M, Oikawa M-a. Epidemiology of racing injuries in Thoroughbred racehorses with special reference to bone fractures: Japanese experience from the 1980s to 2000s. *Journal of Equine Science*. 2016; 27(3):81–97. <https://doi.org/10.1294/jes.27.81> PMC5048355. PMID: 27703403
5. Verheyen KL, Wood JL. Descriptive epidemiology of fractures occurring in British Thoroughbred racehorses in training. *Equine veterinary journal*. 2004; 36(2):167–73. Epub 2004/03/25. PMID: 15038441.
6. Janczarek I, Wilk I. Leisure riding horses: research topics versus the needs of stakeholders. *Animal science journal = Nihon chikusan Gakkaiho*. 2017; 88(7):953–8. Epub 2017/04/20. <https://doi.org/10.1111/asj.12800> PMID: 28422370.
7. Mejdell CM, Jørgensen GHM, Rehn T, Fremstad K, Keeling L, Bøe KE. Reliability of an injury scoring system for horses. *Acta Veterinaria Scandinavica*. 2010; 52(1):68–. <https://doi.org/10.1186/1751-0147-52-68> PMC3023730. PMID: 21194451
8. Auer JA. Chapter 81—Principles of Fracture Treatment. *Equine Surgery* (Third Edition). Saint Louis: W.B. Saunders; 2006. p. 1000–29.
9. Auer JA, Watkins JP. Treatment of radial fractures in adult horses: an analysis of 15 clinical cases. *Equine veterinary journal*. 1987; 19(2):103–10. Epub 1987/03/01. PMID: 3569192.
10. Jacobs Carrie C, Levine David G, Richardson Dean W. Use of locking compression plates in ulnar fractures of 18 horses*. *Veterinary Surgery*. 2017; 46(2):242–8. <https://doi.org/10.1111/vsu.12607> PMID: 28146292
11. Turek B, Potynski A, Drewnowska O. Own-design external fixator for the treatment of diaphyseal fractures of the third metacarpal bone in horses. *Med Weter*. 2016; 72(3):197–202. WOS:000371281800010.
12. Cohen JM, Southwood LL, Engiles J, Leitch M, Nunamaker DM. Effects of a novel hydrogel on equine bone healing: a pilot study. *Veterinary and comparative orthopaedics and traumatology: VCOT*. 2012; 25(3):184–91. Epub 2012/03/01. <https://doi.org/10.3415/VCOT-11-01-0006> PMID: 22366873.
13. Govoni KE. HORSE SPECIES SYMPOSIUM: Use of mesenchymal stem cells in fracture repair in horses. *Journal of animal science*. 2015; 93(3):871–8. Epub 2015/05/29. <https://doi.org/10.2527/jas.2014-8516> PMID: 26020865.
14. Rosset P, Deschaseaux F, Layrolle P. Cell therapy for bone repair. *Orthopaedics & traumatology, surgery & research: OTSR*. 2014; 100(1 Suppl):S107–12. Epub 2014/01/15. <https://doi.org/10.1016/j.otsr.2013.11.010> PMID: 24411717.
15. McDuffee LA, Pack L, Lores M, Wright GM, Esparza-Gonzalez B, Masaoud E. Osteoprogenitor cell therapy in an equine fracture model. *Veterinary surgery: VS*. 2012; 41(7):773–83. Epub 2012/07/19. <https://doi.org/10.1111/j.1532-950X.2012.01024.x> PMID: 22804243.
16. Murphey ED, Schneider RK, Adams SB, Santschi EM, Stick JA, Ruggles AJ. Long-term outcome of horses with a slab fracture of the central or third tarsal bone treated conservatively: 25 cases (1976–1993). *Journal of the American Veterinary Medical Association*. 2000; 216(12):1949–54. Epub 2000/06/23. PMID: 10863595.
17. Enneking WF, Burchardt H, Puhl JJ, Piotrowski G. Physical and biological aspects of repair in dog cortical-bone transplants. *The Journal of bone and joint surgery American volume*. 1975; 57(2):237–52. Epub 1975/03/01. PMID: 1089671.

18. Kolar P, Gaber T, Perka C, Duda GN, Buttgerit F. Human early fracture hematoma is characterized by inflammation and hypoxia. *Clin Orthop Relat Res*. 2011; 469(11):3118–26. Epub 2011/03/17. <https://doi.org/10.1007/s11999-011-1865-3> PMID: 21409457; PubMed Central PMCID: PMC3183184.
19. Schmidt-Bleek K, Schell H, Kolar P, Pfaff M, Perka C, Buttgerit F, et al. Cellular composition of the initial fracture hematoma compared to a muscle hematoma: a study in sheep. *Journal of orthopaedic research: official publication of the Orthopaedic Research Society*. 2009; 27(9):1147–51. Epub 2009/04/22. <https://doi.org/10.1002/jor.20901> PMID: 19382195.
20. Martini L, Fini M, Giavaresi G, Giardino R. Sheep model in orthopedic research: a literature review. *Comparative medicine*. 2001; 51(4):292–9. Epub 2002/04/02. PMID: 11924786.
21. Holstein JH, Garcia P, Histing T, Kristen A, Scheuer C, Menger MD, et al. Advances in the establishment of defined mouse models for the study of fracture healing and bone regeneration. *Journal of orthopaedic trauma*. 2009; 23(5 Suppl):S31–8. Epub 2009/04/29. <https://doi.org/10.1097/BOT.0b013e31819f27e5> PMID: 19390374.
22. Seok J, Warren HS, Cuenca AG, Mindrinos MN, Baker HV, Xu W, et al. Genomic responses in mouse models poorly mimic human inflammatory diseases. *Proceedings of the National Academy of Sciences of the United States of America*. 2013; 110(9):3507–12. Epub 2013/02/13. <https://doi.org/10.1073/pnas.1222878110> PMID: 23401516; PubMed Central PMCID: PMC3587220.
23. Pearce AI, Richards RG, Milz S, Schneider E, Pearce SG. Animal models for implant biomaterial research in bone: a review. *European cells & materials*. 2007; 13:1–10. Epub 2007/03/06. PMID: 17334975.
24. Marsell R, Einhorn TA. The biology of fracture healing. *Injury*. 2011; 42(6):551–5. Epub 04/13. <https://doi.org/10.1016/j.injury.2011.03.031> PMID: 21489527.
25. Hoff P, Gaber T, Strehl C, Jakstadt M, Hoff H, Schmidt-Bleek K, et al. A Pronounced Inflammatory Activity Characterizes the Early Fracture Healing Phase in Immunologically Restricted Patients. *International journal of molecular sciences*. 2017; 18(3). Epub 2017/03/12. <https://doi.org/10.3390/ijms18030583> PMID: 28282868; PubMed Central PMCID: PMC5372599.
26. Klenke S, Renckhoff K, Engler A, Peters J, Frey UH. Easy-to-use strategy for reference gene selection in quantitative real-time PCR experiments. *Naunyn-Schmiedeberg's archives of pharmacology*. 2016; 389(12):1353–66. Epub 2016/09/22. <https://doi.org/10.1007/s00210-016-1305-8> PMID: 27650728.
27. Baddela VS, Baufeld A, Yenuganti VR, Vanselow J, Singh D. Suitable housekeeping genes for normalization of transcript abundance analysis by real-time RT-PCR in cultured bovine granulosa cells during hypoxia and differential cell plating density. *Reproductive biology and endocrinology: RB&E*. 2014; 12:118. Epub 2014/11/29. <https://doi.org/10.1186/1477-7827-12-118> PMID: 25430436; PubMed Central PMCID: PMC4280684.
28. Kawamoto T, Kawamoto K. Preparation of thin frozen sections from nonfixed and undecalcified hard tissues using Kawamoto's film method (2012). *Methods in molecular biology (Clifton, NJ)*. 2014; 1130:149–64. Epub 2014/02/01. https://doi.org/10.1007/978-1-62703-989-5_11 PMID: 24482171.
29. Dominici M, Le Blanc K, Mueller I, Slaper-Cortenbach I, Marini FC, Krause DS, et al. Minimal criteria for defining multipotent mesenchymal stromal cells. The International Society for Cellular Therapy position statement. *Cytotherapy*. 2006; 8(4):315–7. <https://doi.org/10.1080/14653240600855905> WOS:000239953200002. PMID: 16923606
30. Pittenger MF, Mackay AM, Beck SC, Jaiswal RK, Douglas R, Mosca JD, et al. Multilineage potential of adult human mesenchymal stem cells. *Science*. 1999; 284(5411):143–7. <https://doi.org/10.1126/science.284.5411.143> WOS:000079509000053. PMID: 10102814
31. De Schauwer C, van de Walle GR, Piepers S, Hoogewijs MK, Govaere JL, Meyer E, et al. Successful isolation of equine mesenchymal stromal cells from cryopreserved umbilical cord blood-derived mononuclear cell fractions. *Equine veterinary journal*. 2013; 45(4):518–22. Epub 2012/12/05. <https://doi.org/10.1111/evj.12003> PMID: 23206252.
32. Maia L, Landim-Alvarenga FC, Da Mota LS, De Assis Golim M, Laufer-Amorim R, De Vita B, et al. Immunophenotypic, immunocytochemistry, ultrastructural, and cytogenetic characterization of mesenchymal stem cells from equine bone marrow. *Microscopy research and technique*. 2013; 76(6):618–24. Epub 2013/03/28. <https://doi.org/10.1002/jemt.22208> PMID: 23533133.
33. Radtke CL, Nino-Fong R, Gonzalez BPE, Stryhn H, McDuffee LA. Characterization and osteogenic potential of equine muscle tissue- and periosteal tissue-derived mesenchymal stem cells in comparison with bone marrow- and adipose tissue derived mesenchymal stem cells. *American journal of veterinary research*. 2013; 74(5):790–800. WOS:000318203500017. <https://doi.org/10.2460/ajvr.74.5.790> PMID: 23627394
34. Ranera B, Remacha AR, Alvarez-Arguedas S, Romero A, Vazquez FJ, Zaragoza P, et al. Effect of hypoxia on equine mesenchymal stem cells derived from bone marrow and adipose tissue. *BMC veterinary*

- research. 2012; 8:142. Epub 2012/08/24. <https://doi.org/10.1186/1746-6148-8-142> PMID: [22913590](https://pubmed.ncbi.nlm.nih.gov/22913590/); PubMed Central PMCID: [PMC4055040](https://pubmed.ncbi.nlm.nih.gov/PMC4055040/); PMCPMC3483288.
35. Barberini DJ, Freitas NPP, Magnoni MS, Maia L, Listoni AJ, Heckler MC, et al. Equine mesenchymal stem cells from bone marrow, adipose tissue and umbilical cord: immunophenotypic characterization and differentiation potential. *Stem Cell Research & Therapy*. 2014; 5(1):25–. <https://doi.org/10.1186/scrt414> PMC4055040. PMID: [24559797](https://pubmed.ncbi.nlm.nih.gov/24559797/)
 36. Paebst F, Piehler D, Brehm W, Heller S, Schroeck C, Tarnok A, et al. Comparative immunophenotyping of equine multipotent mesenchymal stromal cells: an approach toward a standardized definition. *Cytometry Part A: the journal of the International Society for Analytical Cytology*. 2014; 85(8):678–87. Epub 2014/06/05. <https://doi.org/10.1002/cyto.a.22491> PMID: [24894974](https://pubmed.ncbi.nlm.nih.gov/24894974/).
 37. Treonze KM, Alves K, Fischer P, Hagmann WK, Hora D, Kulick A, et al. Characterization of alpha(4) beta(1) (CD49d/CD29) on equine leukocytes: potential utility of a potent alpha(4)beta(1) (CD49d/CD29) receptor antagonist in the treatment of equine heaves (recurrent airway obstruction). *Veterinary immunology and immunopathology*. 2009; 130(1–2):79–87. Epub 2009/03/03. <https://doi.org/10.1016/j.vetimm.2009.01.011> PMID: [19250687](https://pubmed.ncbi.nlm.nih.gov/19250687/).
 38. De Schauwer C, Piepers S, Van de Walle GR, Demeyere K, Hoogewijs MK, Govaere JL, et al. In search for cross-reactivity to immunophenotype equine mesenchymal stromal cells by multicolor flow cytometry. *Cytometry Part A: the journal of the International Society for Analytical Cytology*. 2012; 81(4):312–23. Epub 2012/03/14. <https://doi.org/10.1002/cyto.a.22026> PMID: [2241893](https://pubmed.ncbi.nlm.nih.gov/2241893/).
 39. Yeo WM, Osterrieder N, Stokol T. Equine herpesvirus type 1 infection induces procoagulant activity in equine monocytes. *Veterinary research*. 2013; 44:16. Epub 2013/03/19. <https://doi.org/10.1186/1297-9716-44-16> PMID: [23497076](https://pubmed.ncbi.nlm.nih.gov/23497076/); PubMed Central PMCID: [PMCPMC3618259](https://pubmed.ncbi.nlm.nih.gov/PMC4055040/).
 40. Keramaris NC, Kaptanis S, Moss HL, Loppini M, Pneumaticos S, Maffulli N. Endothelial progenitor cells (EPCs) and mesenchymal stem cells (MSCs) in bone healing. *Current stem cell research & therapy*. 2012; 7(4):293–301. Epub 2012/05/09. PMID: [22563666](https://pubmed.ncbi.nlm.nih.gov/22563666/).
 41. Knight MN, Hankenson KD. Mesenchymal Stem Cells in Bone Regeneration. *Adv Wound Care (New Rochelle)*. 2013; 2(6):306–16. Epub 2014/02/15. <https://doi.org/10.1089/wound.2012.0420> PMID: [24527352](https://pubmed.ncbi.nlm.nih.gov/24527352/); PubMed Central PMCID: [PMCPMC3842877](https://pubmed.ncbi.nlm.nih.gov/PMC4055040/).
 42. Kovach TK, Dighe AS, Lobo PI, Cui Q. Interactions between MSCs and immune cells: implications for bone healing. *Journal of immunology research*. 2015; 2015:752510. Epub 2015/05/23. <https://doi.org/10.1155/2015/752510> PMID: [26000315](https://pubmed.ncbi.nlm.nih.gov/26000315/); PubMed Central PMCID: [PMCPMC4427002](https://pubmed.ncbi.nlm.nih.gov/PMC4055040/).
 43. Wagegg M, Gaber T, Lohanatha FL, Hahne M, Strehl C, Fangradt M, et al. Hypoxia promotes osteogenesis but suppresses adipogenesis of human mesenchymal stromal cells in a hypoxia-inducible factor-1 dependent manner. *PloS one*. 2012; 7(9):e46483. Epub 2012/10/03. <https://doi.org/10.1371/journal.pone.0046483> PMID: [23029528](https://pubmed.ncbi.nlm.nih.gov/23029528/); PubMed Central PMCID: [PMCPMC3459928](https://pubmed.ncbi.nlm.nih.gov/PMC4055040/).
 44. Kovtun A, Bergdolt S, Wiegner R, Radermacher P, Huber-Lang M, Ignatius A. The crucial role of neutrophil granulocytes in bone fracture healing. *European cells & materials*. 2016; 32:152–62. Epub 2016/07/28. PMID: [27452963](https://pubmed.ncbi.nlm.nih.gov/27452963/).
 45. Groggaard B, Gerdin B, Reikeras O. THE POLYMORPHONUCLEAR LEUKOCYTE—HAS IT A ROLE IN FRACTURE-HEALING. *Arch Orthop Trauma Surg*. 1990; 109(5):268–71. <https://doi.org/10.1007/bf00419942> WOS:A1990DV58200007. PMID: [2271360](https://pubmed.ncbi.nlm.nih.gov/2271360/)
 46. Chung R, Cool JC, Scherer MA, Foster BK, Xian CJ. Roles of neutrophil-mediated inflammatory response in the bony repair of injured growth plate cartilage in young rats. *Journal of leukocyte biology*. 2006; 80(6):1272–80. Epub 2006/09/09. <https://doi.org/10.1189/jlb.0606365> PMID: [16959896](https://pubmed.ncbi.nlm.nih.gov/16959896/).
 47. Hoff P, Maschmeyer P, Gaber T, Schutze T, Raue T, Schmidt-Bleek K, et al. Human immune cells' behavior and survival under bioenergetically restricted conditions in an *in vitro* fracture hematoma model. *Cellular & molecular immunology*. 2013; 10(2):151–8. Epub 2013/02/12. <https://doi.org/10.1038/cmi.2012.56> PMID: [23396474](https://pubmed.ncbi.nlm.nih.gov/23396474/); PubMed Central PMCID: [PMCPMC4003042](https://pubmed.ncbi.nlm.nih.gov/PMC4055040/).
 48. Soehnlein O, Lindbom L, Weber C. Mechanisms underlying neutrophil-mediated monocyte recruitment. *Blood*. 2009; 114(21):4613–23. Epub 2009/08/22. <https://doi.org/10.1182/blood-2009-06-221630> PMID: [19696199](https://pubmed.ncbi.nlm.nih.gov/19696199/).
 49. Toben D, Schroeder I, El Khassawna T, Mehta M, Hoffmann JE, Frisch JT, et al. Fracture Healing Is Accelerated in the Absence of the Adaptive Immune System. *J Bone Miner Res*. 2011; 26(1):113–24. <https://doi.org/10.1002/jbmr.185> WOS:000286035600014. PMID: [20641004](https://pubmed.ncbi.nlm.nih.gov/20641004/)
 50. Reinke S, Geissler S, Taylor WR, Schmidt-Bleek K, Juelke K, Schwachmeyer V, et al. Terminally differentiated CD8(+) T cells negatively affect bone regeneration in humans. *Science translational medicine*. 2013; 5(177):177ra36. Epub 2013/03/22. <https://doi.org/10.1126/scitranslmed.3004754> PMID: [23515078](https://pubmed.ncbi.nlm.nih.gov/23515078/).
 51. de Silly RV, Ducimetiere L, Maroun CY, Dietrich PY, Derouazi M, Walker PR. Phenotypic switch of CD8 (+) T cells reactivated under hypoxia toward IL-10 secreting, poorly proliferative effector cells. *Eur J*

- Immunol. 2015; 45(8):2263–75. <https://doi.org/10.1002/eji.201445284> WOS:000359674200012. PMID: [25929785](https://pubmed.ncbi.nlm.nih.gov/25929785/)
52. De Miguel MP, Fuentes-Julian S, Blazquez-Martinez A, Pascual CY, Aller MA, Arias J, et al. Immunosuppressive properties of mesenchymal stem cells: advances and applications. *Current molecular medicine*. 2012; 12(5):574–91. Epub 2012/04/21. PMID: [22515979](https://pubmed.ncbi.nlm.nih.gov/22515979/).
 53. Faiella W, Atoui R. Immunotolerant Properties of Mesenchymal Stem Cells: Updated Review. *Stem cells international*. 2016; 2016:1859567. Epub 2016/02/04. <https://doi.org/10.1155/2016/1859567> PMID: [26839557](https://pubmed.ncbi.nlm.nih.gov/26839557/); PubMed Central PMCID: PMC4709780.
 54. Duffy MM, Ritter T, Ceredig R, Griffin MD. Mesenchymal stem cell effects on T-cell effector pathways. *Stem Cell Res Ther*. 2011; 2(4):34. Epub 2011/08/25. <https://doi.org/10.1186/scrt75> PMID: [21861858](https://pubmed.ncbi.nlm.nih.gov/21861858/); PubMed Central PMCID: PMC3219065.
 55. Nauta AJ, Fibbe WE. Immunomodulatory properties of mesenchymal stromal cells. *Blood*. 2007; 110(10):3499–506. Epub 2007/08/01. <https://doi.org/10.1182/blood-2007-02-069716> PMID: [17664353](https://pubmed.ncbi.nlm.nih.gov/17664353/).
 56. Potian JA, Aviv H, Ponzio NM, Harrison JS, Rameshwar P. Veto-like activity of mesenchymal stem cells: functional discrimination between cellular responses to alloantigens and recall antigens. *Journal of immunology (Baltimore, Md: 1950)*. 2003; 171(7):3426–34. Epub 2003/09/23. PMID: [14500637](https://pubmed.ncbi.nlm.nih.gov/14500637/).
 57. Robey IF, Lien AD, Welsh SJ, Baggett BK, Gillies RJ. Hypoxia-Inducible Factor-1 α and the Glycolytic Phenotype in Tumors. *Neoplasia (New York, NY)*. 2005; 7(4):324–30. PMC1501147.
 58. Ito K, Suda T. Metabolic requirements for the maintenance of self-renewing stem cells. *Nature reviews Molecular cell biology*. 2014; 15(4):243–56. Epub 2014/03/22. <https://doi.org/10.1038/nrm3772> PMID: [24651542](https://pubmed.ncbi.nlm.nih.gov/24651542/); PubMed Central PMCID: PMC4095859.
 59. Gaber T, Dziurla R, Tripmacher R, Burmester GR, Buttgerit F. Hypoxia inducible factor (HIF) in rheumatology: low O₂! See what HIF can do! *Annals of the rheumatic diseases*. 2005; 64(7):971–80. Epub 2005/04/01. <https://doi.org/10.1136/ard.2004.031641> PMID: [15800008](https://pubmed.ncbi.nlm.nih.gov/15800008/); PubMed Central PMCID: PMC1755583.
 60. Semenza GL. Regulation of mammalian O₂ homeostasis by hypoxia-inducible factor 1. Annual review of cell and developmental biology. 1999; 15:551–78. Epub 1999/12/28. <https://doi.org/10.1146/annurev.cellbio.15.1.551> PMID: [10611972](https://pubmed.ncbi.nlm.nih.gov/10611972/).
 61. Liu Y, Berendsen AD, Jia S, Lotinun S, Baron R, Ferrara N, et al. Intracellular VEGF regulates the balance between osteoblast and adipocyte differentiation. *The Journal of clinical investigation*. 2012; 122(9):3101–13. Epub 2012/08/14. <https://doi.org/10.1172/JCI61209> PMID: [22886301](https://pubmed.ncbi.nlm.nih.gov/22886301/); PubMed Central PMCID: PMC3428080.
 62. Berendsen AD, Olsen BR. How vascular endothelial growth factor-A (VEGF) regulates differentiation of mesenchymal stem cells. *The journal of histochemistry and cytochemistry: official journal of the Histochemistry Society*. 2014; 62(2):103–8. Epub 2013/12/07. <https://doi.org/10.1369/0022155413516347> PMID: [24309509](https://pubmed.ncbi.nlm.nih.gov/24309509/); PubMed Central PMCID: PMC3902099.
 63. Kottstorfer J, Kaiser G, Thomas A, Gregori M, Kecht M, Domaszewski F, et al. The influence of non-osteogenic factors on the expression of M-CSF and VEGF during fracture healing. *Injury*. 2013; 44(7):930–4. Epub 2013/04/11. <https://doi.org/10.1016/j.injury.2013.02.028> PMID: [23570706](https://pubmed.ncbi.nlm.nih.gov/23570706/).
 64. Ochman S, Frey S, Raschke MJ, Deventer JN, Meffert RH. Local application of VEGF compensates callus deficiency after acute soft tissue trauma—results using a limb-shortening distraction procedure in rabbit tibia. *Journal of orthopaedic research: official publication of the Orthopaedic Research Society*. 2011; 29(7):1093–8. Epub 2011/02/02. <https://doi.org/10.1002/jor.21340> PMID: [21284032](https://pubmed.ncbi.nlm.nih.gov/21284032/).
 65. Wang CJ, Huang KE, Sun YC, Yang YJ, Ko JY, Weng LH, et al. VEGF modulates angiogenesis and osteogenesis in shockwave-promoted fracture healing in rabbits. *The Journal of surgical research*. 2011; 171(1):114–9. Epub 2010/05/11. <https://doi.org/10.1016/j.jss.2010.01.045> PMID: [20452608](https://pubmed.ncbi.nlm.nih.gov/20452608/).
 66. Schmidt-Bleek K, Schell H, Lienau J, Schulz N, Hoff P, Pfaff M, et al. Initial immune reaction and angiogenesis in bone healing. *Journal of tissue engineering and regenerative medicine*. 2014; 8(2):120–30. Epub 2012/04/13. <https://doi.org/10.1002/term.1505> PMID: [22495762](https://pubmed.ncbi.nlm.nih.gov/22495762/).
 67. Kobayashi T, Onodera S, Kondo E, Tohyama H, Fujiki H, Yokoyama A, et al. Impaired fracture healing in macrophage migration inhibitory factor-deficient mice. *Osteoporosis international: a journal established as result of cooperation between the European Foundation for Osteoporosis and the National Osteoporosis Foundation of the USA*. 2011; 22(6):1955–65. Epub 2010/09/15. <https://doi.org/10.1007/s00198-010-1385-0> PMID: [20838768](https://pubmed.ncbi.nlm.nih.gov/20838768/).
 68. Onodera S, Nishihira J, Yamazaki M, Ishibashi T, Minami A. Increased expression of macrophage migration inhibitory factor during fracture healing in rats. *Histochemistry and cell biology*. 2004; 121(3):209–17. Epub 2004/02/10. <https://doi.org/10.1007/s00418-004-0624-x> PMID: [14767776](https://pubmed.ncbi.nlm.nih.gov/14767776/).
 69. Liu CH, Hwang SM. Cytokine interactions in mesenchymal stem cells from cord blood. *Cytokine*. 2005; 32(6):270–9. Epub 2005/12/27. <https://doi.org/10.1016/j.cyto.2005.11.003> PMID: [16377203](https://pubmed.ncbi.nlm.nih.gov/16377203/).

70. Xia W, Xie C, Jiang M, Hou M. Improved survival of mesenchymal stem cells by macrophage migration inhibitory factor. *Molecular and cellular biochemistry*. 2015; 404(1–2):11–24. Epub 2015/02/24. <https://doi.org/10.1007/s11010-015-2361-y> PMID: [25701358](https://pubmed.ncbi.nlm.nih.gov/25701358/); PubMed Central PMCID: PMC4544672.

2.3 Development of a human *in vitro* fracture gap model

Based on this initial study using equine *in vitro* fracture hematoma models, we successfully transferred this concept to the human system [92] which was further extended to a fracture gap model.

The following text is based on the abstract of the work:

Pfeiffenberger, M., Damerau, A., Ponomarev, I., Bucher, C.H., Chen, Y., Barnewitz, D., Thöne-Reineke, C., Hoff, P., Buttgereit, F., Gaber, T., **Lang, A.** (2021) Functional scaffold-free bone equivalents induce osteogenic and angiogenic processes in a human *in vitro* fracture hematoma model. *Journal of Bone Mineral Research*. Jun 01; 26(6): 1189–1201. [doi: 10.1002/jbmr.4267]

The interaction between the bone and immune cells plays a crucial role in bone pathologies such as disturbed fracture healing. After a trauma, the initially formed fracture hematoma in the fracture gap contains all important components (immune/stem cells, mediators) to directly induce bone regeneration and is therefore of great importance but most susceptible to negative influences. Since common bioengineering approaches exclude the immune component, we introduce an in vitro 3D fracture gap model which combines a fracture hematoma model (FH) with scaffold-free bone-like constructs (SFBCs). The FH consist of human peripheral blood (immune cells) and bone marrow-derived mesenchymal stromal cells (MSCs). SFBCs were produced from MSCs using a macroscale mesenchymal condensation approach. Characterization of the SFBCs revealed permeating mineralization as indicated by increased bone volume and expression of osteogenic markers. Co-cultivation of the SFBC and the FH for 48h showed the osteoinductive capacity of the SFBCs and therefore, provides evidence for biological functionality. The in vitro 3D fracture gap model provides essential osteogenic cues to induce the initial bone healing processes. In order to stratify the model, deferoxamine (DFO) was applied, which promoted hypoxia-adaptive, osteogenic and angiogenic processes. Thus, we were able to distinctly mimic key processes of the initial fracture phase and demonstrated the importance of including the crosstalk between bone and immune cells for preclinical studies.

To achieve a macroscale approach to create scaffold-free constructs, we used our understanding of developmental biology using mesenchymal condensation (self-organization). This approach is not exclusive to bone tissue engineering but also holds great promise for cartilage development.

Functional Scaffold-Free Bone Equivalents Induce Osteogenic and Angiogenic Processes in a Human In Vitro Fracture Hematoma Model

Moritz Pfeiffenberger,^{1,2} Alexandra Damerou,^{1,2} Igor Ponomarev,³ Christian H Bucher,^{4,5} Yuling Chen,^{1,2} Dirk Barnewitz,³ Christa Thöne-Reineke,⁶ Paula Hoff,^{1,7} Frank Buttgerit,^{1,2,4} Timo Gaber,^{1,2,4} and Annemarie Lang^{1,2,4}

¹Department of Rheumatology and Clinical Immunology, Charité – Universitätsmedizin Berlin, Corporate Member of Freie Universität Berlin, Humboldt-Universität zu Berlin, and Berlin Institute of Health, Berlin, Germany

²German Rheumatism Research Centre (DRFZ) Berlin, a Leibniz Institute, Berlin, Germany

³Research Center of Medical Technology and Biotechnology, Bad Langensalza, Germany

⁴Charité – Universitätsmedizin Berlin, Corporate Member of Freie Universität Berlin, Humboldt-Universität zu Berlin, and Berlin Institute of Health, Berlin Institute of Health Center for Regenerative Therapies, Berlin, Germany

⁵Charité – Universitätsmedizin Berlin, Corporate Member of Freie Universität Berlin, Humboldt-Universität zu Berlin, and Berlin Institute of Health, Julius Wolff Institute, Berlin, Germany

⁶Institute of Animal Welfare, Animal Behavior, and Laboratory Animal Science, Department of Veterinary Medicine, Freie Universität Berlin, Berlin, Germany

⁷Endokrinologikum Berlin, MVZ am Gendarmenmarkt, Berlin, Germany

ABSTRACT

After trauma, the formed fracture hematoma within the fracture gap contains all the important components (immune/stem cells, mediators) to initiate bone regeneration immediately. Thus, it is of great importance but also the most susceptible to negative influences. To study the interaction between bone and immune cells within the fracture gap, up-to-date in vitro systems should be capable of recapitulating cellular and humoral interactions and the physicochemical microenvironment (eg, hypoxia). Here, we first developed and characterized scaffold-free bone-like constructs (SFBCs), which were produced from bone marrow-derived mesenchymal stromal cells (MSCs) using a macroscale mesenchymal condensation approach. SFBCs revealed permeating mineralization characterized by increased bone volume (μ CT, histology) and expression of osteogenic markers (*RUNX2*, *SPP1*, *RANKL*). Fracture hematoma (FH) models, consisting of human peripheral blood (immune cells) mixed with MSCs, were co-cultivated with SFBCs under hypoxic conditions. As a result, FH models revealed an increased expression of osteogenic (*RUNX2*, *SPP1*), angiogenic (*MMP2*, *VEGF*), HIF-related (*LDHA*, *PGK1*), and inflammatory (*IL6*, *IL8*) markers after 12 and 48 hours co-cultivation. Osteogenic and angiogenic gene expression of the FH indicate the osteoinductive potential and, thus, the biological functionality of the SFBCs. IL-6, IL-8, GM-CSF, and MIP-1 β were detectable within the supernatant after 24 and 48 hours of co-cultivation. To confirm the responsiveness of our model to modifying substances (eg, therapeutics), we used deferoxamine (DFO), which is well known to induce a cellular hypoxic adaptation response. Indeed, DFO particularly increased hypoxia-adaptive, osteogenic, and angiogenic processes within the FH models but had little effect on the SFBCs, indicating different response dynamics within the co-cultivation system. Therefore, based on our data, we have successfully modeled processes within the initial fracture healing phase in vitro and concluded that the cross-talk between bone and immune cells in the initial fracture healing phase is of particular importance for preclinical studies. © 2021 American Society for Bone and Mineral Research (ASBMR).

KEY WORDS: BIOENGINEERING; FRACTURE HEALING; FRACTURE HEMATOMA; OSTEOIMMUNOLOGY

Received in original form July 24, 2020; revised form January 20, 2021; accepted January 29, 2021. Accepted manuscript online February 3, 2021.

Address correspondence to: Annemarie Lang, PhD, Department of Rheumatology and Clinical Immunology, Charité – Universitätsmedizin Berlin, Corporate Member of Freie Universität Berlin, Humboldt-Universität zu Berlin, and Berlin Institute of Health, Charitéplatz 1, 10117 Berlin, Germany. E-mail: annemarie.lang@charite.de

Additional Supporting Information may be found in the online version of this article.

Journal of Bone and Mineral Research, Vol. 00, No. 00, Month 2021, pp 1–13.

DOI: 10.1002/jbmr.4267

© 2021 American Society for Bone and Mineral Research (ASBMR)

One pathologies such as osteoporosis or disturbed fracture healing lead to pain, immobility, inflexibility, considerable loss of life quality, and even mental illnesses.⁽¹⁾ Traumatic events can result in bone fracturing accompanied by vessel ruptures and the opening of the bone marrow channel. An important event in the initial phase of fracture healing is the formation of the fracture hematoma, which mainly consists of immune and chondro- and osteoprogenitor cells.^(2,3) Negative influences such as medications or comorbidities including diabetes, rheumatoid arthritis, or immunosuppression can lead to dysregulation within the inflammatory phase of fracture healing and to impairments within the following regeneration process.^(4,5) Recent treatment strategies have achieved high-technology standards with regard to fixation systems such as plates or implants, regenerative approaches using autologous bone graft (gold standard), or the additional application of stem cells and/or growth factors.⁽⁶⁾ Therefore, preclinical studies are highly needed to tackle the unmet clinical need, especially with respect to an aging population and the increase of comorbidities.

The surgical removal of the fracture hematoma results in a prolonged healing process, whereas transplantation in an ectopic location leads to endochondral bone formation at the implantation site.⁽⁷⁾ Formation of the fracture hematoma and the constricted interplay of pro- and anti-inflammatory processes are considered as the starting point of bone regeneration.⁽⁸⁾ Because the bone marrow cavity is opened during the fracture, the bone marrow acts as a resource for immune cells as well as chondro- and osteoprogenitor cells such as mesenchymal stromal cells (MSCs). Therefore, it can be hypothesized that osteogenic induction within the fracture gap is directly induced and controlled by signals from bone components in the vicinity of the fracture gap.^(9,10) Hence, the cross-talk between immune cells from peripheral blood (after vessel rupture) and the bone marrow and osteoprogenitor cells is essential and needs to be considered in preclinical studies.⁽¹¹⁾ Today's gold standard of preclinical drug, compound screening, and risk assessment is the use of animal models—mainly rodents (mice and rats)—which is in accordance with most national legal requirements. Nevertheless, trans-species differences may be responsible for the limited transferability of findings to the human patient.⁽¹²⁾ Mimicking the in-patient situation in preclinical studies is highly encouraged and evading cross-species differences by novel in vitro approaches is of great interest. During the past decades, conventional in vitro cell culture systems have been revised and improved to provide more physiological and human-relevant features. Furthermore, the rapid technical evolution allocating sophisticated biomaterials, bioreactors, and microfluidic platforms allows the development of innovative human-relevant in vitro systems as alternative or predictive support to animal testing.⁽¹³⁾

Current in vitro systems focus on mimicking bone development, endochondral ossification, or the bone homeostasis itself by using spheroids, scaffold-based, or scaffold-free model systems.⁽¹³⁾ Common cell sources are either primary bone-related cells such as osteoblasts, osteocytes, osteoclasts, or MSCs as progenitor cells.^(13,14) To mimic fracture healing, models mainly focus on later stages of the regeneration processes, particularly endochondral ossification or remodeling.⁽¹⁵⁾ We have previously described the development of a fracture hematoma model consisting of human whole blood and a certain amount of human (h)

MSCs.⁽¹⁶⁾ However, to study the initiated processes in an interconnected manner and more adequate experimental setting, the combination of the bone components with the fracture hematoma (immune component) remains elusive.

Within our study, we have developed and characterized scaffold-free bone-like constructs (SFBCs) based on mesenchymal condensation, which exceeded the dimensions of spheroids. These SFBCs were co-cultivated with in vitro fracture hematoma (FH) models (i) to confirm the biological functionality of the SFBCs, and (ii) to recapitulate certain aspects of the initial phase of fracture healing allowing cell–cell interactions (immune and bone cells) and providing an adequate microenvironment (hypoxia).

Materials and Methods

Bone marrow-derived MSC isolation, cultivation, and characterization

Human mesenchymal stromal cells (hMSC; $n = 12$) were isolated from bone marrow of patients undergoing total hip replacement (registered and distributed by the “Tissue Harvesting” Core Facility of the Berlin Institute of Health Center for Regenerative Therapies [BCRT]; donor list in Supplemental Table S1). All protocols were approved by the Charité-Universitätsmedizin Ethics Committee and performed according to the Helsinki Declaration (ethical approval EA1/012/13). MSC isolation was performed as described in detail before.⁽¹⁶⁾ Briefly, bone marrow was transferred to a 175 cm² cell culture flask, covered with expansion medium containing DMEM+GlutaMAX (Gibco, ThermoFisher, Waltham, MA, USA), 10 (v/v) % FCS (Biowest, Nuaille, France), 1 (v/v) % penicillin/streptomycin (Gibco, ThermoFisher), 20 (v/v) % StemMACS MSC Expansion Media XF (Miltenyi Biotech, Bergisch Gladbach, Germany), and incubated at 37°C in 5% CO₂ atmosphere (approx. 18% O₂). Medium was changed after 3 to 4 days when cells became adherent. Isolated cells were expanded at 37°C, 5% CO₂. Medium exchange was performed weekly and passaging with Trypsin–EDTA (Gibco, ThermoFisher) was conducted at a cellular confluency of 80% to 90%. For characterization, MSCs were evaluated at passage 3 for their differentiation potential (osteogenic, adipogenic) and the presence and absence of specific cell surface markers (MSC Phenotyping Kit, Miltenyi Biotech) as described in detail before.⁽¹⁶⁾

Fabrication of the 3D bone-like scaffold-free constructs (SFBCs)

SFBCs were produced based on a patented protocol (patent no. EP1550716B1), which was modified by applying osteogenic medium to induce osteogenic differentiation after 1 week and no application of biomechanical loading to avoid matrix destruction. The osteogenic medium for generation and maturation contained DMEM/F-12, 10% (v/v) FCS, 1% (v/v) streptomycin/penicillin, 10 mM β -glycerophosphate, and 10 nM dexamethasone (all Sigma-Aldrich, St. Louis, MO, USA). Approx. 10 to 20 $\times 10^5$ hMSC/cm² (passage 3 to 4) were cultivated in expansion medium until reaching confluency and forming a closed monolayer. The cells were detached and centrifuged at 350g for 15 minutes at room temperature. Afterward, the resulting cell aggregates were cultivated for up to 1 week with medium exchange every day. Cell aggregates were then transferred to a 6-well plate and cultured for up to 12 weeks, enabling a

permeating mineralization of the SFBCs until performing characterization or co-cultivation with the FH model.

Generation of FH and co-cultivation

Human EDTA blood ($n = 3$) was collected from healthy donors with written consent.⁽¹⁶⁾ The FH models were generated as described previously.⁽¹⁶⁾ In brief, 2.5×10^5 hMSCs were resuspended in 100 μ L of EDTA-blood and subsequently mixed with a 10 mM CaCl_2 solution (solved in PBS). The resulting coagulate is referred to as FH. After an incubation time of 30 minutes at 37°C, 5% CO_2 , the FH were placed on a SFBC with direct contact and cultivated in normal medium (NM) containing DMEM+GlutaMAX, 10 (v/v) % FCS, and 1 (v/v) % penicillin/streptomycin. Osteogenic medium components (OMC)—10 mM β -glycerophosphate, 0.1 mM L-ascorbic acid-2-phosphate, and 10 nM dexamethasone—were supplemented for control experiments. For the treatment study, 250 μ M DFO (Sigma-Aldrich) was supplemented to the medium. The generated, combined models were incubated under hypoxic (37°C, 5% CO_2 and $\sim 1\%$ O_2 , flushed with N_2) conditions in a humidified atmosphere for up to 48 hours.

In vitro micro-computed tomography (μ CT)

SFBCs were scanned at a nominal resolution of 8 μ m, with a Sky-Scan 1172 high-resolution microCT (Bruker, Kontich, Belgium). X-ray tube voltage was set at 80 kV, 124 μ A with maximized power of 10 W, and a 0.5 mm aluminum filter was employed to reduce beam hardening effects. The scan orbit was 360° with a rotation step of 0.2°. For reconstruction, the Bruker NRecon software accelerated by GPU was used, and Gaussian smoothing, ring artifact reduction, misalignment compensation, and beam hardening correction were applied. XY alignment was corrected with a reference scan to determine the thermal shift during scan time. The CTAn software (Bruker) was used to analyze the total volume of interest (VOI) of SFBCs. The threshold for bony tissue was set globally (determined by the Otsu method) and kept constant for all SFBCs. For analysis, we used the bone volume (BV), the bone surface (BS), and the trabecular pattern factor (TbPf)⁽¹⁷⁾ as measured and calculated by the software.

Scanning electron microscopy (SEM)

Samples were fixed with 2.5 (v/v) % glutaraldehyde (fixation for 10 minutes), dehydrated with increasing alcohol concentration 30 (v/v) % to 100 (v/v) % (5 steps), and incubated with 100% hexamethyldisilazane (all Sigma-Aldrich). Subsequently, the samples were transferred to a sample holder, and gold coating was performed with a fine gold coater JFC-1200 (JEOL, Tokyo, Japan). For electron microscopy, the JCM-6000 Plus NeoScope (JEOL) was used for imaging, and high vacuum was adjusted.

Histological stainings

SFBCs were fixed for 6 hours in a 4 (v/v) % paraformaldehyde solution (PFA; Carl Roth, Karlsruhe, Germany) followed by an ascending sucrose solution treatment (10 [w/v] %, 20 [w/v] %, and 30 [w/v] %) for 24 hours, respectively, and afterward cryo-embedded with SCEM medium (Section-lab, Hiroshima, Japan). Slices were produced with a cryotom using cryofilms (Section-lab) and afterward air-dried for 20 minutes and fixed with 4 (v/v) % PFA before every histological or immunohistological staining on a microscope slide. Hematoxylin and eosin (H&E)

staining was performed as described previously.⁽¹⁸⁾ In short, slices were fixed with 4 (v/v) % PFA (10 minutes), washed with distilled water, and stained with Harris's hematoxylin solution (MilliporeSigma, Burlington, MA, USA). Staining was followed by several washing steps, a differentiation step (0.25 [v/v] % concentrated HCl), and a second staining step in 0.2 (w/v) % eosin (Chroma, Waldeck, Munster, Germany). Staining was finished by differentiation in 96 (v/v) % and 100 (v/v) % ethanol, fixation with xylol, and covering with Vitro-Clud (R. Langenbrinck GmbH, Emmendingen, Germany). Alizarin Red S staining was conducted by applying slices after fixation and washing to the 2 (w/v) % Alizarin red S staining solution (Sigma-Aldrich; pH 4.1–4.3) for 10 minutes. Afterward, slices were washed in distilled water and differentiation was performed in 0.1 (v/v) % HCL solved in ethanol and fixed by washing two times with 100% ethanol before xylol fixation and covering. Von Kossa staining was conducted according to the following protocol: air drying, fixation, and washing as described above, 3% (w/v) silver nitrate solution (10 minutes), washing step with distilled water, sodium carbonate formaldehyde solution (2 minutes), washing step with tap water, 5% (w/v) sodium thiosulphate solution (5 minutes), washing step with tap water and distilled water, ascending ethanol series (70 [v/v] % to 100 [v/v] %), fixation in xylol, and covering. For Col I, II, and ALP staining, slices were rehydrated with phosphate-buffered saline (PBS) treated with 3 (v/v) % H_2O_2 (30 minutes), washed with PBS, blocked with 5% normal horse or goat serum (Vector Laboratories, Burlingame, CA, USA) in 2 (w/v) % bovine serum albumin (BSA), and incubated overnight with primary antibodies at 4°C (Col I antibody: ab6308, 1:500, Abcam [Cambridge, UK]; Col II antibody, 1:10, Quartett Immunodiagnostika [Berlin, Germany]; ALP antibody, ab95462, Abcam). Afterward, slices were washed and treated with 2 (v/v) % secondary antibody (biotinylated horse anti-mouse IgG antibody – Col I and Col II; biotinylated goat anti-rabbit IgG antibody – ALP, Vector Laboratories) diluted in 2 (v/v) % normal horse/goat serum/2 (v/v) % BSA/PBS (30 minutes), washed with PBS, incubated with avidin-biotin complex (Vectastain Elite ABC HRP Kit, Vector Laboratories) (50 minutes), washed with PBS, incubated with DAB under microscopic control with time measurement (DAB peroxidase (HRP) Substrate Kit, Vector Laboratories) and stopped with PBS. For counterstaining, slices were washed with distilled water and stained with Mayer's hematoxylin (Sigma-Aldrich), washed with tap water, and covered with Aquatex (MilliporeSigma). Pictures were taken with the Axioskop 40 optical microscope (Zeiss, Jena, Germany) using the corresponding AxioVision microscopy software. Von Kossa staining was quantified using ImageJ and the threshold tool to mark positive (black) and negative (brown) stained areas.

Immunofluorescence

For the immunofluorescence staining, the slides were rehydrated with PBS and blocked with PBS with 5 (v/v) % FCS for 30 minutes at room temperature. Primary osteopontin antibody (mouse anti-human, Abcam) or osteocalcin (rabbit anti-human, Abcam) was diluted 1:50 in PBS/5 (v/v) % FCS/0.1 (v/v) % Tween 20 and incubated for 2 hours. After washing with PBS/0.1% Tween 20, the secondary antibody (donkey anti-goat A568; Life Technologies/ThermoFisher) was diluted 1:500 in PBS/5 (v/v) % FCS/0.1 (v/v) % Tween 20 and applied for 1 hour. Pictures were taken with a Keyence fluorescence microscope BZ 9000 (Keyence, Osaka, Japan) using the DAPI, TexasRed, and Cy5 channels.

RNA isolation and quantitative PCR (qPCR)

SFBCs were transferred to RLT-buffer (Qiagen, Hilden, Germany) with 1% 2-Mercaptoethanol (Serva Electrophoresis, Heidelberg, Germany) and disrupted using the Qiagen Tissue Ruptor (Qiagen). Total RNA was extracted using the RNeasy Fibrous Tissue Mini Kit (Qiagen) according to the manufacturer's instructions, and the RNA concentration was determined using the Nanodrop ND-1000 (Peqlab, VWR International, Radnor, PA, USA). RNA was stored at -80°C until further processing. For the co-cultivation experiments, the FH and the SFBC models were analyzed separately. RNA from SFBCs was isolated as described above, and cells from the FH were dissociated by using a cell strainer (Corning, Corning, NY, USA) and washing with PBS. After centrifugation for 10 minutes at 300g, the cell pellet was resuspended in 350 μL RLT buffer with 3.5 μL 2-Mercaptoethanol and total RNA was extracted as described above. RNA quality was assessed via Bioanalyzer (Agilent, Santa Clara, CA, USA). cDNA was synthesized by reverse transcription using TaqMan Reverse Transcription Reagents (Applied Biosystems, Carlsbad, CA, USA) using 100 to 400 ng RNA. qPCR was performed using the DyNAmo Flash SYBR Green qPCR Kit (Thermo Fisher Scientific) and the Stratagene Mx3000P (Agilent Technologies). Initial denaturation was for 7 minutes at 98°C . Afterward, 50 cycles with 5 seconds at 98°C , 7 seconds at 56°C , and 9 seconds at 72°C were performed. The melting curve was analyzed by stepwise increasing the temperature from 50°C to 98°C every 30 seconds. All primers were designed with Primer3, verified with NCBI PrimerBlast, purchased from TIB Molbiol (Berlin, Germany), and tested for efficiency beforehand (Supplemental Table S2). *Eukaryotic translation elongation factor 1 alpha 1 (EF1A)* was used as housekeeper gene because it has been previously reported to be stable under normoxic and hypoxic conditions.^(16,19) The $2^{-\Delta\Delta C(t)}$ method was employed to analyze the gene expression data.

Cytokine and chemokine quantification in supernatants

Supernatants were immediately stored at -80°C after 24 and 48 hours of co-cultivation. The concentration (pg/mL) of cytokines and chemokines was determined using multiplex suspension assay (Bio-Rad Laboratories, Hercules, CA, USA) following the manufacturer's instructions. The following cytokines and chemokines (lower detection limit) were measured: IL-1 β (7.55 pg/mL), IL-2 (18.99 pg/mL), IL-4 (4.13 pg/mL), IL-5 (20.29 pg/mL), IL-6 (25.94 pg/mL), IL-7 (16.05 pg/mL), IL-8 (37.9 pg/mL), IL-10 (37.9 pg/mL), IL-13 (7.21 pg/mL), IL-17 (24.44 pg/mL), interferon-gamma (IFN γ , 56.32 pg/mL), tumor necrosis factor-alpha (TNF α , 59.53 pg/mL), monocyte chemoattractant protein-1 (MCP-1, 27.02 pg/mL), macrophage inflammatory protein MIP-1 β (6.27 pg/mL), granulocyte colony-stimulating factor (G-CSF, 50.98 pg/mL), and granulocyte-macrophage colony-stimulating factor (GM-CSF, 11.82 pg/mL).

Statistical analysis

Statistical tests were performed using GraphPad (La Jolla, CA, USA) Prism Software version 8. Statistical differences towards a hypothetical value were determined by the Wilcoxon signed rank test (unpaired). With respect to the co-cultivation studies, differences between two groups were determined with the Wilcoxon matched-pairs signed rank test, the Mann-Whitney test, or between more groups with the Kruskal-Wallis test with Dunn's multiple comparisons test. Probability values of $p < .05$

were considered to be statistically significant (exact p values are indicated in the figures). Details on the statistics per figure are displayed in the Supplemental Information.

Results

SFBCs are characterized by permeating mineralization

In a first step, we wanted to know if it is possible to employ mesenchymal condensation as a macroscale approach with consistent 3D self-organization and permeating mineralization. Thus, SFBCs were generated by hMSC condensation and treatment with osteogenic medium until analysis at week 12 (Fig. 1A). Macroscopic observation indicated comparable generation of SFBCs from different hMSC donors with a diameter of approx. 1 cm and a thickness of 0.5 cm (Fig. 1B). To verify the mineralization, *in vitro* μCT was performed, showing a consistently high mineralization in the outer area, which was slightly reduced toward the center (Fig. 1C). 3D reconstruction demonstrated the presence of mineralized tissue as indicated by parameters such as bone volume (BV; mean = $5.1 \pm 3.7 \text{ mm}^3$) and bone surface (BS; mean = $276.1 \pm 195.4 \text{ mm}^2$) (Fig. 1D), however with a high standard deviation by means of the bone volume and the bone surface. To quantify the connectedness of the mineralized areas, we additionally examined the trabecular pattern factor (TbPf). This parameter was originally invented to evaluate trabecular bone. Although no osteoclasts were present in the SFBCs and thus the formation of clear trabeculae was not expected, we use this parameter to distinguish between concave (ie, connected) and convex (ie, isolated) structures. Low or even negative values represent hereby high connected tissue, which was found in at least 4 (TbPf < 2) of 9 SFBCs (Fig. 1D). To evaluate the structural morphology of the SFBCs in further detail, we used SEM and found similar morphology when compared with human native cortical/trabecular bone (Fig. 1E, F). In detail, the top view shows strong matrix formation and a closed superficial layer with certain, isolated crystal-like depositions, while the cut face revealed a cancellous-like structure with interconnected mineralized areas. However, the formation of clear trabeculae within the SFBC is not visible when compared with native trabecular bone (Fig. 1F, cut face).

To get a more detailed overview on the matrix composition, assorted histological and immunohistochemical stainings were applied. Cells were homogeneously distributed within the SFBCs as indicated by H&E staining, while Alizarin Red S and von Kossa staining confirmed the deposition of calcium and phosphate, respectively, throughout the tissue (Fig. 2A). Interestingly, SFBCs that showed less von Kossa staining exhibited a more pronounced layer-like structure, while the layers itself were strongly mineralized at the borders (Fig. 2A; lower row). Negative controls were cultivated without osteogenic medium (Fig. 2B). In addition, we observed the expression of *collagen type I* (Col I) and *alkaline phosphatase* (ALP), which are typical markers for osteogenic processes, whereas no Col II, a typical marker of chondrogenesis, was found (Fig. 2C).

SFBCs show profound expression of bone-specific markers

To confirm the previous findings regarding the expression of bone-specific markers, immunofluorescence staining for osteopontin (OPN) and osteocalcin (OC), two non-collagenous bone matrix proteins, were analyzed and yielded the evenly distributed, distinct protein expression (Fig. 3A, B). Although OPN is mainly produced by immature osteoblasts, OC is a marker of

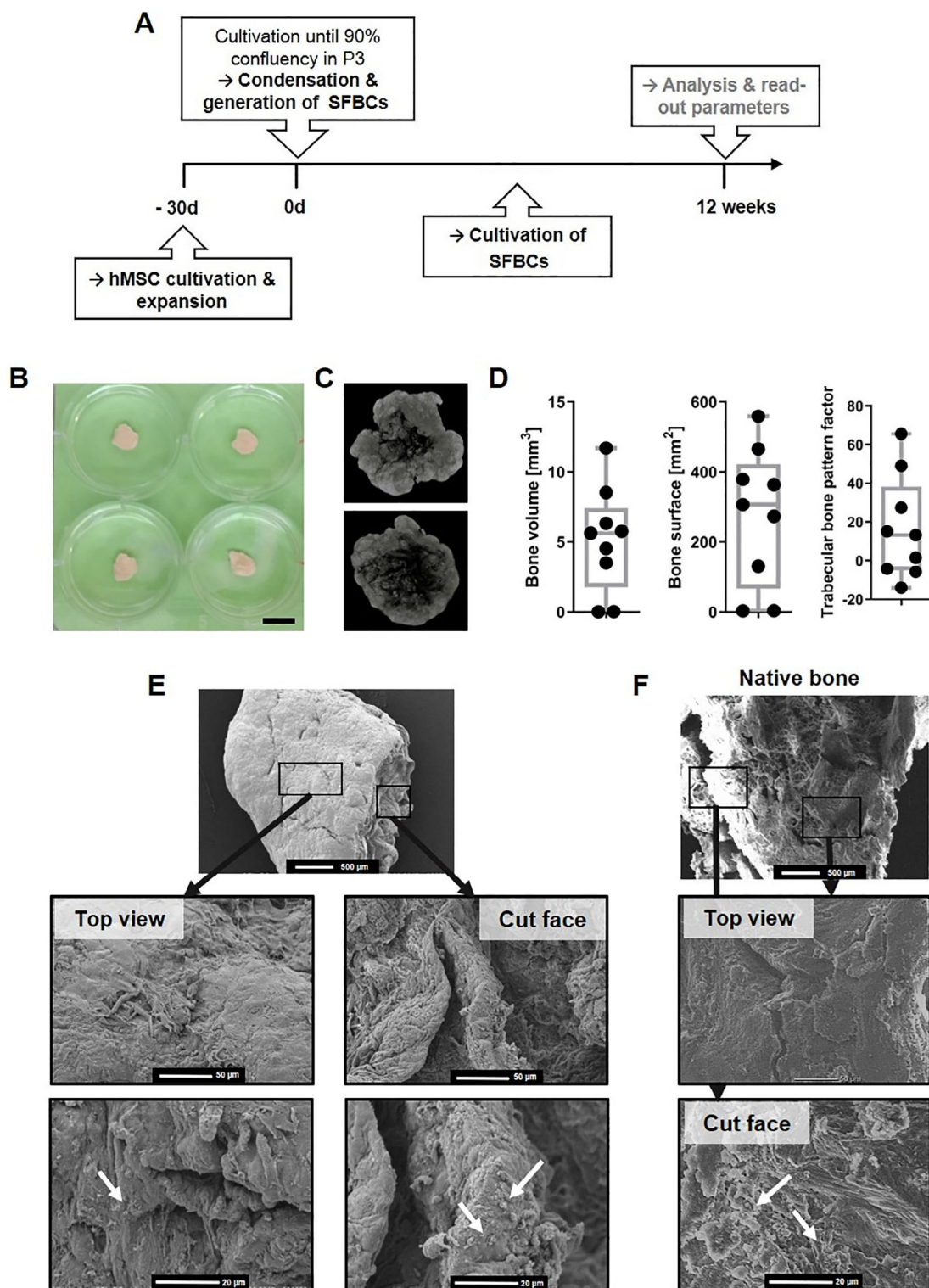


Fig 1. Characterization of the SFBCs with respect to mineralization and structure. (A) Study design. (B) Exemplary images of SFBCs. Scale bar = 1 cm. (C) 3D reconstruction of μ CT. Exemplary images of $n = 9$. (D) Quantitative results from μ CT analysis. Data are shown as box plots with median, interquartile range, max and min values, and all data points. $n = 9$. (E) Structural/morphological examination of the SFBCs in comparison to (F) human native cortical (top view)/trabecular bone (cut face) using scanning electron microscopy. Exemplary images of $n = 3$ SFBCs and $n = 2$ native human bone pieces. Scale bars are indicated in the images. Arrows mark isolated crystal-like depositions.

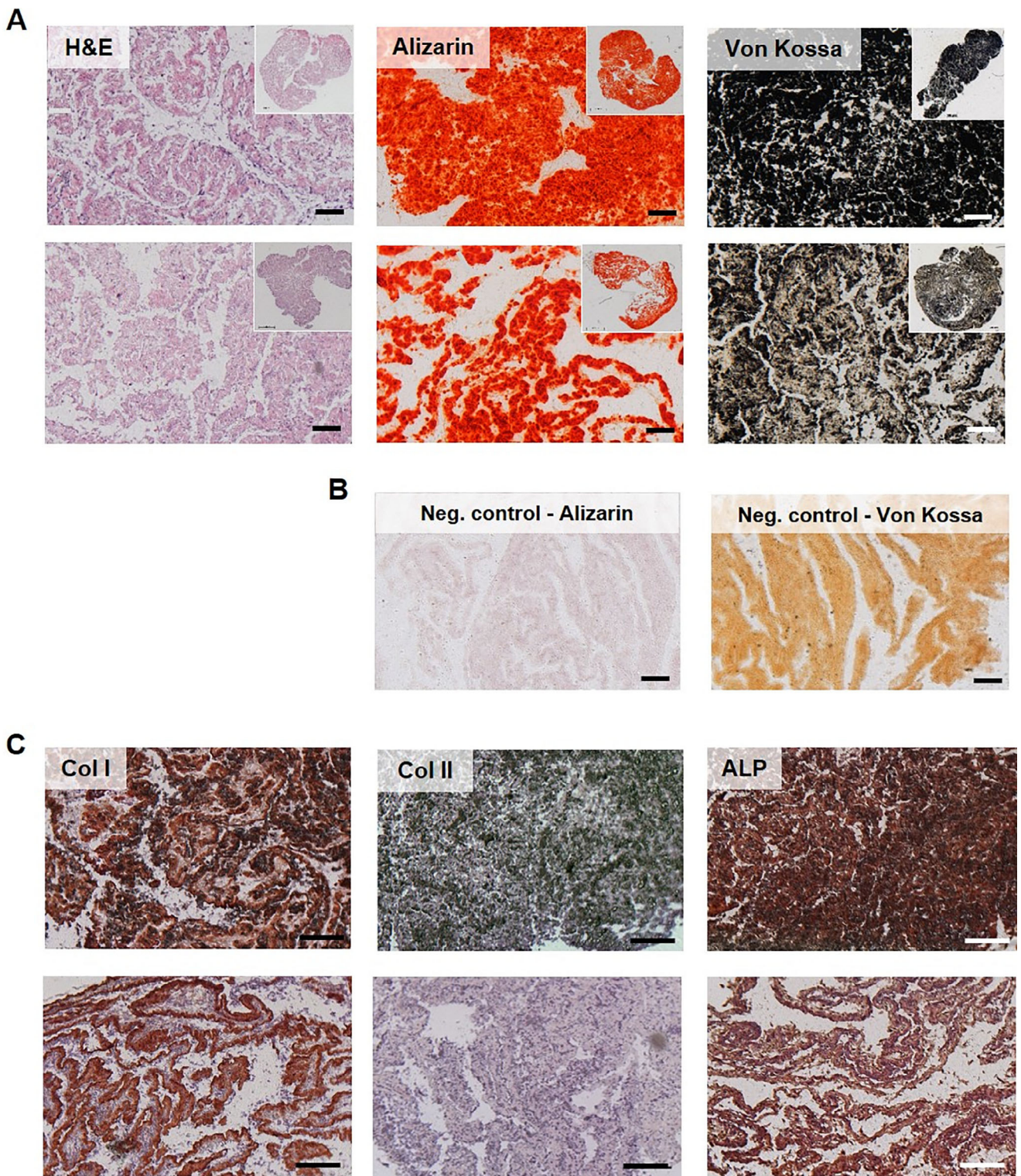


Fig 2. Histological and immunohistochemical examination of the SFBCs. (A) Exemplary images of H&E, Alizarin red staining, and von Kossa stains. Upper row is exemplary for fully calcified SFBCs and lower row for less fully calcified SFBCs. $n = 9$. (B) Negative control for Alizarin red and von Kossa staining. (C) Immunohistochemical stainings for Col I, Col II, and ALP. All scale bars = 200 μm . All images are exemplary for $n = 9$.

late-stage osteoblasts, indicating the presence of different cell states within the SFBCs. mRNA expression analysis showed high levels of osteogenic marker genes such as *secreted*

phosphoprotein 1 (SPP1) and *distal-less homeobox 5 (DLX5)*; Fig. 3C). *SPP1* was significantly higher expressed (10-fold), whereas *DLX5* was higher expressed by trend (8-fold) when

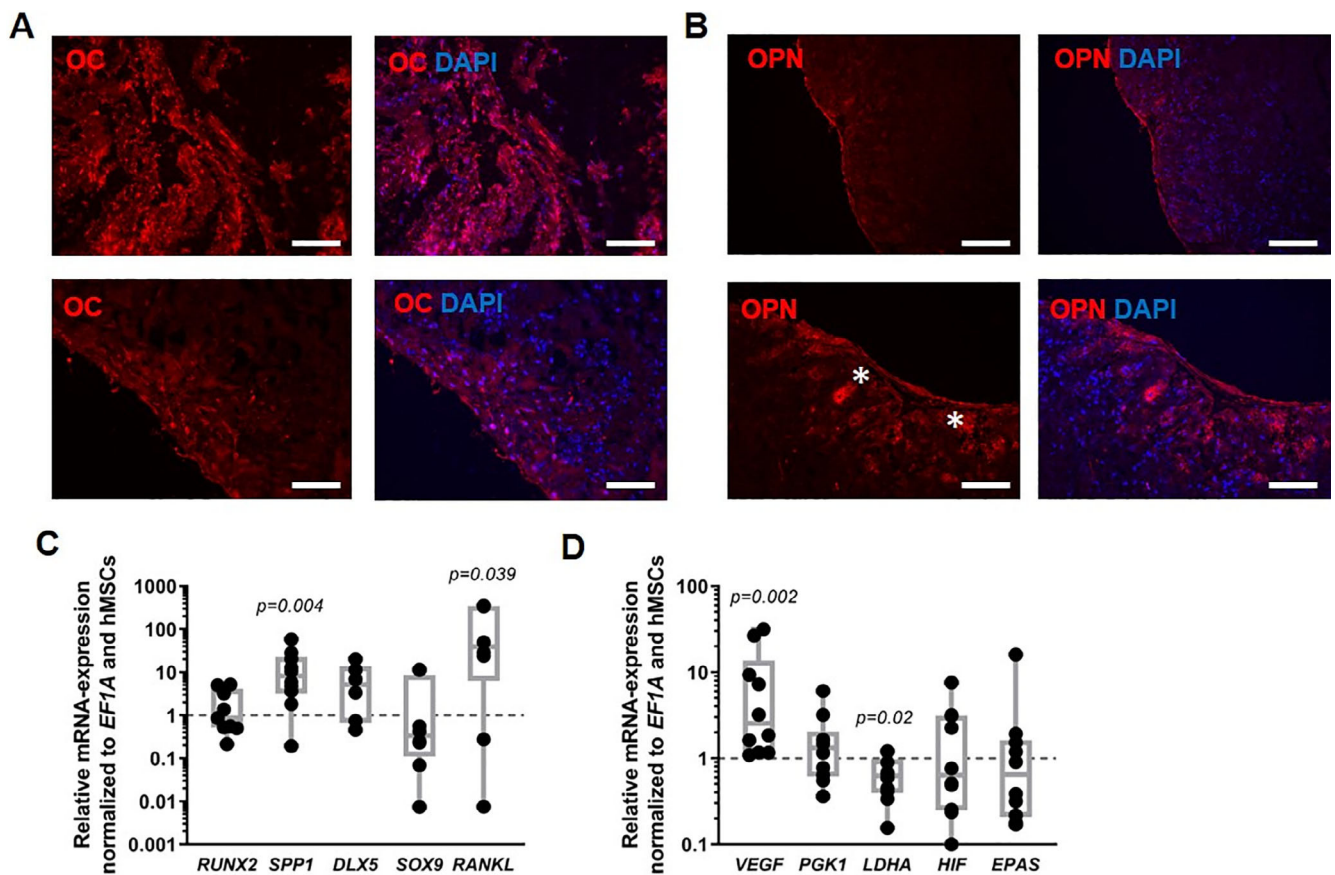


Fig 3. Immunofluorescence and mRNA expression analysis of SFBCs. (A, B) Immunofluorescence staining of osteocalcin (OC; A) and osteopontin (OPN; B). White asterisks highlight cells with high OPN production. To reveal the nuclei of present cells, all slides were counterstained with DAPI. All scale bars = 200 μ m. Images are exemplary for $n = 3$. (C) qPCR results of mature osteogenic markers (*SPP1*, *DLX5*, *RANKL*) ($n = 8$ – 10), and (D) metabolic marker *VEGFA* is highly expressed while other metabolic markers (*PGK1*, *LDHA*, *HIF1*, *EPAS*) and markers indicative for osteoprogenitors (*RUNX2*, *SOX9*) remain at a basal level ($n = 10$). Data are shown as box plots with median, interquartile range, max and min values, and all data points. For statistical analysis, the results were compared with the expression level of monolayer hMSC, and the Wilcoxon signed rank test was used (Supplemental Table S3).

compared with monolayer MSCs. In contrast, the early osteogenic transcription factor *runt-related transcription factor 2 (RUNX2)* and the chondrogenic marker *SRY-box transcription factor 9 (SOX9)* were expressed on a more basal level. Interestingly, *receptor activator of NF- κ B ligand (RANKL)* was highly expressed (Fig. 3C). Moreover, *vascular endothelial growth factor (VEGF)* was significantly higher expressed (10-fold), although other hypoxia-inducible factor (HIF1) target genes such as *phosphoglycerate kinase 1 (PGK1)*, *lactate dehydrogenase A (LDHA)*, *endothelial PAS domain-containing protein 1 (EPAS)*, and *HIF1* were comparably or lower (*LDHA*) expressed as in monolayer MSCs (Fig. 3D).

Co-cultivation indicates biological functionality of SFBCs

To confirm the functionality of the SFBCs and to mimic the initial phase of fracture healing in an adequate experimental setting, SFBCs were directly co-cultivated with FH models under hypoxic conditions (5% CO_2 , \sim 1% O_2) for 12 hours up to 48 hours (Fig. 4A), since the initial phase of fracture healing in humans takes place within the first 72 hours.⁽²⁾ However, preliminary

results indicated a significant loss of living cells within the FH models after an incubation of 72 hours (Supplemental Fig. S1).

Although we have not fixed both models to each other by any technical measures, we observed a close contact of the FH with the corresponding SFBC, allowing direct cell–cell contact and cross-talk between the models. After co-cultivation for 48 hours, H&E staining revealed the typical cell morphology with no obvious alterations within the SFBCs, whereas the cells in the FH seemed to be evenly distributed. The calcification throughout the SFBC was reconfirmed via von Kossa staining with no obvious calcification in the border areas of the FH (Fig. 4B). We have previously shown that the most interesting observations in our in vitro FH were visible between 12 and 48 hours with respect to immune cell survival and activity.⁽¹⁶⁾ Thus, in a first experiment, mRNA expression in the FH and the SFBC was analyzed after 12 and 48 hours and normalized to the mean expression at 0 hours (Fig. 4C, D, respectively). Analysis of the mRNA expression in the FH indicated a time-consistent, upregulated expression of *RUNX2*, *SPP1*, *MMP2*, *VEGF*, *LDHA*, and *PGK1* with only numerical differences between time points—except for *LDHA* (Fig. 4C). The main differences were observed for the inflammatory markers *interleukin 6 (IL6)* and *IL8*, which were slightly lower

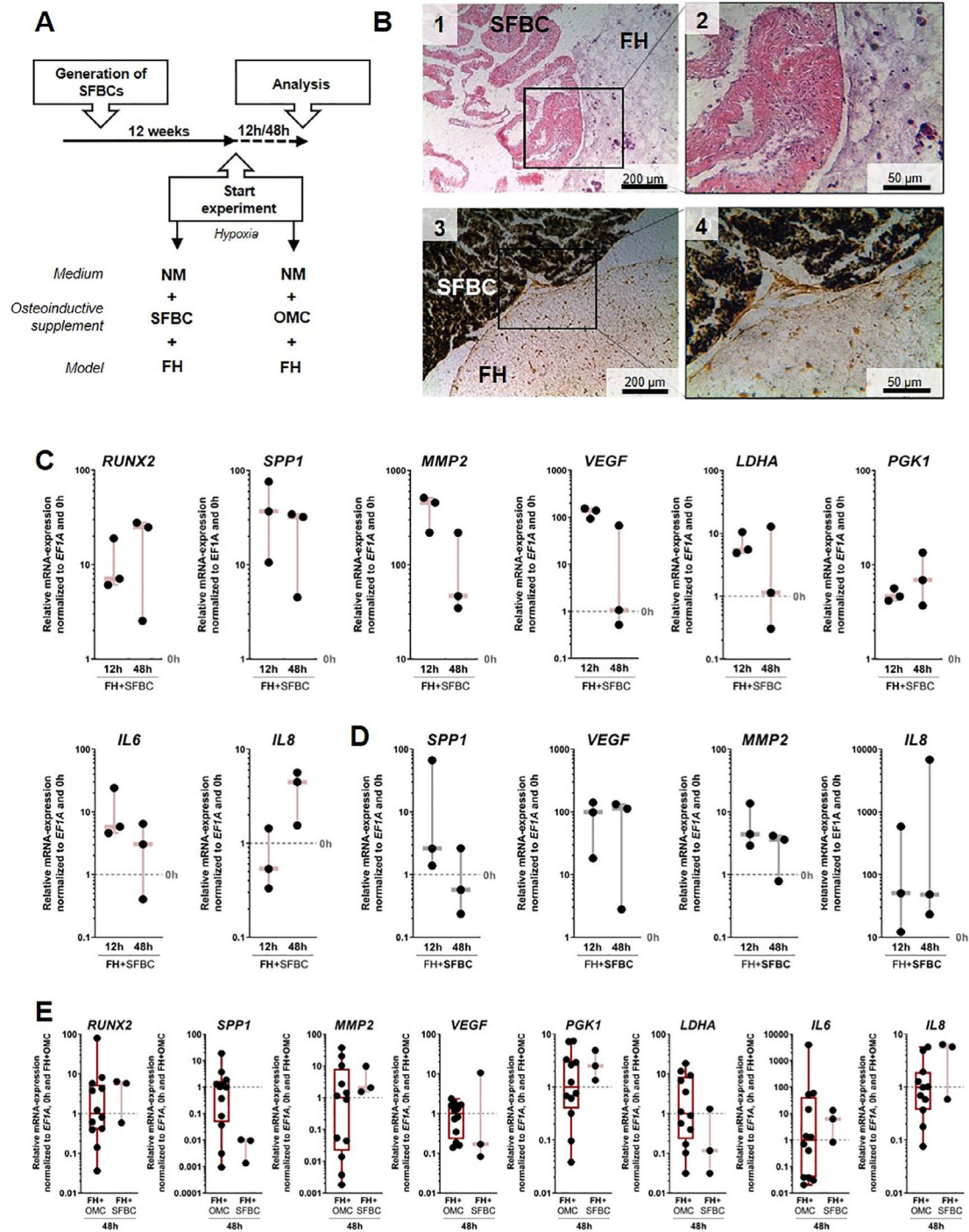


Fig 4. Co-cultivation of SFBCs and in vitro FH. (A) Experimental setup for the co-cultivation study. NM = normal cultivation medium; OMC = osteogenic medium components. (B) Exemplary images of H&E (1, 2) and von Kossa staining (3, 4). Images in the right row (2, 4) are magnifications. Scale bars are indicated. (C) qPCR results of the FH model after 12- and 48-hour co-cultivation with SFBCs under hypoxic conditions. Data are normalized to *EF1A* and 0 hour to verify induction of gene expression by co-cultivation. Data are presented as individual data points with median, max and min values ($n = 3$). Statistical significance was determined using the Wilcoxon signed rank test (matched pairs and unpaired to hypothetical value = 1; Supplemental Tables S4 and S5). (D) qPCR results of the SFBCs after 12- and 48-hour co-cultivation with FH under hypoxic conditions. Data are normalized to *EF1A* and 0 hour. Data are presented as individual data points with median, max and min values ($n = 3$). Statistical significance was determined using the Wilcoxon signed rank test (matched pairs and to hypothetical value = 1; Supplemental Tables S6 and S7). (E) qPCR results of the FH model after 12- and 48-hour co-cultivation with SFBCs compared with the FH + OMC control. Data are normalized to *EF1A*, 0 hour, and the median of FH + OMC. Data are presented as box plots with median, interquartile range, max and min values, and all data points ($n = 3-12$). Statistical significance was determined using the Mann-Whitney test (unpaired; Supplemental Table S8).

expressed after 48 or 12 hours, respectively. Within the SFBCs, *SPP1* was elevated after 12 hours and was marginally lower expressed at 48 hours compared with 0 hours (Fig. 4D). *MMP2*, *VEGFA*, and *IL8* were highly expressed at both time points.

Based on these data, further expression analysis and experiments were conducted after 48 hours of co-cultivation. To verify the biological functionality, in particular the osteoinductive potential of the SFBC, we compared the results from the co-cultivated FH model with a FH + OMC control group (treated only with osteogenic medium components [OMC]: β -glycerophosphate, ascorbic acid, dexamethasone). The normalization of the data to the starting point (0 hours) and the FH + OMC control revealed no substantial differences between both groups (Fig. 4E). Only *SPP1* was lower expressed in the FHs co-cultivated with SFBCs compared with the FH + OMC control. Based on these findings, we concluded that the SFBCs show a comparable osteoinductive capacity as the OMC and, therefore, biological functionality. Control experiments investigating the effect of the medium composition (\pm OMC) on the FH and SFBC revealed only slight differences between the groups regarding *MMP2* and *LDHA* expression after 48 hours in the FH and a time-dependent upregulation of *IL8* within the FH when supplementing OMC (Supplemental Figs. S2 and S3).

Regarding the protein release, we confirmed the secretion of the pro-inflammatory IL-6 and the pro-inflammatory/-angiogenic IL-8. The pro-inflammatory GM-CSF and MIP-1 β were also released (Fig. 5A). All other analyzed cytokines could not be measured because of concentrations lower than the detection level.

DFO treatment intensifies pro-angiogenic processes

For evaluation of the model suitability to identify interfering substances, we supplemented 250 μ M DFO for 48 hours and analyzed the changes in mRNA expression and protein release. DFO is an iron chelator, which inhibits prolylhydroxylases to chemically stabilize HIF and is a well-known osteoinductive substance.⁽²⁰⁾ After co-cultivation for 48 hours and supplementation of DFO, we found that DFO triggered the expression of osteogenic, angiogenic, and hypoxia-related genes in the in vitro FH with barely any effect on the SFBCs (Fig. 5B). In detail, the expression of the osteogenic marker *SPP1* in the FH was higher expressed compared with the untreated control, whereas DFO had no effect on the expression of *RUNX2*. The inflammatory markers *MMP2* and *IL6* were additionally elevated, whereas the pro-angiogenic factor *VEGFA* and the hypoxia-responsive *LDHA* were highly expressed under the influence of DFO compared to the untreated control group (Fig. 5B). Referring to the mRNA expression within the SFBCs, we observed a pattern very similar to untreated conditions, which were expected because of the short treatment period (Fig. 5B). Finally, the protein release of IL-6 and IL-8 was slightly induced after 24 hours with DFO supplementation (Fig. 5C). These results confirm the interfering potential of DFO and indicate different response dynamics within the co-cultivation system.

Discussion

To study the interaction between bone and immune cells within the fracture gap, adequate in vitro systems should recapitulate cell-cell interactions and the microenvironment (hypoxia). Here, we first developed and characterized SFBCs, which were co-cultivated with FH models under hypoxic conditions to verify

the osteoinductive potential of SFBCs and to recapitulate certain aspects of the initial phase of fracture healing. To stratify the model regarding the responsiveness toward potentially interfering substances (eg, therapeutics), DFO was supplemented for 48 hours. Based on our data, we were able to distinctly mimic processes of the initial fracture phase in vitro and highlighted the importance of including the cross-talk between bone and immune cells for preclinical studies. Improved tissue engineering approaches employ mesenchymal condensation as a natural form of 3D self-assembly or self-organization consisting exclusively of the cells and their own produced extracellular matrix (ECM).⁽²¹⁾ MSCs from the bone marrow, but also the adipose tissue as well as primary cells (osteoblasts) or induced pluripotent stem cells, have been used depending on the availability and phenotype stability. It has been described that bone marrow-derived MSCs tend to mineralize than undergo chondrogenesis after mesenchymal condensation.^(14,22) Several techniques are exerted, such as the use of low-attachment plates to induce spontaneous MSC aggregation, membrane-based aggregation (eg, chitosan), or forced aggregation (via centrifugation).⁽²³⁾

The applied technique patented by Ponomarev and colleagues⁽²⁴⁾ exploits the capacity of MSC to undergo mesenchymal condensation on a macroscale level to produce macro-tissues in a highly standardized manner without causing necrosis formation in the center.⁽¹⁸⁾ The advantage of such macroscale approaches is the physiologically relevant size, geometry, and low cell number and density compared with the matrix and mechanical properties when compared to, for example, spheroids.⁽¹⁸⁾ However, the generation and examination of these constructs are time-consuming and require high numbers of cells limiting the throughput of the system but enabling the performance of several analyses from one model. Here, we reported the bone-like structure and ongoing calcification/mineralization of the SFBCs that were verified by in vitro μ Ct (Fig. 1) and histology/immunohistochemistry, showing pronounced expression of ALP and Col I in the absence of Col II (Fig. 2). These findings are comparable to other studies using MSC aggregates analyzed after 1 to 3 weeks.^(25,26) The morphology and structure of the SFBCs resemble immature woven bone regarding the body structure. To identify bone-representative cell types, we applied immunofluorescence staining. Because osteoblasts and osteocytes are the characteristic cells in native bone, we stained for OPN as well as OC. OPN, a glycol-phosphoprotein,⁽²⁷⁾ is mainly expressed in immature osteoblasts and OC can be found in late-stage osteoblasts currently transforming to osteocytes. Thus, we have heterogenic differentiation and maturation states within the SFBCs, indicating a heterogeneous cell population in functional balance. With respect to the mRNA expression, we observed augmented expression of osteogenic relevant markers such as *SPP1*, *DLX5*, *RANKL* and *VEGFA* (Fig. 3). *SPP1*, the coding gene for OPN, is hereby the most distinct upregulated gene, coherent with the expression of OPN within the immunofluorescence staining. Muraglia and colleagues observed comparable trends, including a two- to eightfold increase in OC and OPN expression in MSC aggregates cultivated in low-attachment plates.⁽²⁸⁾ Because *RUNX2* is an early upstream transcription factor, high expression on mRNA level is expected 3 to 7 days after osteogenic induction.⁽²⁶⁾ After 3 weeks, the process of ossification and cellular differentiation toward the osteogenic lineage is already in an advanced state.^(29,30) *VEGFA* is an essential coordinator, not only of angiogenic processes and important for fracture healing, but also in the process of endochondral ossification⁽³¹⁾ and is known to enhance osteogenic differentiation

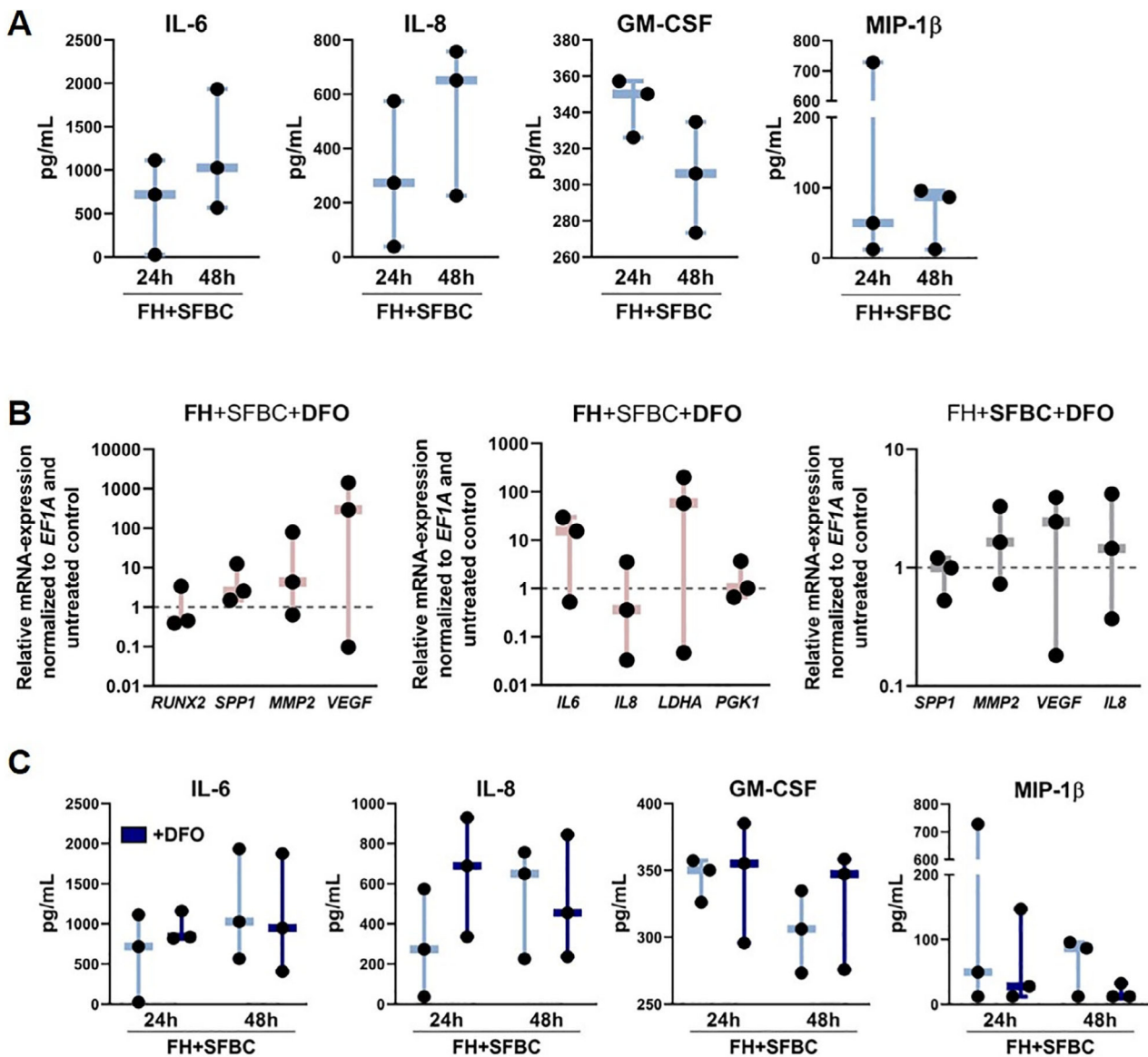


Fig 5. Analysis of the supernatant after co-cultivation and co-cultivation of SFBCs and in vitro FH with supplementation of DFO. (A) Supernatants were collected after 24 and 48 hours and analyzed via multiplex assay. Statistical significance was determined using the Kruskal–Wallis test with Dunn’s multiple comparisons test (Supplemental Table S9). Data are shown as individual data points with median, max and min values. (B) qPCR results of the FH or the SFBCs after 48-hour co-cultivation with supplementation of 250 μ M DFO (bold abbreviations in title indicate analyzed component). Data are normalized to *EF1A* and the untreated control and presented as individual data points with median, max and min values, and all data points ($n = 3$). Statistical significance was determined using the Wilcoxon signed rank test (Supplemental Tables S10 and S11). (C) Supernatants were collected after 24 and 48 hours and analyzed via multiplex cytokine detection assay (dark blue = DFO treated samples). Statistical significance was determined using the Kruskal–Wallis test with Dunn’s multiple comparisons test (Supplemental Table S12). Data are shown as individual data points with median, max and min values.

in vitro.⁽³²⁾ Interestingly, other HIF1 target genes such as *PGK1*, *EPAS*, and *HIF1* were comparably expressed as in monolayer MSCs, although *LDHA* was downregulated (Fig. 3D). Because the SFBCs were not cultivated under hypoxic conditions, the increased expression of *VEGFA* might result from an alternative pathway, eg, induced by transforming growth factor beta 1 (TGF- β 1).⁽³³⁾ *DLX5*, an important transcription factor in

osteogenesis and bone development,⁽³⁴⁾ is also highly expressed within the SFBCs, also indicating an intense ossification process. RANKL is also expressed in mature osteoblasts, differentiating into osteocytes and regulating osteoblastogenesis, indicating the presence of late-stage osteoblasts.⁽³⁵⁾

After characterizing their bone-like quantities, we co-cultivated the SFBCs with in vitro FHs to evaluate the osteoinductive

potential and, therefore, the functionality of the SFBCs. Previously, we developed an in vitro FH model, incubated in osteogenic induction medium, which closely reflects the in vivo situation.^(16,36) One of the main findings was the importance of hypoxia. Therefore, we included hypoxic conditions in our co-cultivation setup. The co-cultivation of the in vitro FH and SFBCs in NM for up to 48 hours under hypoxic conditions revealed significant initiation of cellular processes (mRNA level) for adaptation to hypoxia and osteogenic induction within the FH (Fig. 4). These findings are in accordance with results from an ex vivo study and an in vitro FH model conducted in our group (Supplemental Table S13).^(16,37)

Based on the comparative analysis with an FH + OMC control, we concluded that the SFBCs show a comparable osteoinductive capacity as the OMC and biological functionality indicated by, for example, *VEGF* and *MMP2* (Fig. 4). Interestingly, *SPP1* was noticeably lower expressed in the FH when co-cultivated with SFBCs compared with the FH + OMC control, which could be explained by either the higher amount of OPN provided by the SFBC (Fig. 3) or the considerable high expression/concentration of IL-6 (Figs. 4 and 5A), as previously reported.⁽³⁸⁾ The level of pro-inflammatory cytokines (eg, IL-6 and IL-8) was abundant, which has been also observed in ex vivo samples from patients (Fig. 5A).^(2,5,37) The microenvironment of the fracture hematoma is described by hypoxia, high lactate and low pH owing to the disruption of vessels, cell death of, for example, erythrocytes, and the lack of nutrients. This cytotoxic environment needs to be counterregulated to allow the invasion of regenerative cells. Therefore, we included whole human blood instead of isolated peripheral blood mononuclear cells (PBMCs). At the initial stage, the microenvironment in the fracture hematoma is acidotic and switched to neutral and slightly alkaline during the regeneration process,⁽³⁹⁾ which can be triggered by hypoxia. Interestingly, upon co-cultivation, *LDHA* was highly upregulated in the FH model (Supplemental Fig. S2).

Furthermore, the effect of certain immune cells during the initial phase of fracture healing has been studied in detail during the last decade. Lymphocytes play a crucial role as shown in *RAG1*^(-/-) mice supposing a detrimental effect of adaptive immune cells.⁽⁴⁰⁾ A negative impact was reported for the presence of CD8⁺ cytotoxic T cells in humans and mice,⁽⁴¹⁾ whereas CD4⁺ cells have been shown to enhance osteogenic differentiation in vitro and upregulated osteogenic markers, eg, *RUNX2* or *OC*.⁽⁴²⁾ This clearly indicates the need to combine bone and immune cells in in vitro approaches to recapitulate the cross-talk, environment, and key features of the in vivo situation.

With respect to the DFO treatment, we found an upregulation of *HIF*-target genes (*VEGFA* and *LDHA*), indicating the effectivity of DFO to stabilize *HIF* (Fig. 5B, C). In addition, pro-inflammatory processes were more pronounced, which is in accordance with current findings in a mouse-osteotomy model revealing the activation of, for example, *C-X-C motif chemokine ligand 3* (*Cxcl3*) or *metallothionein 3* (*Mt3*) expression at day 3 after application of DFO in the fracture gap.⁽²⁰⁾ We did not expect a strong upregulation of osteogenic markers or changes in the SFBCs, which normally require longer treatment periods.⁽²⁹⁾

Nevertheless, there are many ways to foster the current approach. To improve the current protocol to generate SFBC, different approaches such as the addition of specific growth factors, eg, BMPs, fibroblast growth factors (FGFs), or VEGFs, enhancing the differentiation and bone formation in vitro can be considered to fasten up the generation period in the future. Furthermore, bioreactors can be used to approximate the

environment to the actual in vivo situation by dynamic culturing and restrained environment, while overcoming the lack of nutrient transfer and combining cells with scaffolds.⁽⁴³⁾ Bioreactors also provide the possibility to withdraw toxic and cell apoptotic signals, perhaps allowing a longer cultivation period of the model. Moreover, to adequately mimic the fracture gap, the adjacent bone marrow might be included within the system to allow the migration of further immune cells but also, for example, endothelial cells, which invade the fracture hematoma to promote neovascularization.

Nevertheless, we present a first approach to recapitulate key features of the initial phase of fracture healing more closely to the in vivo situation by combining macroscale bone equivalents and FH models. Despite some limitations, we here provide data on a prototype of an in vitro fracture gap model that can be used in the future (i) to study potential underlying mechanisms of fracture-healing disorders, eg, using blood of immunologically restricted patients^(4,5) to produce the FH models; (ii) to be employed as a prediction tool to identify (potential) interfering substances (eg, glucocorticoids, NSAIDs) or new therapeutics; and (iii) to be further optimized and expanded to provide a sufficient alternative method for active implementation of the 3R principle.

Disclosures

All authors state that they have no conflict of interests.

Acknowledgments

The authors thank Manuela Jakstadt for excellent technical assistance. Bone marrow was provided by the “Tissue Harvesting” Core Facility of the Berlin Institute of Health Center for Regenerative Therapies (BCRT). FACS analyses were performed together with the Core Facility at the German Rheumatism Research Centre. AL, FB, AD, MP, and TG are members of Berlin-Brandenburg research platform BB3R and Charité 3^R. This study was funded by the German Federal Ministry for Education and Research (BMBF) (project no. 031A334). AL and AD are currently being supported by the Joachim Herz Foundation (Add-on Fellowship 2019/2020). The work of TG was funded by the Deutsche Forschungsgemeinschaft (353142848). Funding bodies did not have any role in designing the study; in collecting, analyzing, and interpreting the data; in writing this manuscript; and in deciding to submit it for publication. Open Access funding enabled and organized by Projekt DEAL.

The authors declare that all data supporting the findings of this study are available within the article and its supplemental information. Further information is made available by the authors upon request.

Author contributions: Moritz Pfeiffenberger: Conceptualization; data curation; formal analysis; investigation; methodology; writing-original draft. Alexandra Damerau: Formal analysis; methodology. Igor Ponomarev: Conceptualization; formal analysis; methodology; resources. Christian Bucher: Formal analysis; methodology; resources; writing-review & editing. Yuling Chen: Formal analysis; methodology. Dirk Barnewitz: Conceptualization; resources; writing-review & editing. Christa Thöne-Reineke: Conceptualization; project administration; supervision; writing-review & editing. Paula Hoff: Conceptualization; writing-review & editing. Frank Buttgerit: Conceptualization; data curation; funding acquisition; project administration; resources; supervision;

writing-review & editing. Timo Gaber: Conceptualization; data curation; project administration; supervision; writing-review & editing. Annemarie Lang: Conceptualization; data curation; formal analysis; writing-original draft; project administration; supervision; writing-review & editing.

PEER REVIEW

The peer review history for this article is available at <https://publons.com/publon/10.1002/jbmr.4267>.

References

1. Bhandari M, Busse JW, Hanson BP, Leece P, Ayeni OR, Schemitsch EH. Psychological distress and quality of life after orthopedic trauma: an observational study. *Can J Surg*. 2008;51(1):15-22.
2. Hoff P, Gaber T, Strehl C, et al. Immunological characterization of the early human fracture hematoma. *Immunol Res*. 2016;64(5-6):1195-1206.
3. Oe K, Miwa M, Sakai Y, Lee SY, Kuroda R, Kurosaka M. An in vitro study demonstrating that haematomas found at the site of human fractures contain progenitor cells with multilineage capacity. *J Bone Joint Surg*. 2007;89(1):133-138.
4. Hoff P, Gaber T, Schmidt-Bleek K, et al. Immunologically restricted patients exhibit a pronounced inflammation and inadequate response to hypoxia in fracture hematomas. *Immunol Res*. 2011;51(1):116-122.
5. Hoff P, Gaber T, Strehl C, et al. A pronounced inflammatory activity characterizes the early fracture healing phase in immunologically restricted patients. *Int J Mol Sci*. 2017;18(3):583.
6. Winkler T, Sass FA, Duda GN, Schmidt-Bleek K. A review of biomaterials in bone defect healing, remaining shortcomings and future opportunities for bone tissue engineering: the unsolved challenge. *Bone Joint Res*. 2018;7(3):232-243.
7. Grundnes O, Reikeras O. The importance of the hematoma for fracture healing in rats. *Acta Orthop Scand*. 1993;64(3):340-342.
8. Kolar P, Schmidt-Bleek K, Schell H, et al. The early fracture hematoma and its potential role in fracture healing. *Tissue Eng Part B Rev*. 2010;16(4):427-434.
9. Bernhardt A, Lode A, Peters F, Gelinsky M. Optimization of culture conditions for osteogenically-induced mesenchymal stem cells in beta-tricalcium phosphate ceramics with large interconnected channels. *J Tissue Eng Regen Med*. 2011;5(6):444-453.
10. Burska AN, Giannoudis PV, Tan BH, Illas D, Jones E, Ponchel F. Dynamics of early signalling events during fracture healing and potential serum biomarkers of fracture non-union in humans. *J Clin Med*. 2020;9(2):492.
11. Schlundt C, Schell H, Goodman SB, Vunjak-Novakovic G, Duda GN, Schmidt-Bleek K. Immune modulation as a therapeutic strategy in bone regeneration. *J Exp Orthopaed*. 2015;2(1):1.
12. Haffner-Luntzer M, Hankenson KD, Ignatius A, et al. Review of animal models of comorbidities in fracture-healing research. *J Orthop Res*. 2019;37(12):2491-2498.
13. Scheinpflug J, Pfeiffenberger M, Damerou A, et al. Journey into bone models: a review. *Genes*. 2018;9(5):247.
14. Dickhut A, Peltari K, Janicki P, et al. Calcification or dedifferentiation: requirement to lock mesenchymal stem cells in a desired differentiation stage. *J Cell Physiol*. 2009;219(1):219-226.
15. Shih YV, Varghese S. Tissue engineered bone mimetics to study bone disorders ex vivo: role of bioinspired materials. *Biomaterials*. 2019;198:107-121.
16. Pfeiffenberger M, Hoff P, Thöne-Reineke C, Buttgerit F, Lang A, Gaber T. The in vitro human fracture hematoma model—a tool for preclinical drug testing. *ALTEX*. 2020;37(4):561-578.
17. Hahn M, Vogel M, Pompesius-Kempa M, Dellling G. Trabecular bone pattern factor—a new parameter for simple quantification of bone microarchitecture. *Bone*. 1992;13(4):327-330.
18. Weber M-C, Fischer L, Damerou A, et al. Macroscale mesenchymal condensation to study cytokine-driven cellular and matrix-related changes during cartilage degradation. *Biofabrication*. 2019;12:045016.
19. Curtis KM, Gomez LA, Rios C, et al. EF1 α and RPL13a represent normalization genes suitable for RT-qPCR analysis of bone marrow derived mesenchymal stem cells. *BMC Mol Biol*. 2010;11(1):61.
20. Lang A, Helfermeier S, Stefanowski J et al. HIF-stabilization as possible treatment towards fracture healing disorders. *bioRxiv*. 2020. <https://doi.org/10.1101/2020.07.02.182832>.
21. DuRaine GD, Brown WE, Hu JC, Athanasiou KA. Emergence of scaffold-free approaches for tissue engineering musculoskeletal cartilages. *Ann Biomed Eng*. 2015;43(3):543-554.
22. Farrell MJ, Fisher MB, Huang AH, Shin JI, Farrell KM, Mauck RL. Functional properties of bone marrow-derived MSC-based engineered cartilage are unstable with very long-term in vitro culture. *J Biomechan*. 2014;47(9):2173-2182.
23. Sart S, Tsai A-C, Li Y, Ma T. Three-dimensional aggregates of mesenchymal stem cells: cellular mechanisms, biological properties, and applications. *Tissue Eng Part B Rev*. 2014;20(5):365-380.
24. Ponomarev IV, Kochneva LM, Barnewitz D. Effect of 3D chondrocyte culturing conditions on the formation of extracellular matrix in cartilage tissue-engineering constructs. *Bull Exp Biol Med*. 2014;156(4):548-555.
25. Frith JE, Thomson B, Genever PG. Dynamic three-dimensional culture methods enhance mesenchymal stem cell properties and increase therapeutic potential. *Tissue Eng Part C Methods*. 2010;16(4):735-749.
26. Kabiri M, Kul B, Lott WB, et al. 3D mesenchymal stem/stromal cell osteogenesis and autocrine signalling. *Biochem Biophys Res Commun*. 2012;419(2):142-147.
27. Standal T, Borset M, Sundan A. Role of osteopontin in adhesion, migration, cell survival and bone remodeling. *Exp Oncol*. 2004;26(3):179-184.
28. Muraglia A, Corsi A, Riminucci M, et al. Formation of a chondro-osseous rudiment in micromass cultures of human bone-marrow stromal cells. *J Cell Sci*. 2003;116(Pt 14):2949-2955.
29. Hoshiba T, Kawazoe N, Tateishi T, Chen G. Development of stepwise osteogenesis-mimicking matrices for the regulation of mesenchymal stem cell functions. *J Biol Chem*. 2009;284(45):31164-31173.
30. Xu J, Li Z, Hou Y, Fang W. Potential mechanisms underlying the Runx2 induced osteogenesis of bone marrow mesenchymal stem cells. *Am J Transl Res*. 2015;7(12):2527-2535.
31. Gerber HP, Vu TH, Ryan AM, Kowalski J, Werb Z, Ferrara N. VEGF couples hypertrophic cartilage remodeling, ossification and angiogenesis during endochondral bone formation. *Nat Med*. 1999;5(6):623-628.
32. Zhang Y, Madhu V, Dighe AS, Irvine JN Jr, Cui Q. Osteogenic response of human adipose-derived stem cells to BMP-6, VEGF, and combined VEGF plus BMP-6 in vitro. *Growth Factors*. 2012;30(5):333-343.
33. Chae KS, Kang MJ, Lee JH, et al. Opposite functions of HIF- α isoforms in VEGF induction by TGF- β 1 under non-hypoxic conditions. *Oncogene*. 2011;30(10):1213-1228.
34. Chung IH, Han J, Iwata J, Chai Y. Msx1 and Dlx5 function synergistically to regulate frontal bone development. *Genesis*. 2010;48(11):645-655.
35. Nakashima T, Hayashi M, Fukunaga T, et al. Evidence for osteocyte regulation of bone homeostasis through RANKL expression. *Nat Med*. 2011;17(10):1231-1234.
36. Pfeiffenberger M, Bartsch J, Hoff P, et al. Hypoxia and mesenchymal stromal cells as key drivers of initial fracture healing in an equine in vitro fracture hematoma model. *PLoS One*. 2019;14(4):e0214276.
37. Hoff P, Maschmeyer P, Gaber T, et al. Human immune cells' behavior and survival under bioenergetically restricted conditions in an in vitro fracture hematoma model. *Cell Mol Immunol*. 2013;10(2):151-158.
38. Scutera S, Salvi V, Lorenzi L, et al. Adaptive regulation of osteopontin production by dendritic cells through the bidirectional interaction with mesenchymal stromal cells. *Front Immunol*. 2018;9:1207.

39. Schell H, Duda GN, Peters A, Tsitsilonis S, Johnson KA, Schmidt-Bleek K. The haematoma and its role in bone healing. *J Exp Orthop*. 2017;4(1):5.
40. El Khassawna T, Serra A, Bucher CH, et al. T lymphocytes influence the mineralization process of bone. *Front Immunol*. 2017;8:562.
41. Reinke S, Geissler S, Taylor WR, et al. Terminally differentiated CD8(+) T cells negatively affect bone regeneration in humans. *Sci Transl Med*. 2013;5(177):177ra36.
42. Grassi F, Cattini L, Gambari L, et al. T cell subsets differently regulate osteogenic differentiation of human mesenchymal stromal cells in vitro. *J Tissue Eng Regen Med*. 2016;10(4):305-314.
43. Kashte S, Jaiswal AK, Kadam S. Artificial bone via bone tissue engineering: current scenario and challenges. *Tissue Eng Regen Med*. 2017;14(1):1-14.

2.4 *In vitro* and *in silico* modelling to study the pathogenesis of osteoarthritis

The main aim of cartilage tissue engineering is the provision of cartilage equivalents to be transplanted in cartilage defects in the knee or hip joint [93]. These cartilage equivalents can in turn be used for *in vitro* model approaches [71]. Thus, in the next study, we used these scaffold-free constructs to develop an *in vitro* model of matrix degradation during the onset of OA.

The following text corresponds to the abstract of the work:

Weber, M.-C.*, Fischer, L.*, Damerau, A., Ponomarev, I., Pfeiffenberger, M., Gaber, T., Götschel, S., Lang, J., Röblitz, S., Buttgereit, F., Ehrig, R., **Lang, A.** (2020) Macroscale mesenchymal condensation to study cytokine-driven cellular and matrix-related changes during cartilage degradation. *Biofabrication*. Aug 10; 12(4):045016. [doi: 10.1088/1758-5090/aba08f]

“Understanding the pathophysiological processes of cartilage degradation requires adequate model systems to develop therapeutic strategies towards osteoarthritis (OA). Although different in vitro or in vivo models have been described, further comprehensive approaches are needed to study specific disease aspects. This study aimed to combine in vitro and in silico modeling based on a tissue-engineering approach using mesenchymal condensation to mimic cytokine-induced cellular and matrix-related changes during cartilage degradation. Thus, scaffold-free cartilage-like constructs (SFCCs) were produced based on self-organization of mesenchymal stromal cells (mesenchymal condensation) and i) characterized regarding their cellular and matrix composition or secondly ii) treated with interleukin-1 β (IL-1 β) and tumor necrosis factor α (TNF α) for 3 weeks to simulate OA-related matrix degradation. In addition, an existing mathematical model based on partial differential equations was optimized and transferred to the underlying settings to simulate distribution of IL-1 β , type II collagen degradation and cell number reduction. By combining in vitro and in silico methods, we aim to develop a valid, efficient alternative approach to examine and predict disease progression and effects of new therapeutics.”

The advantage of the described model is the macroscale approach which, in contrast to pellets, avoids a physiologically irrelevant size, geometry, cell density, and provides a sufficient sample volume for parallel analyses. Combining *in vitro* and *in silico* modelling enables immediate refitting and adjustments based on the predictions from simulations and therefore, a more stratified and effective optimization process. However, the described *in vitro* model is limited in its complexity and cross-tissue integration

Biofabrication



PAPER

OPEN ACCESS

RECEIVED
11 February 2020

REVISED
9 June 2020

ACCEPTED FOR PUBLICATION
26 June 2020

PUBLISHED
28 July 2020

Original content from this work may be used under the terms of the [Creative Commons Attribution 4.0 licence](#).

Any further distribution of this work must maintain attribution to the author(s) and the title of the work, journal citation and DOI.



Macroscale mesenchymal condensation to study cytokine-driven cellular and matrix-related changes during cartilage degradation

Marie-Christin Weber^{1,9}, Lisa Fischer^{2,9}, Alexandra Damerou^{1,3}, Igor Ponomarev⁴, Moritz Pfeiffenberger^{1,3}, Timo Gaber^{1,3,5}, Sebastian Götschel², Jens Lang⁶, Susanna Röblitz⁷, Frank Buttgereit^{1,3,5}, Rainald Ehrig^{2,8} and Annemarie Lang^{1,3,5,10}

¹ Charité – Universitätsmedizin Berlin, Corporate Member of Freie Universität Berlin, Humboldt-Universität zu Berlin, and Berlin Institute of Health, Department of Rheumatology and Clinical Immunology, Berlin, Germany

² Zuse Institute Berlin, Berlin, Germany

³ German Rheumatism Research Centre (DREZ) Berlin, a Leibniz Institute, Berlin, Germany

⁴ Research Center of Medical Technology and Biotechnology, Bad Langensalza, Germany

⁵ Charité – Universitätsmedizin Berlin, Corporate Member of Freie Universität Berlin, Humboldt-Universität zu Berlin, and Berlin Institute of Health, Berlin Institute of Health Center for Regenerative Therapies, Berlin, Germany

⁶ Technische Universität Darmstadt, Numerical Analysis, Darmstadt, Germany

⁷ Computational Biology Unit, Department of Informatics, University of Bergen, Bergen, Norway

⁸ Charité – Universitätsmedizin Berlin, corporate member of Freie Universität Berlin, Humboldt-Universität zu Berlin, and Berlin Institute of Health, Julius Wolff Institute, Berlin, Germany

⁹ These authors contributed equally.

¹⁰ Author to whom any correspondence should be addressed.

E-mail: annemarie.lang@charite.de

Keywords: *in vitro* model, tissue engineered cartilage, cytokine-induced inflammation, *in silico* model

Supplementary material for this article is available [online](#)

Abstract

Understanding the pathophysiological processes of cartilage degradation requires adequate model systems to develop therapeutic strategies towards osteoarthritis (OA). Although different *in vitro* or *in vivo* models have been described, further comprehensive approaches are needed to study specific disease aspects. This study aimed to combine *in vitro* and *in silico* modeling based on a tissue-engineering approach using mesenchymal condensation to mimic cytokine-induced cellular and matrix-related changes during cartilage degradation. Thus, scaffold-free cartilage-like constructs (SFCCs) were produced based on self-organization of mesenchymal stromal cells (mesenchymal condensation) and (i) characterized regarding their cellular and matrix composition or secondly (ii) treated with interleukin-1 β (IL-1 β) and tumor necrosis factor α (TNF α) for 3 weeks to simulate OA-related matrix degradation. In addition, an existing mathematical model based on partial differential equations was optimized and transferred to the underlying settings to simulate the distribution of IL-1 β , type II collagen degradation and cell number reduction. By combining *in vitro* and *in silico* methods, we aimed to develop a valid, efficient alternative approach to examine and predict disease progression and effects of new therapeutics.

1. Introduction

Cartilage is a highly complex tissue that can be found in different forms at various locations in the body. The cartilage type is determined by the cell density and the composition of the extracellular matrix (ECM) resulting in function-adapted properties. Fibrous cartilage found in the menisci or intervertebral discs is cell-poor and rich of type I collagen, while elastic cartilage has a high cell density and elastic fibers. Articular cartilage, a subtype of

hyaline cartilage, is organized in a unique structure consisting of different layers and distinct chondrocyte phenotypes enabling impact absorbance and pressure distribution within joints. The ECM of articular cartilage is defined by high concentrations of type II collagen and several proteoglycans, mainly aggrecan and glycosaminoglycans binding water within the tissue. Cartilage in general evolves during embryonic development through mesenchymal condensation [1].

Cartilage degradation within articular joints is a major feature of osteoarthritis (OA). OA ranks

among the most common musculoskeletal disorders with no available cure except for joint replacement surgery. The progression of cartilage degradation is driven by an imbalance in anabolic and catabolic metabolic processes that normally ensure cartilage maintenance and homeostasis [2]. The inflammatory microenvironment results in increased expression of specialized matrix-degrading enzymes such as matrix-metalloproteinases (MMP) or a disintegrin and metalloproteinase with thrombospondin motifs (ADAMTS). MMPs, calcium-dependent zinc-containing endopeptidases, are involved in different physiological and pathological remodeling processes. MMP-1, MMP-3, MMP-8 and MMP-13 have been found to be increased in osteoarthritic cartilage and to be responsible for specifically degrading collagen fibers, but also proteoglycans [3].

The pathogenesis of OA has not been fully understood so far, partly due to the lack of an optimal model system which sufficiently incorporates all aspects of the disease [2, 4]. A vast variety of *in vivo*, *ex vivo*, *in vitro* and (to some extent) *in silico* models for OA already exists, and they all mimic distinct features of OA pathophysiology including the degradation of ECM, inflammation and alterations in cell metabolism, viability and differentiation [5–7]. *In vivo* OA models are crucial for translational research, but mainly make use of small rodents, especially mice, although these species show significant differences in articular cartilage anatomy, loading conditions and life span [8, 9]. Thus, *in vitro* models represent an important tool to investigate the mechanisms involved in the pathogenesis of OA and to examine possible therapeutic options. Model systems include monolayer cultures with cell lines or primary chondrocytes, co-cultures, 3D-cultures, cartilage explants from either humans or animals or even new cartilage-on-a-chip approaches [10]. However, a major challenge is the source of primary chondrocytes or explants, since healthy human cartilage samples are rare. Thus, sample collection is mainly undertaken from joint replacement surgeries. Independent of the cell source, it is a consensus that the 3D cultivation of primary chondrocytes resembles the *in vivo* situation more closely [11]. However, most 3D culture systems involve a scaffold to provide the cells with a predetermined structure, although their distinct effects on the cells are often not considered. Recent developments aim to establish scaffold-free tissue engineered cartilage which could serve as a promising approach for cartilage repair *in vivo*, but also as an excellent *in vitro* model, since ECM formation and degradation can be evaluated without the interference of a scaffold [12–14]. The increasing understanding on developmental biology resulted in improved tissue-engineering approaches using e.g. self-assembly and self-organization [12] processes that recapitulate mesenchymal condensation and chondrogenesis [13, 15–18]. Therefore,

mainly mesenchymal stromal cells (MSCs) are used for scaffold-free cartilage tissue engineering owing to their benefits in terms of availability, proliferative capacity and phenotype stability when compared to primary chondrocytes. Several groups have proven the possibility to produce *in vitro* cartilage grown scaffold-free based on MSCs [13, 15]. The main aim is to develop cartilage transplants as a therapeutic option to repair cartilage defects in joints such as the knee or ankle [15]. However, it has been also proposed that those scaffold-free cartilage analogues can be also used for experimental studies [13].

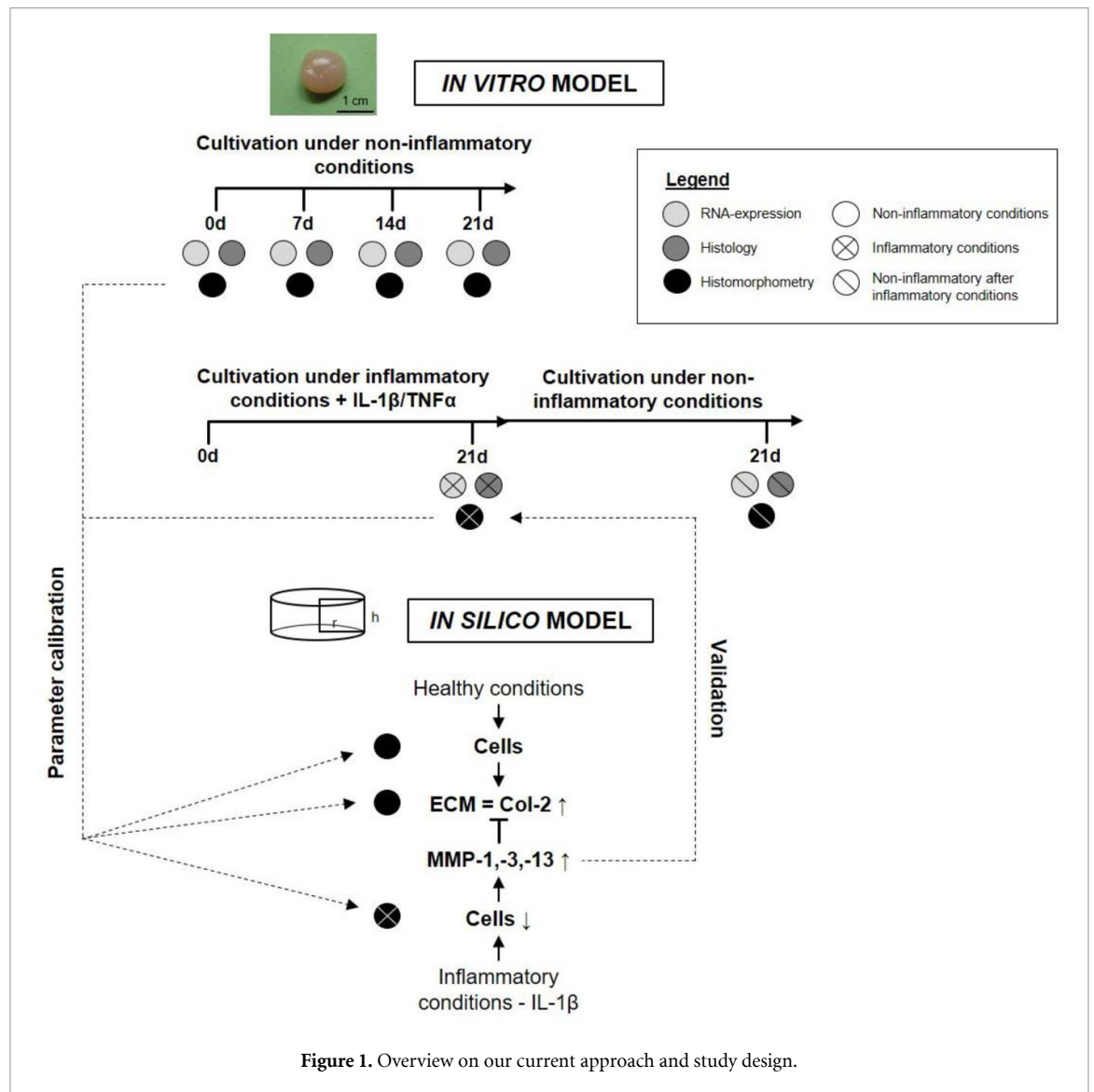
In addition to biological models, *in silico* modeling offers a powerful tool to bring clarity to the processes that evolve during *in vitro* or *in vivo* modeling [19, 20]. Few studies have been performed so far to obtain parameters for *in silico* modeling, although a combination of biological data with mathematical modeling promises to accelerate translation in OA research [21–23]. Catt *et al* describe a partial differential equation (PDE) model of cartilage with a focus on the production of ECM and the growth of chondrocytes synergistically leading to tissue expansion [22]. Moreover, Kar *et al* investigated cartilage degradation induced by interleukin-1 β (IL-1 β) using a PDE model based on data from the literature together with existing experimental data to calibrate their model [23]. In contrast, Baker *et al* used an ordinary differential equation (ODE) system to describe the interaction of anti-inflammatory cytokines, proteinases and fibronectin in osteoarthritic cartilage [24]. Since biomechanical influences are of utmost interest, several approaches have already been used, and these include modelling arthritic cartilage under cyclic compressive loading or a combining of inflammation and biomechanics [25, 26].

In this study, we tested whether scaffold-free cartilage-like constructs (SFCCs), engineered by macroscale mesenchymal condensation and biomechanical stimulation, can be used as an *in vitro* model to investigate cytokine-driven cellular and matrix-related changes during cartilage degradation that occur e.g. during OA. In addition, we evaluated the feasibility to adapt an existing OA-related mathematical model to resemble the matrix degradation processes in these SFCCs (figure 1).

2. Material and methods

2.1. hMSC isolation and expansion

Human mesenchymal stromal cells (hMSCs) were obtained from human femoral bone marrow of patients undergoing hip arthroplasty (provided by the Centre for Musculoskeletal Surgery, Charité—Universitätsmedizin Berlin and distributed by the ‘Tissue Harvesting’ Core Facility of the Berlin Institute of Health Center for Regenerative Therapies (BCRT), Germany). All protocols were approved by the Charité—Universitätsmedizin Ethics Committee



and performed according to the Helsinki Declaration (ethical approval EA1/012/13). Donor information is summarized in table 1. hMSCs were cultivated in DMEM GlutaMAXTM Medium (Thermo Fisher Scientific, MA) with 20% StemMACSTM (Miltenyi Biotech, Germany), 10% fetal calf serum (FCS) (Thermo Fisher Scientific, MA), 100 units ml⁻¹ penicillin and 0.1 mg ml⁻¹ streptomycin (Thermo Fisher Scientific, MA) at a temperature of 37 °C in 5% CO₂ atmosphere. hMSCs were cultured separately for each donor and characterized by flow cytometry (CD90⁺, CD105⁺, CD73⁺, CD14⁻, CD20⁻, CD34⁻, CD45⁻, HLA-DR⁻) as well as osteogenic, adipogenic and chondrogenic differentiation assays. Only cells successfully passing the characterization were further cultivated up to passages 3–5.

2.2. Generation of SFCCs and experimental setup

SFCCs were produced based on a patented protocol (patent no.: EP1550716B1) [27]. In short, around 10–15 million hMSCs from one donor (randomized) were transferred into a 3D state via centrifugation

followed by maturation for 3 to 4 weeks applying biomechanical forces until reaching cartilage-like stiffness [28]. Due to the input of biomechanical forces, the SFCCs are formed by self-organization [12]. Before the experiments, SFCCs were cultured for 4 weeks in DMEM GlutaMAXTM Medium, supplemented with 10% FCS, 100 units ml⁻¹ penicillin, 0.1 mg ml⁻¹ streptomycin (all from Thermo Fisher Scientific, MA) and 9.39 mg l⁻¹ ascorbic acid (Sigma-Aldrich, MO); in the following, this is referred to as ‘standard medium’. In a first step, SFCCs were cultivated under cytokine-free conditions and samples were taken on days 0, 7, 14 and 21 ($n = 3$ per time point). Secondly, to resemble the proinflammatory state that has been described in patients with early OA, stimulation was performed using standard medium supplemented with 50 ng ml⁻¹ recombinant human IL-1 β (2×10^8 IU mg⁻¹) and 100 ng ml⁻¹ recombinant human tumor necrosis factor alpha (TNF α) (2×10^7 IU mg⁻¹; both from ImmunoTools, Germany). Samples of cytokine stimulated SFCCs (STIM) and controls (CTL) were taken on day

Table 1. hMSC donor information and related experiments.

Patient	Age	Sex	Characterization	Type of experiment
1	71	Female	+	Experiments under non-inflammatory conditions Histology RNA analysis
2	56	Female	+	
3	85	Female	+	
4	59	Female	+	Experiments under non-inflammatory and inflammatory conditions Histology RNA analysis
5	79	Male	+	
6	66	Male	+	

21 ($n = 9$ with triplicates of 3 different donors). A subset of cytokine stimulated SFCCs was further cultivated for 21 more days under cytokine free conditions to evaluate whether regeneration is possible (REG) ($n = 9$ with triplicates of 3 different donors). SFCCs from each donor were randomized into groups and analysis was performed in a blinded fashion by numbering samples at random.

2.3. Histological staining and immunofluorescence

Samples for histological analysis were first fixed in 4% paraformaldehyde (PFA) for 6 h and subsequently treated with 10%, 20% and then 30% sucrose solution, each for 24 h. After fixation, samples were cryo-embedded in SCEM embedding medium and cryo-sections of 8- μ m thickness were prepared using cryofilms (Sectionlab, Japan). Prior to each histological and immunohistochemical staining procedure, slices were dried for 20 min at room temperature. Von Kossa and Alizarin red staining were performed as published previously [29].

2.4. H&E and Alcian blue staining

Hematoxylin and eosin (H&E) staining was performed according to the following protocol: fixation with 4% PFA (10 min), washing with distilled water (5 min), first staining step in Harris's hematoxylin solution (7 min) (Merck, Germany), washing with distilled water ($2\times$), differentiation step in 0.25 ml of concentrated HCl in 100 ml of 70% ethanol, washing with tap water ($2\times$ 10 min), second staining step in 0.2% eosin (2 min) (Chroma Waldeck, Germany), differentiation in 96% ethanol, washing in 96% ethanol, 100% ethanol ($2\times$ 2 min), fixation with xylol ($2\times$ 2 min), covering of stained slices with Vitro-Clud[®] (R Langenbrinck GmbH, Germany).

Alcian blue staining was performed according to the following protocol: fixation with 4% PFA (10 min), washing with distilled water (5 min), 3% acetic acid (3 min), first staining step in 1% Alcian blue 8GX (Sigma-Aldrich, MO) in 3% acetic acid, pH 2.5 (30 min), washing in 3% acetic acid, washing in distilled water, second staining step in Nuclear fast red-aluminum sulfate solution (Chroma Waldeck, Germany), washing in distilled water, graded ethanol series (80%, 96%, 100%) (2 min each), fixation with xylol ($2\times$ 2 min), covering of stained slices with Vitro-Clud[®] (R. Langenbrinck GmbH, Germany):

2.5. Immunohistochemistry

Immunohistochemistry was performed according to the following protocol: rehydration with phosphate buffered saline (PBS) (10 min), blocking with 3% H₂O₂ (30 min), washing with PBS (5 min), blocking with 5% normal horse serum (Vector Laboratories, CA) in 2% bovine serum albumin (BSA)/PBS, overnight incubation with primary antibody for type I collagen and type II collagen at 4 °C (ab6308, 1:500, Abcam, UK and Ms 6B3, 1:10, quartett Immunodiagnostika, Germany), washing in PBS ($2\times$ 5 min), incubation with 2% secondary antibody (biotinylated horse anti-mouse IgG antibody, Vector Laboratories, CA) diluted in $2\times$ normal horse serum/2% BSA/PBS (30 min), washing in PBS ($2\times$ 5 min), incubation with avidin-biotin complex (VECTASTAIN[®] Elite[®] ABC HRP Kit, Vector Laboratories, CA) (50 min), washing with PBS ($2\times$ 5 min), incubation with DAB under microscopic control with time measurement (DAB peroxidase (HRP) Substrate Kit, Vector Laboratories, CA), stopping with PBS ($2\times$), washing in distilled water, counterstaining in Mayer's hematoxylin 1:2 (Sigma-Aldrich, MO), blueing in tap water (5 min), washing in distilled water, covering of stained slices with Aquatex[®] (Merck, Germany). Pictures were taken with the Axioskop 40 optical microscope (Zeiss, Germany) with AxioVision microscopy software (Zeiss, Germany).

2.6. Immunofluorescence staining-MMP-1, MMP1-3 and TUNEL

Immunofluorescence staining was used to quantify MMPs. First, the slides were air-dried at room temperature and then rehydrated with PBS for 10 min. Subsequently, unspecific binding sites were blocked with PBS/5% FCS for 30 min. Primary MMP-13 antibody (mouse anti-human; Invitrogen Thermo Fisher Scientific, monoclonal, MA5-14247) was diluted 1:200 in PBS/5% FCS/0.1% Tween[®] 20 and primary MMP-1 antibody (mouse anti-human; Invitrogen Thermo Fisher Scientific, monoclonal, MA5-15872) was diluted 1:500 in PBS/5% FCS/0.1% Tween[®] 20 and incubated according to the manufacturer's instruction for 3 h. After each incubation step, the preparation was washed 3 times with PBS/0.1% Tween[®] 20. The secondary antibody (goat anti-mouse A546; Invitrogen Thermo Fisher Scientific,

A-11003) was diluted 1:500 in PBS/5% FCS/0.1% Tween[®] 20 and applied for 2 h. In the final staining step, core staining was performed using DAPI ($1 \mu\text{g ml}^{-1}$ diluted in PBS/5% FCS/0.1% Tween[®] 20) for 15 min. After air bubble-free covering with FluoroMount covering medium, microscopic evaluation was performed with the fluorescence microscope BZ-9000A (Keyence, Germany) using the DAPI and TRITC channels. Image analysis was performed using ImageJ. In order to determine the cell number, the Find Maxima tool was used for the DAPI image, whereas the area of MMP positive signals was measured using the Color Threshold tool. TUNEL staining (Sigma Aldrich, USA) was performed according to the manufacturer's instructions. The positive control was treated with desoxyribonuclease (DNase) I (0.34 Kunitz units, Qiagen Germany) for 10 min.

2.7. Histomorphometry

Histomorphometry was performed using FIJI ImageJ 1.52i [30, 31]. H&E stained sections were used to analyze the cell count per area and cell distribution within the SFCCs. The cell count per tissue area (cells mm^{-2}) was identified from H&E overview pictures of each SFCC with $50\times$ magnification using a modified color deconvolution method [32] (for additional detail information see figure A1 and table A1). First, a free hand selection tool was used to define the region of interest (ROI) for the section outline representing the Total Area (Tt.A.) of the section. The Gap Area (Gp.A.) where no tissue was present was identified using the Color Threshold tool and subtracted from the Tt.A. to obtain the Total Tissue Area (Tt.T.A.). Next, the Color Deconvolution plugin of ImageJ with a vector to separate hematoxylin and eosin staining into each color layer was applied. Within the hematoxylin layer, the cell nuclei were identified by applying the Threshold tool of ImageJ based on their brightness within the layer. A binary image was created representing the nuclei of the cells within the section. Finally, cell count was performed from these binary images with a combination of the Particle Analysis tool in ImageJ and manual counting.

The cell count for the Tt.T.A. was performed identically for the experiments under normal and inflammatory conditions. A ROI for the Outer Area (Ot.A.) was identified with a manual selection tool for the experiment under normal conditions. For the stimulation experiment, ROIs were determined for the Ot.A. with a reduction of section diameter to 0.95 for X- and Y-axes, which then was further divided into an Outer Core Area (Ot.C.A.) and Inner Core Area (In.C.A.) by another reduction of the diameter by 0.5 for X- and Y-axes. Sections of 2 different levels per SFCC were analyzed respectively and the mean taken for statistical analysis. In order to analyze the immunohistochemically stained sections, the DAB coverage area was measured for type I collagen (Col-1) and type II collagen (Col-2), respectively.

Two to three pictures of $100\times$ magnification per section were analyzed and the mean taken for statistical analysis. Tt.T.A. was determined again by measuring the Tt.A. and subtracting Gp.A. which was identified with the Color Threshold tool in ImageJ. The area stained positive for Col-1 and Col-2 was defined by the Color Threshold tool also. Color Thresholds were determined for each set of staining separately.

2.8. RNA isolation, cDNA synthesis and qPCR

Total RNA was isolated from the SFCCs using the TissueRuptor II (QIAGEN, Germany) to homogenize the tissue and the RNeasy Fibrous Tissue Mini Kit (QIAGEN, Germany) was used to extract the RNA according to the provided protocols. RNA concentrations were measured via NanoDrop Fluorometer (Thermo Fisher Scientific, MA) and RNA integrity was confirmed via the 2100 Bioanalyzer (Agilent Technologies, CA). Sensiscript RT Kit (QIAGEN, Germany) was used for cDNA synthesis with 50 ng per reaction according to the manufacturers' instructions. Primers were designed using Primer Blast (NCBI, MD) and sequence analysis of qPCR products was performed at LGC genomics (LGS genomics GmbH, Berlin, Germany) to confirm primer specificity (for primer sequences see table 2). To analyze RNA expression, quantitative PCR (qPCR) was performed using the DyNAmo ColorFlash SYBR Green qPCR kit (Thermo Fisher Scientific, MA) at a Mx3000P qPCR System (Agilent Technologies, CA) with approximately 1.5 ng cDNA per 20 μl reaction and the following temperature profile: 7 min denaturation at 95 °C, 45 cycles of 5 s at 95 °C, 7 s at 57 °C and 9 s at 72 °C. Two technical replicas per sample and gene were performed. After each qPCR run, a melting curve analysis was performed to confirm primer specificity. In cases where no amplification curve reached the threshold before 45 cycles, the threshold-cycle value (Ct-value) was assumed to be 45. Gene expression data is shown as ΔCt -value ($=2^{-\Delta\text{Ct}}$) with normalization to the housekeeping gene *elongation factor 1-alpha (EF1A)*.

2.9. RNA isolation from human cartilage

Human cartilage was collected from femoral condyles taken during total knee replacement surgeries (ethical approval EA1/012/13). Cartilage was harvested from areas as unaffected as possible and transferred to RNAlater (QIAGEN, Germany) for 1 h at 4 °C: Before cryo-conservation at -80 °C, the RNAlater was removed completely. Cartilage samples were cryo-pulverized (59012N, Biospec, Bartlesville, OK) and gently resuspended in TriFast[™] (VWR, Germany) mixed with 1-bromo-3-chloropropane (Sigma Aldrich, MO). Centrifugation was performed after 10 min of incubation for 10 min at $10\,000\times g$. The top aqueous phase was further used for RNA isolation using the RNeasy Mini Kit (QIAGEN, Germany)

Table 2. Sequences of primers used for qPCR.

Gen symbol	Sequence of forward primer	Sequence of reverse primer
<i>EF1A</i>	5'-GTTGATATGGTTCCTGGCAAGC-3'	5'-TTGCCAGCTCCAGCAGCCT-3'
<i>COL1A1</i>	5'-AGGTCACAGGTCTCGAAAAAGC-3'	5'-CTCCTGACGCACGGCC-3'
<i>COL2A1</i>	5'-GTGGGGCAAGACTGTTATCG-3'	5'-AGGTCAGGTCAGCCATTTCAG-3'
<i>COL10A1</i>	5'-CCAGCACGCAGAATCCATCT-3'	5'-TATGCCCTGTGGGCATTTGGT-3'
<i>ACAN</i>	5'-AACGCAGACTACAGAAGCGG-3'	5'-GGCGGACAAATTAGATGCGG-3'
<i>MMP1</i>	5'-CTCTGGAGTAATGTCACACCTCT-3'	5'-TGTTGGTCCACCTTTCATCTTC-3'
<i>MMP3</i>	5'-ATCCTACTGTTGCTGTGCGT-3'	5'-CATCACCTCCAGAGTGTCCGG-3'
<i>MMP13</i>	5'-TCCTGATGTGGGTGAATACAATG-3'	5'-GCCATCGTGAAGTCTGGTAAAAAT-3'
<i>TNF</i>	5'-GTCTCCTACCAGACCAAG-3'	5'-CAAAGTAGACCCTGCCAGACTC-3'
<i>IL1B</i>	5'-AGCTACGAATCTCCGACCAC-3'	5'-CGTTATCCCATGTGTGCAAGAA-3'
<i>IL8</i>	5'-GAATGGGTTTGCTAGAATGTGATA-3'	5'-CAGACTAGGGTTGCCAGATTTAAC-3'
<i>IL6</i>	5'-TACCCCCAGGAGAAGATTCC-3'	5'-TTTTCTGCCAGTGCCCTTTT-3'

according to the protocols provided. cDNA synthesis and qPCR were performed as described above.

2.10. Statistical analysis

Statistical analysis was performed with the GraphPad Prism V.8 software. Quantitative data is shown as mean \pm SEM for gene expression data and mean \pm SD for all other data. Since the number of samples was small and Gaussian distribution was not assumed, we used the Kruskal-Wallis test with Dunn's multiple comparison as non-parametric statistical test for group differences. Each SFCC from one donor was assumed to be an individual replicate, and thus paired analysis was not performed. Statistical numbers and adjusted p-values are listed in supplementary results. A p-value of <0.05 was considered to be statistically significant. Image analysis was carried out blinded for treatment groups. Important numbers and adjusted p-values are stated either in the text or in the graphs. Due to the explorative character of this study, no sample size calculation was performed.

2.11. In silico model generation

To describe the temporal evolution of the spatial distribution of cellular and matrix-related processes in the *in vitro* model of OA, PDEs were used to interpret the experimental outcomes and to enable the identification of key steps within the progression of matrix degradation. The parameters of the *in silico* model were calibrated based on the histomorphometric *in vitro* data for distribution of type II collagen (Col-2) and cell numbers. Since each section of the SFCCs which were analyzed had a thickness of 8 μm , we transformed the dimension from area (mm^2) to volume (m^3). The geometrical shape of the SFCCs was approximated by a cylindrical form (radius $r = x = 5.0 \cdot 10^{-3}$ m and height $h = y = 4.5 \cdot 10^{-3}$ m) (figures 1 and 4A). SFCCs show a cylinder-like shape comparable to the disc form that has been described by others before [33, 34]. This cylinder-like construct was surrounded by culture medium, so that the added IL-1 β was able to diffuse

into the SFCC from all surfaces. The cylindrical form of the SFCC was radially symmetric around its center. Therefore, the computations were performed on a two-dimensional rectangle instead of the full three-dimensional domain (figures 1 and 4(A)). In this first modeling approach, we only focused on the effects of IL-1 β , although the *in vitro* model was additionally stimulated with TNF α . Based on the mathematical model by Kar *et al* (table A2) the adapted model (table 3) was obtained as described in the following. For equation (1), it was possible to distinguish between the decrease due to the matrix formation and due to IL-1 β by comparing the reduction of the cell density under non-inflammatory and inflammatory conditions in the *in vitro* models. Thus, we could identify the parameters p_1 (non-inflammatory conditions) and p_9 (inflammatory conditions) separately. Following Kar *et al*, we expected a small increase of Col-2 under non-inflammatory conditions (small value for p_2) which was negligible compared to the significant decrease induced by the MMPs [23]. Furthermore, we have omitted equation (3) for degCol-2. This component cannot be reliably measured and has no significant impact on other components. MMP measurements are only used for verification (figure 1), and therefore, parameter p_4 and the basal MMP activity p_6 —for which no estimates exist, have been omitted. Finally, in the IL-1 β equation (5), the diffusion from outside is certainly the predominant source of IL-1 β , which can also be verified e.g. by performing simulations of the model of Kar *et al* with and without a correspondingly simplified equation for IL-1 β .

The generated systems of time-dependent PDEs were solved using the state-of-the-art software package KARDOS [35, 36]. Given a user-specified accuracy tolerance, the code automatically computes numerical approximations by means of a fully adaptive grid in space and time based on local error estimates with optimal computational complexity. The graphical outputs were produced using MATLAB (Version 2017b, The MathWorks, Inc., Natick, MA).

Table 3. Reduced mathematical model of *in vitro* model resembling onset of OA.

No.	Equation	Biological reference
(1)	$\frac{\partial \text{Cell}}{\partial t} = -p_1 \text{Cell} - p_9 \text{IL Cell}$	Cell apoptosis stimulated by IL-1 β
(2)	$\frac{\partial \text{Col}}{\partial t} = -p_3 \text{MMP Col}$	Decrease of Col-2 by MMP-1/-3/-13-induced degradation
(3)	$\frac{\partial \text{MMP}}{\partial t} = D_{\text{MMP}} \nabla^2 \text{MMP} + p_5 \text{Cell IL}$	Change of MMP-1/-3/-13 due to diffusion and increased MMP-1/-3/-13 release by IL-1 β stimulated cells
(4)	$\frac{\partial \text{IL}}{\partial t} = D_{\text{IL}} \nabla^2 \text{IL}$	Diffusion of IL-1 β

3. Results

3.1. SFCCs show stable cartilage-like phenotype over 3 weeks

To evaluate the cellular and matrix composition of the SFCCs under non-inflammatory conditions, samples were taken weekly over a period of 3 weeks (d0, 7, 14, 21; $n = 3$; one sample per donor at each time point). Alcian blue staining for SFCC sections was performed at all time points and revealed the constant presence of glycosaminoglycans (GAGs) (figure 2(A)). Hematoxylin & Eosin (H&E) staining showed heterogeneity of the formed constructs but no obvious morphological changes in cell and matrix composition between time points (figures 2(A) and (B)). In addition, a layer-like structure was visible that led to a certain loose morphology as a result of the embedding procedure. Cell density decreased over the period of 3 weeks from a mean cell density of 1.378 ± 694 cells mm^{-2} at d0 to a mean cell density of 505 ± 268 cells mm^{-2} at d21 (figure 2(C)). Although this difference is not statistically significant, there is a clear biological relevance that should be considered. In addition, histomorphometry revealed a higher cell count in the Outer Area (Ot.A.) than in the Total Area (Tt.A.), indicating a spatial arrangement of cells within the construct (figure 2(C)). Type I collagen (Col-1) coverage was higher than type II collagen coverage (Col-2) although no difference could be identified between time points (figure 2(D)). qPCR analysis revealed the mRNA expression of the cartilage specific markers *COL2A1* and *ACAN*, although *COL1A1* expression was higher when compared to that of *COL2A1* (figure 2(E)). *COL10A1* expression was low in comparison with all other genes. No statistical differences were found between time points indicating a stable phenotype over time. With respect to the induction of chondrogenesis, we found a strong upregulation of *COL2A1* at day 0 when compared to monolayer MSCs (figure A3(A)). In addition, there is a more pronounced expression of *COL2A1* than *COL1A1* or *COL10A1* (figure A3(A)). Although significant differences do remain when comparing the results to native human cartilage (figure A3(B)), we did not observe osteogenic induction/mineralization (figure A4). Hence, SFCCs revealed a cartilage-like as evidenced by gene expression and histological analysis (figure 2).

3.2. Stimulated SFCCs show cellular changes and matrix degradation

To model the inflammatory environment of OA, SFCCs were treated with IL-1 β and TNF α . Both are considered to be the most important proinflammatory cytokines during the onset of OA. Cytokines were applied with concentrations of 50 ng ml^{-1} for IL-1 β , and 100 ng ml^{-1} for TNF α , representing a highly aggressive proinflammatory stimulation in order to achieve maximal effects on the SFCCs. Tissue softening was observed macroscopically by volume increase of SFCCs stimulated for 3 weeks (STIM) compared to untreated controls (CTL) which was partly reversed after 3 additional weeks without cytokine treatment (REG) (figures 3(A) and A2). This observation was supported by histological H&E staining, microscopically indicating pronounced water retention, maceration of the superficial cell layer and morphological changes in cell phenotypes in the STIM group (figure 3(B)). Immunohistological analysis showed a constant Col-1 coverage with no statistically significant differences between groups (figure 3(C)). Col-2 coverage however decreased after stimulation with IL-1 β and TNF α to a mean coverage of $14.4 \pm 5.5\%$ (STIM) and moreover significantly to $8.8 \pm 5.9\%$ (REG), when compared to the untreated controls ($25.3 \pm 4.7\%$; figure 3(C)). Histomorphometry revealed statistically significant changes between groups in cell count per area for the Tt.A., Ot.A. and Outer Core Area (Ot.C.A.; figure 3(D)). Therefore, a lower cell density was observed in the STIM group compared to the CTL, while slight changes were also seen in the REG group compared to CTL. No significant differences were found in the In.C.A. (figure 3(D)). TUNEL staining showed a few TUNEL positive cells in the CTL group while more TUNEL positive cells were found in the STIM group (figure A5).

On mRNA level, *COL1A1* was significantly down-regulated upon cytokine stimulation in comparison with controls (figure 4(E)). The gene expression of *COL2A1* and *ACAN* was obviously lower in the STIM and REG group. Interestingly, *COL10A1* was upregulated in the REG group (figure 3(E)). As expected, gene expression levels of the inflammatory markers *IL1*, *IL6* and *IL8* were significantly upregulated compared to untreated controls (figure 3(F)). Gene expression of *TNF* was not found to be different

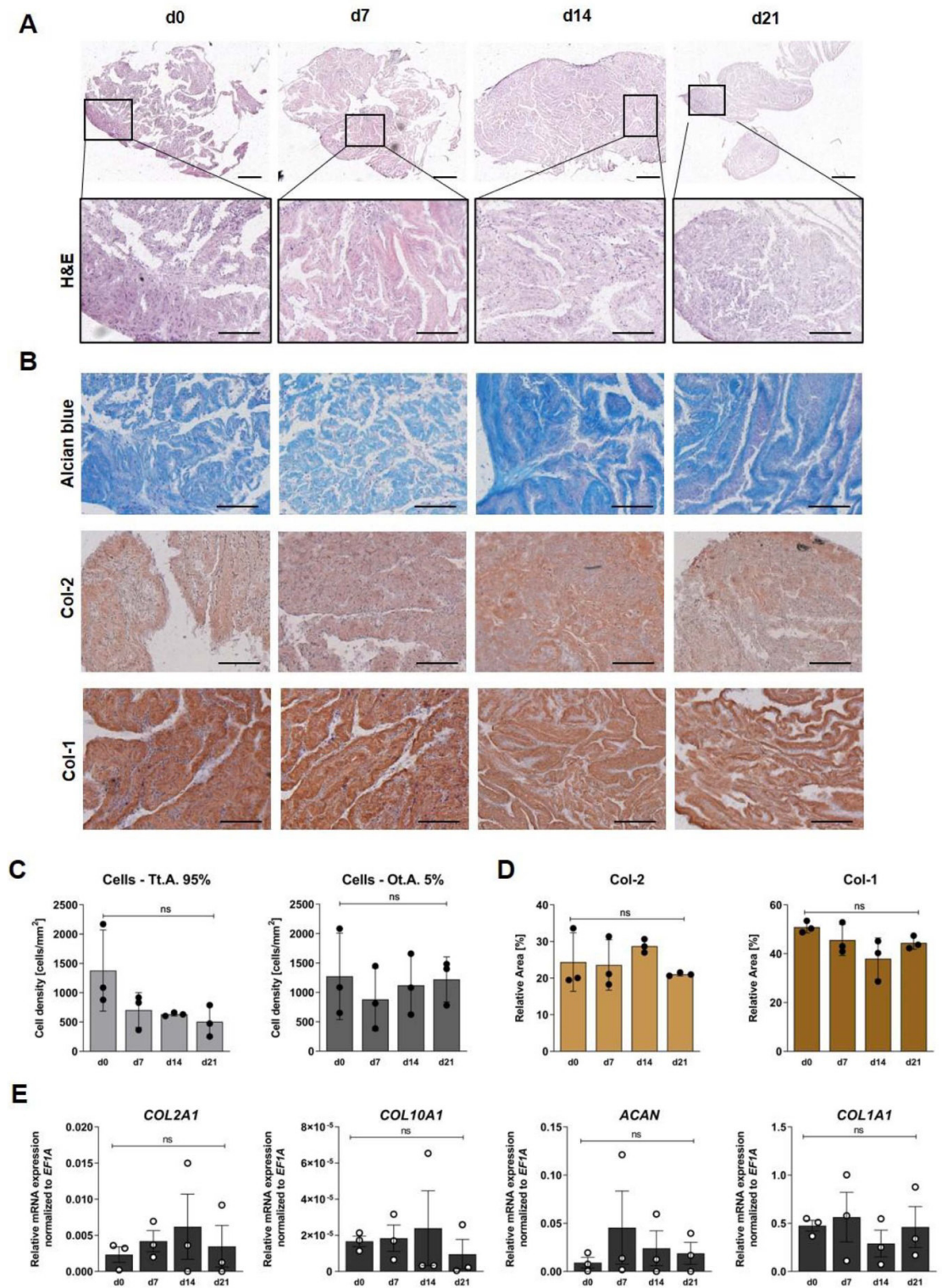


Figure 2. Experimental results after cultivating SFCCs for 3 weeks under non-inflammatory conditions. (A) Exemplary images of histological staining with hematoxylin & eosin (H&E) in two different magnifications. (B) Exemplary images of Alcian blue staining, Col-2 and Col-1 immunohistochemistry, scale bars = 200 μm at 100 \times magnification. (C) Histomorphometry results for cell count within total area (Tt.A.) and outer area (Ot.A.). X-axes show time points from d0–d21, y-axes show cell count [cells m^{-3}], bars indicate mean \pm SD and individual data points. (D) Immunohistochemistry coverage for Col-2 and Col-1. X-axes show time points from d0–d21, y-axes show relative coverage area in %, bars indicate mean \pm SD and individual data points. (E) Gene expression studied via qPCR for *COL2A1*, *COL10A1*, *ACAN* and *COL1A1*. X-axes show time points from d0–d21, y-axes show relative mRNA expression normalized to the housekeeper *EF1A* graph bar with mean \pm SEM and individual data points. Statistical differences between groups were tested with the Kruskal-Wallis test and Dunn's multiple comparisons test (see also table A3). ns = $p > 0.05$.

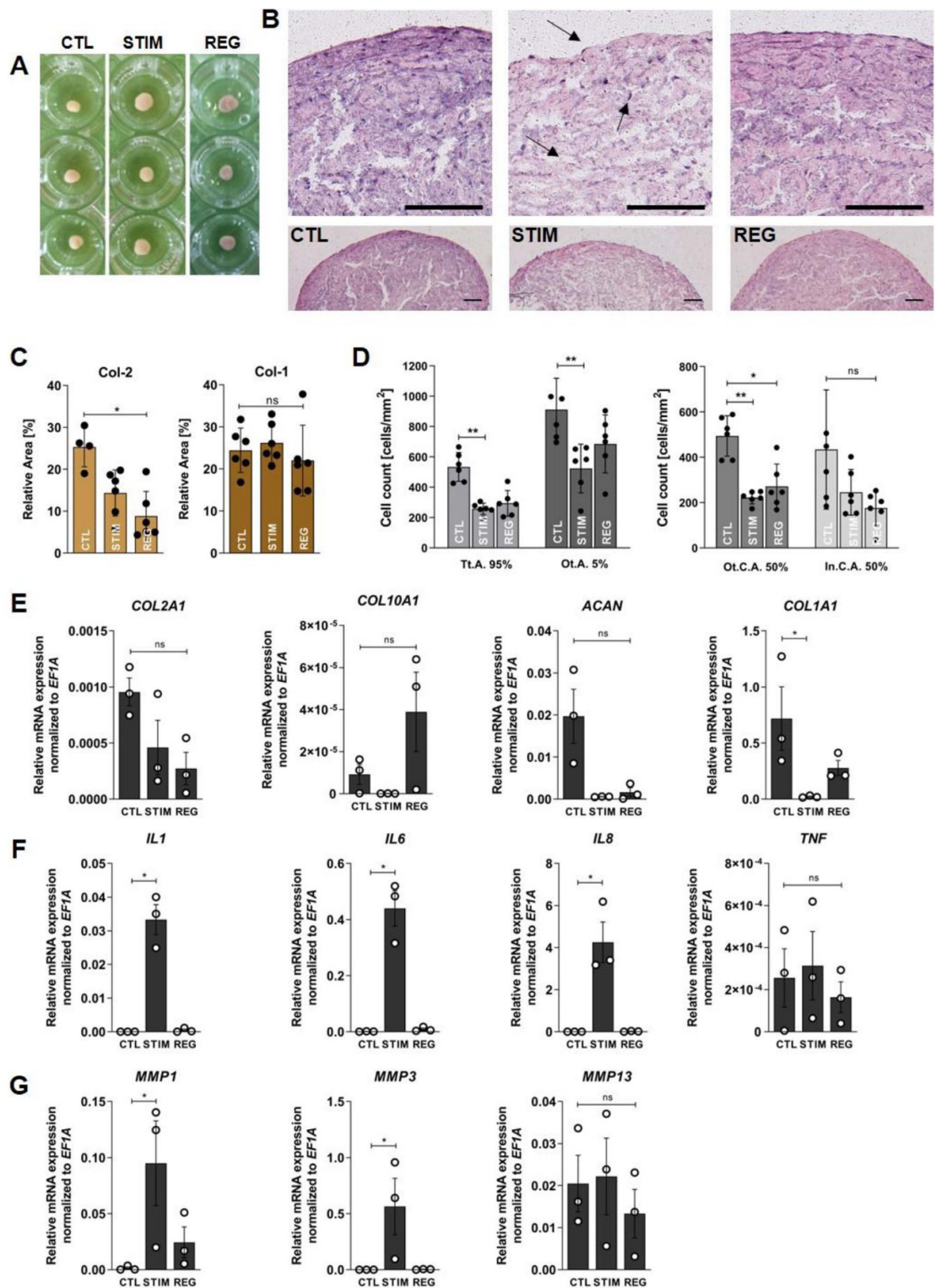


Figure 3. Experimental results after cultivating SFCCs for 3 weeks under non-inflammatory conditions (CTL), with $IL-1\beta$ and $TNF\alpha$ (STIM) or under non-inflammatory conditions for additional 3 weeks after stimulation (REG). (A) Macroscopic overview on different SFCCs exemplary for each condition. (B) Exemplary images of SFCCs stained with H&E for CTL, STIM and REG group. Scale bars = 200 μm . Arrows indicate tissue softening and changes of cellular phenotypes. (C) Immunohistochemistry coverage for Col-2 and Col-1. *x*-axes show experimental groups, *y*-axes show relative coverage area in %, bars indicate mean \pm SD and individual data points. (D) Histomorphometry results for cell count per area within total area (Tt.A.), outer area (Ot.A.), outer core area (Ot.C.A.) and inner core area (In.C.A.). *x*-axes show time points from d0–d21, *y*-axes show cell count [cells m^{-3}], bars indicate mean \pm SD and individual data points. (E)–(G) Gene expression studied via qPCR. Graph bar show with mean \pm SEM and individual data points. Statistical differences between groups were tested with the Kruskal-Wallis test and Dunn's multiple comparisons test (see also tables A4 and A5). ns = $p > 0.05$, * $p < 0.05$, ** $p < 0.01$.

between the experimental groups. However, *IL1*, *IL6* and *IL8* were numerically diminished in the REG compared to the STIM group although no statistical significance was detected (figure 3(F)). *MMP1* and

MMP3 were significantly upregulated in the cytokine-treated group compared to the CTL group and numerically downregulated in the REG compared to the STIM group (figure 3(G)). There were no significant differences in gene expression for *MMP13* within the experimental groups. In summary, stimulation with IL-1 β and TNF α leads to OA-like changes which can be observed *in vivo* during the early phase of the disease. Additional cultivation for 3 weeks without cytokines after stimulation did partially reverse those changes.

3.3. Refining an existing mathematical model result in a reduced PDE model of the *in vitro* observations

In order to focus on the main processes of cartilage degradation expected during OA onset, the *in silico* model was built on the assumption that under non-inflammatory conditions, the chondrocytes (termed here as cells) produce ECM (here mainly Col-2) while under inflammatory conditions with the addition of IL-1 β , cells release MMPs, which then degrade the ECM, and potentially go into apoptosis (see figure 1). Within the mathematical model, we focused on the specific Col-2 degrading enzymes MMP-1, -3 and -13. Table 3 shows the underlying equations derived from the pathway described above and our *in vitro* observations (adapted from [23]). Considering the underlying *in vitro* experiments and the complexity of the derived *in silico* model, it was necessary to derive a reduced model preserving our *in vitro* observations and the underlying biology.

First, we studied the stability of the homogeneous nonlinear dynamical system derived from our reduced order model by neglecting diffusive processes. It turned out that all states of equilibrium are Lyapunov stable, i.e. small perturbations of the equilibrium points stay small for all times. Next, applying a sensitivity analysis, we found out that all parameters exhibit sufficiently large sensitivities with respect to variations in cell and Col-2 concentrations. This formed the basis for our parameter calibration described in the following.

In table 4 the parameter values, initial values and the boundary conditions to solve the mathematical (PDE) system are described. Concerning the parameter values, the cell apoptosis rate p_1 was fitted by a least squares approach, utilizing measurements of the cell concentration ($n = 3, d = 0, 7, 14, 21$). Since the MMP-1/-3/-13 measurements have been neglected up to now, the diffusion coefficient is taken from the literature (MMP-1 [37]). The remaining parameters have been calibrated with our *in vitro* observations using a least squares fitting. For MMP-1/-3/-13, we assumed that there are homogeneous Neumann boundary conditions for all surfaces. Because the evolution of the cell number and Col-2 was described by ODEs, i.e. where no diffusion is present, there exist no boundary conditions for these components.

Due to the diffusion of IL-1 β into the SFCC with a constant concentration of IL-1 β in the surrounding media, inhomogeneous Dirichlet boundary conditions were assumed to be present on the outer surfaces. For the inner surface of the construct (center of the cartilage construct), homogeneous Neumann boundary conditions were applied ensuring the symmetry assumption on the SFCC.

3.4. Modeling the *in vitro* findings of cytokine-stimulated SFCCs *in silico* to resemble basic processes of cartilage degradation

Since the cells are inhomogeneously, spatially distributed (figure 2), we determined an initial distribution based on the *in vitro* observations (figure A6). Computational results of the *in silico* model are shown in figure 4. The model described in table 1 makes it possible to represent the *in vitro* experiments. Under proinflammatory stimulation with IL-1 β , the cell number decreased over time given the initial distribution (first row of figure 4(B)), which matches the *in vitro* measurements (figure 3(D)). Col-2 decreased spatiotemporally assuming a homogeneous initial distribution (second row in figure 4(B)). Since IL-1 β entered from the outside and stimulated the MMP-1/-3/-13 production, MMPs increased on the boundaries first and diffused further into cartilage (third row in figures 4(B) and (C)). Under non-inflammatory conditions, the IL-1 β concentration was assumed to be zero. This also holds true for MMP-1/-3/-13 (see table 3, equations (3) and (4)). Thus, Col-2 was constant over time and cells decrease only due to matrix formation leading to a representation of the healthy state observed *in vitro* as well.

To predict cellular and matrix-related changes over a longer time period (5 weeks) and a 10-fold lower concentration of IL-1 β stimulation (5 ng ml⁻¹) - which is more comparable to the *in vivo* situation - we accordingly adapted the *in silico* model. We observed a full penetration of IL-1 β and MMP-1/-3/-13, a fast decline in the cell number, but a rather slower Col-2 degradation when compared to the 3 weeks simulation which had higher IL-1 β concentrations (supplementary video (available online at stacks.iop.org/BF/12/045016/mmedia) Appendix A).

3.5. MMP staining in the SFCCs verifies *in silico* simulations

In order to verify the mathematical model, MMP-1 and MMP-13 were stained via immunofluorescence for CTL, STIM and REG sections and analyzed for their spatial distribution and displayed as a sum of that. Therefore, MMP coverage normalized to the cell number was slightly higher in the STIM group (figure 4(D)). The relative MMP coverage was lower in the inner core area (In.C.A.) than it was in that of the Ot.C.A. (figures 4(E) and (F)). This also matches the

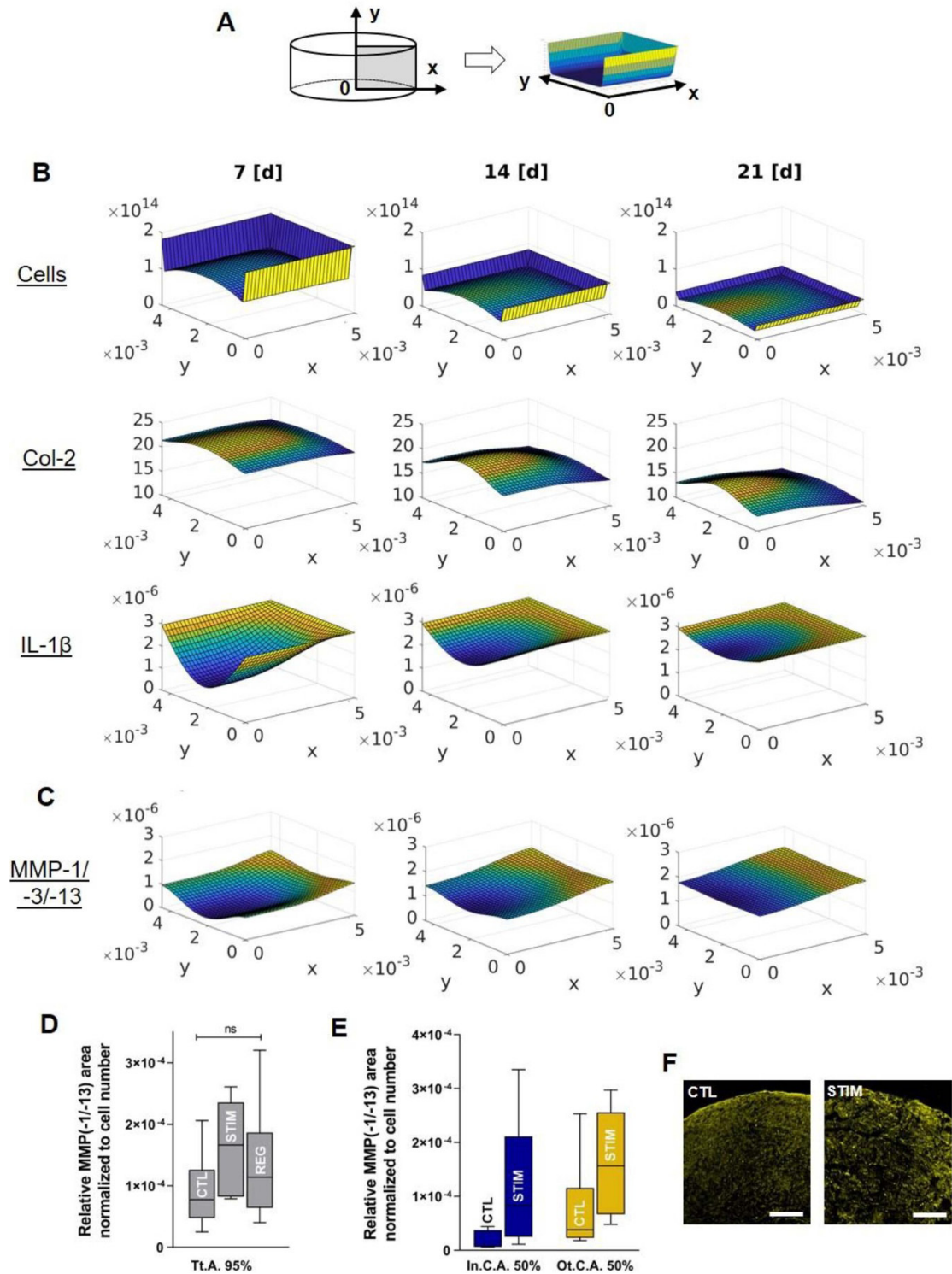


Figure 4. Results from the *in silico* model. (A) Explanation of the dimensions and axes. (B) Spatial-temporal development of Cell [1 m^{-3}] (first row), Col-2 [%] (second row), IL-1 β [mol m^{-3}] (last row) and (C) MMP-1/-3/-13 [mol m^{-3}] (third row) over 3 weeks. The PDE model described in Table 3 was solved with the adaptive finite element toolbox KARDOS [24, 25] and MATLAB. (D) MMP-1/-13 were stained in CTL, STIM and REG and normalized to the cell count (total area = Tt.A.). (E) Quantitative analysis was performed for inner core (In.C.A.) and outer core area (Ot.C.A.) for CTL and STIM are only to be compared to the results from the *in silico* model. Graphs show box and whiskers plots (Min-Max). (F) Exemplary images for MMP-1 staining of CTL vs. STIM. The scale bar indicates $200 \mu\text{m}$.

Table 4. Parameter list, initial values and boundary conditions for reduced PDE model (table 3).

Parameter	Description	Value	Unit	Reference/Source
p_1	Chondrocyte natural apoptosis rate	0.0601	$[\frac{1}{d}]$	Least-squares parameter using <i>in vitro</i> data
p_9	Apoptosis rate due to IL-1 β	17280	$[\frac{m^3}{mol \cdot d}]$	Own calibration
p_3	Col-2 degradation rate	25000	$[\frac{m^3}{mol \cdot d}]$	Own calibration
D_{MMP}	Diffusivity of MMP-1	$8.64 \cdot 10^{-8}$	$[\frac{m^2}{d}]$	[37]
D_{IL}	Diffusivity of IL-1 β	$1.728 \cdot 10^{-7}$	$[\frac{m^2}{d}]$	Own calibration
p_5	MMP-1/-3/-13 production due to IL-1 β	$5.31 \cdot 10^{-16}$	$[\frac{m^3}{d}]$	Own calibration
Initial values				
$Cell_0$	Initial cell concentration	Supplemental results figure 2	$[\frac{1}{m^3}]$	H&E staining <i>in vitro</i> data
Col_0	Initial Col-2 volume fraction	23.56	[%]	Average of histochemical <i>in vitro</i> data
MMP_0	Initial MMP-1/-3/-13 concentration	0	$[\frac{mol}{m^3}]$	Basal MMP-1/-3/-13 activity is almost zero and thus negligible
IL_0	Initial IL-1 β concentration	0	$[\frac{mol}{m^3}]$	Only diffusion from the outside to the inside of the cartilage
Boundary conditions				
MMP	$D_{MMP} \nabla MMP = 0$			No transfer of MMP-1/-3/-13 to culture medium, matches <i>in vitro</i> observations
IL	$D_{IL} \nabla IL = 0$ for $x = 0$ (figure 5(A)); $IL = \frac{50 \cdot 10^{-6}}{17} [\frac{mol}{m^3}]$			Constant IL in culture medium and radial symmetry at $x = 0$ (molecular weight of IL is 17 kDA)

results gained from the *in silico* model and nicely verifies our approach.

4. Discussion

Since multiple approaches and a variety of OA model systems are necessary to fully understand the complexity of this disease, we here report on a successful combination of *in vitro* and *in silico* modeling to simulate the main features of OA, matrix degradation and the upregulation of proinflammatory cytokines induced by stimulating scaffold-free cartilage-like constructs with IL-1 β and TNF α .

In most cases, cartilage explants or monolayer cell cultures are used as an *in vitro* model to study OA and its underlying mechanism or to test potential therapeutic options. However, there are some studies using tissue-engineered cartilage for their experiments such as those of Mohanraj *et al* reported similar outcomes using tissue-engineered cartilage compared to cartilage explants in a model of post-traumatic OA [10, 38]. However, most studies on tissue engineered cartilage still focus on the development of regenerative approaches for cartilage repair and do not consider using their tissues as *in vitro* models for the study of cartilage and OA pathophysiology [12, 14, 15, 39, 40]. SFCCs revealed a cartilage-like phenotype detected by gene expression and histological analysis (figure 2); however, significant differences do remain when comparing the results to native human cartilage (figure A3(B)). Thus, the gene expression of *COL1A1* and the presence of Col-1 on a protein level were still visible in all SFCCs examined. hMSCs have the potential to differentiate into different lineages including the chondrogenic, osteogenic and adipogenic lineage, although it has not been yet described that MSCs can fully form human articular cartilage *in vitro* or *in vivo*. The major challenges to achieve full phenotypic conversion are the profound induction of chondrogenesis as indicated by e.g. upregulated *COL2A1* expression (figure A3(A)) and the maintenance of the chondrogenic phenotype over a longer time period (figures 2(C)–(E)). The 3D structure of the SFCCs was gained through biomechanical loading [41, 42]. However, it is clear that further improvements can be achieved by e.g. adding transforming growth factor beta (TGF β) [13, 15, 41], using culture regimes that are specifically adapted to the timepoint of chondrogenesis [18, 43] or using iPSCs as cell source [44, 45]. Of note, we could not observe hypertrophic cells or mineralization which has been described for mesenchymal condensation *in vitro* [16, 46]. By using a macroscale approach (constructs app. 0.5 cm diameter), we avoid the disadvantages of pellets regarding their physiologically irrelevant size, geometry, high cell number and density compared to the matrix and mechanical properties [15].

The *in vitro* simulation of the inflammatory environment in OA through a cytokine treatment

with IL-1 β at 50 ng ml⁻¹ and TNF α at 100 ng ml⁻¹ allowed us to observe significant changes in the SFCCs with regard to a decrease in cell density and matrix degradation (figure 3) [47, 48]. Although the *in vivo* concentrations for IL-1 β and TNF α are known to be much lower as demonstrated in synovial fluid of patients suffering from knee OA [49], cytokine concentrations of 1–100 ng ml⁻¹ are usually applied when mimicking the proinflammatory environment in early OA *in vitro*. The latter situation is necessary in order to shorten the length for treatment by adapting the *in vitro* experiments, because the chronic degenerative joint disease OA in humans usually evolves over decades. IL-1 β and TNF α do not only contribute to the upregulation of proteases but also inhibit the synthesis of ECM molecules, mainly Col-2 and aggrecan [50, 51]. MMPs are one predominant group of enzymatic proteins which plays an important role in the pathogenesis of OA [3, 52]. In both our *in vitro* studies and in the *in silico* model, we focused on MMP-1, -3, and -13 as main Col I and II degrading enzymes [53] since MMP-2 (gelatinase A) and MMP-9 (gelatinase B) are known to interact with Col IV (MMP-2) and are mainly involved in wound healing (both) or bone development (MMP-9) [54–56]. Furthermore, MMP-9 is induced by MMP-3 and -13 [57].

Mathematical models are very flexible, enabling adjustments and testing of various hypotheses in parallel. However, biological experiments are most often complex, expensive and resource-demanding, leading to a gain of less experimental data than model parameters can provide [58]. Thus, problems with model non-identifiability can occur, since model parameters cannot be estimated properly. Experimental design approaches aim to resolve these problems by identifying the data gap and proposing the required additional experimental data. The flexibility of mathematical models including experimental design can be used to structure future *in vitro* or *in vivo* models efficiently. However, the first considered mathematical model, which takes most of the prominent mechanisms of OA pathogenesis into account, has unidentifiable parameters (table A2). Its applicability is nevertheless limited, since neither enough experimental human data nor reliable literature-based parameters are available for model calibration and validation. This means that more quantitative measurements of the components at different time and spatial points are needed. The reduced model, however, does allow us to reproduce the experimental data with significantly fewer parameters (table 3). Validation concerning MMP-1/–13 measurements which were not used to calibrate the model indicates that the reduced *in silico* model is suited to investigate the influence of different targets for matrix degradation (figure 4). In addition, the Supplementary video in this article shows the feasibility of the *in silico* model as a prediction tool for further *in*

vitro experiments. The observed fast decline in the cell number accompanied by a slower Col-2 degradation is in accordance with a previously published study indicating a high chondrocyte death before matrix changes occur [59]. In comparison to the model described by Kar *et al* [23], our model still considers changes of the cell concentration in space as well as over time. A more detailed analysis of the model proposed by Kar *et al* revealed IL-1 α as the driving force in the model, while MMP-1/-3/-13, Col-2 and degraded Col-2 only have a small influence on the remaining components. Thus, the simplified model in our study displays the same features but at the same time involves a smaller number of parameters and uncertainties. Other mathematical simulation approaches for OA cartilage degradation and cartilage focus on e.g. poroelastic models or coupling cellular phenotype and mechanics [26, 60, 61].

Nevertheless, there are many ways to foster the current approach. The proposed *in vitro* model displays only one specific part of the disease and includes only one tissue type, although OA has been described as a whole organ disease including several tissues such as the synovial membrane and the subchondral bone. Thus, we are currently working on a more complex whole joint model for both *in vitro* and *in silico* aspects. Furthermore, biomechanical loading has not yet been addressed within the first *in vitro* and *in silico* models presented here, although one's awareness of its tremendous impact has already been published [62]. Moreover, we shortened the experimental time window by using high concentrations of the proinflammatory cytokines IL-1 β and TNF α in our experiments. That bridges the long-lasting cumulative effect of these cytokines over years and decades in the course of OA pathogenesis. Finally, an extension of the *in silico* model should include the treatment with TNF α due to its important role in OA. For a profound model validation and parameter fitting, more quantitative *in vitro* data will be necessary.

5. Conclusion

In this study, we describe a human 3D *in vitro* model based on SFCC (mesenchymal condensation) which simulates the main features of cartilage degradation— inflammation and upregulation of matrix degrading enzymes. Advantages of such a model include the 3D environment, the possibility for mid-throughput analysis, a sufficient sample volume (macroscale) for several analyses and a wide availability of tissue-engineered cartilage with more scaffold-free approaches emerging. With the

combination of *in vitro* and *in silico* modeling, we aim to allow the immediate adaptation and modifications of different models. We strived to develop a mathematical model to refine and optimize the *in vitro* model and vice versa, especially regarding the development of a whole joint *in vitro/in silico* model.

Acknowledgments

The authors would like to thank Manuela Jakstadt for her excellent technical assistance. Bone-marrow was provided by the Tissue Harvesting Core Facility of the BIH Berlin. We also thank Kar *et al* for making their mathematical model available for our study. The scientific discussions with David Smith (The University of Western Australia) and Atte Eskelinen (University of Eastern Finland) were very helpful and greatly appreciated. AL, FB, AD, MP and TG are members of Berlin-Brandenburg research platform BB3R and Charité 3^R. This study was funded by the German Federal Ministry for Education and Research (BMBF) (project No. 031L0070) and partly by the Wolfgang Schulze Foundation ('ArthroMo'). The work of SR was partly funded by the Trond Mohn Foundation. The work of TG was funded by the Deutsche Forschungsgemeinschaft (353142848). AL is currently being supported by the Joachim Herz Foundation. Additionally, the project was distinguished with the Berlin-Brandenburg Award for Alternatives to Animal Testing 2019 (AL and RE as official awardees). Funding bodies did not have any role in designing the study, in collecting, analyzing and interpreting the data, in writing this manuscript, and in deciding to submit it for publication.

Authors contributions

AL, SR, FB and RE designed the study. MCW, AD, MP, TG, FB and AL collected, analyzed and interpreted data on the *in vitro* model. IP generated SFCCs. LF, SG, JL, SR and RE developed mathematical model and performed simulations. AL, RE, MCW, AD and LF discussed and optimized mathematical model. MCW, LF, SG, RE and AL prepared the main manuscript text. All authors contributed to writing or reviewing the manuscript and final approval.

Conflict of interest

The authors declare no conflict of interests.

Appendix A

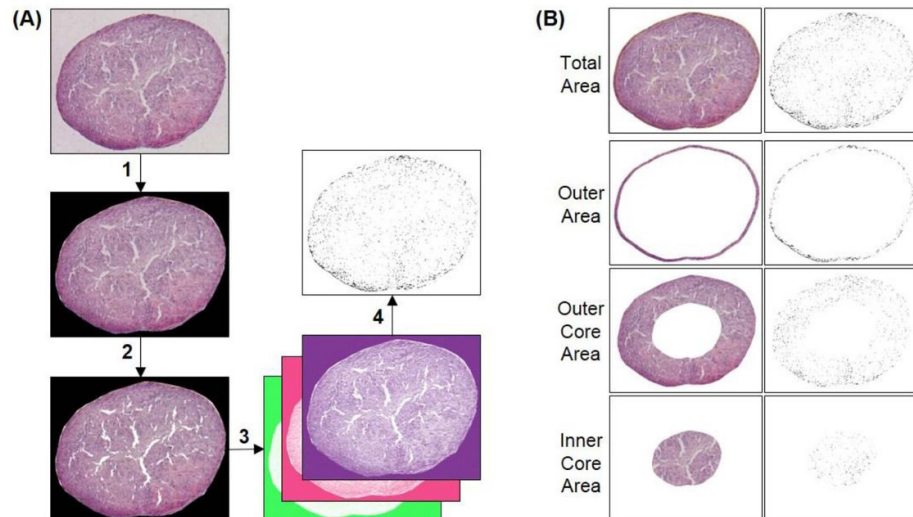


Figure A1. Pipeline for histomorphometric analysis. (A) Histomorphometric analysis for cell count per area using a modified color deconvolution method. A $50\times$ magnification overview image of an H&E stained section was taken. The section outline was defined using the Polygonal Selection tool in ImageJ (1). In order to subtract the background (or gap area) the Color Threshold tool was utilized (2). Next, the Color Deconvolution plugin (3) was used to obtain the hematoxylin color channel only in which the cell nuclei could be identified using a threshold for brightness (4). Particle analysis could then be performed based on the binary image attained in the previous step to obtain the cell count per area [cells mm^{-2}]. (B) For further analysis, the ‘Total Area’ was further divided into an ‘Outer Area’ by scaling the region of interest (ROI) for ‘Total Area’ to 0.95 for X- and Y-axes. The remaining ‘Core Area’ was then divided into an ‘Outer Core Area’ and an ‘Inner Core Area’ by scaling the ROI for the ‘Core Area’ by 0.5 for the X- and Y-axes.

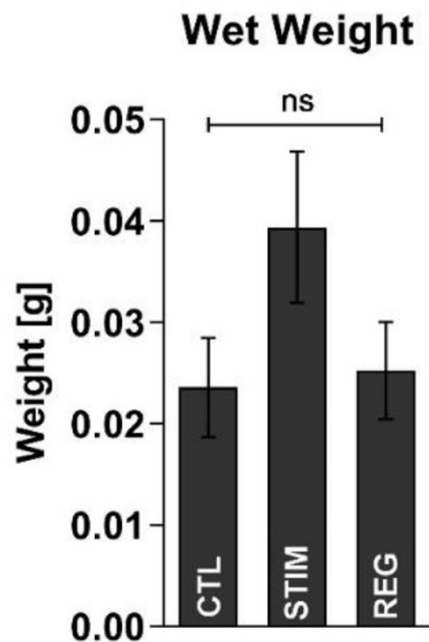


Figure A2. Comparison of the wet weight after stimulation for 3 weeks. The increase in the wet weight indicates water retention induced by matrix degradation. Graph bars show with mean \pm SEM. Statistical differences between groups were tested with the Kruskal-Wallis test and Dunn’s multiple comparisons test.

Table A1. Histomorphometry parameters.

Histomorphometry parameter	Description	Abbreviation	Unit
<i>Both experimental set-ups</i>			
Total Area	Total section area as determined by a Polygonal Selection tool in ImageJ based on overview images of full size sections.	Tt.A.	[mm ³]
Gap Area	Gap or background area of sections determined by the Color Threshold in ImageJ.	Gp.A.	[mm ³]
Total Tissue Area	Total tissue area determined by the subtraction of gap area from total area (Tt.A.—Gp.A.)	Tt.T.A.	[mm ³]
Cell count per Area	Number of cell nuclei identified by histomorphometry in relation to the total tissue area		[cells mm ⁻³]
<i>Steady state experiment</i>			
Outer Area	Outer border of SFCC determined by a free hand selection tool in ImageJ.	Ot.A.	[mm ³]
Core Area	Outer area subtracted from the total area	C.A.	[mm ³]
<i>Stimulation experiment</i>			
Outer Area	Outer border of SFCC determined by a reduction of the diameter by 0.95 for X- and Y-axes	Ot.A.	[mm ³]
Outer Core Area	Outer area subtracted from total area, diameter reduced by 0.5 for X- and Y-axes, outer part of the remaining area represents the outer core area, the inner part the inner core area.	Ot.C.A.	[mm ³]
Inner Core Area		In.C.A.	[mm ³]

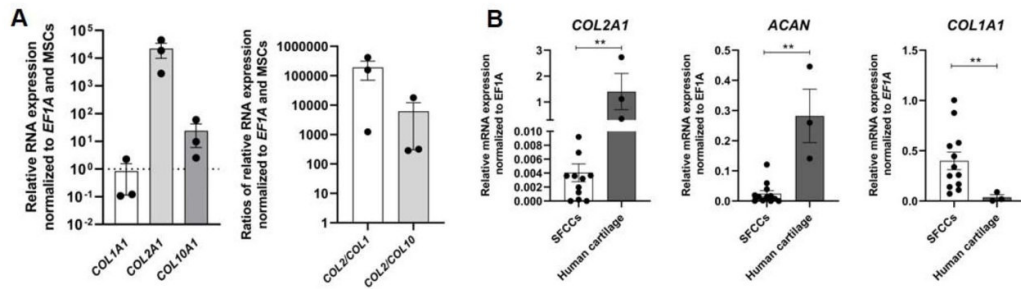


Figure A3. RNA expression of *COL1A1*, *COL2A1* in *italic* and *ACAN* in SFCCs compared to undifferentiated monolayer hMSCs and native human cartilage. (A) Relative mRNA expression ($2^{-\Delta\Delta C_t}$) normalized to the housekeeper *EF1A* and MSCs and *COL2/COL1* and *COL2/COL10* ratio; (B) Relative mRNA expression ($2^{-\Delta C_t}$) normalized to the housekeeper *EF1A* graph bar with mean \pm SEM. For SFCCs all data from d0-21 were grouped together (figure 2(D)). Cartilage was collected from three different donors from almost unaffected sites (femoral condyles). Statistical differences between groups were tested with the Mann-Whitney test. ** $p < 0.01$. Graph bars with mean \pm SEM and individual data points.

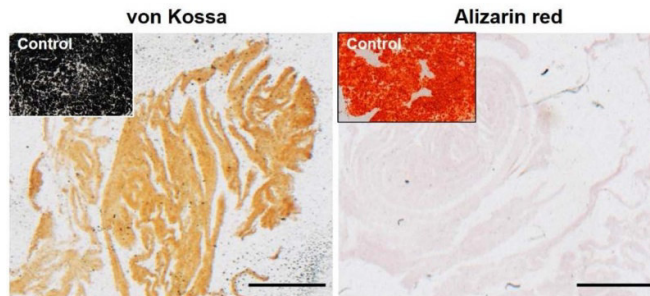


Figure A4. Exemplary von Kossa and Alizarin red staining of SFCCs at day 21 compared to a control which was treated during SFCC generation with osteogenic induction medium. Scale bars = 200 μm at 100 \times magnification.

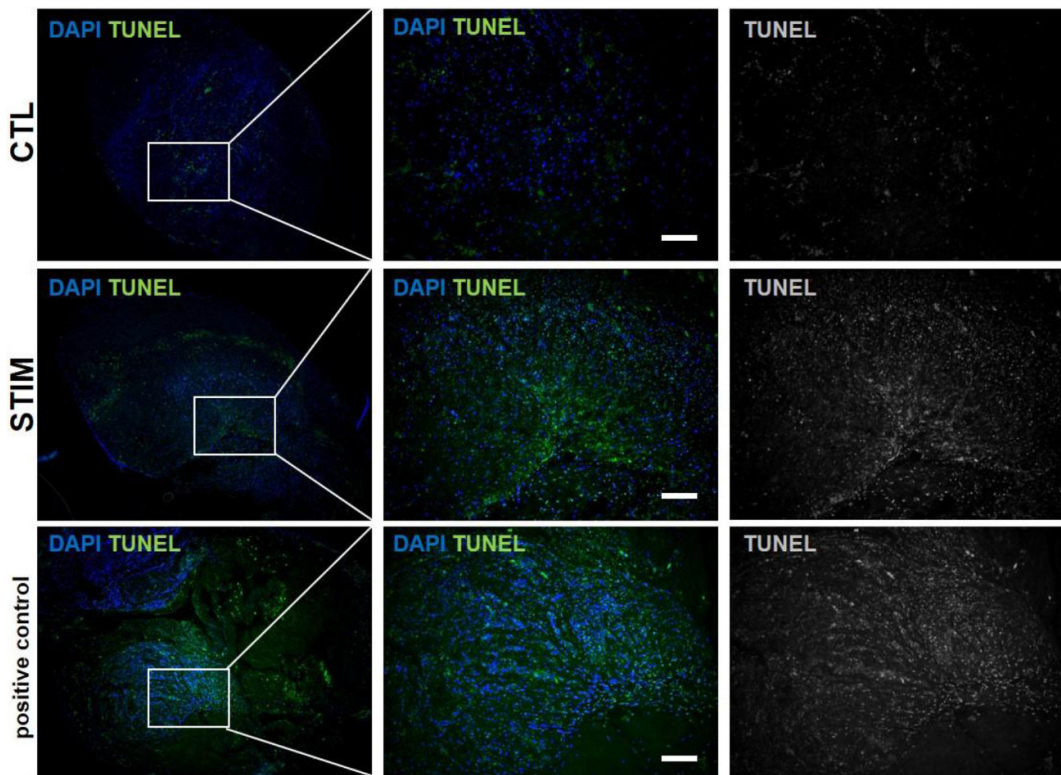


Figure A5. Exemplary TUNEL staining of SFCCs at day 21 comparing CTL and STIM. Scale bars = 200 μm . Positive control was treated with DNase I prior to staining.

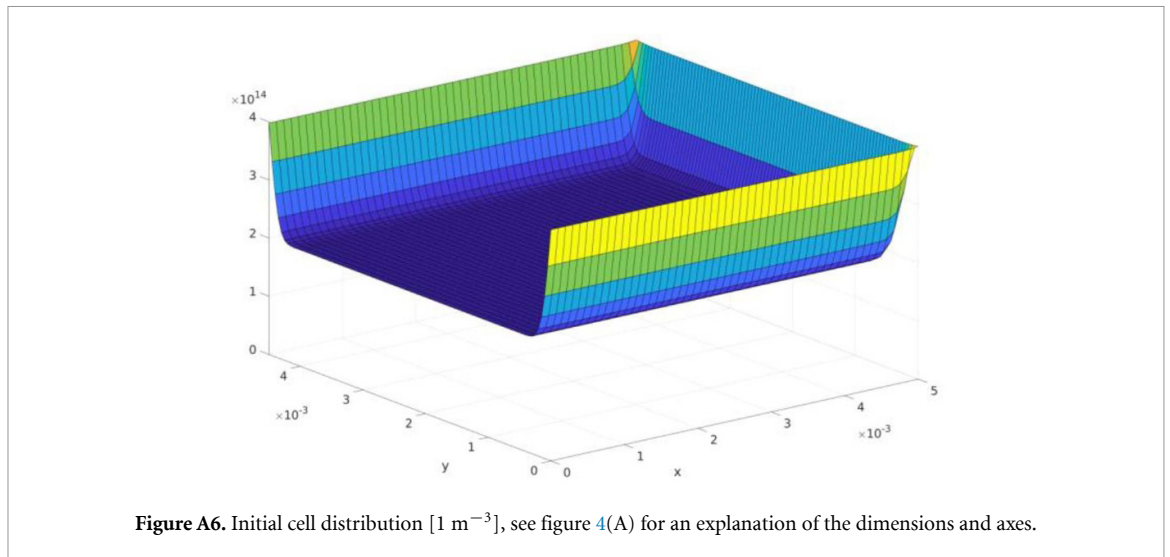


Figure A6. Initial cell distribution [1 m⁻³], see figure 4(A) for an explanation of the dimensions and axes.

Table A2. PDE model of the *in vitro* model resembling the onset of OA modified from Kar et al [23].

No.	Equation	Biological reference
(1)	$\frac{\partial \text{Cell}}{\partial t} = -p_1 \text{Cell} - p_9 \text{IL Cell}$	Cell apoptosis stimulated by IL-1 β
(1.1)	$-p_1 \text{Cell}$	Normal decrease due to ECM formation
(1.2)	$-p_9 \text{IL Cell}$	Cell apoptosis due to IL-1 β
(2)	$\frac{\partial \text{Col}}{\partial t} = p_2 \text{Cell} - p_3 \text{MMP Col}$	Increase of Col-2 over time depending on cell concentration and decrease of Col-2 by MMP-induced degradation
(2.1)	$+p_2 \text{Cell}$	Production by cells
(2.2)	$-p_3 \text{MMP Col}$	Degradation by MMPs
(3)	$\frac{\partial \text{degCol}}{\partial t} = D_{\text{degCol}} \nabla^2 \text{degCol} + p_3 \text{MMP Col}$	Change of degraded Col-2 due to diffusion, and its source—degradation of Col-2 caused by MMPs
(3.1)	$+D_{\text{degCol}} \nabla^2 \text{degCol}$	Diffusion of degCol-2
(3.2)	$+p_3 \text{MMP Col}$	Production by MMP-based Col-2 degradation
(4)	$\frac{\partial \text{MMP}}{\partial t} = D_{\text{MMP}} \nabla^2 \text{MMP} - p_4 \text{MMP degCol} + p_5 \text{Cell IL} + p_6$	Change of MMP due to diffusion, and its source—increased MMP release by IL-1 β stimulated cells
(4.1)	$+D_{\text{MMP}} \nabla^2 \text{MMP}$	Diffusion of MMP
(4.2)	$-p_4 \text{MMP degCol}$	MMP activity decreases by degradation of Col-2
(4.3)	$+p_5 \text{Cell IL}$	Production by IL-1 β stimulated cells
(4.4)	$+p_6$	Basal MMP activity
(5)	$\frac{\partial \text{IL}}{\partial t} = D_{\text{IL}} \nabla^2 \text{IL} - p_5 \text{Cell IL} - p_7 \text{IL} + p_8 \text{Cell IL}$	Change of IL-1 β due to diffusion, and its source—increased by stimulated cells
(5.1)	$+D_{\text{IL}} \nabla^2 \text{IL}$	Diffusion of IL-1 β
(5.2)	$-p_5 \text{Cell IL}$	Decrease by IL-1 β induced cell apoptosis
(5.3)	$-p_7 \text{IL}$	Natural decrease of IL-1 β —consumption
(5.4)	$+p_8 \text{Cell IL}$	Production by stimulated cells

Cell in 1 m⁻³ = chondrocytes/differentiated hMSCs; Col = Col-2 volume fraction; degCol = degraded Col-2 volume fraction; MMP = Matrix-metalloproteinases; IL = Interleukin-1 β

Table A3. Results from the Kruskal-Wallis test for figure 2.

Figure 2	Specification	Kruskal-Wallis test	
		H	p-value
B	Cells - Tt.A. 95%	6.39	0.79
	Cells - Ot.A. 5%	0.15	0.99
C	Col-1	5.77	0.12
	Col-2	1.97	0.63
D	COL1A1	2.93	0.62
	COL2A1	7.45	0.09
	ACAN	2.23	0.74
	COL10A1	4.57	0.37

Table A4. Results from the Kruskal-Wallis test for figure 3.

Figure 3	Specification	Kruskal-Wallis test	
		H	p-value
C	Col-1	2.68	0.27
	Col-2	8.59	0.006
D	Tt.A. 95%	10.71	0.001
	Ot.A. 5%	9.36	0.004
	Ot.C.A. 50%	10.33	0.002
	In.C.A. 50%	5.07	0.075
E	COL1A1	6.49	0.012
	COL2A1	4.62	0.1
	ACAN	5.60	0.05
	COL10A1	5.96	0.03
F	IL1	7.2	0.004
	IL6	7.2	0.004
	IL8	6.49	0.01
	TNF	0.36	0.88
G	MMP1	6.49	0.01
	MMP3	7.2	0.004
	MMP13	1.16	0.63

Table A5. Results from the Dunn's multiple comparisons test—figure 3.

Specification	Comparison	Dunn's multiple comparisons test
		Adjusted p-value
Figure 3(C) Col-2	CTL vs. STIM	0.20
	STIM vs. REG	0.68
	CTL vs. REG	0.01
Figure 3(D) Tt.A. 95%	CTL vs. STIM	0.005
	STIM vs. REG	0.99
	CTL vs. REG	0.05
Figure 3(D) Ot.A. 5%	CTL vs. STIM	0.007
	STIM vs. REG	0.48
	CTL vs. REG	0.30
Figure 3(D) Ot.C.A. 50%	CTL vs. STIM	0.008
	STIM vs. REG	0.99
	CTL vs. REG	0.03
Figure 3(E) COL1A1	CTL vs. STIM	0.03
	STIM vs. REG	0.41
	CTL vs. REG	0.89
Figure 3(F) IL1	CTL vs. STIM	0.02
	STIM vs. REG	0.54
	CTL vs. REG	0.54
Figure 3(F) IL6	CTL vs. STIM	0.02
	STIM vs. REG	0.54
	CTL vs. REG	0.54
Figure 3(F) IL8	CTL vs. STIM	0.03
	STIM vs. REG	0.41
	CTL vs. REG	0.89
Figure 3(G) MMP1	CTL vs. STIM	0.03
	STIM vs. REG	0.41
	CTL vs. REG	0.89
Figure 3(G) MMP3	CTL vs. STIM	0.02
	STIM vs. REG	0.54
	CTL vs. REG	0.54

ORCID iD

Annemarie Lang  <https://orcid.org/0000-0002-6539-9476>

References

- [1] Decker R S 2017 Articular cartilage and joint development from embryogenesis to adulthood *Semin. Cell Dev. Biol.* **62** 50–56
- [2] Loeser R F, Goldring S R, Scanzello C R and Goldring M B 2012 Osteoarthritis: a disease of the joint as an organ *Arthritis Rheum.* **64** 1697–707
- [3] Tetlow L C, Adlam D J and Woolley D E 2001 Matrix metalloproteinase and proinflammatory cytokine production by chondrocytes of human osteoarthritic cartilage: associations with degenerative changes *Arthritis Rheum.* **44** 585–94
- [4] Cope P J, Ourradi K, Li Y and Sharif M 2019 Models of osteoarthritis: the good, the bad and the promising *Osteoarthr. Cartil.* **27** 230–9
- [5] Thysen S, Luyten F P and Lories R J U 2015 Targets, models and challenges in osteoarthritis research *Dis. Models Mech.* **8** 17–30
- [6] Poulet B 2017 Models to define the stages of articular cartilage degradation in osteoarthritis development *Int. J. Exp. Pathol.* **98** 120–6
- [7] Glyn-Jones S, Palmer A J, Agricola R, Price A J, Vincent T L, Weinans H and Carr A J 2015 Osteoarthritis *Lancet* **386** 376–87
- [8] Bapat S, Hubbard D, Munjal A, Hunter M and Fulzele S 2018 Pros and cons of mouse models for studying osteoarthritis *Clin. Transl. Med.* **7** 36
- [9] Malfait A M and Little C B 2015 On the predictive utility of animal models of osteoarthritis *Arthritis Res. Ther.* **17** 225
- [10] Johnson C I, Argyle D J and Clements D N 2016 In vitro models for the study of osteoarthritis *Vet. J.* **209** 40–49
- [11] Caron M M, Emans P J, Coolen M M, Voss L, Surtel D A, Cremers A, van Rhijn L W and Welting T J 2012 Redifferentiation of dedifferentiated human articular chondrocytes: comparison of 2D and 3D cultures *Osteoarthr. Cartil.* **20** 1170–8
- [12] DuRaine G D, Brown W E, Hu J C and Athanasiou K A 2015 Emergence of scaffold-free approaches for tissue engineering musculoskeletal cartilages *Ann. Biomed. Eng.* **43** 543–54
- [13] Murdoch A D, Grady L M, Ablett M P, Katopodi T, Meadows R S and Hardingham T E 2007 Chondrogenic differentiation of human bone marrow stem cells in transwell cultures: generation of scaffold-free cartilage *Stem Cells* **25** 2786–96
- [14] Yasui Y, Ando W, Shimomura K, Koizumi K, Ryota C, Hamamoto S, Kobayashi M, Yoshikawa H and Nakamura N 2016 Scaffold-free, stem cell-based cartilage repair *J. Clin. Orthop. Trauma* **7** 157–63
- [15] Bhumiratana S, Eton R E, Oungoulouian S R, Wan L Q, Ateshian G A and Vunjak-Novakovic G 2014 Large, stratified, and mechanically functional human cartilage grown *in vitro* by mesenchymal condensation *Proc. Natl. Acad. Sci. USA* **111** 6940–5
- [16] Farrell M J, Fisher M B, Huang A H, Shin J I, Farrell K M and Mauck R L 2014 Functional properties of bone marrow-derived MSC-based engineered cartilage are unstable with very long-term *in vitro* culture *J. Biomech.* **47** 2173–82
- [17] Hu J C and Athanasiou K A 2006 A self-assembling process in articular cartilage tissue engineering *Tissue Eng.* **12** 969–79
- [18] Ng J J, Wei Y, Zhou B, Bernhard J, Robinson S, Burapachaisri A, Guo X E and Vunjak-Novakovic G 2017 Recapitulation of physiological spatiotemporal signals promotes *in vitro* formation of phenotypically stable human articular cartilage *Proc. Natl. Acad. Sci. USA* **114** 2556–61
- [19] Kitano H 2002 Computational systems biology *Nature* **420** 206–10
- [20] Lesage R, Kerkhofs J and Geris L 2018 Computational modeling and reverse engineering to reveal dominant regulatory interactions controlling osteochondral

- differentiation: potential for regenerative medicine *Front. Bioeng. Biotechnol.* **6** 165
- [21] Ayati B P, Kapitanov G I, Coleman M C, Anderson D D and Martin J A 2017 Mathematics as a conduit for translational research in post-traumatic osteoarthritis *J. Orthop. Res.* **35** 566–72
- [22] Catt C J, Schuurman W, Sengers B G, van Weeren P R, Dhert W J, Please C P and Malda J 2011 Mathematical modelling of tissue formation in chondrocyte filter cultures *Eur. Cell Mater.* **22** 377–92
- [23] Kar S, Smith D W, Gardiner B S, Li Y, Wang Y and Grodzinsky A J 2016 Modeling IL-1 induced degradation of articular cartilage *Arch. Biochem. Biophys.* **594** 37–53
- [24] Baker M, Brook B S and Owen M R 2017 Mathematical modelling of cytokines, MMPs and fibronectin fragments in osteoarthritic cartilage *J. Math. Biol.* **75** 985–1024
- [25] Bandejas C and Completo A 2017 A mathematical model of tissue-engineered cartilage development under cyclic compressive loading *Biomech. Model. Mechanobiol.* **16** 651–66
- [26] Orozco G A, Tanska P, Florea C, Grodzinsky A J and Korhonen R K 2018 A novel mechanobiological model can predict how physiologically relevant dynamic loading causes proteoglycan loss in mechanically injured articular cartilage *Sci. Rep.* **8** 15599
- [27] Ponomarev I and Wilke I 2004 Manufacturing process of three dimensional tissue structures and structures obtainable thereby *European Patent* EP1550716B1
- [28] Ponomarev I V, Kochneva L M and Barnewitz D 2014 Effect of 3D chondrocyte culturing conditions on the formation of extracellular matrix in cartilage tissue-engineering constructs *Bull. Exp. Biol. Med.* **156** 548–55
- [29] Lang A *et al* 2019 Collagen I-based scaffolds negatively impact fracture healing in a mouse-osteotomy-model although used routinely in research and clinical application *Acta Biomater.* **86** 171–84
- [30] Schneider C A, Rasband W S and Eliceiri K W 2012 NIH Image to ImageJ: 25 years of image analysis *Nat. Methods* **9** 671–5
- [31] Schindelin J *et al* 2012 Fiji: an open-source platform for biological-image analysis *Nat. Methods* **9** 676–82
- [32] Vayrynen J P, Vornanen J O, Sajanti S, Bohm J P, Tuomisto A and Makinen M J 2012 An improved image analysis method for cell counting lends credibility to the prognostic significance of T cells in colorectal cancer *Virchows Arch.* **460** 455–65
- [33] Anderson D E, Markway B D, Weekes K J, McCarthy H E and Johnstone B 2017 Physioxia promotes the articular chondrocyte-like phenotype in human chondroprogenitor-derived self-organized tissue *Tissue Eng. Part A* **24** 264–74
- [34] Giovannini S, Diaz-Romero J, Aigner T, Heini P, Mainil-Varlet P and Nedic D 2010 Micromass co-culture of human articular chondrocytes and human bone marrow mesenchymal stem cells to investigate stable neocartilage tissue formation in vitro *Eur. Cell Mater.* **20** 245–59
- [35] Lang J 2000 *Adaptive Multilevel Solution of Nonlinear Parabolic PDE Systems. Theory, Algorithm, and Applications* (Berlin: Springer)
- [36] Erdmann B, Lang J and Roitzsch R 1993 KASKADE – manual *Tr* 93–5 (Berlin: Konrad-Zuse-Zentrum)
- [37] Sarkar S K, Marmar B, Goldberg G and Neuman K C 2012 Single-molecule tracking of collagenase on native type I collagen fibrils reveals degradation mechanism *Curr. Biol.* **22** 1047–56
- [38] Mohanraj B, Meloni G R, Mauck R L and Dodge G R 2014 A high-throughput model of post-traumatic osteoarthritis using engineered cartilage tissue analogs *Osteoarthr. Cartil.* **22** 1282–90
- [39] Park I S, Jin R L, Oh H J, Truong M D, Choi B H, Park S H, Park D Y and Min B H 2018 Sizable scaffold-free tissue-engineered articular cartilage construct for cartilage defect repair *Artif. Organs* **42** 278–87
- [40] Whitney G A, Mera H, Weidenbecher M, Awadallah A, Mansour J M and Dennis J E 2012 Methods for producing scaffold-free engineered cartilage sheets from auricular and articular chondrocyte cell sources and attachment to porous tantalum *Biores. Open Access* **1** 157–65
- [41] Li Z, Kupcsik L, Yao S-J, Alini M and Stoddart M J 2010 Mechanical load modulates chondrogenesis of human mesenchymal stem cells through the TGF-beta pathway *J. Cell. Mol. Med.* **14** 1338–46
- [42] Zhang Y, Chen S and Pei M 2016 Biomechanical signals guiding stem cell cartilage engineering: from molecular adaption to tissue functionality *Eur. Cell Mater.* **31** 59–78
- [43] Ng J, Wei Y, Zhou B, Burapachaisri A, Guo E and Vunjak-Novakovic G 2016 Extracellular matrix components and culture regimen selectively regulate cartilage formation by self-assembling human mesenchymal stem cells *in vitro* and *in vivo* *Stem Cell Res. Ther.* **7** 183
- [44] Diederichs S, Klampfleuthner F A M, Moradi B and Richter W 2019 Chondral differentiation of induced pluripotent stem cells without progression into the endochondral pathway *Front. Cell Dev. Biol.* **7** 270
- [45] Lach M S, Wroblewska J, Kulcenty K, Richter M, Trzeciak T and Suchorska W M 2019 Chondrogenic differentiation of pluripotent stem cells under controllable serum-free conditions *Int. J. Mol. Sci.* **20** 2711
- [46] Dickhut A, Pelttari K, Janicki P, Wagner W, Eckstein V, Egermann M and Richter W 2009 Calcification or dedifferentiation: requirement to lock mesenchymal stem cells in a desired differentiation stage *J. Cell. Physiol.* **219** 219–26
- [47] Little C B, Flannery C R, Hughes C E, Goodship A and Caterson B 2005 Cytokine induced metalloproteinase expression and activity does not correlate with focal susceptibility of articular cartilage to degeneration *Osteoarthr. Cartil.* **13** 162–70
- [48] Macrory L, Vaughan-Thomas A, Clegg P D and Innes J F 2009 An exploration of the ability of tepoxalin to ameliorate the degradation of articular cartilage in a canine in vitro model *BMC Vet. Res.* **5** 25
- [49] Vincent H K, Percival S S, Conrad B P, Seay A N, Montero C and Vincent K R 2013 Hyaluronic acid (HA) viscosupplementation on synovial fluid inflammation in knee osteoarthritis: a pilot study *Open Orthop. J.* **7** 378–84
- [50] Funato S, Yasuhara R, Yoshimura K, Miyamoto Y, Kaneko K, Suzawa T, Chikazu D, Mishima K, Baba K and Kamijo R 2017 Extracellular matrix loss in chondrocytes after exposure to interleukin-1beta in NADPH oxidase-dependent manner *Cell Tissue Res.* **368** 135–44
- [51] Wehling N, Palmer G D, Pilapil C, Liu F, Wells J W, Muller P E, Evans C H and Porter R M 2009 Interleukin-1beta and tumor necrosis factor alpha inhibit chondrogenesis by human mesenchymal stem cells through NF-kappaB-dependent pathways *Arthritis Rheum.* **60** 801–12
- [52] Li H, Feng F, Bingham C O 3rd and Elisseeff J H 2012 Matrix metalloproteinases and inhibitors in cartilage tissue engineering *J. Tissue Eng. Regen. Med.* **6** 144–54
- [53] Rose B J and Kooyman D L 2016 A tale of two joints: the role of matrix metalloproteases in cartilage biology *Dis. Markers* **2016** 4895050
- [54] Duerr S, Stremme S, Soeder S, Bau B and Aigner T 2004 MMP-2/gelatinase A is a gene product of human adult articular chondrocytes and is increased in osteoarthritic cartilage *Clin. Exp. Rheumatol.* **22** 603–8
- [55] Salo T, Mäkelä M, Kylmäniemi M, Autio-Harjainen H and Larjava H 1994 Expression of matrix metalloproteinase-2 and -9 during early human wound healing *Lab. Invest.* **70** 176–82
- [56] Vu T H, Shipley J M, Bergers G, Berger J E, Helms J A, Hanahan D, Shapiro S D, Senior R M and Werb Z 1998 MMP-9/gelatinase B is a key regulator of growth plate angiogenesis and apoptosis of hypertrophic chondrocytes *Cell* **93** 411–22

- [57] Dreier R, Grassel S, Fuchs S, Schaumburger J and Bruckner P 2004 Pro-MMP-9 is a specific macrophage product and is activated by osteoarthritic chondrocytes via MMP-3 or a MT1-MMP/MMP-13 cascade *Exp. Cell Res.* **297** 303–12
- [58] Bock H G, Carraro T, Jäger W, Körkel S, Rannacher R and Schlöder J 2013 *Model Based Parameter Estimation. Contributions in Mathematical and Computational Sciences* (Berlin: Springer)
- [59] Haase T, Sunkara V, Kohl B, Meier C, Bussmann P, Becker J, Jagielski M, von Kleist M and Ertel W 2019 Discerning the spatio-temporal disease patterns of surgically induced OA mouse models *PLoS One* **14** e0213734
- [60] Smith D W, Gardiner B S, Davidson J B and Grodzinsky A J 2016 Computational model for the analysis of cartilage and cartilage tissue constructs *J. Tissue Eng. Regen. Med.* **10** 334–47
- [61] Sunkara V and von Kleist M 2016 Coupling cellular phenotype and mechanics to understand extracellular matrix formation and homeostasis in osteoarthritis *IFAC-Papers OnLine* **49** 38–43
- [62] Eskelinen A, Orozco G, Tanska P, Grodzinsky A J and Korhonen R K 2019 Combining mechanical stimulus and cytokine-mediated degradation mechanisms in injured cartilage *ORS Annual Meeting (Austin, Texas)*

2.5 Recapitulating arthritis-related effects on the osteochondral unit *in vitro*

Persistent inflammation of the joints characterizes RA – and therefore, clearly stands out from OA. The systemic, chronic inflammatory autoimmune features of RA are responsible for the progressive cartilage destruction but also the advancing subchondral bone erosion in late stages. Since adequate models recapitulating the crosstalk between bone and cartilage within the osteochondral unit are missing, we here aimed at providing a model which appropriately mimics the microenvironment of a healthy or an inflamed joint in a later disease stage

The following text corresponds to the abstract of the work:

Damerau, A., Pfeiffenberger, M., Weber, M.-C., Burmester, G.-R., Buttgereit, F., Gaber, T. *, **Lang, A.*** (2021). Mimicking cytokine-induced key features of arthritis in a human *in vitro* 3D osteo-chondral tissue model. *International Journal of Molecular Sciences*. Dec 24; 22(1): 128. [doi: 10.3390/ijms22010128] (*shared last authorship)

“Adequate tissue engineered models are required to further understand the (patho)physiological mechanism involved in the destructive processes of cartilage and subchondral bone during rheumatoid arthritis (RA). Therefore, we developed a human in vitro 3D osteochondral tissue model (OTM), mimicking cytokine-induced cellular and matrix-related changes leading to cartilage degradation and bone destruction in order to ultimately provide a preclinical drug screening tool. To this end, the OTM was engineered by co-cultivation of mesenchymal stromal cell (MSC)-derived bone and cartilage components in a 3D environment. It was comprehensively characterized on cell, protein, and mRNA level. Stimulating the OTM with pro-inflammatory cytokines, relevant in RA (tumor necrosis factor, interleukin-6, macrophage migration inhibitory factor), caused cell- and matrix-related changes, resulting in a significantly induced gene expression of lactate dehydrogenase A, interleukin-8 and tumor necrosis factor in both, cartilage and bone, while the matrix metalloproteases 1 and 3 were only induced in cartilage. Finally, application of target-specific drugs prevented the induction of inflammation and matrix-degradation. Thus, we here provide evidence that our human in vitro 3D OTM mimics cytokine-induced cell- and matrix-related changes—key features of RA—and may serve as a pre-clinical tool for the evaluation of both new targets and potential drugs in a more translational setup.”



Article

A Human Osteochondral Tissue Model Mimicking Cytokine-Induced Key Features of Arthritis In Vitro

Alexandra Damerau ^{1,2}, Moritz Pfeiffenberger ^{1,2}, Marie-Christin Weber ¹, Gerd-Rüdiger Burmester ^{1,2}, Frank Buttgerit ^{1,2}, Timo Gaber ^{1,2,*} and Annemarie Lang ^{1,2}

¹ Charité—Universitätsmedizin Berlin, Corporate Member of Freie Universität Berlin, Humboldt-Universität zu Berlin, and Berlin Institute of Health, Department of Rheumatology and Clinical Immunology, 10117 Berlin, Germany; alexandra.damerau@charite.de (A.D.); moritz.pfeiffenberger@charite.de (M.P.); marie-christin.weber@charite.de (M.-C.W.); gerd.burmester@charite.de (G.-R.B.); frank.buttgerit@charite.de (F.B.); annemarie.lang@charite.de (A.L.)

² German Rheumatism Research Centre (DRFZ) Berlin, a Leibniz Institute, 10117 Berlin, Germany

* Correspondence: timo.gaber@charite.de

† These authors contributed equally.

Abstract: Adequate tissue engineered models are required to further understand the (patho)physiological mechanism involved in the destructive processes of cartilage and subchondral bone during rheumatoid arthritis (RA). Therefore, we developed a human in vitro 3D osteochondral tissue model (OTM), mimicking cytokine-induced cellular and matrix-related changes leading to cartilage degradation and bone destruction in order to ultimately provide a preclinical drug screening tool. To this end, the OTM was engineered by co-cultivation of mesenchymal stromal cell (MSC)-derived bone and cartilage components in a 3D environment. It was comprehensively characterized on cell, protein, and mRNA level. Stimulating the OTM with pro-inflammatory cytokines, relevant in RA (tumor necrosis factor α , interleukin-6, macrophage migration inhibitory factor), caused cell- and matrix-related changes, resulting in a significantly induced gene expression of lactate dehydrogenase A, interleukin-8 and tumor necrosis factor α in both, cartilage and bone, while the matrix metalloproteinases 1 and 3 were only induced in cartilage. Finally, application of target-specific drugs prevented the induction of inflammation and matrix-degradation. Thus, we here provide evidence that our human in vitro 3D OTM mimics cytokine-induced cell- and matrix-related changes—key features of RA—and may serve as a preclinical tool for the evaluation of both new targets and potential drugs in a more translational setup.

Keywords: mesenchymal stem cells; tissue engineering; osteochondral unit; in vitro model; rheumatoid arthritis



Citation: Damerau, A.; Pfeiffenberger, M.; Weber, M.-C.; Burmester, G.-R.; Buttgerit, F.; Gaber, T.; Lang, A. A Human Osteochondral Tissue Model Mimicking Cytokine-Induced Key Features of Arthritis In Vitro. *Int. J. Mol. Sci.* **2021**, *22*, 128. <https://dx.doi.org/10.3390/ijms22010128>

Received: 26 November 2020

Accepted: 23 December 2020

Published: 24 December 2020

Publisher's Note: MDPI stays neutral with regard to jurisdictional claims in published maps and institutional affiliations.



Copyright: © 2020 by the authors. Licensee MDPI, Basel, Switzerland. This article is an open access article distributed under the terms and conditions of the Creative Commons Attribution (CC BY) license (<https://creativecommons.org/licenses/by/4.0/>).

1. Introduction

The osteochondral unit is an essential part of the joint and commits the functional association of the articular cartilage, calcified cartilage and the subchondral bone. Its main function is to transfer mechanical strain during weight-bearing and to ensure the mechanical and metabolic homeostasis as well as the overall joint integrity. Articular cartilage is surfacing the subchondral bone, adsorbing mechanical loading and distributing forces within the joint, while the subchondral bone provides mechanical stability, maintains the joint shape and supplies nutrient and oxygen for the deeper layers of the avascular cartilage [1].

Several pathologies have been demonstrated to affect the osteochondral unit e.g., microcracks, microedema, microbleeding, the development of subchondral bone cysts and osteophytes co-localizing with regions of articular cartilage damage [2–4]. All these changes are also attributed to the degenerative joint disease osteoarthritis (OA) or chronic

autoimmune-mediated joint inflammation such as found in rheumatoid arthritis (RA), which is a systemic autoimmune disease. OA is principally characterized by articular cartilage degeneration often accompanied with subchondral bone erosions due to a higher load impact and the presence of certain mediators and growth factors [5,6]. On the other hand, the progressive, destructive processes in RA are driven by a persistent inflammation of the joint. The complex pathogenesis of RA involves a diverse interplay between various humoral factors, cell types and tissues, though many underlying triggers and mechanism are still unclear. Beside the production of autoantibodies, the release of pro-inflammatory cytokines, such as tumor necrosis factor (TNF) α , interleukin (IL)-1, -6, -17 and macrophage migration inhibitory factor (MIF) and the induction of matrix degrading enzymes such as matrix metalloproteases (MMPs) drives both inflammation and destructive processes within cartilage and subchondral bone leading to an imbalance in metabolic processes [7]. During RA, MMP1, MMP3, MMP8, and MMP13 are predominantly involved in the extracellular matrix remodeling and degradation of cartilage collagens and proteoglycans but may also affect bone (e.g., MMP3, MMP13) [8,9].

As long as the causes of the disease are unknown, current therapies in clinical application aim to reduce the inflammatory mechanisms in the pathogenesis of RA, whereby their unwanted effects with regard to joint and bone homeostasis are often neglected or accepted, as exemplified by the use of glucocorticoids and their pro-osteoporotic effects [10]. According to current recommendations, today's treatment goal is to achieve remission or at least low disease activity [11]. Despite major progress in the treatment of RA, a strong unmet medical need remains, as not all patients reach the treat-to-target goal, i.e., sustained clinical remission or low disease activity; about 25% still suffer from moderate or even high disease activity [11]. Therefore, preclinical models which reflect the complexity of the functional unit of the joint are essential to improve our understanding of pathophysiological mechanisms, to increase our knowledge on adverse drug effects in clinical use, and to develop and verify new therapeutic approaches.

Until today, animal models represent an integral part of the preclinical drug discovery process. While animals do not develop spontaneously autoimmune conditions such as RA—which constitutes an inherent limitation of these models—arthritis can be induced in these animals by a single agent or by genetic manipulations [12–14]. Finally, non-humanized rodent models are not suitable to test treatment strategies which are highly specific for human target proteins [12]. Understanding the homeostasis within the osteochondral unit as well as RA-related mechanisms is essential for determining treatment strategies. Therefore, different *in vitro* models have been developed and evaluated during the last years ranging from tissue explants, simplified (co)culture systems and complex tissue engineered three-dimensional (3D) (multi)component systems to chip approaches [14]. Most of the current *in vitro* cell culture systems in monolayer are used to study the effect of e.g., humoral factors or therapeutics on chondrocytes [15,16], aggregate-cell interactions or cell-cell interplay [14,17], lacking the complexity of (patho)physiologically relevant cell-cell and cell-matrix interactions and nutrient gradients [14,18]. Today, complex 3D *in vitro* systems include the co-cultivation of e.g., bovine cartilage discs with human synovial fibroblasts mimicking early cartilage destructive processes [19], porcine chondrocytes with an RA-derived cell line [20], RA synovium with bone explants [21] or cartilage explants from either humans or animals [22]. Cartilage and bone differ in matrix characteristics and microenvironmental and mechanical cues. Therefore, osteochondral tissue engineering requires (i) a unique cell and matrix composition, (ii) a certain organization of the artificial tissue with or without scaffold and (iii) specific biological properties. To date, promising *in vitro* tissue engineering approaches have been developed using (i) scaffold-based bone and scaffold-free cartilage [23], (ii) different scaffolds for both bone and cartilage [24], (iii) a single heterogeneous scaffold [25] or (iv) a single homogenous scaffold for both [26]. A major challenge is the restriction to obtain human primary cells or explants, the limited lifespan of explants [27] and the unstable phenotype of chondrocytes during monolayer expansion [28]. Therefore, mesenchymal stromal cells (MSCs) are often used to engineer

cartilage and bone equivalents [14]. Despite major progress especially due to emerging techniques such as 3D bioprinting, so far, there is no appropriate in vitro model which is able to mimic an inflamed joint with respect to the osteochondral unit allowing the preclinical testing of a variety of specific therapeutic approaches.

Here, we describe a human in vitro 3D osteochondral tissue model (OTM) as potential part of an artificial joint, comprising a scaffold-free cartilage-like component and a tricalcium phosphate (TCP)-based bone-like component (TBBC). In addition, we aimed at demonstrating that this engineered human OTM can be used as in vitro model to study cytokine-driven cell- and matrix-related changes during osteochondral degradation—key feature of RA. Moreover, we evaluated the feasibility of our OTM by using approved biologics, which prevented these cytokine-related changes. An overview on the experimental setup is given in Figure 1.

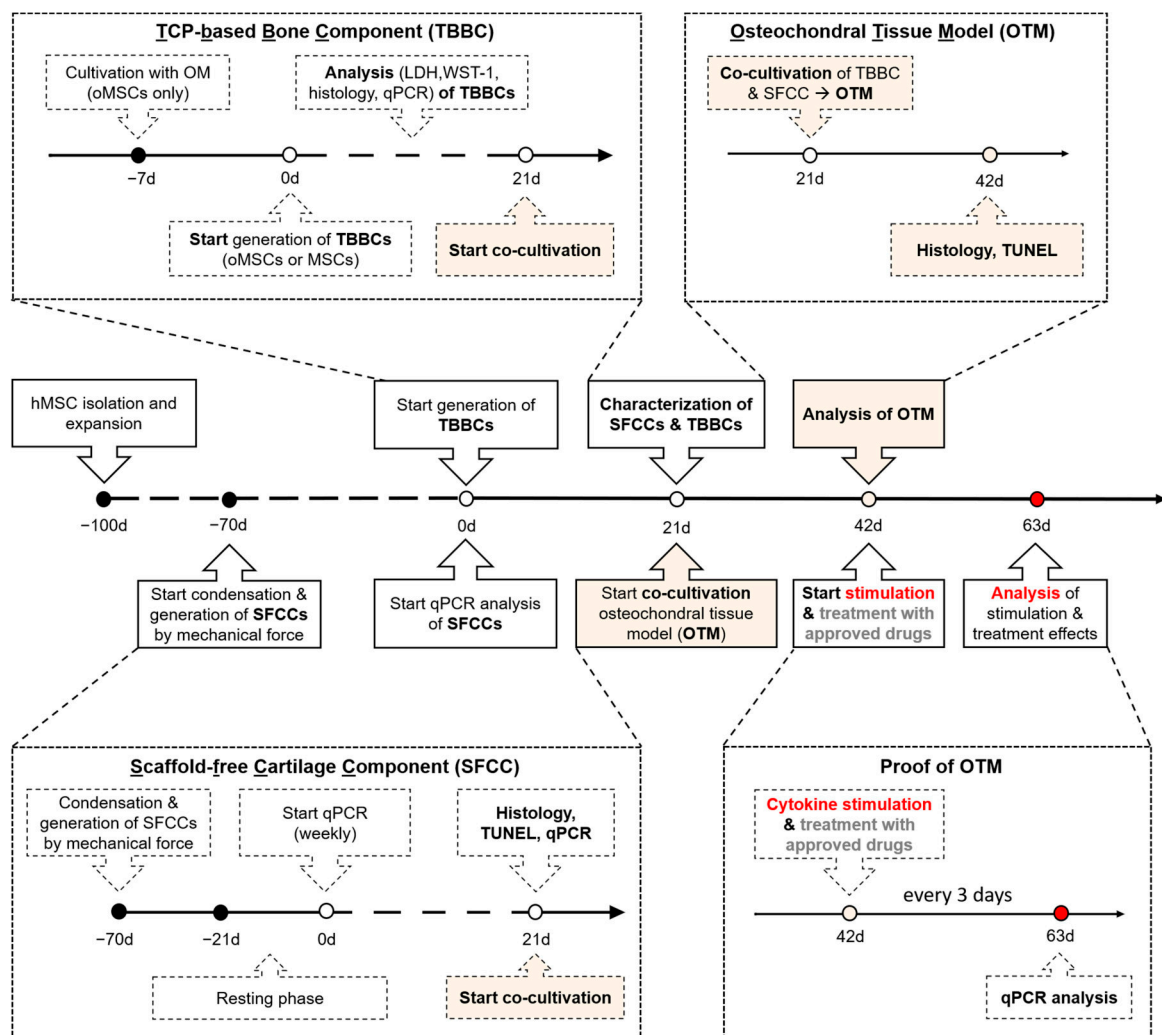


Figure 1. Schematic overview of the timely interlocked processes to generate the human in vitro 3D osteochondral tissue model of arthritis. Based on human bone marrow-derived mesenchymal stromal cells (MSCs), the in vitro 3D TCP-based bone components (TBBCs) and scaffold-free cartilage components (SFCCs) were developed. The osteochondral tissue model (OTM) was engineered by co-cultivation of both tissue components for 21 days. To replicate cytokine-mediated features of rheumatoid arthritis (RA), the osteochondral tissue model was stimulated with typical RA-related cytokines (tumor necrosis factor α , interleukin-6, and macrophage migration inhibitory factor) and finally treated with approved drugs (Proof of OTM). oMSC, one-week osteogenic pre-differentiated MSCs; OM, osteogenic medium; TCP, tricalcium phosphate; LDH, lactate dehydrogenase.

2. Results

2.1. Optimization of the TCP-Based Bone Component Results in a Valid and Sustainable Osteogenic Phenotype Replicating the Subchondral Bone Compartment

Firstly, we determined a cell/TCP ratio of approximately 1×10^6 cells/12 mg (0.8×10^5 cells/mg) as being optimal for the in vitro 3D TCP-based bone component (TBBC) since higher initial cell densities led to increased cell death (Appendix A Figure A1). To test whether osteogenic pre-differentiation of seeded MSCs influences the TBBC formation, we pre-differentiated MSCs using osteogenic differentiation medium for one week (oMSCs) and colonized TCP particles with either MSCs or oMSCs (Figure 2A). Scanning electron microscopy revealed that both MSCs and oMSCs became adherent to the TCP scaffold and invaded the TCP scaffold within 21 days (Figure 2B). Both, MSCs and oMSCs colonized the TCP scaffold within 21 days without any sign of cytotoxicity as demonstrated by the lack of differences in LDH release when compared to the spontaneous release of a TCP-free monolayer (ML), but a significant lower release compared to the positive control (Figure 2C). Analyzing cell viability after 21 days of incubation using LIVE/DEAD staining, we observed a significant lower amount of viable oMSCs (Calcein AM+; green) and an increase in EthD1+ oMSCs (dead, red) when compared to the corresponding MSCs and the respective ML (Figure 2D,E). Analyzing cellular metabolic activity using the WST-1 assay, we detected a significantly reduced metabolic activity in oMSCs compared to MSCs after 21 days (Figure 2F). Interestingly, co-cultivation of MSCs or oMSCs with osteoconductive TCP significantly increased calcium deposition after 7 and 21 days when compared to the monolayer incubated in osteogenic medium but without TCP. Calcification was more pronounced in MSCs than oMSCs (Figure 2G).

Taken together, MSCs and oMSCs colonized the TCP scaffold within 21 days without any sign of cytotoxicity while cell viability, metabolic activity, and calcification were more pronounced in MSCs than oMSCs (Figure 2C–G).

To investigate the spatial distribution, matrix formation and the osteogenic phenotype of either MSCs or oMSCs on the TCP scaffold, we quantified TBBC sections for the expression of actin, laminin and osteopontin (OPN) normalized to the cell nuclei (DAPI) using immunofluorescence staining (Figure 3A). To assess the spatial distribution, the total area of TBBC section was sub-divided into an outer, middle, and inner area and analyzed for the expression of actin. At day 21, seeded MSCs demonstrate a more pronounced and distributed staining for actin throughout the total area of TBBC section than oMSCs as indicated by significantly more actin staining in the total, middle, and inner area (Figure 3A). To assess the matrix formation, we normalized the relative expression of the extracellular protein laminin as quantified at day 21 to day 1. We found an up to 2-fold increase of matrix production in MSCs and oMSCs over time without observing differences between the two groups (Figure 3B). When focusing on the OPN expression as a measure of osteogenic phenotype, we observed significantly more OPN expression per cell in the TBBCs populated with MSCs than those with oMSCs both in the total area and in the middle and inner area (Figure 3C). Together with the observed actin distribution within the TCP, the OPN results indicate that the invading cells differentiate towards the osteogenic lineage. In this line of observation, the upregulation of runt-related transcription factor 2 (*RUNX2*), secreted phosphoprotein 1 (*SPP1*), osteonectin (*ON*), and collagen type 1 alpha 1 (*COL1A1*), respectively, were superior over time in MSCs as compared to oMSCs (Figure 3D). Based on these findings, we proceeded with the use of MSCs for the generation of TBBCs.

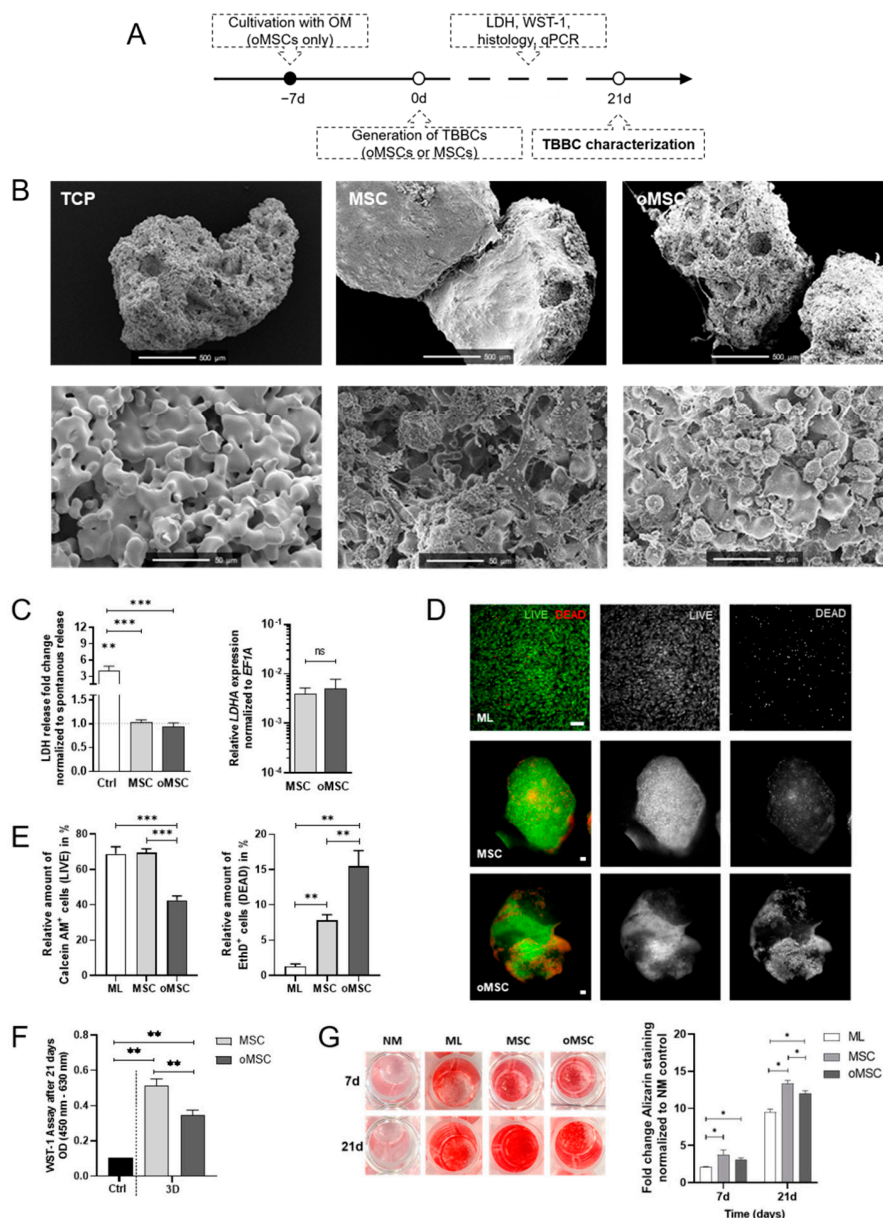


Figure 2. In vitro studies on β -TCP biocompatibility and cell survival comparing the suitability of human mesenchymal stromal cells (MSCs) and osteogenic pre-differentiated MSCs (oMSCs). **(A)** Experimental design of the in vitro TCP-based bone component (TBBC). **(B)** Structural evaluation of β -TCP using scanning electron microscopy. Exemplary images of $n = 6$. Scale bars show 500 μm and 50 μm as indicated in the images. **(C)** LDH-assay was conducted after 24 h to confirm the biocompatibility of β -TCP. Ctrl = 2% of Triton X-100. Data are shown as mean \pm SEM for $n = 10$ –12. Gene expression of lactate dehydrogenase A (*LDHA*) was determined by qPCR and normalized to the housekeeper gene *EF1A*. Data are shown as mean \pm SEM for $n = 4$. Mann-Whitney U-test was used to determine the statistical significance between groups and Wilcoxon signed-ranked test for the spontaneous LDH release control. **(D)** LIVE/DEAD staining was performed after 21 days and **(E)** quantified using ImageJ. As control MSCs in monolayer (ML) were stained. Green and red colors discriminated between living and dead cells (scale bar = 100 μm). Representative images are shown accordingly for $n = 4$ –6. Data are shown as mean \pm SEM. **(F)** WST-1 assay was conducted to confirm metabolically active cells after 21 days of 3D cultivation. Ctrl = 2% of Triton X-100. Data are shown as mean \pm SEM for $n = 6$. Mann-Whitney U-test was used. **(G)** MSCs and oMSCs were cultivated for 7 and 21 days in normal medium (NM control), in osteogenic medium without β -TCP (ML) and with β -TCP populated with MSCs (MSC) or pre-differentiated MSCs (oMSC). Alizarin Red staining was quantified (562 nm). Data are shown as mean \pm SEM for $n = 5$. Wilcoxon matched-pairs signed rank test was used to determine the statistical significance. p -values are indicated in the graphs with * $p < 0.05$, ** $p < 0.01$ and *** $p < 0.001$ (ns = not significant). TCP, tricalcium phosphate; LDH, lactate dehydrogenase; *EF1A*, eukaryotic translation elongation factor 1 alpha.

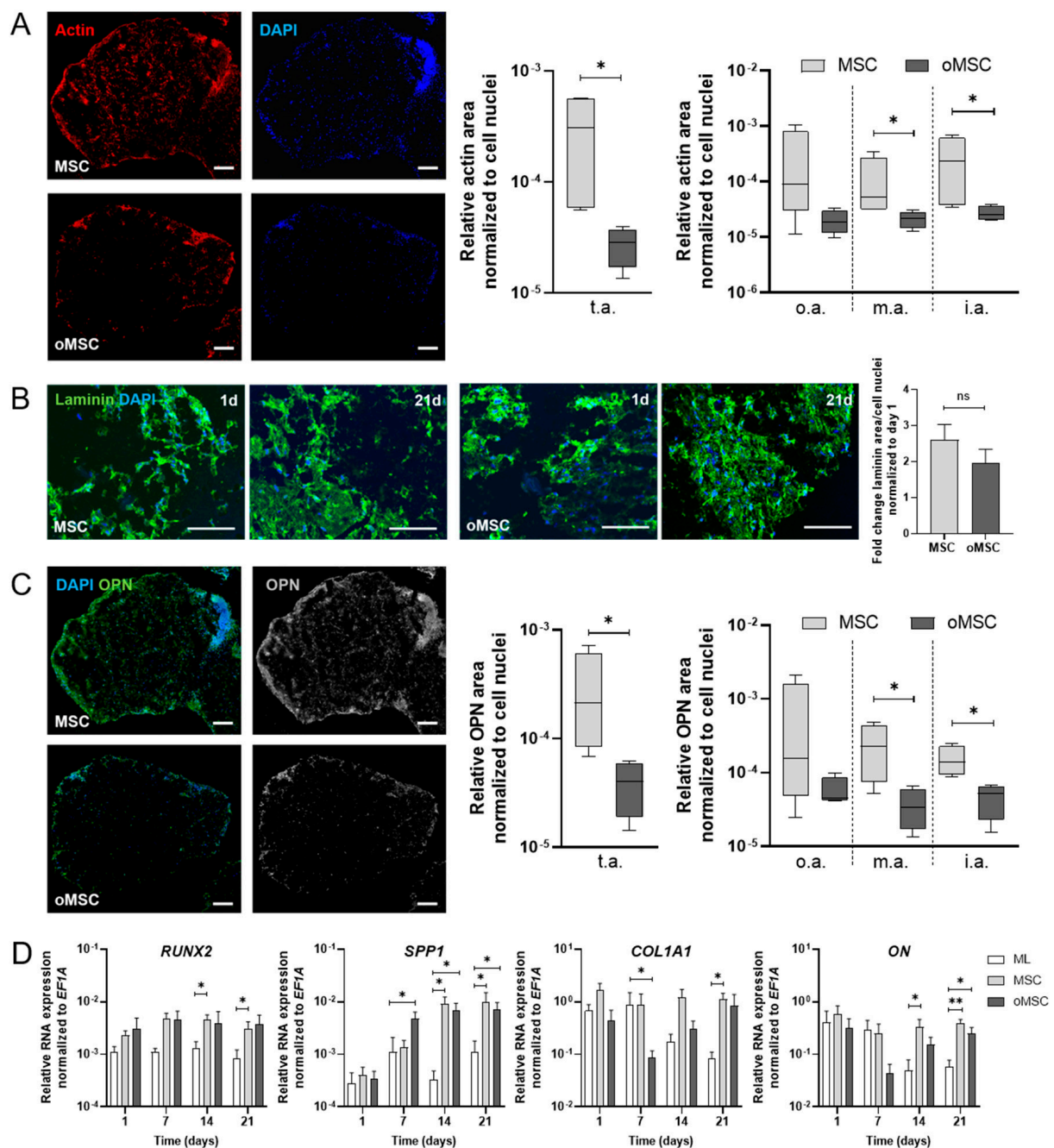


Figure 3. Characterization of the human in vitro tricalcium phosphate-based bone component (TBBC) using both MSCs and oMSCs. **(A)** The amount of actin (in pixels) per cell nuclei (DAPI+) after 21 days within total area (t.a.), outer area (o.a.; outer border determined by a reduction of the diameter by 0.95 for X- and Y-axes), middle area (m.a.; outer area subtracted from total area, diameter reduced by 0.5 for X- and Y-axes) and inner area (i.a.; remaining inner part of the outer area subtracted from total area, diameter reduced by 0.5 for X- and Y-axes) were quantified via ImageJ. Data are shown as Box and Whiskers plot with median \pm min/max for $n = 4$. Scale bar indicates 100 μ m. **(B)** Laminin and DAPI were stained after day 1 and 21 and quantified via ImageJ. Data are shown as mean \pm SEM for $n = 3$. Scale bar indicates 100 μ m. **(C)** Osteopontin (OPN) and DAPI were stained after 21 days. The amount of OPN (in pixels) per cell within t.a., o.a., m.a., and i.a. were quantified via ImageJ. Data are shown as Box and Whiskers plot with median \pm min/max for $n = 4$. Representative images are shown accordingly (scale bar = 100 μ m). **(D)** Total RNA extraction was performed from MSC monolayer (ML) and 3D cultures with MSCs and oMSCs after 1, 7, 14 and 21 days. Gene expression was normalized to the housekeeper gene *EF1A*. Data are shown as mean \pm SEM for $n = 4$ –6. Mann-Whitney U-test was used to determine the statistical significance; * $p < 0.05$, ** $p < 0.01$ (ns = not significant). MSC, mesenchymal stromal cell; oMSC, one-week osteogenic pre-differentiated MSC; *EF1A*, eukaryotic translation elongation factor 1 alpha.

The final TBBCs were produced in sizes with a diameter up to 0.5 cm and cultivated for 21 days (Figure 4A). Exemplary images of actin and DAPI immunofluorescence staining over time (day 1, 7, 14, 21) further supported prior endpoint analyses demonstrating the invasion of cells into the TCP scaffold (Figure 4B). Furthermore, TBBCs cultivated for 21 days displayed a cell and matrix formation comparable to native bone as analyzed by scanning electron microscopy (Figure 4C). H&E staining clearly indicated a matrix formation, the interconnection between cells and the TCP particles, and the beginning of osteoid formation at day 21 (Figure 4D). Additionally, seeded MSCs maintained their metabolic activity over 21 days when compared to day 1 and the respective monolayer control (ML; Figure 4E). Analyzing bone formation using μ CT, we observed a numerical increase in bone volume at day 21 compared to day 0 (TCP only) and day 14 (Figure 4F). Finally, gene expression of bone specific markers revealed a significant upregulation of *RUNX2*, *SPP1*, *ON*, *COL1A1* and osteocalcin (*OC*) as compared to the osteogenic differentiated ML (Figure 4G). In summary, using MSCs to produce TBBCs is valid to achieve a sustainable osteogenic phenotype and to recapitulate the subchondral bone compartment in our OTM approach.

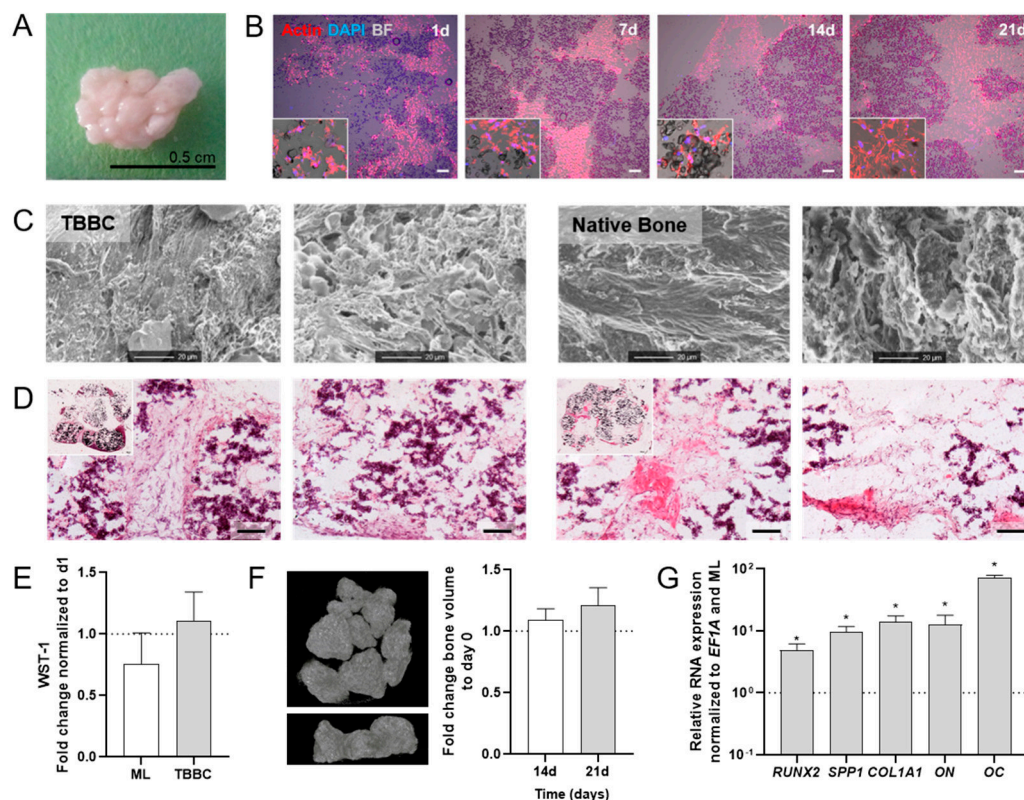


Figure 4. Human in vitro 3D TCP-based bone component (TBBC) based on MSCs. (A) Macroscopic overview of the in vitro 3D TBBC. (B) Exemplary images to highlight cell localization and extracellular matrix formation as shown by immunofluorescence staining for actin (red) and DAPI (blue) after day 1, 7, 14 and 21. Bright field (BF) shows the β -TCP scaffold. Exemplary images of $n = 4$ (scale bar = 100 μ m). (C) Structural examination of the TBBC in comparison to native bone using scanning electron microscopy. Exemplary images of $n = 8$ TBBC and $n = 2$ human native bone. (D) Histological evaluation of the morphology via H&E staining. Exemplary images for $n = 8$. Scale bars indicate 100 μ m. (E) WST-1 assay was conducted to confirm metabolically active cells after 21 days of cultivation compared to day 1 and monolayer control (ML). Data are shown as mean \pm SEM (duplicates per donor in two independent experiments) for $n = 6$. Mann-Whitney U-test was used to determine the statistical significance. (F) In vitro 3D μ CT reconstruction and quantitative results. Data are shown as mean \pm SEM for $n = 3$. (G) Total RNA extraction was performed from ML and TBBCs after 21 days of osteogenic differentiation. The relative gene expression was normalized to the housekeeper gene *EF1A* and osteogenic differentiated ML. Data are shown as mean \pm SEM (duplicates per gene) for $n = 6$. Wilcoxon Signed Rank Test was used to determine the statistical significance; p -values are indicated in the graphs with * $p < 0.05$. MSC, mesenchymal stromal cell; TCP, tricalcium phosphate; *EF1A*, eukaryotic translation elongation factor 1 alpha.

2.2. Characterization of the Scaffold-Free Cartilage Component Demonstrates a Valid Cartilage-Like Phenotype Including Zonal Organization

The cartilage-like component was produced as described previously. In short, the procedure is based on mesenchymal condensation and the cyclic application of biomechanical force which finally leads to the self-organized 3D scaffold-free cartilage component (SFCC) [18]. Thus, we were asking the question whether we can maintain a cartilage-like phenotype of the SFCCs for 21 days, which is the time point that coincides with the start of co-cultivation with TBBCs (Figure 1). SFCCs were produced in a diameter sized up to 0.5 cm (Figure 5A). H&E staining of histological sections demonstrated an almost homogenous cell matrix distribution with a higher cell density and more flattened cells in the outer surface area similar to the superficial zone of native cartilage (Figure 5B). Additionally, the inner area was characterized by spherical and randomly oriented cells reflecting characteristics of the middle zone of native cartilage. Using TUNEL staining at day 21, we observed only a low number of apoptotic cells within the SFCC (Figure 5C). Histochemistry and immunohistochemistry revealed the presence of glycosaminoglycans (Alcian blue staining) and collagen type 2 (Figure 5D). We also found collagen type 1 expressed in the tissue, although its extent of expression was clearly lower as compared to the TBBC control. However, mineralization was not present as shown by Alizarin and von Kossa staining (Figure 5D). Comparing the gene expression of SFCCs to undifferentiated MSCs in ML at day 21, we observed an up-regulation of cartilage specific markers such as collagen type 2 alpha 1 (*COL2A1*), aggrecan (*ACAN*) and collagen type 10 alpha 1 (*COL10A1*), while the expression of the bone specific markers *COL1A1* and *RUNX2* was downregulated as compared to the monolayer control (Figure 5E). In addition, the cartilage specific transcription factor *SOX9*, which is an early marker of chondrogenesis during cartilage development, was also downregulated (Figure 5E). However, the temporal course of the analyzed marker gene expression revealed no significant changes over 21 days as assessed weekly (Appendix A Figure A2). Based on our findings, we continued with the in vitro generated SFCCs displaying a stable chondrogenic phenotype and characteristics of native cartilage.

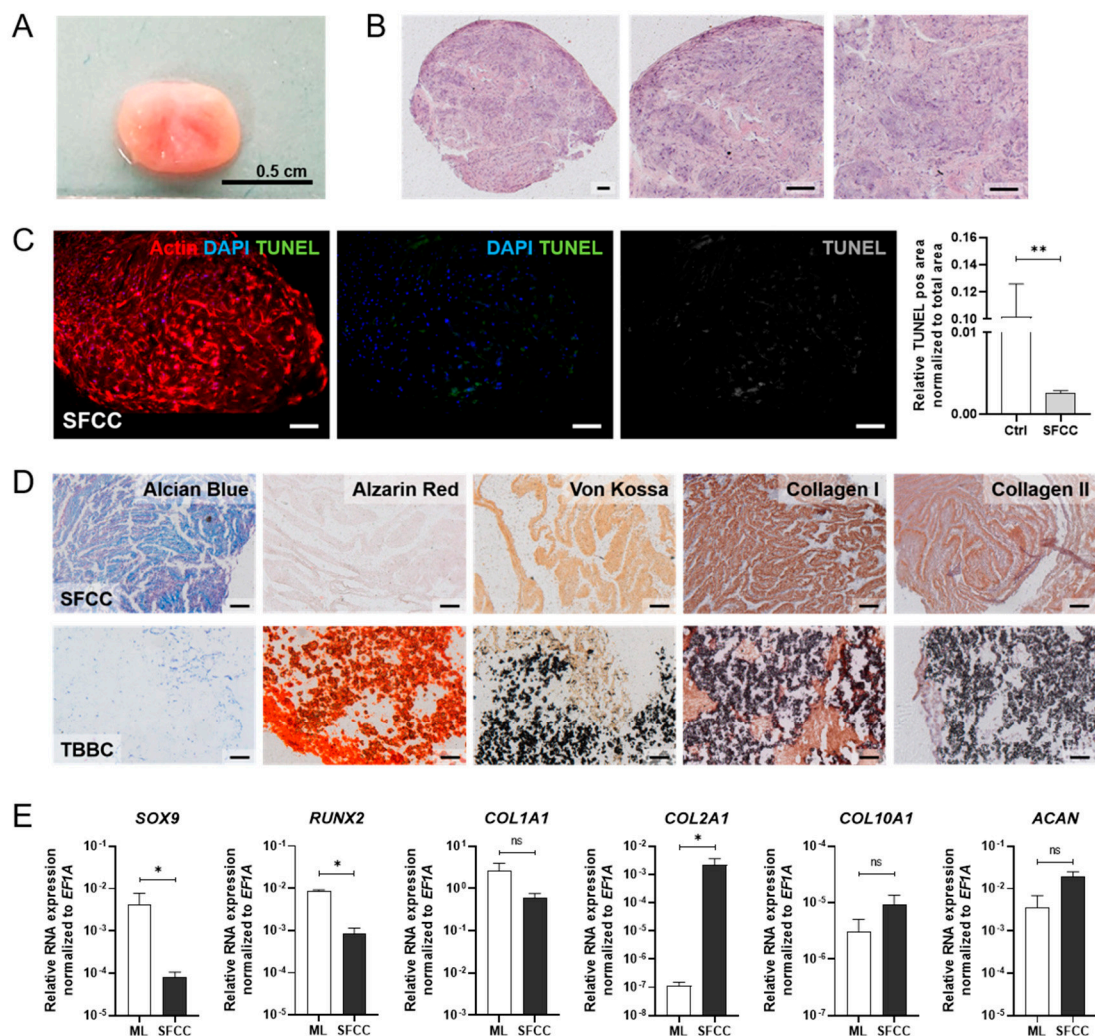


Figure 5. In vitro studies on the 3D scaffold-free cartilage constructs (SFCC) based on human MSCs. (A) Macroscopic overview of the in vitro 3D SFCCs. (B) Histological evaluation of the morphology via H&E staining. Exemplary images for $n = 6$. Scale bars indicate 200 μm . (C) Detecting apoptotic cells (green) using TUNEL staining after 21 days without mechanical force. Exemplary image for $n = 4$. Scale bars indicate 200 μm . Pos. ctrl = incubation with DNase I for 10 min. (D) Histological (Alcian Blue, Alizarin Red, von Kossa) and immunohistochemistry staining (collagen type 1 and collagen type 2) of the SFCC in comparison with the tricalcium phosphate-based bone component (TBBC) control. Exemplary images for $n = 4$. Scale bars indicate 200 μm . (E) Total RNA extraction was performed from 3D cultures after 21 days. Gene expression was normalized to the housekeeper gene *EF1A*. Data are shown as mean \pm SEM (duplicates per gene) for $n = 3$ –6. Mann-Whitney U-test was used to determine the statistical significance; p -values are indicated in the graphs with * $p < 0.05$, ** $p < 0.01$ (ns = not significant). MSC, mesenchymal stromal cell; *EF1A*, eukaryotic translation elongation factor 1 alpha.

2.3. Co-Cultivation of Scaffold-Free Cartilage Components and In Vitro 3D Tricalcium Phosphate-Based Bone Components Lead to Formation of a Subchondral Bone-Like Zone

Since we aimed to develop a complex human in vitro 3D OTM to mimic the part of a joint which is affected during the late stages of RA, we cultivated the SFCC on top of the TBBC. Therefore, TBBCs and SFCCs were produced as outlined before (Figures 1 and 6A) and cultivated for 21 days before analysis (day 42). H&E staining of OTMs showed that SFCC and TBBC were sticking together without any gap formation (Figure 6B). Although both parts could still be discriminated morphologically by H&E staining, we additionally phenotypically discriminated the SFCC from the TBBC part using Toluidine blue combined with von Kossa staining visualizing the chondrogenic phenotype by Toluidine blue dye attaching to the negative charges of the proteoglycans while calcified tissue phenotype

was confirmed by von Kossa (Figure 6C). Moreover, we observed a rearrangement of the cytoskeleton after 21 days of co-cultivation in the bridging area between both components reflecting a subchondral bone-like zone of the osteochondral tissue as visualized by actin and DAPI (cytoskeleton, nucleus) staining (Figure 6D). To confirm cellular viability after 21 days of co-cultivation, we conducted a TUNEL staining (green: apoptotic cells) showing only a few apoptotic cells compared to the positive control with induced apoptosis by DNase I treatment (Figure 6E). Taken together, co-cultivation of SFCC and TBBC led to the formation of a connecting OTM with cellular rearrangements in the bridging area.

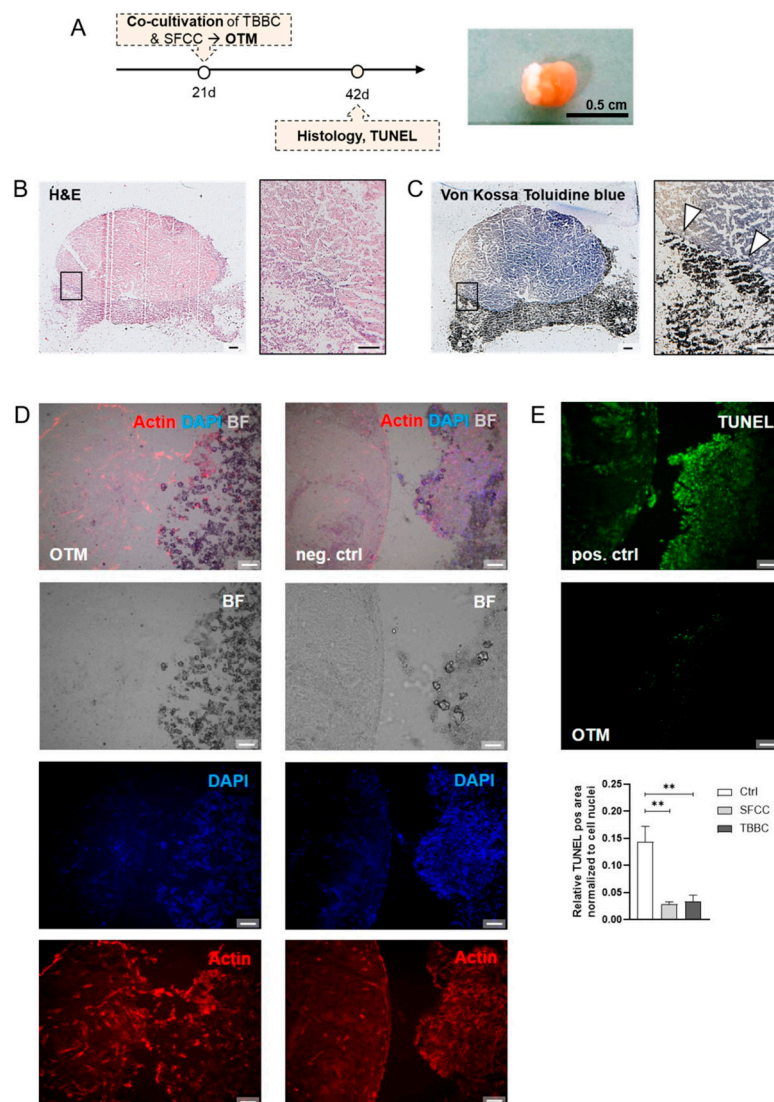


Figure 6. Human in vitro 3D osteochondral tissue model (OTM). Both components were developed independently and subsequently co-cultured in a cell culture insert for 21 days. (A) Experimental design of the in vitro 3D OTM. (B) Histological evaluation via H&E and (C) Toluidine blue combined with von Kossa staining. Exemplary image for $n = 4$. Scale bars indicate 500 μm . White asterisks highlight initial mineralization. (D) Actin and DAPI staining were performed to visualize the transitional bridging area between both components. Neg. ctrl = co-cultivation for 1 day, simulating a not unified OTM. Exemplary image for $n = 4$. Scale bars indicate 200 μm . (E) The number of apoptotic cells (green; TUNEL staining) normalized to cell nuclei (DAPI+) in both TBBC and SFCC after 21 days of co-cultivation was quantified via ImageJ. Exemplary images for $n = 5$. Scale bars indicate 200 μm . Pos. ctrl = incubation with DNase I for 10 min to induce apoptosis. Mann-Whitney U-test was used to determine the statistical significance compared to the control, p -values are indicated in the graphs with ** $p < 0.01$. TBBC, tricalcium phosphate-based bone component; SFCC, scaffold-free cartilage component.

2.4. The Osteochondral Tissue Model Shows Cell- and Matrix-Related Changes after Cytokine Stimulation Which Were Prevented by Application of Anti-Rheumatic Drugs

To mimic the chronic inflammatory environment of RA, our osteochondral tissue model was treated for a prolonged period of 21 days repetitively (every 3 days) using a cocktail of three major RA-related cytokines, namely TNF α (10 ng/mL), IL-6 (30 ng/mL) and MIF (10 ng/mL) at pathophysiological, non-cytotoxic concentrations (Figure 7A–C). Cytokine concentrations were used as reported from synovial fluid of patients with RA (STIM) or left untreated (CTRL). The cytokine cocktail was applied with or without drugs to quantify both the effects of the cytokines and the preventive potential of the drugs under investigation. To this end, we added a combination of clinically available drugs in their therapeutic dosage (10 μ g/mL adalimumab, 8 μ g/mL tocilizumab, 5 μ g/mL milatuzumab; TREAT). After sustained repetitive treatment for 21 days mimicking chronic inflammation, we analyzed the transcriptional response of our model and identified a significant cytokine-mediated upregulation of the metabolic marker lactate dehydrogenase A (*LDHA*) in the STIM group compared to CTRL which was significantly reduced in both SFCC and TBBC when treated with the combination of chosen drugs (TREAT; Figure 7D,E). Additionally, a cytokine-induced upregulation of the angiogenic marker vascular endothelial growth factor A (*VEGFA*) was observed, which was prevented in the TREAT group. The expression of *IL6* was numerically reduced after both cytokine stimulation (STIM) and therapeutic treatment (TREAT) as compared to CTRL in SFCCs (Figure 7D) but was significantly reduced in TBBCs (Figure 7E). Conversely, *IL8* and *TNF* were significantly upregulated after stimulation, while this effect was prevented by the drugs. In the SFCC model, *MMP1* and *MMP3* were significantly upregulated in the cytokine-treated group compared to the CTRL group (Figure 7D). This effect was reversed in the drug-treated group compared to the STIM group. There were no significant differences in gene expression for *MMP13* within the experimental groups. However, in the bone-like model, *MMP1* expression was numerically diminished in both the STIM and TREAT group compared to the CTRL group (Figure 7E). There was no significant difference in gene expression of *MMP3* within CTRL and STIM, while we observed a significant downregulation in the TREAT group. Moreover, there were no significant differences in gene expression for *MMP13* within the experimental groups. Of note, cartilage and bone component differentially responded to cytokine-mediated stimulation with respect to the significantly upregulated expression of *MMP1* and *MMP3*.

In summary, stimulation with TNF α , IL-6 and MIF lead to cytokine-mediated cartilage degradation, a key feature of arthritis. These findings are in accordance with *in vivo* data from animal studies and with observations made in human pathophysiology. Cultivation in the presence of immunomodulatory drugs did sufficiently prevent these cytokine-induced changes.

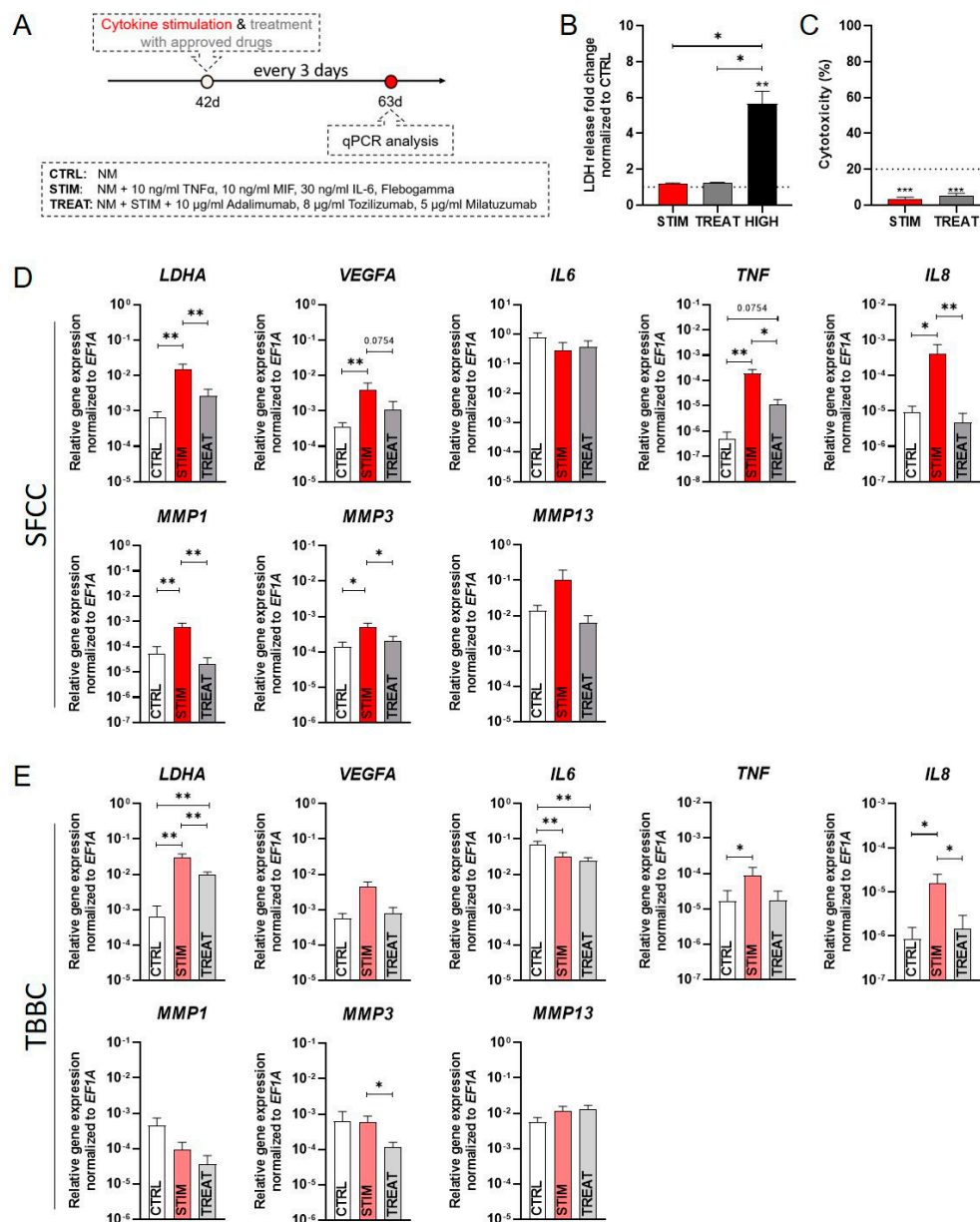


Figure 7. Experimental results of our osteochondral tissue model incubated for 21 days under non-inflammatory conditions (CTRL), repetitive cytokine stimulation with a cocktail of TNF α , IL-6 and MIF (STIM) and under treatment conditions (TREAT). **(A)** Schematic overview of the experimental design. **(B)** LDH-assay was performed after 1 day to cover any cytotoxic effects using supernatant from the OTM treated with cytokines (STIM—10 ng/mL TNF α , 30 ng/mL IL-6, 10 ng/mL MIF) and in combination with clinically available drugs (TREAT—10 μ g/mL adalimumab, 8 μ g/mL tocilizumab, 5 μ g/mL milatuzumab). CTRL = untreated control; HIGH = 2% of Triton X-100 to induce LDH release. Data are shown as mean \pm SEM for $n = 5$. Wilcoxon matched-pairs signed rank test was used to determine the statistical significance between groups and One sample t test for the spontaneous LDH release control (CTRL). **(C)** Percentage of cytotoxicity was determined by the following equation [%] = (exp. value – CTRL)/(HIGH – CTRL) \times 100 for $n = 5$. Data are shown as mean \pm SEM. One sample t test was used with a cytotoxicity cut off of 20% [29]. **(D)** Gene expression studied via qPCR for *LDHA*, *VEGFA*, *IL6*, *TNF*, *IL8*, *MMP1*, *MMP3* and *MMP13* for scaffold-free cartilage components (SFCCs) and **(E)** tricalcium phosphate-based bone components (TBBCs). Data were normalized to the housekeeper gene *EF1A* and are shown as mean \pm SEM (duplicates per gene) for $n = 5$. Mann-Whitney U-test was used to determine the statistical significance, p -values are indicated in the graphs with * $p < 0.05$, ** $p < 0.01$, *** $p < 0.001$. LDH, lactate dehydrogenase; TNF, tumor necrosis factor; IL, interleukin; MIF, macrophage migration inhibitory factor; *LDHA*, lactate dehydrogenase A; *VEGFA*, vascular endothelial growth factor A; *MMP*, matrix metalloproteinases; *EF1A*, eukaryotic translation elongation factor 1 alpha.

3. Discussion

Until today, no appropriate human in vitro model exists so far, which can appropriately mimic the (patho)physiological relevant environment of a healthy or an inflamed joint specifically focusing on the later stage of disease involving cartilage matrix degradation and subchondral bone erosion with the need for a crosstalk between bone and cartilage within the osteochondral unit. Simulating such features in a preclinical drug screening tool would be transformative for the translational process necessary for optimizing rheumatological care. Here, we have developed a human MSC-derived OTM and described its capacity to create a RA-like phenotype, which replicated in part the immunomodulatory effect of well-known anti-rheumatic drugs such as adalimumab [30,31] and tocilizumab [32,33], but also the antineoplastic agent milatuzumab [34].

As in our current study, MSCs are widely used as suitable cell source to engineer in vitro tissue owing to their availability, isolation simplicity, high proliferation rate and differentiation capacity towards individual resident cell types of bone and cartilage [35,36]. Since there has been evidence that high-density scaffold-free chondrogenic cultures and ceramic bone scaffolds might lead to the formation of well-integrated OTMs [37], we firstly engineered bone components by using TCP ceramic particles, which mimic the mineral bony part. Comparable in vitro and in vivo approaches to promote osteogenesis and bone regeneration have been published during the last decade [38,39]. With respect to the biocompatibility and prominent osteoconductive activity of TCP [40], our results (Figures 2 and 3) are in line with a study conducted by Herten et al. where both MSCs and osteoblasts were cultivated on TCP particles [41]. Additionally, we confirmed the osteogenic phenotype based on upregulated expressions of early osteoblast-specific genes, including *RUNX2*, *SPP1* and *COL1A1* and enhanced expression of mature osteoblast markers (*SPP1*, *ON*), indicating the mineralization capacity of MSCs within the tissue models (Figure 4) [42,43]. Secondly, in order to generate cartilage-like tissue components, emerging tissue engineering approaches use mesenchymal condensation based on cell-sheet formation, self-assembly or self-organization to engineer scaffold-free constructs [44–47]. Although MSCs are well-known to differentiate into various lineages, their capacity to form mature chondrocytes and full articular cartilage is limited. However, chondrogenic differentiated MSCs still provide sufficient similarities to articular cartilage which renders them eligible to serve as therapeutic option for e.g., cartilage defects [48] or in vitro models [18,49]. Furthermore, Li et al. showed that adding mechanical load additionally promotes chondrogenesis of MSCs by up-regulating TGF- β . An approach which is identical to the procedure we applied here. As a result, chondroblastic cells form a functional network, embedded into their self-synthesized matrix comprising both superficial and middle zone and abundant expression of collagen type 2 but also collagen type 1 (Figure 5). The latter is a prerequisite for chondrogenic MSC differentiation, because MSCs firstly reside within the pre-cartilaginous matrix rich in collagen type 1 inducing cell-cell contact, which finally results in an increased expression of *SOX9* and differentiation [50–52].

The crosstalk between bone and cartilage within the osteochondral unit is supposed to play an important role in the etiopathogenesis of cartilage matrix degradation and subchondral bone erosion and needs, therefore, to be considered in emerging therapeutic strategies and preclinical testing tools. To mimic the osteochondral unit, common in vitro approaches use a bi-layered scaffold where chondrocytes or MSCs are embedded in polymers and the bone layer is based on e.g., ceramics [53]. Both layers are most often fixed by adhesives such as fibrin resulting in a barrier for cell-cell contacts. Conversely, Lin et al. encapsulated iPSCs-derived MSCs in a gelatin scaffold and cultivated these scaffolds in a dual-flow bioreactor [54]. In contrast to our approach, they directly generated a stable bridging zone between the components but neglected the different cellular demands on the given ECM (stiffness, matrix composition) and microenvironment (oxygen supply) [53]. As shown in our study, co-cultivation for 21 days in a static culture system led to the formation of a bridging zone, suggesting a functional interplay between the two tissue components (subchondral bone-like zone; Figure 6).

Studies have shown that synovial fibroblasts and different immune cells (e.g., neutrophils, macrophages, T-cells) are a major source of pro-inflammatory cytokines in RA. For example, TNF α , IL-6 and MIF activate resident chondrocytes to produce TNF α , IL-8, IL-6 and matrix metalloproteinases (MMP1, MMP3, MMP13) promoting cartilage degeneration and subsequent bone erosion. In line with our results, Pretzel et al. analyzed cartilage degradation of bovine cartilage discs co-cultivated with human synovial fibroblasts and supplemented IL-1 β and TNF α . They were able to demonstrate an upregulation of tissue-degrading enzymes (MMP1, MMP3) and pro-inflammatory cytokines (IL-6, IL-8). In addition, several studies report an increased production of matrix metalloproteinases (MMP3, MMP13) in chondrocytes and cartilage explants after IL-6 treatment, which is in accordance with our results (Figure 7) [55–57]. Moreover, TNF α and IL-6 have been recently shown to have overlapping and synergistic effects, even though some of these effects are regulated by separate mechanisms [58]. Interestingly, Honorati et al. analyzed chondrocytes from non-inflammatory pathology in comparison with RA chondrocytes showing that inflammation seems to play an important role in inducing the chondrocyte-related VEGF secretion [59]. Here, we demonstrate that exposure to TNF α , IL-6 and MIF [60–62] does induce arthritic transformation followed by activation of the angiogenic marker *VEGFA* in the SFCC (Figure 7) [63]. In contrast, we did not observe a cytokine-related upregulation of *IL6* which has been already described after TNF α exposure. It was shown that the self-activation of pY-STAT3 by newly synthesized IL-6 leads to a transient auto-inhibition of further IL-6 transcription [64]. Thus, the supplementation of IL-6 may be responsible for the absence of induced IL-6 expression in our study.

Finally, we provide first evidence that effects of immunomodulatory drug candidates can be demonstrated in our MSC-derived OTM on mRNA level (Figure 7). We used adalimumab [30,31], tocilizumab [32,33] and milatuzumab [34] for proof of concept, as these are clinically used monoclonal antibodies directed against TNF α , IL-6 and MIF. Recent work has indicated that TNF α may mediate its angiogenic effect in RA via IL-8 and VEGF [65]. In fact, treatment strategies aimed at decreasing TNF α resulted in decreased angiogenic IL-8 production in vitro and decreased serum levels of angiogenic VEGF in RA patients [66,67]. We reported that treatment in a pharmacologically relevant dose does prevent pro-inflammatory effects, attenuating the TNF and IL-6 signaling pathway. Preclinical testing of therapeutics towards RA is a major challenge, since current therapeutic approaches target specific molecules or pathways by e.g., antibodies or small molecules which are unique in humans. Nevertheless, recent studies have indicated that there are differences in functionality and binding capacity between the human and murine system leading to the potential failure of promising antibodies during clinical trials as exemplified by anti-IL-17 antibodies (e.g., secukinumab) [68] as an biological disease-modifying antirheumatic drugs or the phosphodiesterase 4 inhibitor apremilast [69] which were both tested successfully in mice but failed to provide clinical efficacy in patients suffering from RA [70–72].

Nevertheless, the model has still some limitations that need to be addressed in the future. So far, the TBBC does not include bone remodeling processes and our current version of the OTM omits circulating cells such as leukocytes and endothelial cells. However, there is the opportunity to expand our model by including e.g., osteoblasts/osteoclasts, selected RA-related leukocyte populations or human umbilical vein endothelial cells. Finally, an approach that offers possibilities to investigate the cellular behavior and intercellular interactions in a perfused 3D context is given by the organ-on-a-chip technology [73].

4. Materials and Methods

4.1. MSC Isolation, Cultivation and Characterization

Primary human mesenchymal stromal cells (MSCs) were isolated from bone marrow obtained from patients undergoing total hip replacement (provided by the Center of Musculoskeletal Surgery, Charité-Universitätsmedizin Berlin, donor list in Table 1). Study design and protocols were approved by the Charité-Universitätsmedizin Ethics Commit-

tee and performed according to the Helsinki Declaration (ethical approval EA1/012/13, 31 January 2013). Briefly, bone marrow was transferred into a T-175 flasks (Greiner Bio-one International GmbH, Kremsmünster, Austria) with Dulbecco's Modified eagle minimal Essential Medium (DMEM) GlutaMAX™ (Gibco, Waltham, MA, USA) supplemented with 10% fetal calf serum (FCS, Biowest, Nuaille, France), 100 U/mL penicillin (Gibco, Waltham, MA, USA), 100 µg/mL streptomycin (Gibco, Waltham, MA, USA) and 20% StemMACS™ MSC Expansion Media Kit XF (Miltenyi Biotech, Bergisch Gladbach, Germany). After incubation for two days (37 °C, 5% CO₂), medium was changed, remaining tissue parts were removed, and the adherent cells were washed with phosphate-buffered saline (PBS; pH 7.4). Reaching 90% confluency, cells were passaged. MSCs were characterized after three passages using differentiation assays (adipogenic, osteogenic, chondrogenic) and flow cytometry (MSC Phenotyping Kit; Miltenyi Biotech, Bergisch Gladbach, Germany; CD90+, CD105+, CD73+, CD14−, CD20−, CD34−, CD45−, and HLA-DR−, Appendix A Figure A3). Only MSCs successfully passing the characterization were further used for experiments until passage 3–8.

Table 1. Human MSCs donor information and conducted experiments.

Donor	Age	Sex	Type of Experiments	Used Methods
MSC 1	62	m		LDH, WST-1, gene expression analysis, histology, immunofluorescence
MSC 2	78	m		
MSC 3	56	w		
MSC 4	69	w		
MSC 5	57	m		
MSC 6	74	w		
MSC 7	75	w	Characterization of TBBCs	LDH, µCT, SEM, Alizarin Red, histology, immunofluorescence
MSC 8	76	w		
MSC 9	77	m		
MSC 10	77	w		
MSC 11	66	m		
MSC 12	53	m		
MSC 13	63	m		
MSC 14	84	w	Characterization of SFCCs	Gene expression analysis, histology
MSC 15	71	w		
MSC 16	66	m		
MSC 17	59	w		
MSC 18	79	m		
MSC 19	78	m		
MSC 20	64	m	Co-cultivation (OTM), proof of OTM experiments	Gene expression analysis, histology
MSC 21	67	w		
MSC 22	72	w		
MSC 23	76	w		
MSC 24	57	m		

For differentiation, MSCs were seeded at a density of 1×10^4 cells per well in a 96-well plate (Greiner Bio-one International GmbH, Kremsmünster, Austria) and cultivated in appropriate differentiation medium for three weeks (37 °C, 5% CO₂). For adipogenic differentiation, MSCs were incubated in StemMACS™ AdipoDiff medium (Miltenyi Biotech, Bergisch Gladbach, Germany). After 3 weeks, cells were fixed in 4% paraformaldehyde (PFA; Electron Microscopy Sciences, Hatfield, PA, USA) for 15 min. After washing with 60% isopropanol, cells were stained with 60% Oil Red O solution dissolved in ddH₂O (Sigma-Aldrich Chemie GmbH, Munich, Germany: freshly prepared and passed through a 0.45 µm filter; stock solution: 0.3% Oil Red O dissolved in 100% isopropanol) for 15 min, washed with 60% isopropanol. Finally, ddH₂O was added and intracellular lipid droplets were analyzed microscopically.

For osteogenic differentiation, MSCs were cultivated in StemMACS™ OsteoDiff medium (Miltenyi Biotech, Bergisch Gladbach, Germany) for three weeks. Alizarin Red staining was performed according to the following protocol: cells were washed with PBS, fixed with 4% PFA for 15 min, washed with PBS and stained using a 0.5% Alizarin Red S staining solution (pH 4; Sigma-Aldrich Chemie GmbH, Munich, Germany) dissolved in ddH₂O for 15 min. After the final washing step with ddH₂O, calcium deposition was analyzed microscopically.

For chondrogenic differentiation MSCs were transferred in a 3D state (pellet cultivation) via centrifugation for 10 min at 400 × *g* and cultivated in StemMACS™ ChondroDiff medium (Miltenyi Biotech, Bergisch Gladbach, Germany). Slices were prepared and Alcian Blue staining was performed to analyze the presence of acidic mucopolysaccharides microscopically.

4.2. Generation of the Osteogenic Component—TCP-Based Bone Component (TBBC)

The 3D cultivation was performed in cell culture inserts (Sarstedt AG, Nümbrecht, Germany) with a 0.3 cm² growth area and a polyethylene terephthalate (PET) membrane (8 μm pore size). Approximately 12 mg of β-tricalcium phosphate (TCP) granules (Cerasorb®M, Curasan AG, Kleinostheim, Germany) were preincubated with 1 mL of DMEM GlutaMAX™ supplemented with 10% FCS, 100 U/mL penicillin, 100 μg/mL streptomycin, in the following referred to as normal medium (NM) for one day. To optimize the 3D TCP-based bone component (TBBC), 1 × 10⁶ MSCs or pre-differentiated MSCs (pre-incubated in osteogenic differentiation medium for one week, oMSCs) were seeded onto TCP granules. Cell suspension and TCP particles were gently mixed and cultured in osteogenic medium (OM, NM supplemented with 0.5 mM ascorbic acid, 10^{−8} M dexamethasone, 10 mM L-glycerophosphate). Medium was changed twice a week.

4.3. Generation of the Scaffold-Free Cartilage Component (SFCC)

The 3D scaffold-free cartilage components (SFCCs) were generated based on a patented method (No. 10 2004 001 225, German Patent and Trade Mark Office, 2004) purchased from the Research Center of Medical Technology and Biotechnology (fzmb GmbH), Bad Langensalza, Germany. Briefly, approximately 6 × 10⁶ MSCs were detached and transferred into a 3D state via centrifugation for 10 min at 400 × *g*. After 5 to 7 days, biomechanical forces were applied for 3 to 4 weeks to the self-assembled 3D component. SFCCs were then cultivated for up to 21 days without biomechanical forces (resting phase) in NM supplemented with 9.39 mg/L ascorbic acid (Sigma-Aldrich Chemie GmbH, Munich, Germany), in the following referred to as chondrogenic medium (CM).

4.4. Generation of the Osteochondral Tissue Model and Experimental Setup

An overview on the experimental setup is given Figure 1. Co-cultivation of both SFCC and TBBC was performed in cell culture inserts by placing the SFCC on top of the TBBC. Chondrogenic medium was added and both components were cultured for 21 days at 37 °C, 5% CO₂ to develop the osteochondral tissue model by allowing cell-cell interaction. To mimic chronic cytokine-mediated joint inflammation, stimulation was performed using CM (CTRL) supplemented with 10 ng/mL recombinant human macrophage migration inhibitory factor (MIF) [60], 30 ng/mL recombinant human IL-6 [62], 10 ng/mL recombinant human tumor necrosis factor alpha (TNFα; all ImmunoTools GmbH, Friesoythe; Germany) [61] using concentrations as reported from synovial fluid of patients with RA and 23 μg/mL Flebogamma (Grifols, Barcelona, Spain) in the following referred to as STIM. To evaluate the impact of specific therapeutic approaches, CM was supplemented with cytokines and well-known clinically available drugs in their therapeutic dosage: 10 μg/mL adalimumab (Amgen, Thousand Oaks, CA, USA) [30,31], 8 μg/mL tocilizumab (Roche, Basel, Switzerland) [32,33] and 5 μg/mL milatuzumab (Immunomedics, Morris Plains, NJ, USA) [34], in the following referred to as TREAT. Medium was changed every

3 days including the respective supplements resulting in a repetitive chronic cytokine stimulation in case of STIM and a repeated counter-treatment in case of TREAT.

4.5. Viability and Cytotoxicity Assay

Cell Proliferation Reagent WST-1 Kit (Sigma-Aldrich Chemie GmbH, Munich, Germany) was used according to the manufacturer's instructions. Samples were mixed with WST-1 solution and incubated for 30 min at 37 °C, 5% CO₂. Supernatants were measured photometrically using a standard 96-well plate reader (Synergy™ HT Reader, BioTek Instruments, Bad Friedrichshall, Germany) at a wavelength of 450 nm (reference wavelength 630 nm). To induce cell death, a control group of cells was incubated with 2% Triton X-100 (Sigma-Aldrich Chemie GmbH, Munich, Germany) for one day (Ctrl). The assay was performed in two independent experiments with duplicates.

Cytotoxicity Detection LDH Kit (Sigma-Aldrich Chemie GmbH, Munich, Germany) was used to detect cytotoxic effects of TCP particles, cell/TCP ratio, cytokine and treatment concentrations. According to the manufacturer's instructions the OD-values were measured at a wavelength of 490 nm (reference wavelength 630 nm). Additionally, to induce LDH release via cell death, cells were incubated with 2% Triton X-100 for one day, in the following referred as high control (Ctrl). The LDH assay was performed in duplicates.

LIVE/DEAD® Viability/Cytotoxicity Kit (Invitrogen AG, Carlsbad, CA, USA) was used to determine cell viability and to visualize 3D cell colonization. Samples were first washed with PBS, transferred to a slide and subsequently incubated with LIVE/DEAD® staining solution (established concentration: 2 µM Calcein AM, 4 µM EthD-1) for 35 min at RT in the dark. Evaluation was performed with the fluorescence microscope BZ-9000 (Keyence, Itasca, IL, USA).

4.6. Alizarin Red Assay

For calcium quantification, Alizarin Red assay was performed. MSCs were seeded at a density of 1×10^4 cells per well in a 96-well plate and cultivated in NM (NM control), in OM without TCP (ML) and in OM with TCP co-cultivating MSCs (MSC) or pre-differentiated MSCs (oMSC). To exclude TCP-related staining, the OD value of TCP cultivated in OM without cells was subtracted from the TCP OD value. Medium was removed and cells were fixed in 4% PFA (10 min) and stained with Alizarin Red S staining solution (10 min), washed with ddH₂O, staining was dissolved with 10% cetylpyridiniumchlorid and OD-values were measured with a plate reader at a wavelength of 562 nm (reference wavelength 630 nm). Data were normalized to the NM OD-values. The assay was performed in duplicates.

4.7. Scanning Electron Microscopy

First, samples were washed twice with PBS and then fixed with 2.5% glutaraldehyde (Sigma-Aldrich Chemie GmbH, Munich, Germany) solved in PBS (10 min, room temperature—RT). After washing with PBS, samples were dewatered using ascending ethanol concentrations 30%, 50%, 70%, 80%, 90%, 95% and twice 100% for 5 min each. Afterwards samples were incubated with hexamethyldisilazane (1×5 min, 2×10 min; Sigma-Aldrich Chemie GmbH, Munich, Germany). Finally, samples were air dried overnight and coated with gold using a Fine Coater JFC-1200 (Jeol GmbH, Freising, Germany). The imaging with the scanning electron microscope JCM-6000 Plus Neo Scope™ (Jeol GmbH, Freising, Germany) was performed under high vacuum.

4.8. Histochemistry

Slices were prepared using the Kawamoto method to allow the embedding of samples without decalcification [74]. Samples were first fixed in 4% PFA for 3 h followed by an ascending sucrose solution treatment (10%, 20% and 30%) for one day each at 4 °C. Afterwards, the samples were embedded with SCEM embedding medium (Sectionlab, Hiroshima, Japan) and stored at −80 °C. We prepared cryo-sections of 7 µm thickness using Kawamoto cryofilm type 2C (Sectionlab, Hiroshima, Japan). Prior to each staining

procedure, slices were dried for 20 min at RT and at the final step covered with DPX Mountant (Sigma-Aldrich Chemie GmbH, Munich, Germany).

Hematoxylin and Eosin (H&E) staining was conducted using the following protocol: fixing with 4% PFA for 10 min, washing with ddH₂O for 5 min, first staining with Harris's hematoxylin for 7 min (Merck, Darmstadt, Germany), washing twice with ddH₂O, differentiating in 0.25 mL HCl solution (37% HCl, Merck, Darmstadt, Germany) in 100 mL of 70% ethanol. After washing with tap water for 10 min, second staining with Eosin (0.2%, 2 min; Chroma Waldeck GmbH & Co KG, Münster, Germany) was performed, differentiation step in 96% ethanol, followed by 100% ethanol (2 × 2 min) and xylol (2 × 2 min) treatments.

Von Kossa Toluidine blue staining was performed according to the following protocol: fixing with 4% PFA (10 min), washing with ddH₂O (5 min), staining in silver nitrate solution (3% in ddH₂O, 10 min), washing with ddH₂O, staining in sodium carbonate/formaldehyde solution (2 min), washing with ddH₂O, followed by a staining step in sodium thiosulfate solution (5% in ddH₂O, 5 min). After washing with tap water for 10 min, slices were washed with ddH₂O, counter stained in Toluidine blue solution for 8 min, washed with ddH₂O, differentiated in 70% ethanol, 100% ethanol and fixed in xylol (each 2 × 2 min).

Alcian Blue staining was performed according to the following protocol: fixing with 4% PFA (10 min), washing with ddH₂O (5 min), treating with 3% acetic acid (3 min), staining step in 1% Alcian Blue for 30 min (Sigma-Aldrich Chemie GmbH, Munich, Germany), washing in 3% acetic acid (pH 2.5), washing with ddH₂O, staining step in nuclear fast red aluminum sulfate for 4 min, washing with ddH₂O, followed by 80%, 96% and 100% ethanol (2 min each) and fixing with xylol (2 × 2 min).

4.9. Immunohistochemistry

Immunohistochemistry was performed according to the following protocol: rehydrating with PBS (10 min), blocking with 3% H₂O₂ (30 min), washing with PBS (5 min), blocking with 5% normal horse serum (Vector Laboratories, Burlingame, CA, USA) in 2% bovine serum albumin (BSA, Sigma-Aldrich Chemie GmbH, Munich, Germany)/PBS, first incubation step with primary antibody for collagen type I (1:500, Abcam plc, Cambridge, UK) or collagen type II (1:10, Quartett GmbH, Berlin, Germany) at 4 °C overnight, washing in PBS (2 × 5 min), second incubation step with 2% biotinylated horse anti-mouse IgG antibody (secondary antibody, Vector Laboratories, Burlingame, CA, USA) diluted in 5% normal horse serum/2% BSA/PBS for 30 min and washing in PBS (2 × 5 min). After incubation with Vecastain[®] Elite[®] ABC HRP Kit (Vector Laboratories, Burlingame, CA, USA) for 50 min, slices were washed with PBS (2 × 5 min), incubated with DAB Peroxidase HRP Substrate Kit (microscopic control, Vector Laboratories, Burlingame, CA, USA), thus the reaction was stopped with PBS, followed by washing with ddH₂O, counter staining step in Mayer's hematoxylin (2 min, Sigma-Aldrich Chemie GmbH, Munich, Germany), washing in tap water (10 min) and finally washing in ddH₂O.

4.10. Immunofluorescence Staining

Immunofluorescence staining was performed in a dark, humid chamber at RT. First, slices were air dried and then rehydrated with PBS for 10 min. Subsequently, unspecific binding sites were blocked with PBS/5% FCS for 30 min. Afterwards, primary antibody was diluted in PBS/5% FCS/0.1% Tween[®] 20 (Qbiogene Inc., Carlsbad, CA, USA) and incubated according to the manufacturer's instructions, followed by washing with PBS/0.1% Tween[®] 20 (3×). Secondary antibody was diluted in PBS/5% FCS/0.1% Tween[®] 20 and applied for 2 h, washed with PBS/0.1% Tween[®] 20 (3×) and nuclei staining was performed using 4',6-diamidino-2-phenylindole (DAPI; 1 µg/mL diluted in PBS/5% FCS/0.1% Tween[®] 20, 15 min). After bubble-free covering with FluoroMount (Sigma-Aldrich Chemie GmbH, Munich, Germany) covering medium, imaging was performed with the fluorescence microscope BZ-9000 (Keyence). Image analysis was performed using ImageJ. Primary and secondary antibodies used for immunofluorescence staining are listed in Table 2.

Table 2. Primary and secondary antibodies used for immunofluorescence staining.

Primary Antibody	Dye	Host	ID	Concentration [mg/mL]	Company
Phalloidin	TRITC	-	P1951	1.5	Sigma-Aldrich
Laminin	-	rabbit	NB300	0.8	Novus Biologicals LLC
Osteopontin	A488	rabbit	ab8448	1	Abcam
Collagen 1	-	mouse	ab6308	1.5	Abcam
Collagen 2	-	mouse	CO072	1	Quartett
Secondary Antibody	Dye	Host	ID	Concentration [mg/mL]	Company
Anti-mouse	Biotin	horse	BA-2000	1.5	Vector Laboratories Inc.
Anti-rabbit	A488	goat	A32731	2	Thermo Fisher Scientific

TUNEL assay (Sigma-Aldrich Chemie GmbH, Munich, Germany) was performed to detect apoptotic cells. As a positive control, slices were treated with desoxyribonuclease (DNase) I (0.34 Kunitz units, Qiagen GmbH, Hilden, Germany) for 10 min and washed twice with PBS. Staining was performed with TUNEL reaction mixture (5 μ L TUNEL enzyme + 45 μ L TUNEL label) for 1 h at 37 °C and then washed twice with PBS. A negative control was incubated with TUNEL label without TUNEL enzyme.

4.11. Image Analysis with ImageJ

Evaluation of immunofluorescence images was performed using FIJI ImageJ 1.52p (National Institutes of Health, Bethesda, MD, USA). First, a free hand selection tool was used to define the region of interest (ROI) representing the total area (t.a.). The outer area (o.a.) was determined by a reduction of the diameter by 0.95 for X- and Y-axes. Another reduction of the diameter by 0.5 for X- and Y-axes leads to the middle area (m.a.; outer area subtracted from total area, diameter reduced by 0.5 for X- and Y-axes) and inner area (i.a.; remaining inner part). The positive stained areas were defined using the color threshold tool. Finally, the cell count was performed with a combination of the Find Maxima tool in ImageJ and manual counting.

4.12. In Vitro μ CT

TBBCs were scanned at a nominal resolution of 4–5 μ m, with a Bruker SkyScan 1172 high-resolution microCT (Bruker, Kontich, Belgium). X-ray tube voltage was of 80 kV and a 0.5 mm aluminum filter was employed. The scan orbit was 360 degrees with a rotation step of 0.3 degree. For reconstruction the SkyScan NRecon software was used and Gaussian smoothing, ring artifact reduction, misalignment compensation, and beam hardening correction were applied. CTAn (Bruker MicroCT, Kontich, Belgium) software was used to analyze the total VOI.

4.13. RNA Isolation, cDNA Synthesis and qPCR

Total RNA from the 3D components was isolated according to the manufacturer's instructions using the RNeasy[®] Fibrous Tissue Mini Kit (Qiagen GmbH, Hilden, Germany) after homogenization with the TissueRuptor II (Qiagen GmbH, Hilden, Germany). Total RNA from monolayer (ML) cultivations was isolated according to the manufacturer's instructions using the RNeasy[®] Mini Kit (Qiagen GmbH, Hilden, Germany). RNA concentrations were determined via NanoDrop[®]-ND-1000 Spectrophotometer (Thermo Fisher Scientific, Waltham, MA, USA) and stored at –80 °C. TaqMan[®] Reverse Transcription Reagents Kit (Applied Biosystems Inc., Foster City, CA, USA) was used for cDNA synthesis with more than 50 ng per reaction whereas Sensiscript Reverse Transcriptase Kit (Qiagen GmbH, Hilden, Germany) was used for cDNA synthesis with less than 50 ng per reaction. Primers were designed using Primer Blast (NCBI, Bethesda, MD, USA). Sequence analyses of qPCR products were confirmed by LGC Genomics GmbH (Berlin, Germany) and evalu-

ated using the Chromas software 2.6.4 (Technelysium Pty Ltd., South Brisbane, Australia). Quantitative PCR (qPCR) was carried out using the DyNAmo ColorFlash SYBR Green qPCR Kit (Thermo Fisher Scientific, Waltham, MA, USA) in the Stratagene Mx3000P™ (Agilent Technologies Inc., Santa Clara, CA, USA). The qPCR was conducted in duplicates with a non-template control (NTC) for each mastermix using the following temperature profile: 7 min initial denaturation at 95 °C, 45 to 60 cycles of 10 s denaturation at 95 °C, 7 s annealing at 60 °C and 9 s elongation at 72 °C. After every run, a melting curve analysis was performed to confirm primer specificity. In cases where the amplification curve did not reach the threshold within the cycles, the value of the maximum cycle number was used. All primers were purchased from TIB Molbiol Berlin, Germany (Table 3).

Table 3. Sequences of primers, fragment size and GenBank ID used for qPCR.

Gene	Sequence of Forward Primer	Sequence of Reverse Primer	GenBank ID
EF1A	GTTGATATGGTTCCTGGCAAGC	TTGCCAGCTCCAGCAGCCT	NM_001402.5
RUNX2	TTACTTACACCCCGCCAGTC	TATGGAGTGCTGCTGGTCTG	NM_001015051.3
SPP1	GCCGAGGTGATAGTGTGGTT	TGAGGTGATGTCCTCGTCTG	NM_001251830.1
COL1A1	CAGCCGCTTCACCTACAGC	TTTGTATTCAATCACTGTCTTGCC	NM_000088.3
ON	ACCAGCACCCCATGACG	AGGTCACAGGTCTCGAAAAAGC	NM_001309443.1
SOX9	CGCCTTGAAGATGGCGTTG	GCTCTGGAGACTTCTGAACGA	NM_000346.3
PPARG2	CAAACCCCTATTCCATGCTGTT	AATGGCATCTCTGTGTCAACC	NM_015869.4
COL2A1	GTGGGGCAAGACTGTTATCG	AGGTCAGGTCAGCCATTCAG	NM_033150.3
COL10A1	CCAGCACGCAGAATCCATCT	TATGCCTGTGGGCATTGGT	NM_000493.4
ACAN	AACGCAGACTACAGAAGCGG	GCGGACAAATTAGATGCGG	NM_001369268.1
MMP1	CTCTGGAGTAATGTACACCTCT	TGTTGGTCCACCTTTCATCTTC	NM_001145938.2
MMP3	ATCCTACTGTTGCTGTGCGT	CATCACCTCCAGAGTGTCCG	NM_002422.5
MMP13	TCCTGATGTGGTGAATACAATG	GCCATCGTGAAGTCTGGTAAAT	NM_002427.4
TNF	GTCTCCTACCAGACCAAG	CAAAGTAGACCCTGCCAGACTC	NM_000594.4
IL6	TACCCCAAGGAGAAGATTCC	TTTTCTGCCAGTGCCTCTTT	NM_001371096.1
IL8	GAATGGGTTTGTAGAAATGTGATA	CAGACTAGGGTTGCCAGATTTAAC	NM_000584.4
LDHA	ACCCAGTTTCCACCATGATT	CCCAAATGCAAGGAACACT	NM_005566.4
VEGFA	AGCCTTGCTTGCTGCTCTA	GTGCTGGCCTTGGTGAGG	NM_001025366.3

4.14. Statistical Analysis

Statistical analysis was performed using the GraphPad® Prism V.8.4.1 software (Graph-Pad Software, La Jolla/San Diego, CA, USA). All values are shown as the mean ± SEM if not indicated otherwise. Mann-Whitney U test was applied for independent datasets while dependent datasets were compared by means using the Wilcoxon-signed rank test. Values of $p < 0.05$ were considered as statistically significant.

5. Conclusions

We herein describe a novel alternative approach simulating key features of RA including cartilage destruction and subchondral bone erosion in late stages of disease to be used as preclinical drug screening tool. The 3D osteochondral tissue model replicates the interaction of cells within a physiological matrix and environment, the crosstalk between the major resident cells of human cartilage and anabolic bone, and the option to further expand cellular interactions by the application of e.g., leukocytes.

Author Contributions: Conceptualization, A.D., A.L., T.G.; methodology, A.D.; validation, A.D., A.L., T.G.; formal analysis, A.D., M.P., M.-C.W.; investigation, A.D., T.G., A.L.; data curation, A.D., T.G., A.L., F.B.; writing—original draft preparation, A.D., T.G., A.L., F.B.; writing—review and editing, A.D., T.G., A.L., F.B., G.-R.B., M.P., M.-C.W.; visualization, A.D.; supervision, T.G., A.L.; project administration, F.B.; funding acquisition, T.G., A.L., F.B. All authors have read and agreed to the published version of the manuscript.

Funding: This research was funded by the German Federal Ministry for Education and Research (BMBF), project number 031L0070A and Lush Prize Award 2018: Alexandra Damerou—Young Researcher, Rest of World. The work of A.D. was additionally supported by the Studienstiftung des deutschen Volkes. A.L. is currently being supported by the Joachim Herz Foundation (Add-on Fellowship 2019). The work of T.G. was supported by the Deutsche Forschungsgemeinschaft (353142848). Funding bodies did not have any role in designing the study, in collecting, analyzing and interpreting the data, in writing this manuscript, and in deciding to submit it for publication.

Institutional Review Board Statement: The study was conducted according to the guidelines of the Declaration of Helsinki, and approved by the Ethics Committee of the Charité-Universitätsmedizin Berlin (ethical approval EA1/012/13, 31 January 2013).

Informed Consent Statement: Informed consent was obtained from all subjects involved in the study.

Data Availability Statement: The data presented in this study are available on request from the corresponding author. The data are not publicly available due to privacy and ethical restrictions.

Acknowledgments: The authors would like to thank Manuela Jakstadt for excellent technical assistance, and Thomas Leeuw for providing technical advice. Bone-marrow was provided by the Tissue Harvesting Core Facility of the BIH Berlin. A.D., M.P., F.B., T.G. and A.L. are members of Berlin-Brandenburg research platform BB3R and Charité3R.

Conflicts of Interest: The authors declare no conflict of interest.

Appendix A

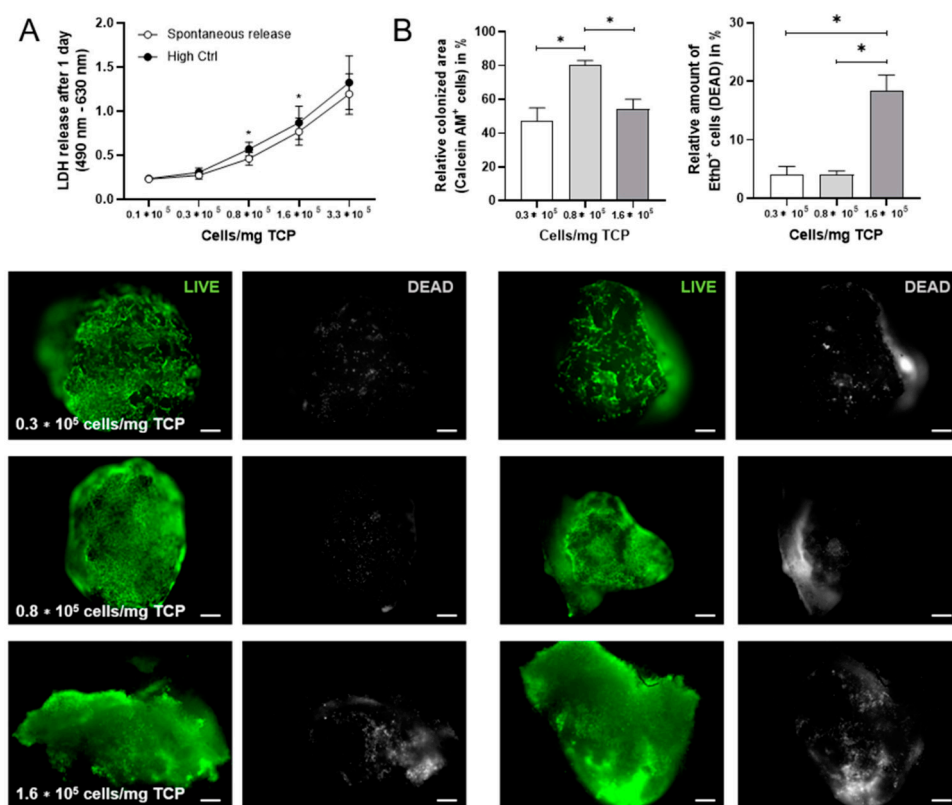


Figure A1. Cell number/mg TCP. (A) LDH assay was performed after 1 day and different cell densities (0.1×10^5 , 0.3×10^5 , 0.8×10^5 , 1.6×10^5 , 3.3×10^5 cells/mg TCP). High Ctrl = 2% of Triton X-100 to induce LDH release. Data are shown as mean \pm SEM (duplicates per donor) for $n = 4$. For statistical analysis the Wilcoxon matched-pairs signed rank test was used; * $p < 0.05$. (B) LIVE/DEAD staining was performed after 21 days and different cell densities (0.3×10^5 , 0.8×10^5 , 1.6×10^5 cells/mg TCP). Images were quantified using ImageJ. Green and grey colors discriminated between living and dead cells (scale bars = 100 μ m). Representative images are shown accordingly for $n = 5$. Data are shown as mean \pm SEM. For statistical analysis the Wilcoxon matched-pairs signed rank test was used; * $p < 0.05$. TCP, tricalcium phosphate; LDH, lactate dehydrogenase.

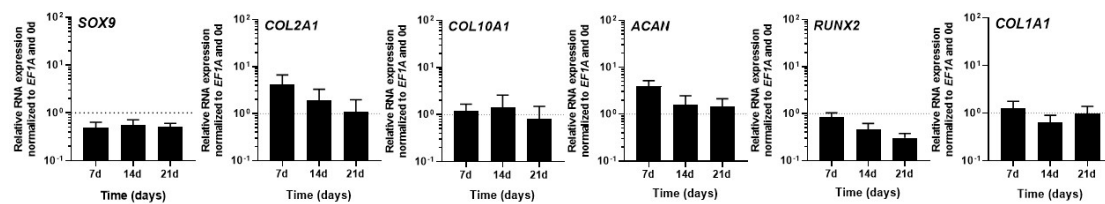


Figure A2. Gene expression analysis of scaffold-free cartilage components for *SOX9*, *COL2A1*, *COL10A1*, *ACAN*, *RUNX2* and *COL1A1* were performed after 0, 7, 14 and 21 days. The relative gene expression was normalized to the housekeeper gene *EF1A* and day 0. Data are shown as mean \pm SEM (duplicates per gene) for $n = 3$. Mann-Whitney U-test was used to determine the statistical significance. *SOX9*, SRY-box transcription factor 9; *COL2A1*, collagen type II alpha 1; *COL10A1*, collagen type X alpha 1; *ACAN*, aggrecan; *RUNX2*, runt-related transcription factor 2; *COL1A1*; collagen type I alpha 1; *EF1A*, eukaryotic translation elongation factor 1 alpha.

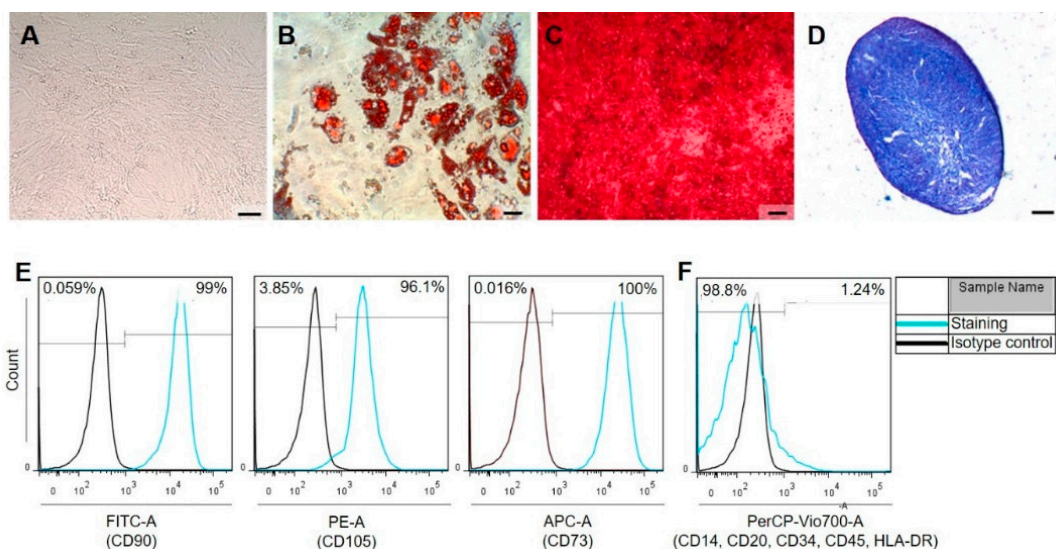


Figure A3. Bone marrow-derived mesenchymal stromal cells are characterized (A) by plastic adherence, by their differentiation capacity towards (B) adipogenesis using Oil Red O staining, (C) osteogenesis using Alizarin Red staining (scale bars = 100 μ m), (D) chondrogenesis using Alcian Blue staining (scale bar = 200 μ m), (E) the expression of surface marker CD90, CD105, CD73 and (F) lack of CD14, CD20, CD34, CD45 and HLA-DR.

References

1. Lepage, S.I.M.; Robson, N.; Gilmore, H.; Davis, O.; Hooper, A.; St John, S.; Kamesan, V.; Gelis, P.; Carvajal, D.; Hurtig, M.; et al. Beyond Cartilage Repair: The Role of the Osteochondral Unit in Joint Health and Disease. *Tissue Eng. Part. B Rev.* **2019**, *25*, 114–125. [[CrossRef](#)]
2. Burr, D.B.; Radin, E.L. Microfractures and Microcracks in Subchondral Bone: Are They Relevant to Osteoarthritis? *Rheum. Dis. Clin. N. Am.* **2003**, *29*, 675–685. [[CrossRef](#)]
3. Goldring, S.R.; Goldring, M.B. Changes in the Osteochondral Unit during Osteoarthritis: Structure, Function and Cartilage–Bone Crosstalk. *Nat. Rev. Rheumatol.* **2016**, *12*, 632–644. [[CrossRef](#)]
4. Imhof, H.; Sulzbacher, I.; Grampp, S.; Czerny, C.; Youssefzadeh, S.; Kainberger, F. Subchondral Bone and Cartilage Disease: A Rediscovered Functional Unit. *Investig. Radiol.* **2000**, *35*, 581–588. [[CrossRef](#)]
5. Kurz, B.; Lemke, A.K.; Fay, J.; Pufe, T.; Grodzinsky, A.J.; Schünke, M. Pathomechanisms of Cartilage Destruction by Mechanical Injury. *Ann. Anat. Anat. Anz.* **2005**, *187*, 473–485. [[CrossRef](#)]
6. Martel-Pelletier, J.; Barr, A.J.; Cicuttini, F.M.; Conaghan, P.G.; Cooper, C.; Goldring, M.B.; Goldring, S.R.; Jones, G.; Teichtahl, A.J.; Pelletier, J.-P. Osteoarthritis. *Nat. Rev. Dis. Primers* **2016**, *2*, 16072. [[CrossRef](#)]
7. McInnes, I.B.; Schett, G. The Pathogenesis of Rheumatoid Arthritis. *N. Engl. J. Med.* **2011**, *365*, 2205–2219. [[CrossRef](#)] [[PubMed](#)]
8. Hardy, E.; Fernandez-Patron, C. Destroy to Rebuild: The Connection between Bone Tissue Remodeling and Matrix Metalloproteinases. *Front. Physiol.* **2020**, *11*, 47. [[CrossRef](#)] [[PubMed](#)]
9. Otero, M.; Goldring, M.B. Cells of the Synovium in Rheumatoid Arthritis. Chondrocytes. *Arthritis Res. Ther.* **2007**, *9*, 220. [[CrossRef](#)] [[PubMed](#)]
10. Buttgerit, F. Views on Glucocorticoid Therapy in Rheumatology: The Age of Convergence. *Nat. Rev. Rheumatol.* **2020**, *16*, 239–246. [[CrossRef](#)]

11. Burmester, G.R.; Pope, J.E. Novel Treatment Strategies in Rheumatoid Arthritis. *Lancet* **2017**, *389*, 2338–2348. [[CrossRef](#)]
12. Schinnerling, K.; Rosas, C.; Soto, L.; Thomas, R.; Aguillón, J.C. Humanized Mouse Models of Rheumatoid Arthritis for Studies on Immunopathogenesis and Preclinical Testing of Cell-Based Therapies. *Front. Immunol.* **2019**, *10*, 203. [[CrossRef](#)] [[PubMed](#)]
13. Trentham, D.E.; Townes, A.S.; Kang, A.H. Autoimmunity to Type II Collagen an Experimental Model of Arthritis. *J. Exp. Med.* **1977**, *146*, 857–868. [[CrossRef](#)] [[PubMed](#)]
14. Damerau, A.; Gaber, T. Modeling Rheumatoid Arthritis in Vitro: From Experimental Feasibility to Physiological Proximity. *Int. J. Mol. Sci.* **2020**, *21*, 7916. [[CrossRef](#)] [[PubMed](#)]
15. Murphy, G.; Lee, M.H. What Are the Roles of Metalloproteinases in Cartilage and Bone Damage? *Ann. Rheum. Dis.* **2005**, *64*, iv44. [[CrossRef](#)]
16. Gaber, T.; Brinkman, A.C.K.; Pienczikowski, J.; Diesing, K.; Damerau, A.; Pfeiffenberger, M.; Lang, A.; Ohrndorf, S.; Burmester, G.R.; Buttgerit, F.; et al. Impact of Janus Kinase Inhibition with Tofacitinib on Fundamental Processes of Bone Healing. *Int. J. Mol. Sci.* **2020**, *21*, 865. [[CrossRef](#)]
17. Donlin, L.T.; Jayatilleke, A.; Giannopoulou, E.G.; Kallioli, G.D.; Ivashkiv, L.B. Modulation of Tnf-Induced Macrophage Polarization by Synovial Fibroblasts. *J. Immunol.* **2014**, *193*, 2373–2383. [[CrossRef](#)]
18. Weber, M.C.; Fischer, L.; Damerau, A.; Ponomarev, I.; Pfeiffenberger, M.; Gaber, T.; Gotschel, S.; Lang, J.; Roblitz, S.; Buttgerit, F.; et al. Macroscale Mesenchymal Condensation to Study Cytokine-Driven Cellular and Matrix-Related Changes During Cartilage Degradation. *Biofabrication* **2020**, *12*, 045016. [[CrossRef](#)]
19. Pretzel, D.; Pohlers, D.; Weinert, S.; Kinne, R.W. In Vitro Model for the Analysis of Synovial Fibroblast-Mediated Degradation of Intact Cartilage. *Arthritis Res. Ther.* **2009**, *11*, R25. [[CrossRef](#)]
20. Lubke, C.; Ringe, J.; Krenn, V.; Fernahl, G.; Pelz, S.; Kreuzsch-Brinker, R.; Sittinger, M.; Paulitschke, M. Growth Characterization of Neo Porcine Cartilage Pellets and Their Use in an Interactive Culture Model. *Osteoarthr. Cartil.* **2005**, *13*, 478–487. [[CrossRef](#)]
21. Chabaud, M.; Miossec, P. The Combination of Tumor Necrosis Factor A Blockade with Interleukin-1 and Interleukin-17 Blockade Is More Effective for Controlling Synovial Inflammation and Bone Resorption in an Ex Vivo Model. *Arthritis Rheum.* **2001**, *44*, 1293–1303. [[CrossRef](#)]
22. Kim, T.W.; Lee, M.C.; Bae, H.C.; Han, H.S. Direct Coculture of Human Chondrocytes and Synovium-Derived Stem Cells Enhances in Vitro Chondrogenesis. *Cell J.* **2018**, *20*, 53–60. [[PubMed](#)]
23. Kandel, R.A.; Grynopas, M.; Pilliar, R.; Lee, J.; Wang, J.; Waldman, S.; Zalzal, P.; Hurtig, M. Repair of Osteochondral Defects with Biphasic Cartilage-Calcium Polyphosphate Constructs in a Sheep Model. *Biomaterials* **2006**, *27*, 4120–4131. [[CrossRef](#)] [[PubMed](#)]
24. Schaefer, D.; Martin, I.; Jundt, G.; Seidel, J.; Heberer, M.; Grodzinsky, A.; Bergin, I.; Vunjak-Novakovic, G.; Freed, L.E. Tissue-Engineered Composites for the Repair of Large Osteochondral Defects. *Arthritis Rheum.* **2002**, *46*, 2524–2534. [[CrossRef](#)]
25. Schek, R.M.; Taboas, J.M.; Segvich, S.J.; Hollister, S.J.; Krebsbach, P.H. Engineered Osteochondral Grafts Using Biphasic Composite Solid Free-Form Fabricated Scaffolds. *Tissue Eng.* **2004**, *10*, 1376–1385. [[CrossRef](#)] [[PubMed](#)]
26. Fukuda, A.; Kato, K.; Hasegawa, M.; Hirata, H.; Sudo, A.; Okazaki, K.; Tsuta, K.; Shikinami, Y.; Uchida, A. Enhanced Repair of Large Osteochondral Defects Using a Combination of Artificial Cartilage and Basic Fibroblast Growth Factor. *Biomaterials* **2005**, *26*, 4301–4308. [[CrossRef](#)]
27. Gilbert, S.J.; Singhrao, S.K.; Khan, I.M.; Gonzalez, L.G.; Thomson, B.M.; Burdon, D.; Duance, V.C.; Archer, C.W. Enhanced Tissue Integration During Cartilage Repair In Vitro Can Be Achieved by Inhibiting Chondrocyte Death at the Wound Edge. *Tissue Eng. Part. A* **2009**, *15*, 1739–1749. [[CrossRef](#)]
28. Darling, E.M.; Athanasiou, K.A. Rapid Phenotypic Changes in Passaged Articular Chondrocyte Subpopulations. *J. Orthop. Res.* **2005**, *23*, 425–432. [[CrossRef](#)]
29. Vinken, M.; Blaauboer, B.J. In Vitro Testing of Basal Cytotoxicity: Establishment of an Adverse Outcome Pathway from Chemical Insult to Cell Death. *Toxicol. Vitro.* **2017**, *39*, 104–110. [[CrossRef](#)]
30. Nguyen, D.X.; Cotton, A.; Attipoe, L.; Ciurtin, C.; Dore, C.J.; Ehrenstein, M.R. Regulatory T Cells as a Biomarker for Response to Adalimumab in Rheumatoid Arthritis. *J. Allergy Clin. Immunol.* **2018**, *142*, 978–980.e979. [[CrossRef](#)]
31. Pattacini, L.; Boiardi, L.; Casali, B.; Salvarani, C. Differential Effects of Anti-Tnf-A Drugs on Fibroblast-Like Synoviocyte Apoptosis. *Rheumatology* **2009**, *49*, 480–489. [[CrossRef](#)] [[PubMed](#)]
32. Gaber, T.; Hahne, M.; Strehl, C.; Hoff, P.; Dörrfel, Y.; Feist, E.; Burmester, G.-R.; Buttgerit, F. Disentangling the Effects of Tocilizumab on Neutrophil Survival and Function. *Immunol. Res.* **2016**, *64*, 665–676. [[CrossRef](#)] [[PubMed](#)]
33. Shin, B.-H.; Ge, S.; Mirocha, J.; Jordan, S.C.; Toyoda, M. Tocilizumab (Anti-IL-6r) Suppressed Tnf α Production by Human Monocytes in an in Vitro Model of Anti-HLA Antibody-Induced Antibody-Dependent Cellular Cytotoxicity. *Transplant. Direct* **2017**, *3*, e139. [[CrossRef](#)] [[PubMed](#)]
34. Stein, R.; Smith, M.R.; Chen, S.; Zalath, M.; Goldenberg, D.M. Combining Milatuzumab with Bortezomib, Doxorubicin, or Dexamethasone Improves Responses in Multiple Myeloma Cell Lines. *Clin. Cancer Res.* **2009**, *15*, 2808. [[CrossRef](#)] [[PubMed](#)]
35. Gimble, J.M.; Guilak, F.; Nuttall, M.E.; Sathishkumar, S.; Vidal, M.; Bunnell, B.A. In Vitro Differentiation Potential of Mesenchymal Stem Cells. *Transfus. Med. Hemother.* **2008**, *35*, 228–238. [[CrossRef](#)]
36. Larson, B.L.; Ylöstalo, J.; Prockop, D.J. Human Multipotent Stromal Cells Undergo Sharp Transition from Division to Development in Culture. *Stem Cells* **2008**, *26*, 193–201. [[CrossRef](#)]
37. Tuli, R.; Nandi, S.; Li, W.-J.; Tuli, S.; Huang, X.; Manner, P.A.; Laquerriere, P.; Nöth, U.; Hall, D.J.; Tuan, R.S. Human Mesenchymal Progenitor Cell-Based Tissue Engineering of a Single-Unit Osteochondral Construct. *Tissue Eng.* **2004**, *10*, 1169–1179. [[CrossRef](#)]

38. Boukhechba, F.; Balaguer, T.; Michiels, J.-F.; Ackermann, K.; Quincey, D.; Bouler, J.-M.; Pyerin, W.; Carle, G.F.; Rochet, N. Human Primary Osteocyte Differentiation in a 3d Culture System. *J. Bone Miner. Res.* **2009**, *24*, 1927–1935. [[CrossRef](#)]
39. Gao, P.; Zhang, H.; Liu, Y.; Fan, B.; Li, X.; Xiao, X.; Lan, P.; Li, M.; Geng, L.; Liu, D.; et al. Beta-Tricalcium Phosphate Granules Improve Osteogenesis In Vitro and Establish Innovative Osteo-Regenerators for Bone Tissue Engineering In Vivo. *Sci. Rep.* **2016**, *6*, 23367. [[CrossRef](#)]
40. Liu, G.; Zhao, L.; Cui, L.; Liu, W.; Cao, Y. Tissue-Engineered Bone Formation Using Human Bone Marrow Stromal Cells and Novel B-Tricalcium Phosphate. *Biomed. Mater.* **2007**, *2*, 78–86. [[CrossRef](#)]
41. Hertzen, M.; Rothamel, D.; Schwarz, F.; Friesen, K.; Koegler, G.; Becker, J. Surface- and Nonsurface-Dependent In Vitro Effects of Bone Substitutes on Cell Viability. *Clin. Oral Investig.* **2009**, *13*, 149–155. [[CrossRef](#)] [[PubMed](#)]
42. Kulterer, B.; Friedl, G.; Jandrositz, A.; Sanchez-Cabo, F.; Prokesch, A.; Paar, C.; Scheideler, M.; Windhager, R.; Preisegger, K.-H.; Trajanoski, Z. Gene Expression Profiling of Human Mesenchymal Stem Cells Derived from Bone Marrow During Expansion and Osteoblast Differentiation. *BMC Genom.* **2007**, *8*, 70. [[CrossRef](#)] [[PubMed](#)]
43. Wrobel, E.; Leszczynska, J.; Brzoska, E. The Characteristics of Human Bone-Derived Cells (Hbdc) during Osteogenesis In Vitro. *Cell. Mol. Biol. Lett.* **2016**, *21*, 26. [[CrossRef](#)]
44. DuRaine, G.D.; Brown, W.E.; Hu, J.C.; Athanasiou, K.A. Emergence of Scaffold-Free Approaches for Tissue Engineering Musculoskeletal Cartilages. *Ann. Biomed. Eng.* **2015**, *43*, 543–554. [[CrossRef](#)] [[PubMed](#)]
45. Furukawa, K.S.; Suenaga, H.; Toita, K.; Numata, A.; Tanaka, J.; Ushida, T.; Sakai, Y.; Tateishi, T. Rapid and Large-Scale Formation of Chondrocyte Aggregates by Rotational Culture. *Cell Transplant.* **2003**, *12*, 475–479. [[CrossRef](#)]
46. Gilpin, D.A.; Weidenbecher, M.S.; Dennis, J.E. Scaffold-Free Tissue-Engineered Cartilage Implants for Laryngotracheal Reconstruction. *Laryngoscope* **2010**, *120*, 612–617. [[CrossRef](#)]
47. Park, I.-S.; Jin, R.L.; Oh, H.J.; Truong, M.-D.; Choi, B.H.; Park, S.-H.; Park, D.Y.; Min, B.-H. Sizable Scaffold-Free Tissue-Engineered Articular Cartilage Construct for Cartilage Defect Repair. *Artif. Organs* **2019**, *43*, 278–287. [[CrossRef](#)]
48. Bhumiratana, S.; Eton, R.E.; Oungoulian, S.R.; Wan, L.Q.; Ateshian, G.A.; Vunjak-Novakovic, G. Large, Stratified, and Mechanically Functional Human Cartilage Grown In Vitro by Mesenchymal Condensation. *Proc. Natl. Acad. Sci. USA* **2014**, *111*, 6940–6945. [[CrossRef](#)]
49. Addo, R.K.; Heinrich, F.; Heinz, G.A.; Schulz, D.; Sercan-Alp, Ö.; Lehmann, K.; Tran, C.L.; Bardua, M.; Matz, M.; Löhning, M.; et al. Single-Cell Transcriptomes of Murine Bone Marrow Stromal Cells Reveal Niche-Associated Heterogeneity. *Eur. J. Immunol.* **2019**, *49*, 1372–1379. [[CrossRef](#)]
50. Kim, I.G.; Ko, J.; Lee, H.R.; Do, S.H.; Park, K. Mesenchymal Cells Condensation-Inducible Mesh Scaffolds for Cartilage Tissue Engineering. *Biomaterials* **2016**, *85*, 18–29. [[CrossRef](#)]
51. Xia, H.; Liang, C.; Luo, P.; Huang, J.; He, J.; Wang, Z.; Cao, X.; Peng, C.; Wu, S. Pericellular Collagen I Coating for Enhanced Homing and Chondrogenic Differentiation of Mesenchymal Stem Cells in Direct Intra-Articular Injection. *Stem Cell Res. Ther.* **2018**, *9*, 174. [[CrossRef](#)] [[PubMed](#)]
52. Raghothaman, D.; Leong, M.F.; Lim, T.C.; Toh, J.K.C.; Wan, A.C.A.; Yang, Z.; Lee, E.H. Engineering Cell Matrix Interactions in Assembled Polyelectrolyte Fiber Hydrogels for Mesenchymal Stem Cell Chondrogenesis. *Biomaterials* **2014**, *35*, 2607–2616. [[CrossRef](#)] [[PubMed](#)]
53. Ng, J.; Bernhard, J.; Vunjak-Novakovic, G. Mesenchymal Stem Cells for Osteochondral Tissue Engineering. *Methods Mol. Biol.* **2016**, *1416*, 35–54. [[PubMed](#)]
54. Lin, Z.; Li, Z.; Li, E.N.; Li, X.; Del Duke, C.J.; Shen, H.; Hao, T.; O'Donnell, B.; Bunnell, B.A.; Goodman, S.B.; et al. Osteochondral Tissue Chip Derived from Ipscs: Modeling Oa Pathologies and Testing Drugs. *Front. Bioeng. Biotechnol.* **2019**, *7*, 411. [[CrossRef](#)]
55. Choy, E.H.S.; Panayi, G.S. Cytokine Pathways and Joint Inflammation in Rheumatoid Arthritis. *N. Engl. J. Med.* **2001**, *344*, 907–916. [[CrossRef](#)]
56. Hashizume, M.; Mihara, M. High Molecular Weight Hyaluronic Acid Inhibits Il-6-Induced Mmp Production from Human Chondrocytes by up-Regulating the Erk Inhibitor, Mkp-1. *Biochem. Biophys. Res. Commun.* **2010**, *403*, 184–189. [[CrossRef](#)]
57. Latourte, A.; Cherifi, C.; Maillot, J.; Ea, H.-K.; Bouaziz, W.; Funck-Brentano, T.; Cohen-Solal, M.; Hay, E.; Richette, P. Systemic Inhibition of Il-6/Stat3 Signalling Protects against Experimental Osteoarthritis. *Ann. Rheum. Dis.* **2017**, *76*, 748. [[CrossRef](#)]
58. Fox, D.A. Cytokine Blockade as a New Strategy to Treat Rheumatoid Arthritis: Inhibition of Tumor Necrosis Factor. *Arch. Intern. Med.* **2000**, *160*, 437–444. [[CrossRef](#)]
59. Honorati, M.C.; Cattini, L.; Facchini, A. Il-17, Il-1 and Tnf Stimulate Vegf Production by Dedifferentiated Chondrocytes. *Osteoarthr. Cartil.* **2004**, *12*, 683–691. [[CrossRef](#)]
60. Leech, M.; Metz, C.; Hall, P.; Hutchinson, P.; Gianis, K.; Smith, M.; Weedon, H.; Holdsworth, S.R.; Bucala, R.; Morand, E.F. Macrophage Migration Inhibitory Factor in Rheumatoid Arthritis: Evidence of Proinflammatory Function and Regulation by Glucocorticoids. *Arthritis Rheum.* **1999**, *42*, 1601–1608. [[CrossRef](#)]
61. Manicourt, D.H.; Poilvache, P.; Van Egeren, A.; Devogelaer, J.P.; Lenz, M.E.; Thonar, E.J. Synovial Fluid Levels of Tumor Necrosis Factor Alpha and Oncostatin M Correlate with Levels of Markers of the Degradation of Crosslinked Collagen and Cartilage Aggrecan in Rheumatoid Arthritis but Not in Osteoarthritis. *Arthritis Rheum.* **2000**, *43*, 281–288. [[CrossRef](#)]
62. Wright, H.L.; Mewar, D.; Bucknall, R.C.; Edwards, S.W.; Moots, R.J. Synovial Fluid Il-6 Concentrations Associated with Positive Response to Tocilizumab in an Ra Patient with Failed Response to Anti-Tnf and Rituximab. *Rheumatology* **2015**, *54*, 743–744. [[CrossRef](#)] [[PubMed](#)]

63. Koch, A.E.; Volin, M.V.; Woods, J.M.; Kunkel, S.L.; Connors, M.A.; Harlow, L.A.; Woodruff, D.C.; Burdick, M.D.; Strieter, R.M. Regulation of Angiogenesis by the C-X-C Chemokines Interleukin-8 and Epithelial Neutrophil Activating Peptide 78 in the Rheumatoid Joint. *Arthritis Rheum.* **2001**, *44*, 31–40. [[CrossRef](#)]
64. Verboogen, D.R.J.; Revelo, N.H.; ter Beest, M.; van den Bogaart, G. Interleukin-6 Secretion Is Limited by Self-Signaling in Endosomes. *J. Mol. Cell Biol.* **2018**, *11*, 144–157. [[CrossRef](#)] [[PubMed](#)]
65. Yoshida, S.; Ono, M.; Shono, T.; Izumi, H.; Ishibashi, T.; Suzuki, H.; Kuwano, M. Involvement of Interleukin-8, Vascular Endothelial Growth Factor, and Basic Fibroblast Growth Factor in Tumor Necrosis Factor Alpha-Dependent Angiogenesis. *Mol. Cell. Biol.* **1997**, *17*, 4015. [[CrossRef](#)]
66. Paleolog, E.M.; Hunt, M.; Elliott, M.J.; Feldmann, M.; Maini, R.N.; Woody, J.N. Deactivation of Vascular Endothelium by Monoclonal Anti-Tumor Necrosis Factor Alpha Antibody in Rheumatoid Arthritis. *Arthritis Rheum.* **1996**, *39*, 1082–1091. [[CrossRef](#)]
67. Paleolog, E.M.; Young, S.; Stark, A.C.; McCloskey, R.V.; Feldmann, M.; Maini, R.N. Modulation of Angiogenic Vascular Endothelial Growth Factor by Tumor Necrosis Factor Alpha and Interleukin-1 in Rheumatoid Arthritis. *Arthritis Rheum.* **1998**, *41*, 1258–1265. [[CrossRef](#)]
68. Koenders, M.I.; van den Berg, W.B. Secukinumab for Rheumatology: Development and Its Potential Place in Therapy. *Drug Des. Dev. Devel Ther.* **2016**, *10*, 2069–2080. [[CrossRef](#)]
69. Genovese, M.C.; Jarosova, K.; Cieslak, D.; Alper, J.; Kivitz, A.; Hough, D.R.; Maes, P.; Pineda, L.; Chen, M.; Zaidi, F. Apremilast in Patients with Active Rheumatoid Arthritis: A Phase II, Multicenter, Randomized, Double-Blind, Placebo-Controlled, Parallel-Group Study. *Arthritis Rheumatol.* **2015**, *67*, 1703–1710. [[CrossRef](#)]
70. Nakae, S.; Nambu, A.; Sudo, K.; Iwakura, Y. Suppression of Immune Induction of Collagen-Induced Arthritis in Il-17-Deficient Mice. *J. Immunol.* **2003**, *171*, 6173–6177. [[CrossRef](#)]
71. Lubberts, E.; Koenders, M.I.; Oppers-Walgreen, B.; van den Bersselaar, L.; Coenen-de Roo, C.J.; Joosten, L.A.; van den Berg, W.B. Treatment with a Neutralizing Anti-Murine Interleukin-17 Antibody after the Onset of Collagen-Induced Arthritis Reduces Joint Inflammation, Cartilage Destruction, and Bone Erosion. *Arthritis Rheum.* **2004**, *50*, 650–659. [[CrossRef](#)] [[PubMed](#)]
72. Tahir, H.; Deodhar, A.; Genovese, M.; Takeuchi, T.; Aelion, J.; Van den Bosch, F.; Haemmerle, S.; Richards, H.B. Secukinumab in Active Rheumatoid Arthritis after Anti-Tnfalpha Therapy: A Randomized, Double-Blind Placebo-Controlled Phase 3 Study. *Rheumatol. Ther.* **2017**, *4*, 475–488. [[CrossRef](#)]
73. Piluso, S.; Li, Y.; Abinzano, F.; Levato, R.; Moreira Teixeira, L.; Karperien, M.; Leijten, J.; van Weeren, R.; Malda, J. Mimicking the Articular Joint with in Vitro Models. *Trends Biotechnol.* **2019**, *37*, 1063–1077. [[CrossRef](#)] [[PubMed](#)]
74. Kawamoto, T.; Kawamoto, K. Preparation of Thin Frozen Sections from Nonfixed and Undecalcified Hard Tissues Using Kawamoto's Film Method (2012). *Methods Mol. Biol.* **2014**, *1130*, 149–164. [[PubMed](#)]

3. DISCUSSION

3.1 Pain management and assessment in mice – Fundamental challenges in the implementation of refinement measures

Animal experiments are a fundamental part of biomedical preclinical research and therefore, *refinement* plays an integral role to ensure the maintenance of the highest degree of animal welfare and its continuous improvement. Besides the obvious contribution to increase animal welfare and enhance animal wellbeing, *refinement* also contains the potential to create awareness for the 3R topic itself. Being aware of one's own handling of laboratory animals and conveying respect towards the fellow creature can stimulate the implementation of the 3R principle and the development of new approaches to avoid the use of animal experiments. This is in line with a current study reporting results from a survey among participants of laboratory animal science courses in different European countries [94]. Animal welfare, particularly appropriate pain management, was named as a major ethical issue with a requirement for higher prioritization rather than *reduction* or *replacement* of animal experiments [94]. This finding is in contrast to the original prioritization by Russell and Burch – stating that *refinement* should be implemented after *replacement* and *reduction* have been completely exhausted [1]. Thus, the above-mentioned study results suggest the occurrence of a prioritization shift, especially among those actively working with laboratory animals, who evidently prioritize *refinement* over *reduction* and *replacement*. However, it can be speculated that a comparable survey under researchers working on non-animal based *in vitro* solutions would have the opposite priorities. This highlights the tension in the field of 3Rs and underlines the importance of my work to span and discuss the perspectives of those working with animal experiments and those developing and favouring non-animal methods.

In their book, Russell and Burch specifically point out that *refinement* is the absolute minimization of any distress and discomfort of animals used in research [1]. Therefore, they exclusively focus on methods to avoid distress during experimental procedures, such as adequate species-adapted anaesthesia and analgesia. Nevertheless, discussions during the last decades resulted in a reframing process of the term “*refinement*” to include the enhancement of the general wellbeing, e.g. by using enrichment and non-invasive handling tools to adapt housing and husbandry [19]. In general, pain is a negative affective state of the animal, like anxiety or distress, while wellbeing refers to a condition linked with a mainly positive affective state [95]. To *refine* or adapt current pain management protocols, it is essential to identify reliable and preferably non-invasive methods to assess and determine the duration and degree of pain, especially in rodents. Commonly used methods to monitor pain in rodents include body weight development, vocalization, pain grimace scale nest building or burrowing behaviour and model-specific scoring systems [96, 97]. However,

most of these symptoms or measurements are not exclusive indicators for pain but can also indicate distress or a general reduction in wellbeing. Moreover, potent analgesics such as opioids or the anaesthesia itself can cause additional pronounced side effects, such as body weight loss, changes in nest-building behaviour or deviations in the pain grimace scale [98]. Thus, one of the major challenges in the field of laboratory animal science is the adequate pain assessment, specifically in rodents, and the precise allocation of the reason for the observed suffering and discomfort (e.g. pain, side effects of analgesics and anaesthesia). Hence, when assessing the effectiveness of an analgesic protocol in terms of adequate pain management, a distinction must be made between pain *per se* and distress or reduced wellbeing. Pain can be verified by analysing model-specific pain parameters, while general clinical signs and model-unspecific, behaviour-based parameters assess states of distress and the animal's wellbeing. Recent advances in the field have shown that it is essential to combine these methods to achieve an overall improvement of welfare and to specifically *refine* experimental procedures in terms of pain management. Thus, many long-established pain management protocols have come under criticism in recent years [99-101]. In this context, traditional clinical scoring systems of changes in the animal's appearance, including an arched back, sunken eyes and decreased grooming, have proven to be reliable indicators of a general reduced state, yet insufficient, as they lack specificity to indicate the precise affective state. More importantly, the absence of these signs has been reported to not exclude states of pain or distress [99, 102, 103]. For example, in the past embryo transfer used to be performed without analgesia due to missing changes in the clinical appearance of the animals. However, behavioural and telemetry-based measurements showed that animals undergoing embryo transfer experience reduced well-being and pain [102, 104]. Combining model-specific, clinical pain parameters with model-unspecific, behavioural parameters allows the differentiation between clinically visible pain, clinically invisible distress and impairments in well-being.

The detection of pain in mouse fracture models is based on different methods: subjective assessments of spontaneous behaviours directly related to the use of the affected limb, such as reduced loading or avoidance of loading of the limb and unusual posture of the limb, observations of behaviour and vocalization after palpation of the affected limb, or automated analyses of gait or stance (e.g., Catwalk (Noldus), capacity meter; [105]). In addition, hyperalgesia developing over time on the affected limb is investigated using classical analgesiometric methods such, as the hotplate test or Von-Frey test [106, 107]. In our study, we combined pain-specific parameters, such as limp score and guarding behaviour and combined it with model-unspecific parameters, such as body weight development, clinical appearance, nest building and explorative behaviour, to assess the effectiveness of tramadol and buprenorphine administered via the drinking water. As a result, we were able to

conclude that by using tramadol and buprenorphine sufficient pain relief can be achieved over 3 days post-surgical in mice undergoing femoral osteotomy. However, we were also able to provide evidence that a potential overdosing of tramadol impacts the general well-being of the animals [30]. In a current study, we are including Catwalk analysis to determine the effectiveness of the pain management protocol more precisely and to correlate model-specific and unspecific parameters to find the optimal strategy to assess different affective states in mouse femoral fracture models [108].

In addition to the optimization of the assessment of affective states in rodents to verify pain management protocols, the route of administering analgesics most effectively is controversially discussed. In our study, we showed that application via the drinking water ensures a continuous and non-invasive uptake of the analgesics [30]. However, this administration route has its limitations with regard to potential under- or overdosing depending on the individual frequency of water uptake, the circadian life rhythms, the oral absorption of analgesics and the potential impairment of the animal. Therefore, injections are often used, which require forced immobilization and potentially intensifying post-operative pain and pain in the musculoskeletal system due to defensive movements. Formulations of analgesics that achieve an adequately high effective level over a long period of time and simultaneously require less frequent manipulations could resolve this issue [40]. Currently these depot/sustained-release formulations are only available in the US and several attempts to import these products to Europe have failed. Schreiner *et al.* recently published a study on the successful development and use of a newly developed poly-lactic-co-glycolic acid (PLGA) based microparticulate buprenorphine formulation for sustained drug release to provide an alternative product within Europe [109]. In a current study, we investigate the effectiveness of newly developed sustained-release buprenorphine, ensuring continuous and sufficient analgesia in mouse femoral fracture models, as a potent alternative to the application of tramadol via drinking water [108]. Overcoming the barrier of unavailability of analgesic depot formulations could be transformative for the field of laboratory animal science and ensure the more active implementation of *refinement* measures.

Another fundamental challenge in including *refinement* approaches in science is the lack of evidence-based data on the improvement these approaches achieve and the potential effects on the studies outcomes. In terms of the reproducibility crisis and the existence of traditional protocols approved by the scientific community, many researchers hesitate to include further *refinement* measures to avoid uncontrollable side effects on the studies outcomes. Therefore, we decided to i) analyse the differences in fracture healing parameters between the different analgesic groups and ii) integrate the study in an ongoing fundamental research study [30]. This study approach had the advantage that we were able to *reduce*

the number of used animals as one of the analgesic groups was part of the fundamental research study and we re-used unoperated control animals (anaesthesia and/or analgesia only). Nevertheless, it must be ensured that the validity and statistical power of both studies are adequately adapted. Although this study design holds great promises to convince more researchers of including comparable *refinement* studies in their ongoing animal experiments, it should be stressed out that the collaboration with laboratory animal experts, especially with respect to behavioural assessment, is inevitable to ensure the appropriate use of methodology and adequate interpretation of data.

Taken together, adequate pain management is highly dependent on precise pain assessment and should always be combined with the examination of further affective states of the animals to monitor distress and wellbeing. Several challenges must be tackled in the future to continuously ensure the maximum possible degree of animal welfare is balanced towards the scientific merit and outcome. *Refinement* measures are, therefore, indispensable and must be integrated whenever possible. In my opinion, all 3Rs must be prioritized to change the traditional way and mindset in biomedical research – a fragmentation of the field is not efficient and only prevents the concentration of forces towards a common goal.

3.2 Recapitulating the initial phase of fracture healing *in vitro* – Modelling the crosstalk between immune cells and bone

Upon trauma, activation of the extrinsic coagulation pathway results in the formation of the fracture hematoma within the fracture gap. The degradation and resorption of the fracture hematoma begin within a short timeframe and have a similar importance as the proper formation, since knockout of plasminogen or absence of fibrinolytic protease genes lead to disturbed fracture healing [110]. The pro- and anti-inflammatory processes during the initial phase of fracture healing are critical to activating the subsequent regeneration cascade [31, 52]. Several studies have shown that the removal of the fracture hematoma within the first days results in delayed regeneration and decreased new bone formation [111-113]. In addition, transplantation experiments of the fracture hematoma to ectopic locations suggested that the hematoma itself contains all important cells and factors to induce bone formation independent from the surrounding tissue origin [114]. The fracture hematoma consists of peripheral-blood-derived immune cells and their progenitors from the bone marrow, hematopoietic and skeletal stem cells and mesenchymal stromal cells, as well as dead cells and debris, attracting e.g. neutrophils during the first hours after trauma [52, 115]. Besides clearing the area from pathogens and debris, neutrophils produce reactive oxygen species (ROS), cytokines and chemokines such as monocyte chemoattractant protein 1 (MCP-1), and chemokine (C-X-C motif) ligand (CXCL) 1, leading to recruitment and invasion of monocytes and macrophages [114, 116-118]. While inflammatory activated macrophages are crucial

for endochondral ossification [119, 120], anti-inflammatory macrophages have been shown to specifically support the revascularization process by close interaction with the endothelium [56]. The role of the adaptive immune system has been more extensively studied during the last years and controversial results have been reported. RAG1(-/-) mice lacking mature T and B cells show enhanced fracture healing, while CD4⁺ T cells have been shown to support osteogenic differentiation and maturation [121, 122]. Moreover, the immune system's experience level was described to influence the healing outcome [123]. In addition, the local microenvironment in the fracture hematoma is characterized by high concentrations of cytokines, chemokines, growth factors and enzymes as well as hypoxia and lack of nutrients [114, 115, 124].

Several of the above-described findings were gathered in animal models allowing us to uncover numerous fundamental pathways and to study the complexity of a whole organism. Nevertheless, inter-species differences especially between distant species like humans and mice, have led to reconsidering companion animals as naturally occurring models and patients. The horse as a patient of considerable economic value offers the opportunity to serve as a naturally occurring model for a variety of musculoskeletal disorders, such as fracture healing and OA. Fractures in horses are often difficult to treat, very expensive, and in many cases a reason for euthanasia. Aside from the racing industry with fracture incidences of 1–2% per race and start, leisure sport and free-range husbandries bear increased risk for contortions and injuries, especially in the fetlock area. Due to its size and anatomically comparable characteristics to humans with respect to bone macro- and microstructure, the horse represents an ideal but most often overlooked animal model for musculoskeletal research. Unfortunately, there is limited knowledge on cellular and molecular processes during fracture repair itself and the initial phase in the horses specifically. General knowledge considers this phase for cleaning to eliminate debris, dead cells and tissue) [125]. Interestingly, due to the often insufficient and delayed healing of fractures in horses, it has been suggested that immunological processes in the initial phase are altered compared to humans [125]. In our study, we aimed at establishing an *in vitro* equine fracture hematoma model for profound characterization, to generate fundamental knowledge on the initial processes during fracture healing in the equine patient [126]. Moreover, we wanted to use the gained knowledge for translation into a human fracture hematoma model [92]. Therefore, equine blood was mixed with equine MSC, clotted to generate an *in vitro* fracture hematoma, and cultivated under normoxic and hypoxic conditions for 6h, 12h, and 48h. As a result, we found striking similarities to the human system with respect to the cell composition, while the mRNA expression indicates clear differences in the fracture healing processes. In addition, we demonstrated that hypoxia favours the survival of MSCs but not immune cells. Furthermore, gene expression of osteogenic and angiogenic markers was

highly elevated under hypoxic conditions [126]. However, further studies using *ex vivo* equine fracture hematoma are required to verify our *in vitro* approaches and to delineate the role of the single components more precisely within the initial phase of fracture healing in horses.

Interaction between immune cells and bone metabolism plays a crucial role in the physiology and pathology of bone regeneration. However, current *in vitro* approaches exclude the immune system due to its complexity. Therefore, in the next step, we specifically focused on the simulation of the crosstalk between immune cells and bone, to mimic the initial phase of fracture healing *in vitro* more closely [127]. For the bone part, we used a patented tissue engineering approach (fzmb GmbH; Ponomarev *et al.*[128]) to create scaffold-free bone-like constructs (SFBCs) in a macroscale approach, based on mesenchymal condensation as natural form of 3D self-assembly or self-organization [129]. Although the generation requires a large number of cells, it allows for the analysis of different aspects with one model due to sufficient material availability. After detailed characterization of the SFBCs and the proof of penetrating calcification and cell mineralization, we co-cultivated the SFBCs with *in vitro* human fracture hematoma models [92] to examine the ability of the SFBCs to induce osteogenic cues, recapitulating key processes of the hematoma-bone crosstalk [127]. Since we found that the hypoxic environment plays a crucial role during the onset of regenerative processes in the fracture gap, we performed the co-cultivation under hypoxic conditions [92, 126]. The results from the co-cultivation indicated striking similarities to already published findings from an *ex vivo* study and an *in vitro* fracture hematoma model (Table 2) [92, 130]. Moreover, we showed that the SFBCs were able to induce regeneration-relevant gene expression indicating the adaptation to hypoxia and osteogenic induction within the fracture hematoma model. In order to verify our approach, we administered deferroxamine (DFO) an osteoinductive compound that stabilizes hypoxia-inducible factor 1 (HIF-1) [91]. In addition to an increased target gene expression, we found elevated pro-inflammatory processes underlining the profound role of suitable cellular adaptation to the microenvironment.

Although our first approach to recapitulate the initial processes during bone regeneration seems to be promising, there are several limitations that need to be addressed to increase the complexity, the stability and extend the investigation timeframe while allowing the monitoring of potential phase-spanning developments. Therefore, current follow-up projects involve the integration of the fracture hematoma models in a perfused bioreactor system to enable debridement and active remodelling of the hematoma tissue.

Table 2: Comparison of gene expression results collected in three different studies. Adapted and reproduced from [127]. Arrow directed upwards indicates an increase in the gene expression while an asterisk indicates the degree of expression.

Gene symbol	<i>ex vivo</i> FHs (< 72 h) [130]	<i>in vitro</i> human FHs (48 h hypoxia) [92]	<i>in vitro</i> fracture gap model (48 h hypoxia) [127]
<i>RUNX2</i>	↑	↑**	↑
<i>SPP1</i>	↑*	↑****	↑
<i>VEGFA</i>	↑*	↑***	↑
<i>IL8</i>	↑***	↑**	↑
<i>IL6</i>	↑***	↑	↑
<i>LDHA</i>	↑**	↑***	↑
<i>MMP2</i>	n.a.	↑*	↑

FH – fracture hematoma; *LDHA* – lactate dehydrogenase A; *RUNX2* – Runt-related transcription factor 2; *SPP1* – secreted phosphoprotein 1 (osteopontin); *VEGFA* – vascular endothelial growth factor A

To sum up, using different *in vitro* approaches (*in vitro* equine fracture hematoma model, 3D *in vitro* fracture gap model), we were able to recapitulate key processes within the fracture hematoma during the initiation of fracture repair. Therefore, these models can be used to i) investigate fundamental (immune-mediated) mechanisms leading to disturbances in fracture repair and ii) as a prediction tool to test and develop sophisticated therapeutic strategies which specifically address the crosstalk between immune cells and bone. As of today, *in vitro* approaches still face major challenges including the maintenance and recapitulation of complex immunological processes. Thus, the simulation of the immune component in different physiological and pathophysiological contexts has so far been impossible to study. Solving this problem will be transformative for the field to provide a sophisticated preclinical tool for basic research, uncover fundamental mechanisms, and enable the development of new therapies without animal experiments.

3.3 Mimicking key features of joint disorders *in vitro* – Technical considerations on complexity and its limitations

A variety of *in vitro* models have been developed to study joint disorders such as OA. The models range from simple 2D chondrocyte monolayer cultures to perform target and substance screening to complex 3D co-cultures and organ-on-a-chip technologies which aim to replicate the whole joint physiology or pathology [6, 7]. However, primary chondrocytes, the sole cell type of cartilage, rapidly dedifferentiate towards a fibroblast-like morphology under monolayer conditions and shift their expression profile from collagen type II (*COL2A1*) to collagen type I (*COL1A1*) [77, 131, 132]. The 3D cultivation of chondrocytes prevents the dedifferentiation and allows the cells to interact with the surrounding extracellular matrix, thereby promoting a spheroidal cell morphology [79]. To achieve three-dimensionality, different approaches are used: scaffold-free or scaffold-based constructs, explant cultures,

co-cultures and microfluidic models based on pellet cultures or hydrogels. Different cell and tissue resources help to emulate *in vivo* conditions, including cartilage explants, primary chondrocytes, stem cells (mesenchymal, induced pluripotent) and cell lines. However, balanced considerations should include the availability and quantity of the cell and tissue resource e.g. as primary chondrocytes are isolated from residual material collected during whole joint replacements during which cartilage is removed over a larger area. Thus, MSCs represent a promising cell resource as they are easy to isolate from bone marrow cells, expandable in higher numbers and are able to differentiate into the chondrogenic lineage. In our study, we used human MSCs to develop a 3D macroscale cartilage construct consisting of cells and their self-produced matrix (scaffold-free; SFCC). These SFCCs exhibit cartilage-like features, including glycosaminoglycan and collagen type II abundance, layering of cells and cartilage marker mRNA expression. However, the continued presence of collagen type I indicates an insufficient maturation of the constructs towards hyaline cartilage, which is in line with observations from other studies [133, 134]. Future directions points towards using induced pluripotent stem cells (iPSC; [135, 136]) or artificially created cell lines [137]. However, since chondrocytes are fully mature cells, the usability and comparability of using rather juvenile cells to simulate a disease complex which evolves through aging is highly questionable and should be considered carefully. Nevertheless, as alternative cell resources are required, sophisticated cell engineering technologies such as CRISPR-Cas9 are promising to create stable, *in vivo*-like cell lines that exhibit the classical features of primary chondrocytes. Macroscale mesenchymal condensation and biomechanical loading during maturation resulted in the 3D shape of the SFCCs without signs of elevated cell death in the inner core of the constructs [138]. Moreover, the macroscale approach (diameter up to 0.5 cm) has the advantage of providing a physiologically relevant size, geometry, lower cell to matrix ratio and adequate mechanical properties compared to pellet cultures [139].

In vitro simulation of an osteoarthritic environment can be induced by either biochemical or mechanical effectors. Commonly, cytokines such as IL-1 β and TNF α are used to mimic the inflammatory response of synovial cells. The selected IL-1 β and TNF α concentrations in our study were higher than in other studies (normal range between 1–100 ng/ml) and exceed the concentration measured in the synovial fluid of patients [140]. However, such an approach is not unusual as it enables the simulation of a chronic progressive process in a shorter timeframe. Prediction experiments using our developed mathematical model indicated that a 10-fold reduction of the IL-1 β and an extension of the timeframes to 5 weeks resulted in a complete distribution of IL-1 β and MMP-1/-3/-13 within the tissue, decreasing cell death, but a rather decelerated collagen type II degradation. These observations are highly comparable with *in vivo* observations reporting the chondrocyte decline as crucial

during the onset of the disease followed by the progressive matrix degradation over time [141, 142]. The close collaboration with mathematicians allowed us to develop an *in silico* model in parallel to our *in vitro* model to serve as a prediction tool for further experimental design and to modify and optimize the *in vitro* model. Our reduced mathematical model allowed us to exclude unidentifiable parameters and uncertainties from the original equation system published by Kar et al. [143]. In general, common *in silico* approaches towards OA are mainly based on poroelastic models or cell mechanics [144-146].

One major limitation of our single component model to study cartilage is the narrow focus on one specific feature of the disease, cartilage degradation, although OA is known to affect the whole joint including the synovial membrane and the subchondral bone. Thus, in a follow-up, we wanted to increase the complexity by combining the chondral part with a bone model to recapitulate the effects of the inflammatory process on the osteochondral unit, to determine and display its role in the pathogenesis of RA. Therefore, we created a dual system that exhibited an RA-like phenotype induced by the administration of an inflammatory cytokine cocktail containing TNF α , IL-6 and macrophage migration inhibitory factor (MIF). Further, our approach studied the immunomodulatory effect of common clinically applied anti-rheumatic drugs, adalimumab [147, 148] and tocilizumab [149, 150], in addition to the antineoplastic agent milatuzumab [151]. In contrast to our parallel approach in the fracture gap model, where the bone part was created by adapted differentiation of the macroscale scaffold-free constructs, we here chose tricalcium phosphate (TCP) ceramic particles for a scaffold-based approach. TCP is a widely used scaffold for clinical bone restoration and its biocompatibility, as well as osteoconductive ability, have been sufficiently proven [152-155]. The use of MSC as a cell resource to generate the chondrogenic as well as osteogenic part allowed for a stringent donor-matched co-cultivation as an osteochondral unit. The formation of a bridging zone between both parts suggested a potential functional interplay between the cells and tissues. However, to create a fully matured bridging area a different approach might be superior in allowing a stable close contact between the tissues and the integrated cell differentiation, which could result in a proper intermediate zone. [156, 157]. In contrast to OA, the disease progression and inflammatory component within the pathophysiology of RA is highly more pronounced mainly driven by synovial fibroblasts and different immune cells (neutrophils, macrophages, T-cells). In our model, we showed an increased expression of matrix metalloproteases (*MMP1*, *MMP3*), especially in the cartilage component, while the expression of metabolic markers such as *LDHA* and *IL8* was elevated in bone components. Overall gene expression changes were more dramatic in the cartilage component than the bone component indicating different adaptation dynamics in both systems. The administration of clinically applied monoclonal antibodies directed against TNF α ,

IL-6 and MIF resulted in reduced pro-inflammatory effects especially inhibiting the TNF and IL-6 signalling pathways.

Despite the increase in complexity that our developed model displays by combining two tissue components into one osteochondral part, major limitations include the lack of immune cells, bone remodelling processes and biomechanical cues. Current and future approaches focus on the integration of the dual system in a bioreactor platform to enable perfusion and tissue adapted provision of differentiation and growth factors. Moreover, we aim at extending the model by introducing a synovial membrane component that will be enriched and triggered with immune cells to enable the precise recapitulation of the disease development in a tissue-hierarchical order. Current approaches from the literature already include all parts of the joints, e.g. combining patient-derived osteochondral plugs co-cultivated with explants from the synovial membrane or using microphysiological systems [6, 158].

Nevertheless, to allow standardization and reproducibility, current *in vitro* approaches mostly focus on simplification and miniaturization of a complex biological system and its disorders which is inevitable accompanied by losing important physiological or pathophysiological information. Nevertheless, with regard to biomedical basic and translational research, simplification and miniaturization can be used to develop and create controllable systems and can serve as a base to study complex biological interplays *in vitro*. However, there must be a fine-balanced and precisely elaborated strategy to maintain complexity in *in vitro* systems. The *in vitro* simulation of musculoskeletal disorders is one of the greatest challenges requiring distinct populations of mature cells, different stiffnesses of the surrounding matrix, stable interconnections between different tissue types, specific environmental conditions (e.g. oxygen and nutrient restriction) and the integration of diverse biomechanical insults. Therefore, while upcoming cutting-edge technologies in tissue- or organ-on-a-chip-technologies and corresponding approaches may be promising, they should be critically reviewed to successfully enhance translatability towards the human orthopaedic patient.

3.4 The active implementation of the 3R principle in biomedical research – Closing thoughts on challenges and opportunities

Efforts for the active implementation of the 3R principle in biomedical research have exponentially increased over the last years. One reason is the increasing public pressure on scientists with the demand for more transparency, exploitation of all possibilities to save animals and optimization of animal welfare to ensure animal wellbeing. Moreover, several 3R centres, initiatives and platforms have been recently formed especially in Europe, mainly triggered by the legislative adaptations included in the Directive 2010/63/EU. Therefore, EU Member States need to “[...] contribute to the development and validation of alternative approaches which could provide the same or higher levels of information as those obtained in procedures using animals, but which do not involve the use of animals or use fewer animals, or which entail less painful procedures” and EU Member States “shall take such other steps as they consider appropriate to encourage research in this field.” ([23]; Article 47). Besides the demand for increased research efforts the directive also includes the requirement for adequate dissemination, education, and training to further accelerate the implementation of the 3R principle and ensure animal welfare on the highest possible level. In 2018 the JRC EURL ECVAM has launched a study on “Mapping education and training on the 3Rs”. Although the data has not yet been published, a preceding study indicated the need for better provision of 3Rs courses and harmonization of materials across Europe [159]. The establishment of centralized structures, such as the establishment of a European 3R network (EU3Rnet), and the linking of decentralized services, e.g. by information platforms (Norecopa, ETPLAS), will play an important role in the future, if we are to expand the range of services and opportunities and offer them in an optimal way that conserves resources. In my opinion, the education of the next generation of scientists is fundamental to achieving a general mind shift towards animal sparing methods and increased animal welfare in the future. Therefore, attractive, and inspiring educational concepts need to be developed to transfer not only content-related information but also train scientific confidence, creativity, the ability to work in an interdisciplinary manner, teamwork and to tackle and implement innovative ideas. Exemplarily, in recent years we have successfully developed and implemented a workshop concept which uses Design Thinking methods to create awareness and stimulate innovative ideas among early-career scientists to accelerate the active use and optimization of the 3R principle – ReThink3R (<https://rethink3r.de/> [cited 2021 November 26]).

Besides the dissemination and distribution of information on the 3R principle, further evidence is required, e.g. for the positive impact of improved handling and housing of laboratory animals (*refinement* measures) on scientific merits and quality of science [160], or the

potential superiority of *in vitro* methods over animal models in terms of translation to the human patient (*replacement*). As already mentioned above, I hold the opinion that all 3Rs must be prioritized to change the traditional way and mindset in biomedical research – a fragmentation of the field will be not successful in the long term. Therefore, funding opportunities need to be much more balanced, to provide more research resources for *refinement* and *reduction* as immediate measures to be implemented. However, resources for *in vitro* approaches must be maintained and increased to facilitate the development of sophisticated alternative systems for the future. Therefore, advances and successes in toxicology can guide the development in biomedical research, although fundamental differences need to be considered with respect to requirements for complexity, multidimensionality, batteries for readout parameters as well as microenvironmental demands.

To conclude, I am certain that the humane treatment of laboratory animals following the 3R principle is not opposed to performing ground-breaking research, but rather strengthens its innovative capacity, forward-thinking sustainability, and rapid translation into the clinic.

“As new fields of biology open in the future, it may become a matter of routine to apply the lessons of the past and turn as soon as possible to the techniques of replacement”. ([1]; Chapter 4 – Other Uses of Microorganisms)

SUMMARY

Musculoskeletal disorders are a challenging clinical problem. Each year, millions of patients worldwide experience bone fractures and 10–15% of these fractures suffer from impaired healing. The global prevalence for osteoarthritis is higher than ever before due to an increased life expectancy and rise in associated risk factors such as physical inactivity and obesity. Sophisticated complex treatment plans with novel biologics allowed to effectively achieve remission in patients with rheumatoid arthritis, however, about 25% of the patients still suffers from moderate or even high disease activity. Thus, further fundamental, and translational preclinical research is imperative to tackle the unmet medical needs for musculoskeletal conditions and ensure health throughout the life course. The current gold-standard in preclinical research is the use of animal models, i.e. mainly rodents (mouse, rat). However, during recent years, we have witnessed the failure of promising therapeutics in clinical testing albeit being based on strong evidence from animal experiments. Therefore, it can be speculated that trans-species differences might be responsible for the limited transferability of findings to the human patient. The 3R principle (*replace, reduce, refine*) published by Russell and Burch in 1959 can be used as a framework for the humane use of animals in research. Moreover, it can enhance and ensure scientific quality and integrity in studies using animals, thereby accelerating the translational process. To enhance the current knowledge on *refinement* measures in fundamental research studies and to provide evidence-based data on pain management protocols in laboratory animals, we evaluated two analgesics, tramadol and buprenorphine in the drinking water, for their efficiency and side effects on experimental readout in the mouse-osteotomy model. Furthermore, we developed novel *in vitro* approaches to evade cross-species differences and to *replace* lab animal usage with a specific focus on fracture healing and joint pathologies. In detail, to recapitulate the initial phase of fracture healing, we specifically focused on integrating the interaction between immune cells and mesenchymal stromal cells/bone-related cells, exemplified by artificial fracture hematoma models containing mesenchymal stromal cells and the combination with three-dimensional scaffold-free bone-like constructs (fracture gap model). This tissue-engineered macroscale approach was used in parallel to mimic cartilage degradation during the onset of osteoarthritis *in vitro*, which was later extended towards an osteochondral unit model by integrating a tricalcium phosphate-based bone equivalent to recapitulate key features of rheumatoid arthritis. Together, within this thesis, I provide an overview of the variety of approaches towards the active implementation of the 3R principle in musculoskeletal-related preclinical research. Thereby, I specifically underline the importance of equivalently prioritizing all 3Rs to effectively rethink traditional research approaches in biomedicine for continuous improvement in animal welfare and successful human patient-driven translation.

ZUSAMMENFASSUNG

Erkrankungen des muskuloskelettalen Systems sind ein herausforderndes klinisches Problem. Jedes Jahr erleiden Millionen von Patienten weltweit Knochenbrüche und bei 10-15 % dieser Frakturen kommt es zu Heilungsstörungen. Die weltweite Prävalenz von Osteoarthritis ist aufgrund der gestiegenen Lebenserwartung und der Zunahme der damit verbundenen Risikofaktoren, wie Bewegungsmangel und Übergewicht, höher als je zuvor. Dank ausgeklügelter komplexer Behandlungspläne mit neuartigen Biologika konnte bei Patienten mit rheumatoider Arthritis eine wirksame Remission erreicht werden, allerdings leiden etwa 25 % der Patienten immer noch unter einer mäßigen oder sogar hohen Krankheitsaktivität. Daher ist weiterführende Forschung unerlässlich, um den verbleibenden medizinischen Bedarf im Bereich der muskuloskelettalen Erkrankungen zu decken. Der derzeitige Goldstandard in der präklinischen Forschung ist die Verwendung von Tiermodellen, insbesondere Nagetieren (Maus, Ratte). Dennoch sind in den letzten Jahren immer wieder neue Therapeutika in der klinischen Testung gescheitert, trotz vielversprechender Daten aus dem Tierversuch. Speziesübergreifende Unterschiede werden für die begrenzte Übertragbarkeit der Ergebnisse auf den menschlichen Patienten verantwortlich gemacht. Das von Russell und Burch 1959 veröffentlichte 3R-Prinzip (*Replace, Reduce, Refine*) kann als Rahmen für den humanen Einsatz von Tieren in der Forschung dienen sowie die Qualität und Integrität von Tierversuchen sicherstellen und so den Translationsprozess beschleunigen. Um das derzeitige Wissen über *Refinement*-Maßnahmen zu erweitern und evidenzbasierte Daten zu Schmerzbehandlungsprotokollen bei Labortieren bereitzustellen, haben wir zwei Analgetika, Tramadol und Buprenorphin im Trinkwasser, auf ihre Wirksamkeit und ihre Nebenwirkungen im Maus-Osteotomie-Modell untersucht. Darüber hinaus haben wir neue *in vitro* Ansätze entwickelt mit speziellem Fokus auf die Frakturheilung und Gelenkpathologien. Um die Anfangsphase der Frakturheilung zu rekapitulieren, konzentrierten wir uns insbesondere auf die Interaktion zwischen Immunzellen und mesenchymalen Stromazellen/Knochenzellen, z. B. durch die Kombination von Frakturhämatom-Modellen mit dreidimensionalen trägerfreien knochenähnlichen Konstrukten (Frakturspaltmodell). Ein vergleichbarer Ansatz wurde verwendet, um den Knorpelabbau während der beginnenden Osteoarthritis *in vitro* zu imitieren. Später wurde dieser Ansatz auf ein Modell der osteochondralen Einheit ausgeweitet, um die Hauptmerkmale der rheumatoiden Arthritis zu rekapitulieren. In dieser Arbeit gebe ich einen Überblick über die Vielfalt der Ansätze zur aktiven Implementierung des 3R-Prinzips in der präklinischen muskuloskelettalen Forschung. Dabei unterstreiche ich insbesondere die gleichwertige Priorisierung aller 3R, um eine kontinuierliche Verbesserung des Tierschutzes und eine erfolgreiche, auf den menschlichen Patienten ausgerichtete Translation zu gewährleisten.

REFERENCES

1. Russel, W.M.S., Burch, R. L. , *The principles of humane experimental technique*. 1959, Wheathampstead (UK): Universities Federation for Animal Welfare (UFAW). Available from: <https://caat.jhsph.edu/principles/the-principles-of-humane-experimental-technique> [cited 2021 November 27]
2. Scheinpflug, J., et al., *Journey into Bone Models: A Review*. Genes (Basel), 2018. **9**(5): p. 247.
3. Schlundt, C., et al., *Clinical and Research Approaches to Treat Non-union Fracture*. Curr Osteoporos Rep, 2018. **16**(2): p. 155-168.
4. Wu, A.-M., et al., *Global, regional, and national burden of bone fractures in 204 countries and territories, 1990-2013: a systematic analysis from the Global Burden of Disease Study 2019*. The Lancet Healthy Longevity, 2021. **2**(9): p. e580-e592.
5. WHO. *Musculoskeletal conditions*. Available from: <https://www.who.int/news-room/fact-sheets/detail/musculoskeletal-conditions> [cited 2021 November 27].
6. Piluso, S., et al., *Mimicking the Articular Joint with In Vitro Models*. Trends in Biotechnology, 2019. **37**(10): p. 1063-1077.
7. Samvelyan, H.J., et al., *Models of Osteoarthritis: Relevance and New Insights*. Calcified Tissue International, 2021. **109**: p. 253-256.
8. Smolen, J.S., et al., *Rheumatoid arthritis*. Nature Reviews Disease Primers, 2018. **4**(1): p. 18001.
9. Smolen, J.S., et al., *EULAR recommendations for the management of rheumatoid arthritis with synthetic and biological disease-modifying antirheumatic drugs: 2013 update*. Ann Rheum Dis, 2014. **73**(3): p. 492-509.
10. Burmester, G.R. and J.E. Pope, *Novel treatment strategies in rheumatoid arthritis*. Lancet, 2017. **389**(10086): p. 2338-2348.
11. Pritzker, K.P., *Animal models for osteoarthritis: processes, problems and prospects*. Ann Rheum Dis, 1994. **53**(6): p. 406-20.
12. Commission, E., *2019 report on the statistics on the use of animals for scientific purposes in the Member States of the European Union in 2015-2017*. Available from: <https://op.europa.eu/en/publication-detail/-/publication/04a890d4-47ff-11ea-b81b-01aa75ed71a1> [cited 2021 November 27]
13. Pfeiffenberger, M., et al., *Fracture Healing Research—Shift towards In Vitro Modeling?* Biomedicines, 2021. **9**(7): p. 748.
14. Busquet, F., et al., *New European Union statistics on laboratory animal use - what really counts!* Altex, 2020. **37**(2): p. 167-186.
15. Weinstein, S.I., E. Yelin, H. , and S.I. Watkins-Castillo. *Funding*. Available from: <https://www.boneandjointburden.org/fourth-edition/ia0/funding>. [cited 2021 November 27]
16. Ehnert, S., et al., *Use of in vitro bone models to screen for altered bone metabolism, osteopathies, and fracture healing: challenges of complex models*. Arch Toxicol, 2020. **94**(12): p. 3937-3958.
17. Hubrecht, R.C. and E. Carter, *The 3Rs and Humane Experimental Technique: Implementing Change*. Animals : an open access journal from MDPI, 2019. **9**(10): p. 754.

18. Strech, D. and U. Dirnagl, *3Rs missing: animal research without scientific value is unethical*. *BMJ Open Science*, 2019. **3**(1): p. bmjos-2018-000048.
19. Tannenbaum, J. and B.T. Bennett, *Russell and Burch's 3Rs then and now: the need for clarity in definition and purpose*. *Journal of the American Association for Laboratory Animal Science : JAALAS*, 2015. **54**(2): p. 120-132.
20. O'Loughlin, P.F., et al., *Selection and development of preclinical models in fracture-healing research*. *J Bone Joint Surg Am*, 2008. **90 Suppl 1**: p. 79-84.
21. Lang, A., et al., *Osteotomy models - the current status on pain scoring and management in small rodents*. *Lab Anim*, 2016. **50**(6): p. 433-441.
22. Wolter, A., et al., *Systematic review on the reporting accuracy of experimental details in publications using mouse femoral fracture models*. *Bone*, 2021. **152**: p. 116088.
23. *European Parliament and Council Directive 2010/63/EU of the European Parliament and of the Council of 22 September 2010 on the Protection of Animals Used for Scientific Purposes*. Available from: <https://eur-lex.europa.eu/legal-content/EN/TXT/?qid=1567099172556&uri=CELEX:32010L0063> [cited 2021 November 26].
24. Carbone, L. and J. Austin, *Pain and Laboratory Animals: Publication Practices for Better Data Reproducibility and Better Animal Welfare*. *PLoS One*, 2016. **11**(5): p. e0155001.
25. Jirkof, P., *Side effects of pain and analgesia in animal experimentation*. *Lab Anim (NY)*, 2017. **46**(4): p. 123-128.
26. Peterson, N.C., E.A. Nunamaker, and P.V. Turner, *To Treat or Not to Treat: The Effects of Pain on Experimental Parameters*. *Comp Med*, 2017. **67**(6): p. 469-482.
27. Santy, J. and C. Mackintosh, *A phenomenological study of pain following fractured shaft of femur*. *Journal of Clinical Nursing*, 2001. **10**(4): p. 521-527.
28. Minick, P., et al., *Long-bone fracture pain management in the emergency department*. *J Emerg Nurs*, 2012. **38**(3): p. 211-7.
29. Bove, S.E., et al., *New advances in musculoskeletal pain*. *Brain Res Rev*, 2009. **60**(1): p. 187-201.
30. Jirkof, P., et al., *Administration of Tramadol or Buprenorphine via the drinking water for post-operative analgesia in a mouse-osteotomy model*. *Sci Rep*, 2019. **9**(1): p. 10749.
31. Kolar, P., et al., *The early fracture hematoma and its potential role in fracture healing*. *Tissue Eng Part B Rev*, 2010. **16**(4): p. 427-34.
32. Simon, A.M., M.B. Manigrasso, and J.P. O'Connor, *Cyclo-oxygenase 2 function is essential for bone fracture healing*. *Journal of Bone and Mineral Research*, 2002. **17**(6): p. 963-976.
33. Gerstenfeld, L.C., et al., *Differential inhibition of fracture healing by non-selective and cyclooxygenase-2 selective non-steroidal anti-inflammatory drugs*. *J Orthop Res*, 2003. **21**(4): p. 670-5.
34. Leonelli, S.M., et al., *Effects of a cyclooxygenase-2 inhibitor (rofecoxib) on bone healing*. *Am J Orthop (Belle Mead NJ)*, 2006. **35**(2): p. 79-84.
35. Koester, M.C. and K.P. Spindler, *Pharmacologic agents in fracture healing*. *Clin Sports Med*, 2006. **25**(1): p. 63-73, viii.
36. Pountos, I., et al., *Do nonsteroidal anti-inflammatory drugs affect bone healing? A critical analysis*. *ScientificWorldJournal*, 2012. **2012**: p. 606404.

37. Wheeler, P. and M.E. Batt, *Do non-steroidal anti-inflammatory drugs adversely affect stress fracture healing? A short review*. British Journal of Sports Medicine, 2005. **39**(2): p. 65-69.
38. Wickerts, L., et al., *Coxibs: is there a benefit when compared to traditional non-selective NSAIDs in postoperative pain management?* Minerva Anestesiol, 2011. **77**(11): p. 1084-98.
39. Iolascon, G., et al., *NSAIDs and opioids in management of fragility fractures*. Aging Clin Exp Res, 2013. **25 Suppl 1**: p. S97-100.
40. Jirkof, P., et al., *Buprenorphine for pain relief in mice: repeated injections vs sustained-release depot formulation*. Lab Anim, 2015. **49**(3): p. 177-87.
41. Mouedden, M.E. and T.F. Meert, *Pharmacological evaluation of opioid and non-opioid analgesics in a murine bone cancer model of pain*. Pharmacol Biochem Behav, 2007. **86**(3): p. 458-67.
42. Aydin, O.N., et al., *The antinociceptive effects of systemic administration of tramadol, gabapentin and their combination on mice model of acute pain*. Agri, 2012. **24**(2): p. 49-55.
43. Evangelista Vaz, R., et al., *Preliminary pharmacokinetics of tramadol hydrochloride after administration via different routes in male and female B6 mice*. Vet Anaesth Analg, 2018. **45**(1): p. 111-122.
44. Matthiesen, T., et al., *The experimental toxicology of tramadol: an overview*. Toxicol Lett, 1998. **95**(1): p. 63-71.
45. Ehrnthaller, C., et al., *Complement C3 and C5 deficiency affects fracture healing*. PLoS One, 2013. **8**(11): p. e81341.
46. GV-SOLAS, *Fachinformation Schmerztherapie bei Versuchstieren aus dem Ausschuss für Anästhesie der GV-SOLAS*. 2015. Available from: <https://docplayer.org/23938076-Schmerztherapie-bei-versuchstieren.html> [cited 2021 November 26].
47. Haffner-Luntzer, M., et al., *Midkine-deficiency delays chondrogenesis during the early phase of fracture healing in mice*. PLoS One, 2014. **9**(12): p. e116282.
48. Heilmann, A., et al., *Systemic treatment with the sphingosine-1-phosphate analog FTY720 does not improve fracture healing in mice*. J Orthop Res, 2013. **31**(11): p. 1845-50.
49. Schlundt, C., et al., *Macrophages in bone fracture healing: Their essential role in endochondral ossification*. Bone, 2018. **106**: p. 78-89.
50. Flecknell, P., *Rodent analgesia: Assessment and therapeutics*. Vet J, 2018. **232**: p. 70-77.
51. Einhorn, T.A. and L.C. Gerstenfeld, *Fracture healing: mechanisms and interventions*. Nat Rev Rheumatol, 2015. **11**(1): p. 45-54.
52. Claes, L., S. Recknagel, and A. Ignatius, *Fracture healing under healthy and inflammatory conditions*. Nat Rev Rheumatol, 2012. **8**(3): p. 133-43.
53. Kowalczewski, C.J., et al., *Reduction of ectopic bone growth in critically-sized rat mandible defects by delivery of rhBMP-2 from keratine biomaterials*. Biomaterials, 2014. **35**(10): p. 3220-3228.
54. Schmidt-Bleek, K., et al., *Initiation and early control of tissue regeneration - bone healing as a model system for tissue regeneration*. Expert Opin Biol Ther, 2014. **14**(2): p. 247-59.
55. McDermott, A.M., et al., *Recapitulating bone development through engineered mesenchymal condensations and mechanical cues for tissue regeneration*. Science Translational Medicine, 2019. **11**(495): p. eaav7756.

56. Stefanowski, J., et al., *Spatial Distribution of Macrophages During Callus Formation and Maturation Reveals Close Crosstalk Between Macrophages and Newly Forming Vessels*. *Front Immunol*, 2019. **10**: p. 2588.
57. Dickhut, A., et al., *Calcification or dedifferentiation: requirement to lock mesenchymal stem cells in a desired differentiation stage*. *J Cell Physiol*, 2009. **219**(1): p. 219-26.
58. Mao, D.Y., et al., *Porous stable poly(lactic acid)/ethyl cellulose/hydroxyapatite composite scaffolds prepared by a combined method for bone regeneration*. *Carbohydrate Polymers*, 2018. **180**: p. 104-111.
59. Stevens, B., et al., *A review of materials, fabrication to enhance bone regeneration in methods, and strategies used engineered bone tissues*. *Journal of Biomedical Materials Research Part B-Applied Biomaterials*, 2008. **85b**(2): p. 573-582.
60. Muschler, G.E., C. Nakamoto, and L.G. Griffith, *Engineering principles of clinical cell-based tissue engineering*. *Journal of Bone and Joint Surgery-American Volume*, 2004. **86a**(7): p. 1541-1558.
61. Bancroft, G.N., et al., *Fluid flow increases mineralized matrix deposition in 3D perfusion culture of marrow stromal osteoblasts in a dose-dependent manner*. *Proc Natl Acad Sci U S A*, 2002. **99**(20): p. 12600-5.
62. Poole, A.R., et al., *Composition and structure of articular cartilage: a template for tissue repair*. *Clin Orthop Relat Res*, 2001. **391**(33): p. S26-33.
63. Newberry, W.N., et al., *Analysis of acute mechanical insult in an animal model of post-traumatic osteoarthritis*. *J Biomech Eng*, 1998. **120**(6): p. 704-9.
64. Johnson, C.I., D.J. Argyle, and D.N. Clements, *In vitro models for the study of osteoarthritis*. *Vet J*, 2016. **209**: p. 40-9.
65. Lin, H., et al., *Stem cell-based microphysiological osteochondral system to model tissue response to interleukin-1beta*. *Mol Pharm*, 2014. **11**(7): p. 2203-12.
66. Lozito, T.P., et al., *Three-dimensional osteochondral microtissue to model pathogenesis of osteoarthritis*. *Stem Cell Res Ther*, 2013. **4 Suppl 1**: p. S6.
67. Peck, Y., et al., *Establishment of an in vitro three-dimensional model for cartilage damage in rheumatoid arthritis*. *J Tissue Eng Regen Med*, 2018. **12**(1): p. e237-e249.
68. Ringe, J. and M. Sittinger, *Tissue engineering in the rheumatic diseases*. *Arthritis Res Ther*, 2009. **11**(1): p. 211.
69. Schwab, A., et al., *Ex vivo culture platform for assessment of cartilage repair treatment strategies*. *Altex*, 2017. **34**(2): p. 267-277.
70. DuRaine, G.D., et al., *Emergence of scaffold-free approaches for tissue engineering musculoskeletal cartilages*. *Ann Biomed Eng*, 2015. **43**(3): p. 543-54.
71. Murdoch, A.D., et al., *Chondrogenic differentiation of human bone marrow stem cells in transwell cultures: generation of scaffold-free cartilage*. *Stem Cells*, 2007. **25**(11): p. 2786-96.
72. Yasui, Y., et al., *Scaffold-free, stem cell-based cartilage repair*. *J Clin Orthop Trauma*, 2016. **7**(3): p. 157-63.
73. Occhetta, P., et al., *Hyperphysiological compression of articular cartilage induces an osteoarthritic phenotype in a cartilage-on-a-chip model*. *Nature Biomedical Engineering*, 2019. **3**(7): p. 545-557.

74. Piluso, S., et al., *Mimicking the Articular Joint with In Vitro Models*. Trends Biotechnol, 2019. **37**(10): p. 1063-1077.
75. Lv, M., et al., *Identification of Chondrocyte Genes and Signaling Pathways in Response to Acute Joint Inflammation*. Scientific Reports, 2019. **9**(1): p. 93.
76. Dingle, J.T., *The role of cellular interactions in joint erosions*. Clin Orthop Relat Res, 1984(182): p. 24-30.
77. Jenei-Lanzl, Z., A. Meurer, and F. Zaucke, *Interleukin-1 β signaling in osteoarthritis – chondrocytes in focus*. Cellular Signalling, 2019. **53**: p. 212-223.
78. Leizer, T., et al., *Interleukin-1 β and interleukin-1 α stimulate the plasminogen activator activity and prostaglandin E2 levels of human synovial cells*. Arthritis & Rheumatism, 1987. **30**(5): p. 562-566.
79. Bartolotti, I., et al., *A Roadmap of In Vitro Models in Osteoarthritis: A Focus on Their Biological Relevance in Regenerative Medicine*. Journal of clinical medicine, 2021. **10**(9): p. 1920.
80. Burmester, G.R., E. Feist, and T. Dorner, *Emerging cell and cytokine targets in rheumatoid arthritis*. Nat Rev Rheumatol, 2014. **10**(2): p. 77-88.
81. Gaber, T., et al., *Cellular energy metabolism in T-lymphocytes*. Int Rev Immunol, 2015. **34**(1): p. 34-49.
82. Kuhnke, A., et al., *Bioenergetics of immune cells to assess rheumatic disease activity and efficacy of glucocorticoid treatment*. Ann Rheum Dis, 2003. **62**(2): p. 133-9.
83. Gaber, T., et al., *Hypoxia inducible factor (HIF) in rheumatology: low O₂! See what HIF can do!* Ann Rheum Dis, 2005. **64**(7): p. 971-80.
84. Hartung, T., *Food for thought... on animal tests*. Altex, 2008. **25**(1): p. 3-16.
85. Firestein, G.S., *Rheumatoid arthritis in a mouse?* Nat Clin Pract Rheumatol, 2009. **5**(1): p. 1.
86. Damerou, A. and T. Gaber, *Modeling Rheumatoid Arthritis In Vitro: From Experimental Feasibility to Physiological Proximity*. Int J Mol Sci, 2020. **21**(21): p. 7916.
87. Peck, Y., et al., *Establishment of an in vitro three-dimensional model for cartilage damage in rheumatoid arthritis*. J Tissue Eng Regen Med, 2017. **12**(1):e237-e249.
88. Ribel-Madsen, S., et al., *A synoviocyte model for osteoarthritis and rheumatoid arthritis: response to ibuprofen, betamethasone, and ginger extract-a cross-sectional in vitro study*. Arthritis, 2012. **2012**: p. 505842.
89. Li, Z., Lin, Z., Lopez, M.L., O'Donnell, B., Li, X., Moran, I.J., Alexander, P.G., Goodman, S.B., Bunnell, B.A., Ling, H., Tuan, R.S., *Organ-on-a-chip System for the Modeling of Synovial Joint Pathologies*, in ORS Annual Meeting. 2019: Austin, texas.
90. Lang, A., et al., *Collagen I-based scaffolds negatively impact fracture healing in a mouse-osteotomy-model although used routinely in research and clinical application*. Acta Biomater, 2019. **86**: p. 171-184.
91. Lang, A., et al., *MIF does only marginally enhance the pro-regenerative capacities of DFO in a mouse-osteotomy-model of compromised bone healing conditions*. Bone, 2021. **154**: p. 116247.

92. Pfeiffenberger, M., et al., *The in vitro human fracture hematoma model - a tool for preclinical drug testing* ALTEX - Alternatives to animal experimentation., 2020. **37**(4): p. 561-578.
93. Bhumiratana, S., et al., *Large, stratified, and mechanically functional human cartilage grown in vitro by mesenchymal condensation*. Proceedings of the National Academy of Sciences of the United States of America, 2014. **111**(19): p. 6940-6945.
94. Franco, N.H., P. Sandøe, and I.A.S. Olsson, *Researchers' attitudes to the 3Rs—An upturned hierarchy?* PLOS ONE, 2018. **13**(8): p. e0200895.
95. Jirkof, P., J. Rudeck, and L. Lewejohann, *Assessing Affective State in Laboratory Rodents to Promote Animal Welfare—What Is the Progress in Applied Refinement Research?* Animals, 2019. **9**(12).
96. Deuis, J.R., L.S. Dvorakova, and I. Vetter, *Methods Used to Evaluate Pain Behaviors in Rodents*. Frontiers in molecular neuroscience, 2017. **10**: p. 284-284.
97. Turner, P.V., D.S. Pang, and J.L. Lofgren, *A Review of Pain Assessment Methods in Laboratory Rodents*. Comp Med, 2019. **69**(6): p. 451-467.
98. Jirkof, P., *Side effects of pain and analgesia in animal experimentation*. Lab Animal, 2017. **46**(4): p. 123-128.
99. Jirkof, P., et al., *Burrowing behavior as an indicator of post-laparotomy pain in mice*. Frontiers in behavioral neuroscience, 2010. **4**: p. 165-165.
100. Jirkof, P., et al., *Burrowing is a sensitive behavioural assay for monitoring general wellbeing during dextran sulfate sodium colitis in laboratory mice*. Lab Anim, 2013. **47**(4): p. 274-83.
101. Matsumiya, L.C., et al., *Using the Mouse Grimace Scale to reevaluate the efficacy of postoperative analgesics in laboratory mice*. J Am Assoc Lab Anim Sci, 2012. **51**(1): p. 42-9.
102. Arras, M., et al., *Assessment of post-laparotomy pain in laboratory mice by telemetric recording of heart rate and heart rate variability*. BMC Vet Res, 2007. **3**: p. 16.
103. Jirkof, P., et al., *Assessment of postsurgical distress and pain in laboratory mice by nest complexity scoring*. Lab Anim, 2013. **47**(3): p. 153-61.
104. Leach, M.C., et al., *The assessment of post-vasectomy pain in mice using behaviour and the Mouse Grimace Scale*. PLoS One, 2012. **7**(4): p. e35656.
105. Minville, V., et al., *Mouse model of fracture pain*. Anesthesiology, 2008. **108**(3): p. 467-72.
106. Majuta, L.A., et al., *Orthopedic surgery and bone fracture pain are both significantly attenuated by sustained blockade of nerve growth factor*. Pain, 2015. **156**(1): p. 157-165.
107. Vermeirsch, H., et al., *Bone cancer pain model in mice: evaluation of pain behavior, bone destruction and morphine sensitivity*. Pharmacology Biochemistry and Behavior, 2004. **79**(2): p. 243-251.
108. Lang, A., Wolter, A., Bucher, C., Jirkof, P., Rapp, A. E. , *Testing a New Microparticulate Depot Formulation of Buprenorphine for Sustained Post-Surgical Analgesia in Mouse Femoral Fracture Models* in ORS Annual Meeting. 2022: Tampa, FL.
109. Schreiner, V., et al., *Design and in vivo evaluation of a microparticulate depot formulation of buprenorphine for veterinary use*. Sci Rep, 2020. **10**(1): p. 17295.

110. Rundle, C.H., et al., *Fracture healing in mice deficient in plasminogen activator inhibitor-1*. *Calcif Tissue Int*, 2008. **83**(4): p. 276-84.
111. Grundnes, O. and O. Reikeras, *The importance of the hematoma for fracture healing in rats*. *Acta Orthop Scand*, 1993. **64**(3): p. 340-2.
112. Park, S.H., et al., *Effect of repeated irrigation and debridement on fracture healing in an animal model*. *J Orthop Res*, 2002. **20**(6): p. 1197-204.
113. Schell, H., et al., *The haematoma and its role in bone healing*. *J Exp Orthop*, 2017. **4**(1): p. 5.
114. Kolar, P., et al., *Human early fracture hematoma is characterized by inflammation and hypoxia*. *Clin Orthop Relat Res*, 2011. **469**(11): p. 3118-26.
115. Hoff, P., et al., *Immunological characterization of the early human fracture hematoma*. *Immunol Res*, 2016. **64**(5-6): p. 1195-1206.
116. Bastian, O.W., et al., *Neutrophils contribute to fracture healing by synthesizing fibronectin+ extracellular matrix rapidly after injury*. *Clin Immunol*, 2016. **164**: p. 78-84.
117. Chung, R., et al., *Roles of neutrophil-mediated inflammatory response in the bony repair of injured growth plate cartilage in young rats*. *J Leukoc Biol*, 2006. **80**(6): p. 1272-80.
118. Kovtun, A., et al., *The crucial role of neutrophil granulocytes in bone fracture healing*. *Eur Cell Mater*, 2016. **32**: p. 152-62.
119. Alexander, K.A., et al., *Resting and injury-induced inflamed periosteum contain multiple macrophage subsets that are located at sites of bone growth and regeneration*. *Immunology & Cell Biology*, 2017. **95**(1): p. 7-16.
120. Schlundt, C., et al., *Macrophages in bone fracture healing: Their essential role in endochondral ossification*. *Bone*, 2015. **106**: p. 78-89.
121. Toben, D., et al., *Fracture healing is accelerated in the absence of the adaptive immune system*. *Journal of Bone and Mineral Research*, 2011. **26**(1): p. 113-124.
122. Grassi, F., et al., *T cell subsets differently regulate osteogenic differentiation of human mesenchymal stromal cells in vitro*. *J Tissue Eng Regen Med*, 2016. **10**(4): p. 305-14.
123. Bucher, C.H., et al., *Experience in the Adaptive Immunity Impacts Bone Homeostasis, Remodeling, and Healing*. *Frontiers in Immunology*, 2019. **10**: p. 797.
124. Hoff, P., et al., *A Pronounced Inflammatory Activity Characterizes the Early Fracture Healing Phase in Immunologically Restricted Patients*. *Int J Mol Sci*, 2017. **18**(3): p. DOI: 10.3390/ijms18030583.
125. Auer, J.A. and D.W. Grainger, *Fracture management in horses: Where have we been and where are we going?* *Vet J*, 2015. **206**(1): p. 5-14.
126. Pfeiffenberger, M., et al., *Hypoxia and mesenchymal stromal cells as key drivers of initial fracture healing in an equine in vitro fracture hematoma model*. *PLOS ONE*, 2019. **14**(4): p. e0214276.
127. Pfeiffenberger, M., et al., *Functional Scaffold-Free Bone Equivalents Induce Osteogenic and Angiogenic Processes in a Human In Vitro Fracture Hematoma Model*. *Journal of Bone and Mineral Research*, 2021. **36**(6): p. 1189-1201.
128. Ponomarev, I.V., L.M. Kochneva, and D. Barnewitz, *Effect of 3D chondrocyte culturing conditions on the formation of extracellular matrix in cartilage tissue-engineering constructs*. *Bull Exp Biol Med*, 2014. **156**(4): p. 548-55.

129. DuRaine, G.D., et al., *Emergence of scaffold-free approaches for tissue engineering musculoskeletal cartilages*. *Annals of biomedical engineering*, 2015. **43**(3): p. 543-554.
130. Hoff, P., et al., *Human immune cells' behavior and survival under bioenergetically restricted conditions in an in vitro fracture hematoma model*. *Cellular & Molecular Immunology*, 2013. **10**(2): p. 151-158.
131. Lin, Z., et al., *Gene expression profiles of human chondrocytes during passaged monolayer cultivation*. *Journal of Orthopaedic Research*, 2008. **26**(9): p. 1230-1237.
132. Duan, L., et al., *Epigenetic regulation in chondrocyte phenotype maintenance for cell-based cartilage repair*. *American journal of translational research*, 2015. **7**(11): p. 2127-2140.
133. Bernstein, P., et al., *Expression pattern differences between osteoarthritic chondrocytes and mesenchymal stem cells during chondrogenic differentiation*. *Osteoarthritis and Cartilage*, 2010. **18**(12): p. 1596-1607.
134. Mauck, R.L., X. Yuan, and R.S. Tuan, *Chondrogenic differentiation and functional maturation of bovine mesenchymal stem cells in long-term agarose culture*. *Osteoarthritis and Cartilage*, 2006. **14**(2): p. 179-189.
135. Diederichs, S., et al., *Chondral Differentiation of Induced Pluripotent Stem Cells Without Progression Into the Endochondral Pathway*. *Frontiers in Cell and Developmental Biology*, 2019. **7**: p. 270.
136. Lee, J., et al., *Human iPSC-derived chondrocytes mimic juvenile chondrocyte function for the dual advantage of increased proliferation and resistance to IL-1 β* . *Stem cell research & therapy*, 2017. **8**(1): p. 244-244.
137. Katz, D.B., et al., *An immortalized human adipose-derived stem cell line with highly enhanced chondrogenic properties*. *Biochemical and Biophysical Research Communications*, 2020. **530**(1): p. 252-258.
138. Li, Z., et al., *Mechanical load modulates chondrogenesis of human mesenchymal stem cells through the TGF-beta pathway*. *Journal of cellular and molecular medicine*, 2010. **14**(6A): p. 1338-1346.
139. Bhumiratana, S., et al., *Large, stratified, and mechanically functional human cartilage grown in vitro by mesenchymal condensation*. *Proc Natl Acad Sci U S A*, 2014. **111**(19): p. 6940-5.
140. Vincent, H.K., et al., *Hyaluronic Acid (HA) Viscosupplementation on Synovial Fluid Inflammation in Knee Osteoarthritis: A Pilot Study*. *Open Orthop J*, 2013. **7**: p. 378-84.
141. Haase, T., et al., *Discerning the spatio-temporal disease patterns of surgically induced OA mouse models*. *PLOS ONE*, 2019. **14**(4): p. e0213734.
142. Hwang, H.S. and H.A. Kim, *Chondrocyte Apoptosis in the Pathogenesis of Osteoarthritis*. *International Journal of Molecular Sciences*, 2015. **16**(11): p. 26035-54.
143. Kar, S., et al., *Modeling IL-1 induced degradation of articular cartilage*. *Arch Biochem Biophys*, 2016. **594**: p. 37-53.
144. Orozco, G.A., et al., *A novel mechanobiological model can predict how physiologically relevant dynamic loading causes proteoglycan loss in mechanically injured articular cartilage*. *Sci Rep*, 2018. **8**(1): p. 15599.
145. Smith, D.W., et al., *Computational model for the analysis of cartilage and cartilage tissue constructs*. *J Tissue Eng Regen Med*, 2016. **10**(4): p. 334-47.

146. Sunkara, V. and M. von Kleist, *Coupling cellular phenotype and mechanics to understand extracellular matrix formation and homeostasis in osteoarthritis*. IFAC-PapersOnLine, 2016. **49**(26): p. 38-43.
147. Nguyen, D.X., et al., *Regulatory T cells as a biomarker for response to adalimumab in rheumatoid arthritis*. J Allergy Clin Immunol, 2018. **142**(3): p. 978-980.e9.
148. Pattacini, L., et al., *Differential effects of anti-TNF- α drugs on fibroblast-like synoviocyte apoptosis*. Rheumatology, 2009. **49**(3): p. 480-489.
149. Gaber, T., et al., *Disentangling the effects of tocilizumab on neutrophil survival and function*. Immunologic Research, 2016. **64**(3): p. 665-676.
150. Shin, B.-H., et al., *Tocilizumab (Anti-IL-6R) Suppressed TNF α Production by Human Monocytes in an In Vitro Model of Anti-HLA Antibody-Induced Antibody-Dependent Cellular Cytotoxicity*. Transplantation Direct, 2017. **3**(3): p. e139.
151. Stein, R., et al., *Combining Milatuzumab with Bortezomib, Doxorubicin, or Dexamethasone Improves Responses in Multiple Myeloma Cell Lines*. Clinical Cancer Research, 2009. **15**(8): p. 2808.
152. Boukhechba, F., et al., *Human Primary Osteocyte Differentiation in a 3D Culture System*. Journal of Bone and Mineral Research, 2009. **24**(11): p. 1927-1935.
153. Gao, P., et al., *Beta-tricalcium phosphate granules improve osteogenesis in vitro and establish innovative osteo-regenerators for bone tissue engineering in vivo*. Sci Rep, 2016. **6**: p. 23367.
154. Liu, G., et al., *Tissue-engineered bone formation using human bone marrow stromal cells and novel β -tricalcium phosphate*. Biomedical Materials, 2007. **2**(2): p. 78-86.
155. Herten, M., et al., *Surface- and nonsurface-dependent in vitro effects of bone substitutes on cell viability*. Clin Oral Investig, 2009. **13**(2): p. 149-55.
156. Lin, Z., et al., *Osteochondral Tissue Chip Derived From iPSCs: Modeling OA Pathologies and Testing Drugs*. Frontiers in Bioengineering and Biotechnology, 2019. **7**(411).
157. Ng, J., J. Bernhard, and G. Vunjak-Novakovic, *Mesenchymal Stem Cells for Osteochondral Tissue Engineering*. Methods in molecular biology (Clifton, N.J.), 2016. **1416**: p. 35-54.
158. He, Y., et al., *Pathogenesis of Osteoarthritis: Risk Factors, Regulatory Pathways in Chondrocytes, and Experimental Models*. Biology (Basel), 2020. **9**(8): p. 194.
159. Holley, T., Bowe, G., Campia, I., Belz, S., Bergren, E., Janusch Roi, A., Wittwehr, C., Whelan, M., *Inventory of the 3Rs knowledge sources*, J.R.C.J. European Commission, Editor. 2017. Available from: <http://data.europa.eu/89h/jrc-eurl-ecvam-eurl-ecvam-3rs> [cited 2021 November 26].
160. Poole, T., *Happy animals make good science*. Lab Anim, 1997. **31**(2): p. 116-24.

Danksagung

Mein besonderer Dank gilt Prof. Dr. Frank Buttgerit für seine motivierende und stetige Unterstützung bei der Initiierung und Durchführung der 3R-Projekte und meiner persönlichen Weiterentwicklung hin zur Selbstständigkeit. Weiterhin gilt mein Dank der gesamten Arbeitsgruppe Buttgerit - insbesondere Dr. Timo Gaber, Dr. Paula Hoff, Manuela Jakstadt, Gabriele May und Dr. Cindy Strehl für ihren jahrelangen Beistand, ihre Kollegialität und Unterstützung bei der Umsetzung diverser Projekte. Ganz besonders möchte ich mich bei meinen unglaublichen Studentinnen und Studenten bedanken, die mich in den letzten Jahren begleitet und meinen wissenschaftlichen Werdegang auf zahlreiche Weise bereichert haben. Ohne ihre unermüdlichen und großartigen Arbeiten wäre diese Habilitation nicht zustande gekommen. Vielen Dank an Janika Bartsch, Alexandra Damerau, Dr. Mattea Durst, Aditi Kuppe, Dr. Moritz Pfeiffenberger und Dr. Marie-Christin Weber. Dr. Katharina Schmidt-Bleek hat wie keine andere meinen Umgang mit Tieren im Experiment geprägt und mich in meinen Ambitionen im 3R-Bereich immer bestärkt und unterstützt. Danke Kate!

Ich danke meinen zahlreichen Kooperationspartnern. Dabei gilt ein besonderer Dank Dr. Igor Ponomarev und Dr. Dirk Barnewitz für die jahrelange Zusammenarbeit und die Zurverfügungstellung der dreidimensionalen trägerfreien Konstrukte. Weiterhin bedanke ich mich bei Dr. Paulin Jirkof, die meine wissenschaftliche Laufbahn in den letzten Jahren nicht nur als Kooperationspartnerin, sondern auch als Freundin, begleitete und mein Verständnis im Bereich Schmerzmanagement und Schmerzerkennung in der Maus immer wieder erweiterte und bereicherte. Außerdem möchte ich mich bei Dr. Rainald Ehrig und Lisa Fischer für die großartige Zusammenarbeit und mein mathematisches Abenteuer bedanken. Auch Prof. Dr. Christa Thöne-Reineke gilt mein Dank für die unermüdliche Unterstützung in der Betreuung von Doktoranden sowie die hilfreichen Projektdiskussionen und meine persönliche Unterstützung als Nachwuchswissenschaftlerin. Dr. Christian Bucher danke ich für die vielen persönlichen und wissenschaftlichen Austausche während meiner Postdoc-Zeit, sowie die Unterstützung bei dem ein oder anderen Vorhaben „mal wieder etwas zu scannen“. Zu guter Letzt danke ich Dr. Laura Behm für die erfolgreichen und fröhlichen Jahre der Zusammenarbeit an ReThink3R – ich kann mir keine bessere Projektpartnerin vorstellen oder wünschen. Weiterhin gilt mein tiefer Dank Mark, der meinen Weg vom Beginn des Studiums bis hierhin als bester Freund begleitet hat und auch weiterhin begleiten wird. Andy und Mephisto – ihr seid mein Leben und erfüllt mich jeden Tag mit Freude und Liebe – Happy Family! Ich danke meinen Eltern Susanne und Jens sowie meiner Schwester Lissy für die Liebe und unermüdliche Unterstützung in allen Lebenslagen. Es erfüllt mich mit besonderem Stolz, dass unser Lang-Lang-Paper Teil dieser Habilitation ist. Ohne euch wäre ich nicht der Mensch, der ich heute bin.

Erklärung

§ 4 Abs. 3 (k) der HabOMed der Charité

Hiermit erkläre ich, dass

- weder früher noch gleichzeitig ein Habilitationsverfahren durchgeführt oder angemeldet wurde,
- die vorgelegte Habilitationsschrift ohne fremde Hilfe verfasst, die beschriebenen Ergebnisse selbst gewonnen sowie die verwendeten Hilfsmittel, die Zusammenarbeit mit anderen Wissenschaftlern und Wissenschaftlerinnen und mit technischen Hilfskräften sowie die verwendete Literatur vollständig in der Habilitationsschrift abgegeben wurden,
- mir die geltende Habilitationsordnung bekannt ist.

Ich erkläre ferner, dass mir die Satzung der Charité - Universitätsmedizin Berlin zur Sicherung Guter Wissenschaftlicher Praxis bekannt ist und ich mich zur Einhaltung dieser Satzung verpflichte.